

Ionic Self-Assembled Multilayers in a Long Period Grating Sensor
for Bacteria and as a Source of Second-Harmonic Generation
Plasmonically Enhanced by Silver Nanoprisms

Kelly R. McCutcheon

Dissertation submitted to the Faculty of the
Virginia Polytechnic Institute and State University
in partial fulfillment of the requirements for the degree of

Doctor of Philosophy

in

Physics

James R. Heflin, Chair

Mark L. Pitt

Chenggang Tao

Thomas J. Inzana

June 17, 2019

Blacksburg, Virginia

Keywords: ionic self-assembled multilayers, organic thin films, long period fiber gratings,
turn-around point long period gratings, *Brucella*, optical biosensors, nonlinear optics,
second-harmonic generation, plasmonics, silver nanoprisms

Copyright 2019, Kelly R. McCutcheon

Ionic Self-Assembled Multilayers in a Long Period Grating Sensor for Bacteria and as a Source of Second-Harmonic Generation Plasmonically Enhanced by Silver Nanoprisms

Kelly R. McCutcheon

(ABSTRACT)

Ionic self-assembled multilayers (ISAMs) can be formed by alternately dipping a substrate in anionic and cationic polyelectrolytes. Each immersion deposits a monolayer via electrostatic attraction, allowing for nanometer-scale control over film thickness. Additionally, ISAM films can be applied to arbitrary substrate geometries and can easily incorporate a variety of polymers and nanoscale organic or inorganic inclusions. The ISAM technique was used to tune and functionalize a rapid, sensitive fiber optic biosensor for *Brucella*, a family of bacteria that are detrimental to livestock and can also infect humans. The sensor was based on a turn-around point long period fiber grating (TAP-LPG). Unlike conventional LPGs, in which the attenuation peaks shift wavelength in response to environmental changes, TAP-LPGs have a highly sensitive single wavelength peak with variable attenuation. ISAMs were applied to a TAP-LPG to tune it to maximum sensitivity and to facilitate cross-linking of receptor molecules. Biotin and streptavidin were used to attach biotinylated hybridization probes specific to distinct species of *Brucella*. The sensor was then exposed to lysed cell cultures and tissue samples in order to evaluate its performance. The best results were obtained when using samples from *Brucella* infected mice, which produced a transmission change of $6.0 \pm 1.4\%$ for positive controls and $0.5 \pm 2.0\%$ for negative controls. While the sensor was able to distinguish between positive and negative samples, the relatively short dynamic range of the available fiber limited its performance. Attempts to fabricate new TAP-LPGs using

a CO₂ laser were unsuccessful due to poor laser stability. A second application of the ISAM technique was as a source of second-harmonic generation (SHG). SHG is a nonlinear optical process in which light is instantaneously converted to half its wavelength in the presence of intense electric fields. Localized surface plasmons (LSPs) in metal nanoparticles produce strong electric field enhancements, especially at sharp tips and edges, that can be used to increase SHG. Colloidally grown silver nanoprisms were deposited onto nonlinear ISAM films and conversion of 1064 nm Nd:YAG radiation to its 532 nm second-harmonic was observed. Little enhancement was observed when using nanoprisms with LSP resonance near 1064 nm due to their large size and low concentration. When using shorter wavelength nanoprisms, enhancements of up to 35 times were observed when they were applied by immersion, and up to 1380 times when concentrated nanoprisms were applied via dropcasting at high enough densities to broaden their extinction peak towards the excitation wavelength. A maximum enhancement of 2368 times was obtained when concentrated silver nanoprisms with LSP resonance around 900 nm were spincoated with an additional layer of PCBS.

Ionic Self-Assembled Multilayers in a Long Period Grating Sensor for Bacteria and as a Source of Second-Harmonic Generation Plasmonically Enhanced by Silver Nanoprisms

Kelly R. McCutcheon

(GENERAL AUDIENCE ABSTRACT)

Polyelectrolytes are long molecules composed of chains of charged monomers. When a substrate with a net surface charge is dipped into an oppositely charged polyelectrolyte solution, a single layer of molecules will be electrostatically deposited onto the substrate. Because the surface charge now appears to match the charge of the solution, no further deposition occurs. However, the process can be repeated by rinsing the substrate and immersing in a solution with the opposite charge. This technique forms ionic self-assembled multilayers (ISAMs), which can be assembled with nanometer-level control over thickness. The flexibility of polymer chemistry allows ISAMs to be formed from polyelectrolytes with a wide variety of properties. Additionally, the technique can easily incorporate other nanoscale materials, such as nanoparticles, clay platelets, and biological molecules, and has been investigated for applications ranging from dye-sensitized organic solar cells to drug delivery and medical implant coatings. This dissertation presents two applications of ISAM films. In one, ISAM films were used to tune and functionalize an optical biosensor for *Brucella*. Brucellosis primarily infects livestock, in which it causes significant reproductive problems leading to economic losses, but can also cause flu-like symptoms and more serious complications in humans. A rapid, sensitive test for *Brucella* is required to monitor herds and adjacent wild carriers, such as elk and bison. Optical biosensors, which operate by detecting changes due to the interaction between light and the stimulus, could satisfy this need. Long period fiber

gratings (LPGs) are periodic modulations induced in the core of an optical fiber that cause transmitted light to be scattered at a resonant wavelength, resulting in attenuation. Conventional LPGs respond to changes in strain, temperature, or external refractive index by shifting their resonant wavelength. When special conditions are met, an LPG may exhibit a turn-around point (TAP), where dual peaks coalesce into a single peak with a constant wavelength but variable attenuation depth. TAP-LPGs are more sensitive than ordinary LPGs, and could be developed into inexpensive sensors with single-wavelength light sources and detectors. In this work, ISAMs were deposited onto an LPG to tune it near its TAP. Segments of single-stranded DNA, called hybridization probes, that were specific to individual species of *Brucella* were attached to the ISAM film before the sensor was exposed to lysed bacterial cultures. It was found that the sensor could distinguish between *Brucella* and other types of bacteria, but was less successful at distinguishing between *Brucella* species. The project was limited by the available TAP-LPGs, which had less dynamic range than those used in prior work by this group. Attempts were made to establish a new supply of TAP-LPGs by fabrication with a CO₂ laser, but these efforts were unsuccessful due to poor laser stability. The second project discussed in this dissertation investigated ISAM films as a source of second-harmonic generation (SHG), a nonlinear optical process in which light is converted to half its fundamental wavelength in the presence of intense electric fields. Nonlinear ISAMs were constructed by choosing a polyelectrolyte with a hyperpolarizable side group in which SHG can occur. The SHG efficiency was increased by factors of several hundred to several thousand by the addition of silver nanoprisms. Metal nanoparticles can produce strong electric field enhancements, especially at their tips and edges, when incident light causes resonant collective oscillations in their electrons called localized surface plasmons (LSPs). It was found that while silver nanoprisms whose LSP resonant wavelength matched the fundamental wavelength were too dilute to produce noticeable enhancement, better results could be obtained by depositing shorter wavelength nanoprisms at sufficient density to

broaden their extinction peak via interparticle interactions. The best enhancement observed was for a sample where concentrated silver nanoprisms with LSP resonance around 900 nm were dropcast onto an ISAM film and coated with an additional polymer layer, resulting in 2368 times more SHG than the plain ISAM film.

Contents

List of Figures	xiii
List of Tables	xxxi
List of Abbreviations	xxxii
1 Introduction	1
1.1 Ionic self-assembled multilayers	3
1.2 Turn-around point long period gratings	4
1.3 Optical biosensors	6
1.4 Second-harmonic generation	7
1.5 Plasmonic enhancement by silver nanoprisms	8
1.6 Dissertation outline	9
2 Background for the LPG biosensor	15
2.1 Organic thin films	15
2.1.1 Langmuir-Blodgett films	16
2.1.2 Ionic self-assembled multilayers	17
2.1.3 Applications of ISAM films	21

2.1.4	Polymers used in this work	28
2.2	Optical fiber gratings	31
2.2.1	Overview of optical fibers	31
2.2.2	Fiber grating fabrication and types	34
2.2.3	Grating fabrication	34
2.2.4	Types of fiber gratings	40
2.2.5	Phase-matching curves and turn-around point	42
2.3	Optical biosensors	46
2.3.1	Characterization of sensor performance	49
2.4	Bacterial detection	51
2.4.1	Current techniques for bacterial identification	51
2.4.2	Brucellosis	56
3	Background for plasmonic enhancement of second-harmonic generation	60
3.1	Nonlinear optics	60
3.1.1	Noncentrosymmetry	63
3.1.2	SHG theory	64
3.1.3	Wave equation approach to SHG	66
3.1.4	Nonlinear optical materials	75
3.1.5	Nonlinear properties of ISAM films	82

3.1.6	Applications of second-order nonlinear effects	88
3.2	Plasmonics	93
3.2.1	Optical properties of silver nanoprisms	99
3.2.2	Synthesis of silver nanoprisms	100
3.2.3	Enhancement of nonlinear optics by LSPR	103
4	Methods	107
4.1	Polymer preparation	108
4.2	Optical fiber preparation and biosensor assay	108
4.2.1	Initial fiber preparation: tuning the LPG to TAP	109
4.2.2	Running the biosensor test	111
4.2.3	Cleaning the fiber	117
4.3	LPG fabrication by CO ₂ laser	118
4.3.1	Fabrication setup	118
4.3.2	Fabrication procedure and typical parameters	120
4.3.3	Grating evaluation	122
4.4	Sample fabrication for plasmonic enhancement of SHG	123
4.4.1	Preparation of glass slides	124
4.4.2	Applying ISAM films to the slides	124
4.4.3	Applying nanoprisms to the slides	125

4.4.4	Spincasting	127
4.5	Characterization of samples and measurement of plasmonic enhancement . . .	127
4.5.1	Sample characterization	127
4.5.2	Optical setup for SHG measurement	128
4.5.3	SHG measurement procedure	132
5	TAP-LPG biosensor results and discussion	137
5.1	Prior work with <i>Histophilus somni</i>	137
5.2	Typical ISAM deposition	139
5.3	Determination of biological functionalization parameters	141
5.3.1	Streptavidin concentration	142
5.3.2	Varying concentration of second biotin layer	143
5.3.3	Probe concentration	145
5.4	Experiments using bacterial cultures	146
5.4.1	Sample concentration	146
5.4.2	Tests using miscellaneous bacterial species as negative controls	148
5.4.3	USDA samples	151
5.5	Mouse tissues	152
5.6	TAP-LPG fabrication by CO ₂ laser	154
5.6.1	Initial attempts using recommended parameters	154

5.6.2	LPG fabrication with altered parameters	156
5.6.3	Study of physical deformations at high writing powers and longer exposure times	160
5.6.4	Other factors contributing to fabrication failure	163
5.7	Summary of TAP-LPG biosensor results	164
6	Results of plasmonic enhancement of ISAM film SHG by silver nanoprisms	167
6.1	Prior SHG enhancement by this group	167
6.1.1	Silver nanoprisms applied by nanosphere lithography	168
6.1.2	Colloidal gold nanorods	170
6.2	Colloidal silver nanoparticles applied by stationary immersion	171
6.2.1	Early results using 1140 nm peak wavelength particles	171
6.2.2	Attempts to improve deposition	174
6.2.3	Attempts with long immersions (>1 week)	178
6.3	Immersion while stirring with the dipper machine	180
6.3.1	Initial attempts with 1140 nm prisms	180
6.3.2	Prisms (800 nm LSPR) applied to PAH instead of 3.5 bilayers PAH/PCBS	183
6.3.3	Prisms (950 nm LSPR) applied to 3.5 bilayers PAH/PCBS	186
6.4	Prisms applied by centrifuging and dropcasting	188
6.5	Further treatments to deposited nanoparticles	201
6.5.1	Applying ISAMs on top of prisms	203

6.5.2	Spincasting polymers on top	209
6.6	Summary of plasmonic enhancement results	218
7	Conclusions	223
	Bibliography	229

List of Figures

2.1	Diagram of the Langmuir-Blodgett technique. The substrate is carefully drawn through a monolayer of amphiphilic molecules at the liquid-gas interface. Moving barriers maintain the uniformity of the film as it is depleted by deposition.	16
2.2	Process of depositing ISAM layers onto a substrate with a negative surface charge, such as glass. In the third step pictured, 1.5 bilayers have been deposited.	17
2.3	Morphology of polymer deposition at (a) low salinity or high polymer charge and (b) high salinity or near-neutral polymers	19
2.4	Conventional dye-sensitized solar cell. Photons excite electrons in dye (red) that are conducted away by TiO ₂ nanoparticles. The electrons are replaced by ions from an electrolyte solution, completing the circuit. ISAM DSSCs replace the electrolyte, and sometimes the dye, with more stable polyelectrolyte layers.	25
2.5	Chemical structures of (a) PAH, (b) PCBS, and (c) PMMA	29
2.6	Azobenzene functional group structure	30
2.7	Basic structure of an optical fiber. The fiber cross section (a) consists of a central core surrounded by a lower refractive index cladding, confining light to the core by total internal reflection. In the simplest case, a step-index fiber (b) has a sharp change between the core and cladding indexes.	32

2.8	Basic behavior of fiber gratings. Fiber Bragg gratings (a) reflect light by Bragg reflection into identical counterpropagating modes. Long period gratings (b) couple forward propagating light to lossy cladding modes.	41
2.9	Simulated PMCs for coupling to (a) low-order modes and (b) high-order modes. Dots have been added to the higher-order modes indicate the local maxima, where TAP occurs. Generated in Mathematica using Sellmeier coefficient values for 93% silica, 7% GeO ₂ glass, based on theory presented in references [1] and [2].	44
2.10	Behavior near the TAP. The PMC of the $LP_{0,15}$ mode is shown in (a), and a sketch of the transmission spectrum is shown in (b). Before the TAP (blue), the spectrum has a pair of resonant wavelengths. At the TAP (red), these combine into a single attenuation at λ_{TAP} . A little beyond the TAP (black) the coupling rapidly decreases in strength.	45
2.11	Kretschmann configuration of an SPR biosensor. Analyte (green) is flowed past receptor ligands (blue) immobilized on a gold film applied to the back of a prism. A light source is directed at the back side of the sensor surface, and reflection is monitored at different angles of incidence. The resonant angle, at which reflected light is attenuated by SPR absorption, varies when binding occurs.	48

3.1	Schematics of second-order nonlinear optical processes. Sum-frequency generation produces an output wave with a frequency equal to the sum of the input frequencies (a) . Difference-frequency generation produces an output wave with a frequency equal to the difference between the input frequencies (b). Second-harmonic generation produces an output wave with double the input frequency (c).	62
3.2	Relative intensity of normalized field amplitudes for the fundamental and second-harmonic fields as they propagate, for perfect phase-matching and $\Gamma=0$	73
3.3	Plot of intensity versus phase mismatch for SFG. The conversion efficiency falls off rapidly away from $\Delta k = 0$	74
3.4	Configuration of organic chromophores. A diagram of electron orbitals in ethylene (a) demonstrates the difference between σ bonds (teal), which are formed by overlapping orbitals, and π bonds (red), which are formed by adjacent orbitals and thus have less localized electrons. Nearly all NLO chromophores are formed by an electron donor and acceptor linked by a π bond containing bridge (b). The π bond bridge is often a benzene or stilbene analog (c)	79
3.5	Different approaches to nonlinear polymers. In guest-host systems the chromophore is held in place by the polymer framework without covalent bonds. In main-chain and side-chain polymers the chromophore is part of the repeating monomer unit. In cross-linked polymers the chromophore forms part of the cross-linking bridge between separate polymer chains.	81

3.6	Diagrams showing the chromophore tilt angle, ψ , with respect to the substrate normal (a), and showing how a net polar order can still exist (b) when $\bar{\psi}$ is in the range of 30-40°, as has been observed experimentally for PAH/PCBS films.	84
3.7	For a sufficiently small nanoparticle ($d \ll \lambda$), the field can be treated as uniform across the sphere, which is known as the quasi-static approximation (a). The dielectric function for silver [3] (b) has a small imaginary component and a large negative real component, allowing the Frölich condition to be satisfied.	95
3.8	Process of making silver nanoprisms via nanosphere lithography. A monolayer of polystyrene nanospheres is deposited, then a thin silver film is evaporated onto the surface. When the nanospheres are removed silver nanotriangles remain in the interstices.	100
3.9	Process of seed-mediated silver nanoprism formation, as proposed by Aherne [4]. Growth is preferred at the exposed hcp faces and the three edges where the {100} face dominates due to starting asymmetry in the crystal. These edges grow faster, resulting in a triangular shape.	103
4.1	Setup for applying liquids to the fiber grating. The grating was held fixed, and the height-adjustable stage was raised under it such that the fiber nestled in the groove along the length of the block and the grating was located in the larger rounded cavity. Liquids were dropped into this reservoir by pipette and remained in place due to surface tension.	109
4.2	Diagram of change in the bare fiber spectra after repeated cleaning cycles. Over the course of weeks of experiments, the attenuation of the bare fiber would increase, meaning there was less dynamic range available before reaching the TAP. This could be corrected by retuning with HF acid etching.	110

4.3	Chemical structures for (a) biotin, and (b) NHS-LC-LC-biotin	114
4.4	Typical development of the transmission spectrum after each step of the assay. The attenuation increased significantly due to application of the biotin and streptavidin layers. A slight backward change was consistently observed after adding the hybridization probe. Exposure to the positive control increased the attenuation, while exposure to the negative control had almost no effect on the attenuation.	115
4.5	Apparatus for cleaning the fiber by sulfonitric acid. The fiber was secured in a loop shape using a simple alligator clip so the jacketless grating was submerged in slowly stirred steaming sulfonitric acid.	117
4.6	Diagram of the CO ₂ writing setup (a). Alignment of the elliptical laser spot on the fiber (b).	119
4.7	(a) Variable transmission spectra obtained a single length of SMF-28e. The initial transmission (black) was very low, so the ends were recleaved. This improved the transmission strength, but details of the spectrum remained sensitive to the orientation of the fiber connectors attached to the light source and OSA. (b) Possible cleaving flaws that can lead to unpredictable scattering and reflections at connections.	123
4.8	Setup for applying nanoprisms to ISAM-coated slides using the (a) immersion method and (b) dropcast method. In both cases the top was sealed with Parafilm to prevent contamination and excess evaporation.	126

4.9	Optical setup used to measure SHG. A Q-switched Nd:YAG laser provided excitation at 1064 nm, and SHG light produced by the sample at 532 nm was detected by a PMT. The sample was mounted in a movable sample stage to allow the sample to be positioned accurately and undergo automated rotation during measurement. Electronic components are omitted from this diagram, but their attachments can be seen in [5].	129
4.10	Procedure for measuring SHG enhancement. The undecorated ISAM film is measured at a range of angles as a control (a). Next, the nanoprism region of the sample is measured at a lower power to avoid damage to the nanoparticles (b).	133
4.11	Fringes observed from plane-parallel substrates coated on both sides with nonlinear thin films. (a) Variation in path length as the sample angle changes results in an interference pattern. (b) Typical fringe pattern enclosed in an envelope for an ISAM coated slide.	135
5.1	Results for tests of <i>H. somni</i> 2336 cells at 100, 400, 1000, 2000, and 12500 cfu in 0.5 mL. Each assay was run three times and averaged, with error bars representing the standard deviation. Samples containing 0 cfu of <i>H. somni</i> were completed using 50,000 cfu of <i>E. coli</i> DH5 α . These assays utilized a higher sensitivity fiber with a maximum attenuation of -27 dB.	139
5.2	Typical evolution of transmission spectrum in PBS between ISAM deposition steps. The single peak deepens as the coating thickness is increased, achieving a maximum attenuation at the TAP before splitting into dual peaks.	141

5.3	Results for tests comparing the sensor’s performance with different concentrations of streptavidin. Each streptavidin concentration was tested twice and the results were averaged. Higher concentrations of streptavidin did not increase streptavidin deposition or improve the sensor’s ability to detect and distinguish bacterial samples at 10^5 cfu/mL.	142
5.4	Results for tests comparing different concentrations of the second biotin layer. Because tests with bacteria utilize biotinylated hybridization probes attached to streptavidin immobilized on the fiber, biotin was used as a stand-in to economically investigate the benefits of using higher probe concentrations. A negative control consisting of PBS and DMSO, without NHS-LC-LC-biotin, was also tested (0 nmol/mL). The standard 1.2 nmol/mL probe concentration was omitted from these tests with biotin, but was examined in a later comparison of probe concentrations (Section 5.3.3).	144
5.5	Results for tests of the sensor at the typical probe concentration (1.2 nmol/mL), as well as two elevated concentrations. The probe attachment resulted in a negative change in attenuation, for reasons that remain unclear. Higher probe concentrations resulted in slightly higher signals for both the positive (<i>B. abortus</i>) and negative (<i>E. coli</i>) controls.	145
5.6	Results from exposing the biosensor to <i>Brucella</i> samples at 10^4 to 10^6 cfu/mL. The change in transmission was only slightly higher for positive controls than for negative controls, and no correlation with concentration was observed. . .	147

5.7	Results for tests using species specific DNA probes to distinguish individual species of <i>Brucella</i> from other non- <i>Brucella</i> negative controls. The positive controls were (a) <i>B. abortus</i> , (b) <i>B. melitensis</i> , or (c) <i>B. suis</i> . Each <i>Brucella</i> strain was tested versus five non- <i>Brucella</i> bacterial samples. While some negative control species were repeated, each of the fifteen negative bacterial strains were from unique batches (Table 5.1). Each test was repeated and the results were averaged. The average results of all thirty assays is presented in (d). Error bars indicate the standard deviation between the repeated measurements. The transmission change was always larger for the positive controls, but in many cases the standard deviations for positive and negative controls overlapped.	149
5.8	Results of tests distinguishing <i>B. abortus</i> from <i>B. melitensis</i> and <i>B. suis</i> , using samples provided by the USDA (Table 5.2). Individual assays (a) often resulted in a negative change in attenuation, which was the opposite of what was expected. The mean signal of all tests (b) was about the same for positive and negative samples, due to the high variability of the individual assays. . .	152
5.9	Results obtained from tissues of mice infected with different <i>Brucella</i> species. The change in attenuation was slightly greater for spleen samples (a) than for liver samples (b).	153
5.10	Transmission spectra of the first fabricated LPG comparing its behaviors under different tensions (a) and surrounding refractive indexes (b). Apparent changes in the spectra were later attributed to poor stability due to low quality cleaves, rather than mode coupling due to the grating.	155

5.11	Transmission spectra for an LPG fabricated using the recommended parameters, fabricated about a month after the initial attempts. This fiber exhibited no sensitivity to tension or surrounding refractive index, which further supports the hypothesis that the apparent response of the first fiber was an error due to poor connections at the fiber ends.	156
5.12	Transmission spectra of LPGs fabricated with grating periods from 200 to 206 μm (a), with a cutout of the peak near 1400 nm (b). The spectra for all four fibers were recorded with the fiber held taut in air. No resonant attenuation was observed.	157
5.13	Transmission spectra of LPGs fabricated with standard settings and grating periods from 205.5 to 208 μm in SMF-28e (a), or with periods of 204 to 205 μm in SMF-28r. All spectra recorded with the fiber held taut in air. No resonant attenuation was observed.	158
5.14	Selected transmission spectra for an LPGs fabricated at different powers between 10 and 11 W. No significant departures from the bulk spectrum was observed.	159
5.15	Transmission spectra for an LPG written using 6.8 W, 100 ms, and a period of 228.3 μm , based on parameters from literature [6]. The fiber was insensitive to changes in tension and external refractive index.	160
5.16	Images of a fiber written with 100 ms exposures, 7 iterations, 6.7 g prestrain mass, and 10 periods at each power. These powers were sufficient to taper the fiber. The physical deformations of the fiber are irregular, which may indicate that variations in the refractive index modulation from period to period prevented successful grating fabrication.	162

6.1	Extinction results from the nanosphere lithography project [7]. The in-plane dipole resonance caused an extinction of 0.25 (a) for 50 nm thick nanotriangles, when observed at four different locations on the same sample (traces a-d). Reprinted with permission from <i>Nano Letters</i> 7:254-258 [7]. Copyright 2007 American Chemical Society.	168
6.2	SHG results from the nanosphere lithography project [7]. For 72 nm thick nanotriangles on 3 bilayers of PAH/PCBS, the SHG intensity (a) was much larger for the ISAM film with nanoparticles than for a bare 40 bilayer film, or for nanotriangles in the absence of PCBS. The SHG had a quadratic relationship with the power of the fundamental beam, as expected. When increasing the numbers of bilayers (b) the SHG intensity of the bare film increases quadratically, but the intensity for films with nanoparticles saturates as the film thickness exceeds the penetration depth of the plasmonic field enhancements. Reprinted with permission from <i>Nano Letters</i> 7:254-258 [7]. Copyright 2007 American Chemical Society.	169
6.3	Deposition results for initial attempts to deposit 1140 nm wavelength particles onto 3.5 bilayers PAH/PCBS by immersion. The extinction (a) is low, and an SEM image (b) reveals that the nanoprisms were sparsely distributed. . .	172
6.4	SHG results for initial attempts to deposit 1140 nm wavelength particles onto 3.5 bilayers PAH/PCBS by immersion. Due to low prism density, essentially no SHG was observed from the prism decorated film at the low pump power required to avoid damage to the nanoprisms.	173

6.5	Results from a later attempt to deposit 1140 nm wavelength nanoprisms onto 3.5 bilayers PAH/PCBS by immersion, after diluting the nanoprisms. For unknown reasons, higher extinction (a) was achieved in this case than in previous attempts with the same solution. The SHG enhancement (b) compared to the bare film was 2.3 times.	175
6.6	Attempts to improve nanoparticle deposition by varying the underlying ISAM layers. Replacing PCBS with PAA (a) resulted in significant improvement. The concentration (b) of the final PAH layer was increased, which also improved the deposition density. Smaller changes were observed when varying the pH (c) of the final PAH layer and when increasing the dip duration (d) for each polymer layer in the underlying film. Using longer soak times (e) for the final PAH layer produced almost no change in extinction.	176
6.7	Absorbance of ISAM-coated slides immersed in 900 nm silver nanoprisms for about 1 week. The two samples shown came from different batches but the procedure used was the same.	179
6.8	Results for two samples prepared by immersing slides coated with 3.5 bilayers PAH/PCBS in an unused solution of 950 nm nanoprisms for two weeks. The extinction (a) exceeded 0.7 and was significantly broadened. SHG enhancements (b) of 19 and 35 times were observed.	181
6.9	SEM image at 50,000 times magnification of sample 180918-5, which exhibited 35 times SHG enhancement. The prisms appear blurry due to an additional layer of PCBS that was later spincoated onto them as part of the experiments discussed in Section 6.5. The absorbance and SHG prior to the spincoating treatment are presented in Figure 6.8.	182

6.10	Extinction from slides with 3.5 bilayers PAH/PCBS immersed in 2 times diluted 1140 nm silver nanoprisms in the dipper machine for different durations. Because extending the immersion to 48 hours failed to improve the nanoprism density, it was concluded that the nanoparticle solution was too dilute. . . .	183
6.11	SEM images at 50,000 times magnification for 800 nm wavelength prisms deposited onto PAH-coated slides by immersing in the dipper machine while stirring. The samples immersed for 5 hours (a) had less nanoprism density than samples immersed for 10 hours (b).	184
6.12	Absorbance and SHG results for 800 nm wavelength prisms deposited onto PAH-coated slides by immersing in the dipper machine while stirring for 300 minutes and 600 minutes. This resulted in high nanoparticle densities with extinctions (a) exceeding 0.6. Normalized SHG intensity for these samples (b) is plotted, with different axes for the regions with and without nanoprisms due to the enhanced signal from the hybrid films. The SHG for the 300 minute and 600 minute samples was 129 times and 135 times, respectively, larger than the SHG produced by the single PAH layer without added nanoprisms.	185
6.13	Results for 950 nm wavelength prisms applied to 3.5 bilayers PAH/PCBS for 2 hours in the dipper machine. All three slides were prepared with the same procedure, and the extinctions (a) were similar for all three samples. The SHG enhancements (b) ranged from 19 to 34 times.	187

6.14	Comparison of centrifuged and uncentrifuged 600 nm wavelength prisms. The extinction (a) of the nanoparticle solution was slightly lower after centrifuging and redistributing, which may indicate that some of the prisms were lost in the process. SEM images of the redistributed prisms (b) and stock solution (c) show that the nanoparticles retain their triangular shape after centrifugation.	189
6.15	Deposition results of year-old 1140 nm prisms, centrifuged and dropcast onto PAH. The peak extinction (a) was 0.3, which was an order of magnitude larger than what was typically observed in attempts prior to concentrating this solution. An SEM image (b) reveals that the particles remain triangular but appear somewhat damaged, possibly due to age.	190
6.16	SEM images at 50,000 times magnification for 900 nm wavelength prisms dropcast onto 3.5 bilayers PAH/PCBS at high concentration. The images correspond to samples 180528-3 (a) and 180528-4 (b) in Figure 6.17. Much higher density was achieved than for samples prepared by immersion.	191
6.17	Results for 900 nm wavelength prisms dropcast onto 3.5 bilayers PAH/PCBS at high concentration. The extinction (a) is high and very broad for all three samples. A wide range of enhancements to SHG (b), from 113 to 1380 times, was observed. The normalized SHG is plotted on different axes for the regions with and without nanoprisms, in order for fringe shapes from both regions to be discernible.	192

6.18 SEM images taken at 50,000 times magnification for high concentration prisms with LSPR wavelengths of (a) 600 nm, (b) 800 nm, and (c) 950 nm, dropcast onto 3.5 bilayers of PAH/PCBS using the same procedure in all three cases. The 800 nm prisms were later spincast with PCBS as part of the work described in Section 6.5, leading to their obscured appearance in the SEM image.	194
6.19 Extinction for high concentration prisms with LSPR wavelengths of 600 nm, 800 nm, and 950 nm dropcast onto 3.5 bilayers of PAH/PCBS, using the same procedure in all three cases. All three samples show significant broadening on the LSPR peak.	195
6.20 SHG results for high concentration prisms with LSPR wavelengths of 600 nm, 800 nm, and 950 nm, dropcast onto 3.5 bilayers of PAH/PCBS using the same procedure in all three cases. The 600 nm wavelength prisms (a) had an enhancement of 257 times. The 800 nm and 950 nm wavelength prisms (b) had enhancements of 405 times and 230 times, respectively.	196
6.21 SEM images taken at 50,000 times magnification for nanoprisms dropcast at (a) 33, (b) 67, (c) 100, and (d) 240 times the stock concentration. The type of aggregate present at 67 times the stock concentration was also observed at 240 times, but was absent at 33 and 100 times.	198
6.22 SEM images taken at 3000 times magnification for samples prepared at 67 (a) and 240 (b) times the stock concentration. Large aggregates were distributed across the surface in both cases.	199

6.23 Results for samples dropcast at different concentrations. This first attempt to study the influence of concentration on enhancement used nanoprism solutions concentrated by 33 to 240 times. All of the samples had very broad extinction peaks (a). The SHG enhancements (b) appeared to be optimized for a 67 times concentrated solution, for which the enhancements were about 1000 times.	200
6.24 SEM images at 50,000 times magnification of samples prepared at 22 (a) and 67 (b) times the stock concentration from batch 181115 presented in Figure 6.25. The density of the deposited nanoprisms is clearly higher at higher concentrations, although both of these samples failed to achieve enhancements above about 20 times.	201
6.25 Results from two further attempts to study concentration versus enhancement. One set of samples was prepared at concentrations from 22 to 67 times and is shown in shades of orange in both images, while a second was at 29 to 67 times and is shown in shades of blue. All of the extinction peaks (a) were very broad. The enhancement (b) appeared to be weakly correlated with the nanoprism concentration.	202
6.26 SEM images at 50,000 times magnification of samples dropcast at 67 times (a) and 200 times (b) the stock concentration, corresponding to the data presented in Figure 6.27.	203

6.27	Results from a final attempt to study concentration versus enhancement using a larger sample set. Concentrations from 50 to 200 times were tested. Extinctions (a) were very broad in all cases, but could not be obtained for the 200 times concentrated sample due to saturation. The relationship between concentration and enhancement (b) appears randomized.	204
6.28	SEM image at 50,000 times magnification of a sample prepared by immersing a PAH coated slide in 800 nm LSPR nanoprisms in the dipper machine for 300 minutes, with PAH/PCBS ISAM layers applied on top. The absorbance and SHG for this sample can be found in Figures 6.29 and 6.30a.	205
6.29	Extinction before and after applying ISAMs onto prisms deposited on PAH with the dipper for 300 minutes and 600 minutes. The additional ISAM layers had little effect on the peak extinction but did reduce the extinction at 1064 nm.	206
6.30	SHG results before and after applying ISAMs onto prisms deposited on PAH with the dipper machine. The additional ISAM layers caused a substantial decrease in SHG for the prisms deposited for 300 minutes (a), while the SHG remained about the same for the prisms deposited for 600 minutes (b). . . .	207
6.31	Change in peak extinction wavelength due to ISAM layers applied on top of deposited prisms.	208
6.32	Results for 1140 nm wavelength prisms “sandwiched” between ISAMs. The prisms were deposited onto 3.5 bilayers PAH/PCBS, then an additional 3.5 bilayers was applied to the sample. The additional ISAM layers had little effect on the extinction (a). The SHG enhancement (b) was 12.8 times. . . .	210

6.33	Results for PCBS spincast onto glass. Thickness was measured with the Dektak (a) and was found to vary proportionally with concentration. The SHG intensity (b) was of similar magnitude for all the samples tested, indicating that bulk PCBS did not contribute to the SHG.	212
6.34	Results for prisms deposited onto 3.5 bilayers PAH/PCBS using the dipper and then spincast with equal concentrations of PMMA and PCBS. The peak extinction (a) was significantly redshifted by both polymers. The SHG (b) for the PMMA coated slide remained about the same before and after spincasting, but the enhancement for the PCBS coated slide increased from 19.3 times to 140.1 times. The SHG from the regions with and without the nanoprisms is shown on different axes due to the differing magnitudes of normalized SHG.	214
6.35	Drop in extinction of deposited prisms due to a 2 minute exposure to the methanol-PCBS solution prior to spincasting. Methanol was found to be harmful to the nanoprisms, so their exposure was minimized in later experiments by performing the spincasting immediately after applying the methanol solution.	215
6.36	Extinction for 950 nm wavelength prisms applied via immersion and by drop-casting, before and after spincasting with 2 percent by weight PCBS. In both cases, spincasting redshifted the LSPR wavelength and decreased the peak extinction.	216

6.37	SHG for deposited 950 nm wavelength prisms before and after spincasting with 2 percent by weight PCBS. SHG was collected for slides prepared by immersion (a) and dropcasting (b). Spincasting did not increase the enhancement for the immersion slide, which started at about 35 times. Spincasting onto the prism side of the dropcast slide increased the enhancement from 84 times to 135 times.	217
6.38	Deposition results for 900 nm wavelength prisms dropcast at high concentrations. The extinctions (a) for slides prepared with concentrated nanoprisms were high and the peaks were broadened substantially. An SEM image (b) of the sample prepared at the highest achievable concentration for this aliquot volume shows close particle spacing, in contrast to the sparse density (c) observed on a sample prepared with the stock concentration.	219
6.39	SHG results for slides with prisms dropcast at high concentrations. The highest concentration (a) is shown separately from the samples at and at four times, two times, and one times the stock concentration (b) due to its large normalized SHG. An inset shows the normalized SHG for a region without prisms, which was about the same for all four samples.	220

List of Tables

2.1	Sellmeier coefficients used for PMC simulations in this work, based on [1] and [2].	43
5.1	Abbreviations used for negative control samples when attempting to distinguish <i>Brucella</i> species from other genera of bacteria, as presented in Figure 5.7.	150
5.2	Samples tested to distinguish <i>B. abortus</i> from <i>B. melitensis</i> and <i>B. suis</i> , using samples provided by the USDA. Results are presented in Figure 5.8	151
5.3	Default parameters used for writing LPGs, based on advice from a fellow researcher.	154

List of Abbreviations

API analytical profile index

BBO beta barium borate

BCV *Brucella* containing vacuole

BSPP bis(*p*-sulfonatophenyl) phenylphosphine dihydrate dipotassium salt

cDNA complementary DNA

cfu colony-forming units

DDA discrete dipole approximation

DMSO dimethyl sulfoxide

DSSC dye sensitized solar cell

ELISA enzyme-linked immunosorbent assay

FBG fiber Bragg grating

ISAMs ionic self-assembled multilayers

ITO indium tin oxide

KDP potassium dihydrogen phosphate

KTP potassium titanyl phosphate

LB Langmuir Blodgett

LPG long period grating

LSP localized surface plasmon

LSPR localized surface plasmon resonance

MALDI-TOF matrix assisted laser desorption/ionization time-of-flight

MRSA methicillin-resistant *Staphylococcus aureus*

NHS N-hydroxysuccinimide

NLO nonlinear optics

OLED organic light emitting diode

OSA optical spectrum analyzer

OTFT organic thin film transistor

PAA polyacrylic acid

PAH polyallylamine hydrochloride

PAMPs poly-(2-acrylamido-2-methylpropanesulfonic acid)

PBS phosphate buffered saline

PCBS poly-1-[4-(3-carboxy-4-hydroxy-phenylazo)benzenesulfonamido]-1,2-ethanediyl

PCR polymerase chain reaction

PDAC poly(diallyldimethyl ammonium chloride)

PDADMA poly(diallyldimethyl ammonium chloride)

PDDA poly(diallyldimethylammonium)

PMC phase matching curve

PMMA poly(methyl methacrylate)

PSS poly(sodium styrenesulfonate)

PTEBS poly[2-(3-thienyl)-ethoxy-4-butylsulfonate]

PVP poly(vinylpyrrolidone)

SH second-harmonic

SHG second-harmonic generation

SPP surface plasmon polariton

spp. species pluralis

SPR surface plasmon resonance

SWNT single-walled carbon nanotubes

TAP turn-around point

Chapter 1

Introduction

Self-assembled nanoscale thin film coatings, known as ionic self-assembled multilayers (ISAMs), can be applied to charged substrates by alternately submerging them in positively and negatively charged polyelectrolyte solutions. This technique is simple enough to be performed without the need for specialized equipment and allows for easy control of film thickness by changing the ionic strength and concentration of the polyelectrolyte solutions. In this dissertation, two applications of ISAM films are presented. In one, ISAM films were used as a component in an optical fiber biosensor for bacteria. In the second project, ISAM films were used as a medium for nonlinear optics.

The ability to quickly and accurately identify bacteria is necessary for clinical diagnostics, detecting foodborne pathogens, monitoring natural resources such as soil and groundwater, defense against bioterrorism, and a multitude of other applications. The development of rapid, specific, and sensitive biosensors is an area of active research. These demands can be met by optical biosensors, which use changes in light to detect chemical or biological molecules. Fiber optic biosensors have the additional benefits of being lightweight and portable. A fiber optic biosensor can be fabricated by using an optical fiber in which a periodic change in refractive index, called a grating, has been inscribed into the fiber core. The grating renders the fiber sensitive to environmental changes, including changes to the refractive index immediately outside of the fiber. By coating the surface of a fiber grating with receptor molecules, the external index of refraction is altered and binding events by the

analyte can be detected in real time.

ISAM films were applied to a fiber grating in order to assemble a biosensor for bacteria. The ISAM films were used to tune the fiber grating to conditions which maximized its sensitivity, and also facilitated the attachment of single-stranded DNA that was specific to certain bacteria. The biosensor studied in this work was used to identify the presence of different species of *Brucella*. *B. abortus* is a bacterial pathogen that interferes with the reproduction of cattle, sheep, and goats. While it has been largely eradicated from agricultural herds in developed nations, *B. abortus* remains endemic in wild populations of elk and bison. Because livestock can contract *B. abortus* from wild cervids, a sensor that can diagnose *B. abortus* in the field and distinguish it from less harmful *Brucella* species is necessary. In this work, a fiber grating with a self-assembled nanoscale coating used as an optical biosensor for *Brucella* is presented.

A second application of ISAM films, in which they were used as a source of nonlinear optics, was also studied. Nonlinear optics occurs in some materials when exposed to intense electric fields, such as those provided by laser light. While the polarization induced in a conventional material by an electric field is proportional to the field strength, in nonlinear materials the polarization varies with higher powers of the electric field amplitude. This can result in diverse phenomena, including various frequency-mixing processes and intensity dependent refractive indexes. Because conventional nonlinear materials are expensive and difficult to synthesize, there is a need for the development of alternatives. ISAM films can fulfill this need. The polyelectrolytes can be engineered to have hyperpolarizable structures in which nonlinear processes can occur, and the electrostatic environment created by the alternating charged layers helps to ensure the net polar order required for second-order nonlinear phenomena.

The nonlinear properties of ISAM films can be enhanced by the addition of plasmonic

nanoparticles. Electric fields can be enhanced hundreds to thousands of times within a few nanometers of metal nanostructures due to collective oscillations of electrons within the conductor. This is especially true for nanoparticles with sharp points, which cause crowding of the electric field lines, and for particles with high aspect ratios. In the second project presented in this work, silver nanoprisms were applied to self-assembled nanoscale thin films in order to plasmonically enhance the nonlinear behavior of the ISAM films.

The remainder of this chapter presents a brief introduction to the central concepts of these projects, including ISAMs, turn-around point long period gratings (TAP-LPGs), optical biosensors, second-harmonic generation (SHG), and plasmonic enhancement. In addition, an overview of this dissertation is presented.

1.1 Ionic self-assembled multilayers

ISAMs are organic thin films applied to a substrate by alternately dipping it in positive and negative polyelectrolyte solutions [8]. Each immersion deposits a single polyelectrolyte layer onto the substrate due to electrostatic interactions, allowing for easy application of robust and stable films with nanometer control over thickness [9]. It can be applied to a variety of substrate geometries, from microscope slides to filtration membranes to nanoparticles [5, 10, 11]. Due to the flexibility of polymer chemistry, ISAM films can be specifically designed to have useful properties, such as hydrophobicity, a high refractive index, or nonlinear optical effects. ISAMs can also easily incorporate other materials, such as nanoparticles [12–15] or biological molecules [16–18], and have been shown to have excellent stability over long time periods and at elevated temperatures [9].

The ISAM technique was used in both projects presented in this dissertation. The fine control over film thickness provided by the ISAM technique allowed the fiber optic biosensor

to be carefully tuned to its highest sensitivity. The ISAM film deposited on the optical fiber consisted of polymers with amine and carboxyl groups in their side chains, which made it possible to crosslink biological molecules to the sensor surface using standard procedures. The ISAM films could be completely removed with an acid bath, allowing the same fiber to be used for many individual assays. The ISAM technique was therefore a crucial component of the fiber optic biosensor.

When studying plasmonic enhancement of second-harmonic generation, the ISAM technique was used to assemble nonlinear thin films on glass substrates. The thickness control afforded by the ISAM technique was again useful, because plasmonic field enhancements extend only a few nanometers beyond the nanoparticle and the largest SHG enhancements are observed when the nonlinear material is not thicker than this penetration zone. Additionally, the electrostatic environment produced by the anionic and cationic layers helped to induce a net ordering of the chromophores in the polyanions. As discussed in Section 3.1.1, second-order nonlinear effects have a fundamental requirement of noncentrosymmetry, so preserving a net polar order is a necessity. The ability of ISAM layers to produce very thin, repeatable, ordered films was very important to the plasmonic enhancement studies presented here.

1.2 Turn-around point long period gratings

Standard optical fibers are made of concentric cylinders of doped glass. Because the fiber core has a higher index of refraction than the surrounding cladding, total internal reflection occurs at the core/cladding interface. This allows for rapid, low-loss transmission of optical signals over distances of kilometers, leading to a revolution in telecommunications technologies over recent decades [19].

Photosensitive telecommunications fibers can be altered by exposure to electromagnetic radiation such that localized changes in the core refractive index are induced. A fiber grating is made by inducing a periodic variation in the core refractive index [20]. This is often accomplished using UV lasers, either with a point-by-point writing scheme or by using masks or diffraction patterns. Other approaches, such as thermally inducing structural changes by exposure to CO₂ laser or applying periodic pressure by squeezing the fiber against a grooved plate, are also possible [21, 22]. Gratings with sub-micron grating periods are known as fiber Bragg gratings (FBGs). In FBGs, light at a resonant wavelength is constructively reflected by the grating, such that there is a drop in transmission at the resonant wavelength. In contrast, gratings whose periods are on the order of hundreds of microns are known as long period gratings (LPGs). LPGs also exhibit resonant attenuations in transmission, due in this case to coupling between the core mode and a forward propagating cladding mode. Both types of fiber gratings are sensitive to strain, temperature, and surrounding refractive index, and are widely used in sensing applications and as components in fiber optic systems.

Under certain conditions, an LPG can exhibit a highly sensitive dual peak resonance [23]. When these peaks overlap to form a single broad, deep attenuation, it is referred to as the turn-around point (TAP). In addition to offering much higher sensitivity than conventional LPGs, TAP-LPGs also offer the possibility to develop sensors that measure transmission at a single wavelength. This allows for the use of more inexpensive components, such as LED light sources and photodiode detectors, compared to sensing systems in which the position of the resonant wavelength must be monitored. This both lowers the cost of the sensor and allows it to operate in real-time [24, 25]. In this work, an ISAM-coated TAP-LPG is studied as a rapid, low-cost biosensor for *Brucella*.

1.3 Optical biosensors

Biosensors are devices in which biological elements are incorporated in the sensing apparatus [26–28]. They are often used to detect biological materials, such as pathogens, proteins, carbohydrates, or other biological macromolecules, but can also be used for chemical sensing or to monitor physical properties. Optical biosensors, in which light is used as the transduction element, constitute a major subset of biosensors because of their typically rapid response and high sensitivity. Optical biosensors are generally divided into label-based and label-free approaches. In label-based optical biosensors, fluorescent or colorimetric tags are added which produce illumination when the analyte binds to the sensing element. The properties of this emission are then analyzed to gather information about the presence, concentration, and other features of the analyte [28]. Label-based optical biosensing is used in many applications, including enzyme-linked immunosorbent assay (ELISA), monitoring DNA amplification during polymerase-chain reaction (PCR), visualizing bands in gel electrophoresis, and in several specialized types of microscopy.

In some applications, however, the need for fluorescent tags is undesirable, as it can be difficult to achieve and may alter the function of some biological molecules [29]. In these cases, label-free optical biosensors may be preferred, which can often also be more sensitive than label-based techniques. Label-free biosensors produce a signal directly by the interaction between the transducer and the analyte. They often function by setting up a geometry in which the sensing surface is probed by the evanescent field produced by total internal reflection. Attachment of analyte to this surface results in changes to the optical properties of the reflected light, which can be analyzed. Commercially available surface plasmon resonance (SPR) biosensors operate on this principle. In these, light is reflected from the back surface of a thin gold film. High absorption occurs at a resonant angle of

incidence, which is changed by binding events at the front surface of the film [26]. The best SPR biosensors are able to detect analytes at concentrations as low as 10 pM [29], but the instruments suffer from high cost, large size, and poor portability. Optical fiber biosensors operate by observing optical changes due to binding on the fiber surface, and are being widely investigated as compact and inexpensive alternatives to SPR sensors. The biosensor presented in this dissertation used the change in transmission through a TAP-LPG in response to binding events on the fiber surface in order to detect bacteria.

1.4 Second-harmonic generation

Second-order nonlinear optical processes occur when the induced polarization in a material varies quadratically with the incident field strength, and are divided into several distinct processes. One type of second-order effect is second-harmonic generation (SHG), in which two photons at a fundamental input frequency are destroyed and a new photon at twice the fundamental frequency is created. It is considered a parametric process, meaning that it occurs in a single quantum mechanical step and can be described by a real nonlinear susceptibility [30]. SHG is widely applied for frequency doubling, such as converting infrared laser radiation to green. Because even centrosymmetric materials are intrinsically noncentrosymmetric at interfaces, SHG is also exploited in SHG imaging microscopy and second-harmonic spectroscopy [31]. Due to mathematical constraints, second-order nonlinear processes are restricted to materials that lack a center of inversion symmetry. These can include some crystal classes, poled polymers, and other materials with a net polar order [30]. While traditional materials for SHG are often inorganic crystals that are difficult to manufacture, SHG can be observed from some nonlinear-active polymers [32]. In this work, SHG was produced by a nonlinear polymer assembled into ISAM films with intrinsic, stable polar order.

1.5 Plasmonic enhancement by silver nanoprisms

Electric fields exert an electrostatic force on electrons in a material. Valence electrons in conductors are free to move around in response to the incident field, and can form collective oscillations known as plasmons [33, 34]. Plasmons that are confined to metal nanoparticles are referred to as localized surface plasmons (LSPs). When the frequency of the incident field matches the resonant frequency of the collective oscillations, localized surface plasmon resonance (LSPR) occurs. Nanoparticles are highly absorbing at their LSPR wavelength. The peak wavelength and width of the LSPR peak depend on properties such as size, shape, material, interparticle spacing, and the refractive index of the surrounding medium [35]. A well known consequence of the size dependence of LSPR is the coloration of gold nanoparticle solutions. Small gold nanoparticles form red solutions due to strong absorption in the blue-green part of the spectrum. As the size increases, the LSPR shifts to longer wavelengths, and the resulting solution appears more blue or purple.

In addition to strong optical absorption, LSPR produces intense electric fields within a few nanometers of the nanoparticle, particularly at tips and corners. For this reason nanoparticles with interesting shapes are the subject of much study, including spheroids, rods, plates, prisms, cubes, and more exotic structures [36]. In this work, silver nanoprisms synthesized by Assad Khan from the group of Dr. Greg Liu were used. Simulations have shown that silver nanoprisms can exhibit electric field enhancements of several thousand times at their corners [37]. The LSPR of the nanoprisms occurred around 800 to 1140 nm depending on the batch. The relatively long wavelength LSPR of the nanoprisms was due to their high aspect ratio, which can be computed by comparing their edge length ($> 100 \mu\text{m}$) to their thickness (about $10 \mu\text{m}$). This range of LSPR, extending into the near infrared part of the spectrum, was required in order for the absorption peak to match the wavelength of the 1064 nm fundamental beam. The electric field enhancements produced by the silver

nanoprisms were used to increase the SHG conversion in nonlinear ISAM films.

1.6 Dissertation outline

This chapter presented motivations, goals, and a brief background overview of topics related to the optical biosensor and the plasmonic enhancement projects. The following provides an overview of the content and significance of the remainder of this dissertation.

Chapter 2 provides background information relevant to the optical biosensor project. In the first section (Section 2.1), organic thin films are described. The procedures, advantages, and disadvantages of both Langmuir-Blodgett and ISAM films are discussed. ISAM films were used in these projects to tune and functionalize the biosensor and as a source of SHG for studying the plasmonic enhancement of nonlinear effects. Properties of ISAM films, including their thermal and temporal stability and the mechanisms behind their dependence on the ionic strength of the polyelectrolyte solutions, are discussed. An overview of applications in biomedicine, optics, and electronics is presented. The particular polymers used in the optical biosensor and plasmonic enhancement projects are also described in more detail. Section 2.2 discusses optical fiber grating sensors, beginning with a brief introduction to the origin of modes in step-index fibers. Next, fabrication techniques for fiber gratings are discussed, and the principles of fiber Bragg gratings (FBGs) and LPGs are introduced. The consequences and advantages of the TAP, and the role of phase-matching curves (PMCs) in predicting it, are discussed. Section 2.3 provides an overview of optical biosensors, including descriptions of label-assisted and label-free approaches, a more detailed discussion of SPR biosensors, and formal definitions of terms used to characterize sensor performance. Section 2.4 discusses current approaches to bacteria identification and detection to contextualize the need for the optical fiber biosensor. These include traditional methods, such as culture and susceptibility,

as well as more modern molecular and DNA based technologies. Finally, the bacteria studied in this work, *Brucella*, is discussed, including their impact on livestock and agriculture.

Chapter 3 provides background material relevant to the plasmonic enhancement study. Section 3.1 provides an introduction to nonlinear optics. Types of second-order frequency mixing processes are briefly described, and the mathematical properties of SHG are outlined. The requirement for noncentrosymmetry is explained, as well as the role of phase-matching conditions. SHG-producing materials, including common conventional inorganic crystals and various innovative alternatives, are described. Section 3.2 discusses plasmonic enhancement. The approaches of Mie theory and Drude theory are described and their conclusions are presented. Silver nanoprisms and their optical properties are then discussed in more detail. After establishing the plasmonic behavior of silver nanoprisms, physical and colloidal synthesis techniques are described. Finally, a selection of other works concerning plasmonic enhancement of nonlinear optics is presented.

Chapter 4 describes and explains the experimental methods used for the projects presented in this dissertation. Polymer preparation is discussed first (Section 4.1), as the solutions for ISAM deposition were prepared in the same way for both projects. Section 4.2 describes the methods used in the biosensor project. First, the apparatus and procedures used to prepare and tune the fiber to the TAP are described. Next, the procedures for functionalizing the fiber and measuring the transmission spectra are described. Methods for lysing and applying bacteria to the sensor are presented. Finally, the apparatus and procedure for cleaning the fiber at the end of the assay are described. Section 4.3 describes the setup and procedures used in attempts to fabricate TAP-LPGs with a CO₂ laser. Section 4.4 describes sample fabrication methods for the plasmonic enhancement project. This includes procedures for initial cleaning of the substrates and a description of the dipper apparatus used to apply the ISAM films. Next, strategies for nanoprism deposition are introduced, primarily immersion

and dropcasting. Finally, spincasting is discussed as an additional treatment step for some of the plasmonic enhancement samples. Section 4.5 presents the procedures used to measure SHG. The optical setup is described in detail, as well as the use of the Maker fringe method.

Chapter 5 presents the results of the optical biosensor project. Section 5.1 includes results from earlier work by this group using an optical fiber biosensor for *Histophilus somni* as a demonstration of prior success for this procedure. In this project, a highly sensitive fiber with a dynamic range of -27 dB was used to detect *H. somni* at very low concentrations. Exposure to 100 cells of *H. somni* produced a change in transmission intensity of 9.4%, while 50,000 cells of a negative control resulted in only a 1.6% change. In Section 5.2, the evolution of the transmission spectrum towards and past the TAP as the number of ISAM layers on the fiber increases is presented. This section shows the typical behavior for the TAP-LPG used in this work, which had a dynamic range of about -10 dB. Section 5.3 presents the results of several tests attempting to determine an ideal functionalization strategy for the sensor. These include the use of different concentrations of streptavidin, biotin, and biotinylated probe. It was found that elevated concentrations of streptavidin and probe did not improve the sensor's performance. In Section 5.4, the response of the sensor to different bacterial cultures is discussed. When using the sensor to distinguish between *B. abortus* and *B. melitensis*, the change in transmission was $2.2 \pm 0.07\%$ for the positive controls and $0.7 \pm 1.3\%$ for the negative controls, and remained about the same as the sample concentration increased from 10^4 to 10^7 cfu/mL. Another data set in which the sensor was used to distinguish between *Brucella* species was even less successful, as both positive and negative samples produced an average change in attenuation of -0.6%. Better results were obtained when miscellaneous non-*Brucella* bacteria were used as the negative controls, where the average signal for positive samples was $2.8 \pm 0.9\%$ and $0.6 \pm 1.0\%$ for negative samples. Section 5.5 presents results for assays testing spleen and liver tissues from *Brucella* infected mice. These results were better

than for the bacterial cultures, yielding an average change in attenuation of $6.0 \pm 1.4\%$ for samples from infected mice and $0.5 \pm 2.0\%$ for mice injected with a saline solution. Section 5.6 presents the results of the TAP-LPG fabrication attempts. Based on the behavior of the transmission spectra, it was concluded that no LPGs were produced. Studies of physical deformations at higher than necessary writing powers suggest that instability of the laser prevented sufficient periodicity from being induced into the fiber core. The remainder of Chapter 5 (Section 5.7) presents a summary of the results presented in the prior sections.

Chapter 6 presents the results of the plasmonic enhancement project. Section 6.1 includes prior results for studies of plasmonic enhancement of SHG by silver nanotriangles deposited via nanosphere lithography and by colloidal gold nanorods. The silver nanotriangles deposited on nonlinear ISAM films produced SHG enhancements of up to 1600 times compared to the bare ISAM films. The gold nanorods produced weak enhancements when deposited onto ISAM films, but the enhancement was increased to 100 times after wrapping the nanorods with ISAMs to increase the amount of ordered PCBS exposed to the enhanced electric fields. Section 6.2 describes attempts to demonstrate plasmonic enhancement by depositing colloidal silver nanoprisms by stationary immersion, including the use of nanoprisms at several wavelengths. Nanoprisms whose LSPR matched the fundamental wavelength were too dilute to deposit at high densities, and produced a maximum SHG enhancement of 2.3 times compared to the bare film. Nanoprisms with an LSPR peak about 200 nm shorter than the fundamental wavelength were much more concentrated, and SHG enhancements of up to 35 times were observed. Several strategies were tested to improve the deposition density by varying immersion times and properties of the underlying ISAM layers. Significant improvements were observed when PCBS was replaced with PAA and when the sample was re-soaked in PAH and rinsed immediately prior to immersion in the nanoparticle solution, resulting in extinction increases of 1.75 times and 1.5 times, respectively. Other changes

to the underlying films had more modest effects. Section 6.3 describes samples in which the nanoparticles were deposited by immersion using the dipper machine. No improvements were observed for the very dilute prisms whose LSPR matched the fundamental wavelength. Excellent deposition was observed when depositing shorter wavelength prisms onto films of a single PAH layer, but was less dense for films consisting of PAH/PCBS bilayers. Up to 135 times more SHG was observed when silver nanoprisms with an LSPR near 800 nm were deposited on PAH, compared to the SHG produced by the interfaces of the bare PAH film. Due to lower nanoparticle densities, the SHG enhancements for nanoprisms on PAH/PCBS films was only up to 34 times. Section 6.4 describes samples in which the nanoprism concentration was increased by centrifugation, and the low volume but high concentration solutions were dropcast onto ISAM films. The SHG enhancements were routinely 100 times or more greater than for the bare films, with a maximum enhancement of 1380 times observed for one sample. The high density of the deposited nanoprisms enabled their extinction peaks to broaden due to interparticle interactions, resulting in large but unpredictable SHG enhancements. Section 6.5 presents attempts to increase enhancement by applying additional treatments onto deposited prisms. Placing additional ISAM layers onto the prisms was surprisingly unsuccessful, and in some cases decreased the SHG enhancement. Much better results were obtained by spincoating polymers, particularly PCBS, onto the prisms in order to redshift their LSPR peaks. Adding spincoated PCBS to dropcast prisms on PAH/PCBS ISAM films was seen to increase the SHG enhancement by up to 7 times, even though the chromophores in the bulk of the spincoated film should be randomly oriented and should not contribute to the nonlinear effects. The largest SHG enhancement observed in this project, which was 2368 times the SHG from the prism-free region of the sample, utilized this strategy. Section 6.6 provides a summary of the results presented in Chapter 6.

Chapter 7 contains the conclusions of this dissertation. It includes a summary of the

motivations for both projects and the major results described in Chapters 5 and 6. In addition, limitations of the projects are discussed, and strategies for future improvements are suggested.

Chapter 2

Background for the LPG biosensor

This chapter provides a review of topics relevant to the optical fiber biosensor project. These include organic thin films, optical fiber gratings, optical biosensors, current methods of bacteria identification, and *Brucella*.

2.1 Organic thin films

Thin films are useful for a multitude of applications because they have unique properties that differ from the bulk. Compared to inorganic thin films, organic thin films are often cheaper and easier to deposit. In addition, organic thin films allow for more diverse applications due to the variety of organic molecules available and the ease of incorporating other materials, such as nanoparticles and biological molecules, into the film structure. Organic thin films have been used to make a wide variety of electronic devices, including light-emitting diodes [38, 39], photovoltaics [40], photodetectors [41], transistors [42], and flexible and stretchable electronics [43]. They are also useful as coatings for sensors and other functionalized surfaces.

Although in some applications organic films may be deposited with complex equipment, such as organic molecular beam epitaxy [44], two simpler approaches dominate organic thin film studies: the Langmuir-Blodgett (LB) technique and layer-by-layer deposition of ionic self-assembled multilayers (ISAMs).

2.1.1 Langmuir-Blodgett films

The LB technique was developed in the early twentieth century and remained the primary method for organic thin film deposition for several decades [8]. In this technique, insoluble amphiphilic monomers are dispersed at low concentration in a polar solvent, such as water. These molecules consist of a hydrophilic polar end and a hydrophobic non-polar end, which causes them to arrange themselves in particular configurations depending on concentration, temperature, salinity, and other factors. Under the right conditions the undisturbed molecules form a uniformly oriented monolayer at the liquid-gas interface, with the polar ends remaining in the solution and the repelled non-polar ends pointing out. The resulting film is known as a Langmuir film [44]. The substrate for the thin film is then drawn carefully through the Langmuir film such that the monolayer is deposited onto it (Fig. 2.1). Multilayers can be formed by repeating this procedure.

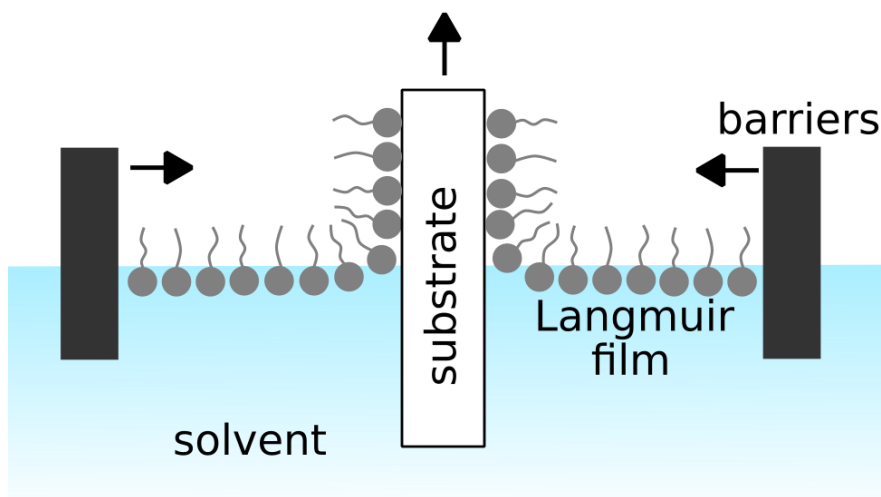


Figure 2.1: Diagram of the Langmuir-Blodgett technique. The substrate is carefully drawn through a monolayer of amphiphilic molecules at the liquid-gas interface. Moving barriers maintain the uniformity of the film as it is depleted by deposition.

Although the LB technique is capable of reliably producing highly ordered films, it has a number of disadvantages. The inherent reliance on amphiphilic molecules severely limits

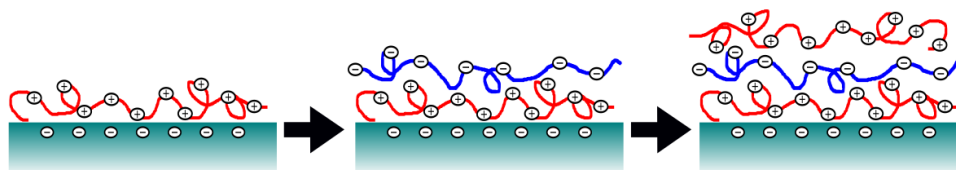


Figure 2.2: Process of depositing ISAM layers onto a substrate with a negative surface charge, such as glass. In the third step pictured, 1.5 bilayers have been deposited.

the choice of materials that can be used [45]. Requirements for substrate size and topology are likewise restrictive, and specific instrumentation is needed to achieve stable and high quality films [8]. A specialized apparatus is needed to maintain repeatable drawing speeds, substrate alignment, solvent temperature, and other factors. The quality of the deposition is sensitive to contaminants in the solvent and in the surrounding air, and a clean room or glove box is necessary for maximum reliability [46]. The difficulties associated with the LB techniques have contributed to the popularity of the ISAM approach.

2.1.2 Ionic self-assembled multilayers

Ionic self-assembly is a simple means of applying multilayer films based on electrostatic interactions. It is sometimes referred to as electrostatic self-assembly or electrostatic layer-by-layer films. To begin, a clean substrate is immersed in a polyelectrolyte solution of relatively high concentration with a charge opposite to that of the substrate surface. The charged polyelectrolyte molecules are electrostatically attracted to the surface charge and deposit on the substrate in a single layer. The deposited molecules screen the surface charge of the substrate from the rest of the solution, preventing further deposition. The substrate is rinsed with water to remove poorly attached polymers and then immersed in a polyelectrolyte of the opposite charge, which similarly deposits a single layer (Fig. 2.2). The process can be repeated until the desired number of layers has been achieved. A pair of oppositely charged

polyelectrolyte layers is referred to as one bilayer. For the projects presented in this work, only a few bilayers were needed. In these cases, the ISAM technique can be performed by hand with simple laboratory glassware. Other applications may require tens or hundreds of bilayers, which can be deposited with automated dipping machines.

The ISAM approach has a number of advantages. Compared to the LB approach, the ISAM technique allows for greater flexibility in substrate geometry and size. In this work, films were applied to optical fibers and microscope slides, however, ISAMs can be applied to colloids, nanoparticles, meshes, tube linings, and other interesting substrates [5, 47, 48]. With a proper choice of polyelectrolytes, ISAMs can be robust and stable for many years and when exposed to a wide range of temperatures [9]. As discussed later in this section, the properties of ISAM films can be easily manipulated by careful selection of the polyelectrolytes used and by altering their concentration, pH, or the salinity of the solution [49]. They can be produced using a wide variety of materials, unlike LB films which require amphiphilicity. In addition to the default ABAB film structure, alternate polyanions or polycations can be substituted to produce films with other sequences, such as ABCBA. ISAMs can also easily incorporate other nanoscale materials, such as nanoparticles [15, 50–55] and biological molecules [56, 57] by taking advantage of their surface charge or by cross-linking them to the deposited polymers. Interesting heterostructures can be developed in this way, allowing ISAMs to be engineered for diverse applications.

Control of ISAM properties via solution conditions

The characteristics of ISAM films are dependent on the salt concentration and pH of the polymer solutions because changing the ionic properties of the solutions alters the characteristic distance of electrostatic interactions. The total ionic strength of the solution can be calculated for low concentration polymer solutions as the sum of the contributions from

salts and hydronium ions, as

$$c_s = c_{NaCl} + 10^{-pH}, \quad (2.1)$$

where c_{NaCl} is the salt concentration. The Debye length, κ^{-1} , is the characteristic length over which electrostatic interactions occur, and depends on the total ionic strength as

$$\frac{1}{\kappa} = \sqrt{\frac{kT}{2c_s z^2 e^2}}, \quad (2.2)$$

where k is Boltzmann's constant, T is the temperature in Kelvin, z is the valency of the counterions, and e is the charge of an electron. Increasing the ionic strength of the solution, by adding salt or by increasing acidity, will result in a reduction in the Debye length. In this case, ions in the solution can screen repulsive charges from distant positions on an individual polymer chain, allowing the molecule to bunch up and form loops or tails (Fig. 2.3b). Another means of achieving conformations with loops and tails is to use solutions near the pKa of the polymer, where the molecule is only weakly charged and will therefore have weak self repulsion. Conversely, at lower ionic strengths the Debye length is longer, meaning that there is more interaction between charges on an individual polymer chain. As charges along the polymer repel each other the molecule is stretched into a long, flat conformation known as a train. Conditions which produce trains will deposit such that they form thinner ISAM films, whereas the bunched up molecules at higher ionic strengths will result in thicker films.

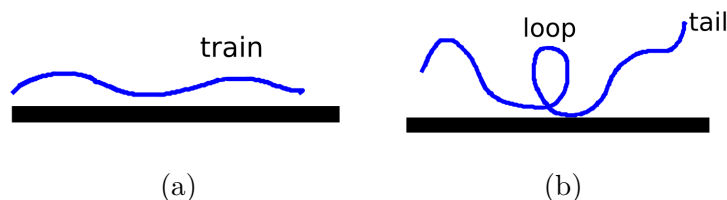


Figure 2.3: Morphology of polymer deposition at (a) low salinity or high polymer charge and (b) high salinity or near-neutral polymers

The ability to control film thickness by altering salt concentration and solution pH has been demonstrated experimentally in prior work by this group [9]. PAH at 10 mM was used as the cation, while the nonlinear polymer dye Poly-S119 was used as the anion. It was found that while holding the pH at 3.5, increasing the salt concentration from 0 to 0.13 M resulted in films with higher absorbance. In each case the absorbance increased linearly as additional bilayers were added, with a larger slope for the solutions with higher salt concentrations. This indicated that more chromophores were present in each layer of Poly-S119, which is consistent with loop and tail conformations. The experiment was repeated at two lower pH values, which showed a weaker dependence on the salt concentration because charges were screened by hydronium ions even in solutions without added salt. By varying the ionic strength and pH of the solutions it was possible to vary the thickness of an individual bilayer from 0.3 nm to greater than 5 nm. This demonstrates that the properties of an ISAM film can be varied dramatically through simple changes to the solution chemistry, allowing for easy control of properties such as film thickness and chromophore density [9]. The sensitivity of film thickness to the solution salt concentration varies depending on the polyelectrolytes selected. Films are less susceptible to thickness control via ionic strength when the polyelectrolytes form strong polymer/polymer ion pairs and when there is poor permeability to small salt ions. The type of salt used to increase the ionic strength also plays a role. More hydrophobic ions have a greater impact on film thickness because their repulsion from water drives them toward the polymer molecules, leading to better screening of the charges [58].

Dubas et al. have shown that when the salt concentration is increased a maximum layer thickness is achieved, after which additional salt rapidly decreases the bilayer thickness [58]. In this case, films constructed with 1 mM poly(acrylic acid) (PAA) and poly(diallyldimethylammonium chloride) (PDADMA) had a peak thickness when the salt concentration was about 0.1 to

0.3 M, depending on the pH. Exposing existing films to solutions with salt concentrations above 0.6 M can lead to film decomposition. At higher salt concentrations the polyelectrolyte charges are too well compensated by the charged ions in the solutions, leading them to form complexes in solution with poor solubility. Therefore, when designing ISAM films controlled by salt concentrations, the response of the polymers selected to the salts in use must be considered in order to achieve films with the desired thickness.

2.1.3 Applications of ISAM films

In this work presented in this dissertation, ISAMS were used to tune and functionalize an optical fiber biosensor and as a source of SHG. A number of alternative uses in biomedicine and electronics are possible due to the versatility of the technique. In particular, the ability to apply ISAMs to unusual substrate geometries and to incorporate other materials, such as nanoparticles or biomolecules, have led to widespread adoption of the ISAM technique. This section presents an overview of examples from the literature to illustrate the breadth of possible applications.

Biomedical applications

ISAM films are particularly attractive for biomedical uses in both clinical and research contexts. A variety of applications have been investigated, such as the development of coatings to prevent arterial damage during revascularization procedures [59] and the construction of artificial extracellular matrices to support long-term cultures of neural cells [60]. Major areas of interest include the use of ISAMs to regulate drug delivery and to provide biocompatible coatings for synthetic implants, both of which are discussed in more detail below.

The ISAM technique can be used to better control drug delivery through several strategies,

including drug-embedded films and drug encapsulation [61]. Drug delivery technology can allow for advantages including control over the speed and location of drug release, reduced side effects, and improved stability for sensitive compounds. Better control over release rates can lead to more stable levels of the drug in the body, which can allow patients to withstand higher doses without suffering the effects of an initial spike in concentration shortly after administration. ISAMs can also be used to help control where in the body drugs are released. Strategies for targeted drug delivery are also important in enabling less invasive drug administration, such as orally instead of requiring injections, and reducing systemic side effects caused by unnecessary presence of the drug elsewhere in the body.

One way to use ISAMs to control drug delivery is to incorporate the compound directly into the ISAM film. Vodouhê et al. demonstrated that polylysine/hyaluronic acid films could be embedded with the chemotherapy drug paclitaxel (also known under the name brand Taxol) without requiring any chemical modification to the polyelectrolytes or the drug [62]. They were able to demonstrate that paclitaxel in ISAM films remained functional with good control of the dose available to human colonic adenocarcinoma cells *in vitro*, and they could regulate accessibility of the drug by capping the drug-embedded layers with synthetic polyelectrolyte layers. Because nanoparticles tend to accumulate in tumors due to their unusual vascular structure, nanoparticles coated with drug embedded thin films such as these could be used to develop targeted cancer therapies. In other cases the composition of the films themselves can contribute to the targeting. Zhang et al. demonstrated drug-embedded films with the ability to target liver cells (hepatocytes) by selecting a polyelectrolyte functionalized with D-galactose, which has a strong interaction with receptors present in the liver [63]. Another way to control drug delivery is by encapsulating nano- or microparticle sized drug aggregates with films that break down when they encounter the correct conditions. In one example, Fan et al. [64] used the ISAM technique to encapsulate insulin nanoparticles

with 8 bilayers of poly(α,β -L-malic acid) and water-soluble chitosan. The insulin remained encapsulated at acidic pH, such as that found in the stomach, and was released at pH 7.4, which is the physiological pH level found in blood and body fluids. Such a system could potentially be used to develop oral insulin therapies, in contrast to current options which require injection [65]. In another application, Cook et al. [66] used alginate/chitosan films to encapsulate probiotic bacteria. The ISAM coating around the probiotics allowed the bacteria to pass unharmed through the stomach, where they would otherwise be killed by acidic conditions, and to be released in the intestines following digestion of the alginate coating. ISAMs could therefore be applied to improve the efficiency of oral probiotic therapies.

Another medical application of ISAM films is in the development of coatings for artificial implants to prevent rejection and improve their incorporation into the body. Coatings can help improve surface roughness and deliver drugs and other biological molecules to the implant site, preventing aseptic and infective loosening that can lead to implant failure [16]. Nawae et al. [18] demonstrated ISAM films composed of silk fibroin, collagen, and PDADMA that had good biological properties and allowed for the adherence and proliferation of osteoblasts, indicating that the films could be used to help improve attachment of titanium dental implants to bone. In another case, Min et al. [17] used medicated ISAM films to improve outcomes *in vivo* of implants drilled into rat tibiae. In the short-term, the antibiotic-embedded upper layers of the film allowed for prevention and treatment of implant-associated infection, while the slower-decaying lower layers contained an osteoinductive growth factor to improve osteointegration. The multifunctional ISAM films were seen to reduce infection rates and improve outcomes in the rats studied. The use of coated implants could also be beneficial in human applications.

ISAMs in optics and electronics

The ISAM technique also has a number of potential applications outside of biology. The development of organic thin film electronics, such as organic thin film transistors (OTFTs), organic LEDs (OLEDs), and photovoltaics has the potential to allow for flexible, low-cost devices. Thin films also lend themselves well to surface coatings, which can be used to tailor the optical properties of surfaces. Representative examples of these applications are discussed in this section.

The ISAM technique can be used to help in the fabrication of improved and novel electronic devices. Li et al. [14] used the ISAM technique to assemble capacitive structures using PDDA as the cation and alternating between PSS-coated graphene and manganese dioxide as the anionic layers. A ten quadlayer sample was found to have a very high specific capacitance of 263 F/g, on the order of the capacitance observed ruthenium oxide, which has excellent capacitance but is much more toxic. Small sized high capacitance materials like this have the potential to be used in supercapacitors, which are a growing area of interest as demand for energy storage technologies increases. In another application, the ISAM technique was used to make conductive paper by coating wood pulp fibers in ISAM layers of ITO nanoparticles and PSS [15]. The ability to combine the flexibility and light-weightness of paper with electronic and magnetic responsivity could enable a variety of applications.

ISAM films can also be used to fabricate organic thin film solar cells. While organic solar cells typically have limited efficiency compared to semiconductor photovoltaics, their advantages in cost, size, and flexibility make them attractive. One important class of organic solar cells is dye-sensitized solar cells (DSSCs), in which conductive nanoparticles (often TiO_2) are decorated with smaller nanoparticles of a dye material. Electrons are excited in the dye by photons, and are transferred to the conductors. The circuit is completed by an electrolyte

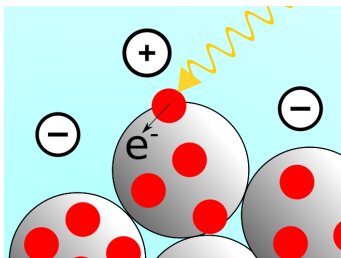


Figure 2.4: Conventional dye-sensitized solar cell. Photons excite electrons in dye (red) that are conducted away by TiO_2 nanoparticles. The electrons are replaced by ions from an electrolyte solution, completing the circuit. ISAM DSSCs replace the electrolyte, and sometimes the dye, with more stable polyelectrolyte layers.

solution that returns electrons to the dye. While DSSCs have been able to achieve good efficiencies, they suffer from poor stability of the liquid electrolyte solution. The ISAM technique can be used to replace the electrolyte solution with a more stable polyelectrolyte layer. Kniprath et al. [67] used the ISAM technique to replace the dye and the hole conductor with the polyelectrolyte poly[2-(3-thienyl)-ethoxy-4-butylsulfonate] (PTEBS). ISAM films were constructed by alternating between PTEBS and TiO_2 nanoparticles. The resulting devices had higher photocurrents than were expected for a planar device of similar composition. The photocurrents were somewhat limited by poor contact between PTEBS molecules in the film which caused restricted hole transport, but the authors expect to mitigate this by the use of larger sized TiO_2 nanoparticles. Agrios et al. [52] reported on solar cells constructed by assembling 50 bilayers of polydiallyldimethyl ammonium chloride (PDAC) and 16 nm TiO_2 nanoparticles. The resulting films had a peak quantum efficiency of about 60%.

Organic thin films deposited by the ISAM technique can also be used for optical applications. For example, ISAMs can act as antireflection coatings, which helps to increase the fraction of light that enters the solar cells and can also have applications in lenses and electronic displays. Rubner et al. [68] were able to demonstrate antireflective coatings by inducing nanoporosity into films composed of inexpensive PAH and PAA. The degrees of porosity could be varied by using pH changes to swell or contract the films, providing a simple

means of tuning the refractive index of the film. More recently, our group has demonstrated antireflective coatings by assembling silica nanoparticles into ISAM films with a quadlayer structure of PAH/PAA/PAH/SiO₂, where the PAA and PAH are thermally crosslinked to improve robustness [12]. ISAMs can also be used in electrochromic devices, in which reversible changes in absorbance or transmittance can be induced by the application of an external voltage. In practice, this often manifests as a voltage-dependent color change which can be useful in devices such as tintable windows or glare-reducing mirrors. In one case, electrochromic polyviologen was paired with poly-(2-acrylamido-2-methylpropanesulfonic acid) (PAMPs) on an ITO substrate using the ISAM technique, and the resulting devices demonstrated good electrochromic behavior with a distinct change from clear to dark purple [69]. As shown in Chapter 6, ISAM films may also be used as nonlinear coatings in order to accomplish phenomena such as frequency doubling, and may be good replacements for more conventional nonlinear media.

Sensing and other applications

The ISAM technique can also be used to develop devices for chemical and biological sensing, water treatment, and a variety of other applications. In the work reported in Chapter 5, ISAM films are used in order to immobilize receptor molecules on a sensing surface, allowing for the detection of bacteria. However, other approaches to sensing with ISAM films are possible. The ability to control the architecture of the thin films allows for the incorporation of sensing elements that can be sensitive to external changes. For example, Lee et al. [13] used the ISAM technique to assemble films whose conductivity was sensitive to the presence of glucose. The polycation was PDDA, and the anion was single-walled carbon nanotubes (SWNTs) in five lower bilayers and glucose oxidase in the upper three bilayers. When the film was applied to a well in a Cr/Au gold film on a glass substrate, pH changes due to

the H_2O_2 producing oxidation of glucose catalyzed by the glucose oxidase embedded in the film led to changes in the SWNT conductivity that allowed them to detect glucose at low concentrations.

Because the ISAM technique can be used to apply thin films to unusually-shaped substrates, it has also been popular as a means to alter the surface properties of filtration membranes. Ahmadiannamini et al. [11] developed nanofiltration membranes by layering PDDA and sulfonated poly(ether ether ketone) onto hydrolyzed polyacrylonitrile supports. The resulting structures were able to selectively filter ions from various salt solutions. Avram et al. [10] fabricated coated membranes using the ISAM technique to concentrate ionic liquids, which are used in the production of biofuels but are expensive to synthesize and difficult to recover because their filters must combine high charge density and a precise molecular weight cutoff. By applying PAH/PSS films to alumina oxide membranes, they were able to produce stable filters that successfully separated an ionic liquid from carbohydrate molecules in the solution. Ishigami et al. [70] used the ISAM technique to apply PAH/PSS films onto reverse osmosis membranes in order to prevent fouling, a process in which molecules or particulates attach to the membrane pores and reduce its performance over time. The ISAM films decreased the rate of fouling by making the membrane more hydrophilic, and optimum performance was observed when four bilayers were applied.

As demonstrated in this section, ISAM films can be useful in a variety of applications in different scientific fields. In general, these applications take advantage of the flexibility in substrate geometry and film composition in order to apply functional surface modifications. These include, but are not limited to, biomedical applications such as drug encapsulation and implant coatings, optical applications such as nonlinear films and antireflection coatings, the development of novel organic electronic devices, and improved filtration membranes.

2.1.4 Polymers used in this work

Polyelectrolytes are large molecules composed of a chain of charged monomers. They are generally divided into strong polyelectrolytes, which remain fully charged over a wide pH range, and weak polyelectrolytes, whose charge density varies more significantly depending on the pH of the solvent. Whether or not the functional groups on a polyelectrolyte are protonated depends on the relationship between the dissociation constant (pKa) of the polyelectrolyte and the pH of the solution. From the Henderson-Hasselbalch equation,

$$pH = pK_a - \log\left(\frac{[A^-]}{[HA]}\right), \quad (2.3)$$

if the pH of the solution equals the pKa of the molecule then there will be an equal concentration of protonated and unprotonated groups, resulting in a 50% charge density. The fraction of protonated groups increases as the pH is lowered below the pKa, and decreases when the pH is above the pKa. Polycations have a higher charge density when the pH is below their pKa. For example, in poly(allylamine hydrochloride) (PAH) the amine groups have a positive charge when they are fully protonated (Fig. 2.5a). Conversely, polyanions have a higher charge density when the pH is above the pKa. The hydroxyl and carboxyl groups found on poly-1-[4-(3-carboxy-4-hydroxy-phenylazo)benzenesulfonamido]-1,2-ethanediyl, sodium salt (PCBS) are neutral when protonated but have a negative charge when the protons are removed, which occurs at elevated pH levels (Fig. 2.5b).

The majority of ISAM films investigated in this work utilized PAH and PCBS. Both were used at a concentration of 10 mM monomer in water at neutral pH. Additionally, PCBS in methanol and poly(methyl methacrylate) (PMMA) (Fig. 2.5c) in chloroform were used in some of the plasmonics experiments to induce a red-shift in the nanoparticles. Structures for these polymers are shown in Figure 2.5.

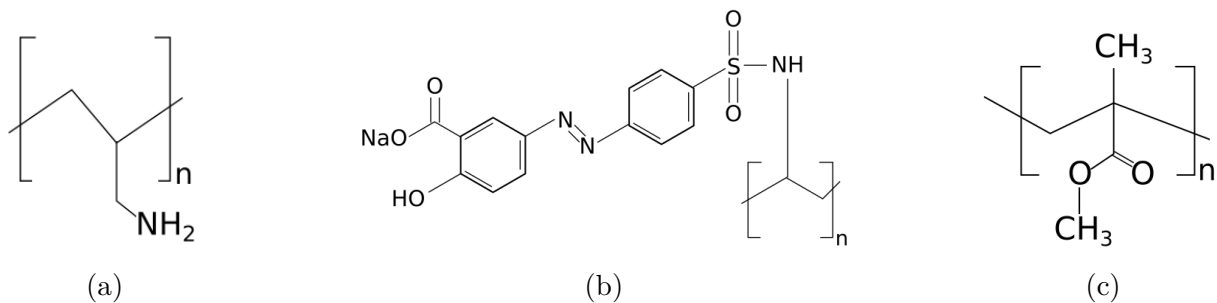


Figure 2.5: Chemical structures of (a) PAH, (b) PCBS, and (c) PMMA

PAH (Fig. 2.5a) was used as the polycation in the ISAM films. It has a pKa in solution of 6.7 [48], and thus had a positive net charge at the working pH. The charge variability comes from the amine groups, which can gain or lose protons depending on the surrounding pH. PAH appears as a clear, colorless solution. Because clean silica has a negative surface charge [71], PAH was the first layer applied to the microscope slides and optical fibers used in this work. When a positive top layer was required, as was usually the case in these studies, PAH was also the final polymer applied.

PCBS (Fig. 2.5b), often referred to as PAZO by other authors, was used as the polyanion in both the second-harmonic generation and the optical biosensor projects. It has an overall pKa of 3.3 [72] and thus was strongly negatively charged at the working pH. PCBS exhibits optical nonlinearity due to the hyperpolarizability of its pendant azobenzene chromophore group. Azobenzenes are interesting photoresponsive structures consisting of two phenyl rings linked by double-bonded nitrogens (Fig. 2.6). PCBS has an electron-donating sulfonamido group located near the polymer backbone, and electron-accepting carboxyl and hydroxyl groups on the phenyl ring at the opposite end. Because electrons in π bonds are relatively mobile, the chromophore has an uneven charge distribution and acts as a dipole, resulting in nonlinear behavior and SHG [73]. Its strongly absorbing aminoazobenzene group also causes PCBS to be brightly colored, and it forms a vibrant orange solution in water [74].

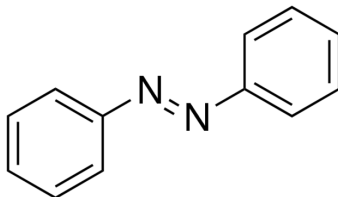


Figure 2.6: Azobenzene functional group structure

The ISAM technique was important in the nonlinear optics project because electrostatic interactions can preserve ordering of the molecules in the film. Due to mathematical constraints, noncentrosymmetry is an absolute requirement for second-order nonlinear processes, including second-harmonic generation (Section 3.1.1). It is therefore crucial for these applications that the chromophores retain nonrandom orientation. The azobenzene chromophores in neutral pH PAH/PCBS ISAM films on glass have been demonstrated to retain polar ordering in films with more than 500 bilayers [75]. Ordering has also been shown to be thermally stable at temperatures up to 150° C [9]. SHG reduction after higher temperatures was observed, but was attributed to chromophore decomposition rather than realignment. At room temperature, the films remained stable over a period of three years.

PCBS was chosen as the polyanion for the biosensor project for several reasons. First, PCBS has a relatively high refractive index. Because the type of optical fiber sensor utilized has more sensitivity with higher refractive index coatings, PCBS was ideal for this application [76]. Additionally, well-established cross-linking procedures exist which allowed for the formation of covalent bonds between the PCBS carboxyl group and amine groups on biological molecules. Functionalization of the sensor surface with biological molecules was therefore straightforward.

2.2 Optical fiber gratings

2.2.1 Overview of optical fibers

Most optical fibers are cylindrical glass structures in which propagating light is confined to the central region by total internal reflection. They were first demonstrated by Hopkins and Kapany in the 1950s [77]. By the 1970s, the technology was sufficiently developed to transmit telephone signals over distances of a few kilometers [19]. In the following decades, improvements to manufacturing purity and regularity, along with the invention of the laser, transformed optical fibers from curiosities to extremely useful tools. Because they are small, lightweight, and nonconducting, they are advantageous in a wide variety of applications.

Perhaps the simplest use of optical fibers is to direct light into small and confined spaces. They can be used to provide illumination to delicate targets without inadvertently supplying heat from the light source. Similarly, they can be used to image these hard-to-reach spaces by directing light back to detectors, allowing for minimally invasive medical procedures such as endoscopy and laparoscopy [78]. In addition to directing light from external sources such as LEDs and diodes, optical fibers can themselves be light sources. Rare-earth doped optical fibers are used as gain media in fiber lasers, which are rugged, compact, capable of high power, and tunable [79, 80].

Optical fibers are key elements in telecommunications, where they have a number of advantages over the metal wires that formerly dominated information transmission. Compared to metal cables, optical fibers suffer from less attenuation and can therefore transmit signals over longer distances with fewer intermediate repeaters [19, 78]. They are smaller and lighter than metal wires, which is important in small devices, ships, planes, and spacecraft, where space or mass is at a premium [19]. Because optical fibers are composed of dielectrics, they

are also less susceptible to electromagnetic interference and electrical accidents [19, 78]. This property also enables them to offer more secure communications than copper wires, because the signal is confined within the core and can be shielded from eavesdroppers by simply applying an opaque jacket [19]. They can also accommodate more communication capacity due to having higher bandwidths than copper wires [19]. As a result, optical fiber networks are rapidly replacing older infrastructures.

Typical optical fibers are made of ultrapure doped glass, although more exotic fibers composed of photonic crystals and plastics have been developed. In general, an optical fiber consists of a central core and a surrounding cladding with a slightly lower refractive index (RI) (Fig. 2.7a). Light propagates through the fiber core and is totally internally reflected at the core-cladding interface. This allows the signal to traverse the length of the fiber, which may be many kilometers long. In addition, an exterior plastic jacket is usually added to provide mechanical support and protection.

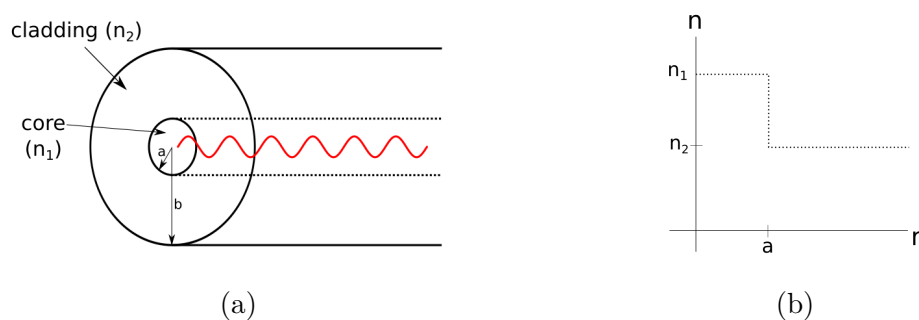


Figure 2.7: Basic structure of an optical fiber. The fiber cross section (a) consists of a central core surrounded by a lower refractive index cladding, confining light to the core by total internal reflection. In the simplest case, a step-index fiber (b) has a sharp change between the core and cladding indexes.

The simplest cross section for an optical fiber is when the core and cladding each have a constant refractive index with a sharp change in between them (Fig. 2.7b). These fibers are called step-index fibers. Due to their radial symmetry, we can study the propagation

of an electromagnetic wave in a step-index fiber by applying boundary conditions to the cylindrical wave equation,

$$\frac{\partial^2 \psi}{\partial r^2} + \frac{1}{r} \frac{\partial \psi}{\partial r} + \frac{1}{r^2} \frac{\partial^2 \psi}{\partial \phi^2} + q^2 \psi = 0, \quad (2.4)$$

where ϕ is E_z or H_z . Because the solutions must be electromagnetic waves, we assume that they will be separable and that the t , ϕ , and z dependences will take the usual forms for waves propagating along the z -axis,

$$E_z(r, \theta, z) = AF_1(r)e^{j(\omega t + \nu \phi - \beta z)}. \quad (2.5)$$

Plugging this form for E_z into the cylindrical wave equation yields

$$F_1''(r) + \frac{1}{r} F_1'(r) + \left[q^2 - \frac{\nu^2}{r^2} \right] F_1(r) = 0, \quad (2.6)$$

which has the form of the Bessel equation. Solutions for $F_1(r)$, and thus $E_z(r, \phi, z, t)$ and $H_z(r, \phi, z, t)$, are Bessel functions. Because the Bessel functions are discrete, light propagates through the fiber in discrete allowed patterns, called modes.

Modes which successfully propagate through the core of the fiber are called core modes. A single-mode fiber supports only one core mode, and typically has a core diameter of 8-10 μm . Multimode fiber cores are on the order of tens of microns in diameter, allowing them to accommodate multiple core modes. Other modes, which extend into the fiber cladding and propagate poorly, are called cladding modes. Under certain conditions, core modes and cladding modes can couple, causing the transmission through the fiber to be sensitive to external conditions such as temperature or refractive index. The sensors studied in this work operated via core-cladding coupling in single-mode fibers.

2.2.2 Fiber grating fabrication and types

Fiber gratings are small periodic variations in the refractive index of a fiber core that cause certain wavelengths to be attenuated in the transmission spectrum. They are typically on the order of millimeters to a few centimeters long with an induced refractive index change of around 10^{-4} . Fiber gratings are broadly categorized based on the length of the grating period, which can range from hundreds of nanometers to hundreds of micrometers. Fiber gratings can be used as sensors, notch filters, end reflectors in fiber lasers, and for other photonic applications.

2.2.3 Grating fabrication

Fiber gratings are most often induced by UV laser, CO₂ laser, or electric arc-discharge. More exotic techniques, including femtosecond laser exposure, mechanical microbends, etched corrugations, and ion beam implantation have also been explored [81]. The TAP-LPG used for the biosensor assay was fabricated by UV laser, and attempts were made to produce additional TAP-LPGs using a CO₂ laser.

Gratings fabricated by UV laser

In the UV laser method, gratings are applied by photoionizing the core of a Ge-doped fused silica single-mode fiber with UV radiation [82]. Sites in the fiber where a Ge atom is bonded to a Si or Ge atom, rather than an oxygen atom, form structures known as germanium oxygen deficient centers which absorb strongly at 242 nm [82]. When exposed to UV light, these structures undergo a change that alters the refractive index of the glass, although the underlying physical mechanism is not well understood [83]. In addition to absorption in germanium oxygen deficient centers, other mechanisms, including stress relief and glass

densification, have been proposed as possible explanations for the resulting refractive index change [21].

The most popular UV writing technique, due to its simplicity and high reliability, is to pass the incident UV light through a phase-mask, which diffracts the beam into a fringe pattern. This exposes the fiber to a periodic variation in UV light intensity, resulting in a periodic modulation in refractive index. In cases where more flexibility in the fabrication parameters is required, other techniques may be employed. An interference pattern may be formed by intersecting two UV laser beams, and the period of the grating can be controlled by selecting the angle between the beams [84]. The grating can also be written using the point-by-point technique, where the beam is focused to a single spot to modulate the refractive index at each period individually, either by moving the beam focus across the fiber or by moving the fiber under the beam focus [85]. Compared to the phase-mask approach, point-by-point writing and interference pattern exposure allow for easier variation of the grating period but may be more difficult to control. In either case, the sensitivity of the fiber to the UV writing procedure can be increased by using co-doped fibers and by hydrogen loading the fiber prior to UV exposure [21]. Gratings written by UV laser can weaken over time, especially at elevated temperatures, as the changes induced into the photosensitive fiber relaxes. Therefore, alternative approaches with improved stability are a subject of investigation.

Grating fabrication by CO₂ laser

The LPGs used in this work were fabricated by Siddharth Ramachandran, who was first at the OFS Laboratories and later at Boston University. Around 2015 he became unable to supply additional LPGs. We therefore pursued the CO₂ laser method in an attempt to establish an additional source of TAP-LPGs for the biosensor experiments. This technique

was first demonstrated by Davis et al. in 1998 as part of an investigation of the mechanisms behind the refractive index modulation in conventional UV written LPGs [21]. CO₂ lasers are IR gas lasers that utilize a mixture of CO₂, N₂, and He as the active medium. They are usually used to produce 10.6 μm radiation via relaxation of CO₂ vibrational modes, and are known for being capable of high power and efficiency [86]. Gratings written by CO₂ laser are usually induced point-by-point using laser powers on the order of watts onto a fiber held under tension by a weight. Properties of the grating can be controlled by altering the fiber type, writing power, pulse time, tension, and the grating length and period. An example of such a setup is discussed in Chapter 4.

In contrast to UV fabrication, the refractive index modulation produced in CO₂ writing is based on thermal effects. The heat delivered by the focused IR radiation can result in several separate mechanisms, the relative contributions of which depend on the base fiber and the fabrication parameters. Perhaps the most straightforward mechanism is physical deformation of the fiber. When the pulse from the laser softens the glass, the tension in the fiber causes the softened section to thin and elongate. At smaller diameters more energy is required to maintain the softening temperature, so the tapering ceases. By careful choice of fabrication parameters, a “self-regulating” diameter can be achieved [87]. In addition to tapering, the radiation also ablates some of the glass from the surface of the fiber, allowing gratings to be formed by grooves or microbends [88]. Another mechanism responsible for refractive index modulation is modification of the glass structure. In unannealed fibers this takes the form of glass densification, which results in an increased refractive index. Fibers annealed above 380 °C, meanwhile, exhibit glass volume increase and a decrease in refractive index [81]. At higher tensions, refractive index modulation is predominately achieved by residual stress relaxation. Inherent stresses are present in optical fibers as a result of the different material properties of the core and cladding. Interactions between these two regions

during the manufacturing process result in stresses that are frozen in when the glass cools. Residual stress in optical fibers takes two main forms: thermal stresses occur because the regions have different thermal expansion coefficients, while mechanical stresses occur due to their different viscoelastic properties. The mechanical stress can be relieved by the CO₂ writing process, resulting in a lower refractive index [81]. Due to residual stress relaxation the use of heavier tensioning weights results in larger refractive index changes.

The CO₂ writing technique is attractive due to its low cost. LPGs can be written into standard telecommunications fibers using inexpensive but powerful industrial CO₂ lasers. Compared to the UV technique it can be performed on a wider variety of fibers because it is not restricted by a need for photosensitivity. CO₂-written LPGs also have better stability at elevated temperatures than UV written fibers, because the refractive index modulations are due to structural changes that do not decay over time [85]. However, this method is subject to several limitations. In fibers exposed to severe writing conditions, physical deformations of the fiber, such as grooves or tapers, can lead to increased mechanical weakness of the already delicate jacketless grating. Another limitation of the CO₂ technique is that the long wavelength of the radiation means that the spot size can be fairly large compared to the grating dimensions. A Gaussian beam of diameter w_0 focused by a converging lens of focal length f has a beam waist diameter, w_f , given by

$$w_f = \frac{\lambda f}{\pi w_0}. \quad (2.7)$$

For example, a 10.6 μm laser with a 1 cm beam can be focused to a spot size of about 50 μm with a 15 cm lens. The resolution of the CO₂ technique is therefore insufficient for writing FBGs, whose grating period is smaller than the spot size of the CO₂ laser, and is restricted to LPGs. Another issue with the CO₂ writing technique is that it has poor reproducibility. LPGs fabricated in the same setup with the same writing parameters can

fail to have identical transmission behavior. The reasons behind this variability are poorly understood. Because residual stress relaxation is a major source of the induced refractive index change, slight changes in the residual stress along the length of the fiber leftover from the manufacturing process may play a role. Other explanations are related to the thermal origins of the refractive index change. Changes in air currents at the fiber surface may transfer irregular amounts of heat away from the fiber and slight differences in the position of the fiber under the laser spot may lead to problematic variations in exposure intensity, both of which may contribute to differences in the strength of the thermal effects [89]. Superposition of the thermal effects from one grating period to another may also contribute to variability. When short grating periods or large refractive index changes are desired, heat due to the writing of one period can be conducted to the locations of the adjacent periods and may not be dissipated before the next laser exposure. This superposition can result in complicated, hard to predict interactions that lead to differences from fiber to fiber. Nespereira et al. [90] reported the rate at which they successfully produced LPGs with greater than 5 dB attenuation using their CO₂ laser setup. Using the same incident power, writing time, fiber type, and tensioning weight, their fabrication was successful only 25% of the time for periods less than 400 μm , but 60-100% of the time for periods greater than 400 μm .

Alternative approaches to grating fabrication

In addition to techniques with UV or CO₂ lasers, other approaches to LPG fabrication have been explored. One of the more popular alternatives is the electric arc-discharge method. In this approach, the fiber is mounted under tension between two electrodes and a current, usually 1 to 20 mA, is briefly applied [91]. The resulting arc induces thermal changes in the refractive index through the same physical mechanisms as the CO₂ technique. The

main advantage of the arc-discharge technique is that it can be performed with commercially available splicers, which many fiber optics facilities already have on hand. However, it is even less repeatable than the CO₂ laser technique and not practical for reliable LPG production.

Less mainstream approaches to refractive index modulation have also been reported. Another method of writing photoinduced gratings is the use of NIR femtosecond laser pulses. The mechanism behind this technique was initially thought to be glass densification [92], but is now attributed to nonlinear photon absorption and multi-photon ionization [93]. Because of its nonlinear origin, the femtosecond laser technique allows for inscribing features smaller than the diffraction limit of the laser radiation, providing a means of writing temperature-stable FBGs [93]. Another method of inducing thermally stable refractive index changes is ion beam implantation. This technique has the advantage of producing an index modulation that is linear with the ion dose, rather than the more complicated refractive index profiles in photoinduced gratings. In one example of this technique, Fujimaki et al. [94] directed He ions through a mask onto a thinned optical fiber, resulting in a grating with 15 dB attenuation. In another, a focused beam of protons was used to write gratings point-by-point into several types of telecommunications fibers, resulting in a maximum attenuation of 7 dB [95]. While femtosecond writing and ion beam implantation focus on refractive index modulations in the fiber core, changes to the cladding can also result in grating behavior. The group of Chunn-Yenn Lin has investigated gratings induced by chemically etching a corrugated pattern into the fiber cladding [96]. They have also studied the potential of corrugated gratings as sensors for strain, bending, and twisting, with maximum attenuations approaching 30 dB [97].

An alternative to the above techniques is to produce LPGs by physically manipulating the fiber rather than subjecting it to permanent or semipermanent internal changes. In mechanically induced LPGs the optical fiber is squeezed against a grooved plate in order to exert periodic pressures on it. The properties of the transmission spectrum are polarization

dependent due to the asymmetry of the pressure, and can be tuned by changing the pressing force or by turning the grooved plate in order to change the grating period [22, 98]. When two grooved plates are used, the resulting microbends in the fiber cause it to behave as an LPG [88]. Both mechanically induced LPGs and LPGs produced by microbends are especially interesting because, as long as the pressure remains within the elastic range of the material, the bulk behavior is recovered when the pressure is removed. This means that these gratings are reversible and can be easily tuned, although they can be made permanent by exerting stronger forces on them. Additionally, these gratings can be designed to operate with the plastic jacket intact, allowing for more robust fiber devices [22].

2.2.4 Types of fiber gratings

Fiber gratings are classified as fiber Bragg gratings (FBGs) and long period gratings (LPGs), depending on the grating period. Both types cause an attenuation in the transmission of a particular wavelength, however, the mechanisms by which they operate differ.

FBGs have a period of less than 1 μm and function by reflecting light at the rejected wavelength (Fig. 2.8a). Each period in the grating acts as an interface from which the light can be reflected into an identical mode propagating in the opposite direction [20]. The resonant wavelength for reflection of a mode with effective refractive index $n_{eff,1}$ into a mode of $n_{eff,2}$ is given by

$$\lambda = (n_{eff,1} + n_{eff,2})\Lambda, \quad (2.8)$$

where Λ is the period of the FBG. The effective refractive index, or modal index, differs from the actual refractive index of the material due to the cross-sectional profile of the mode. When the incident and reflected rays are forward and backward propagating versions



Figure 2.8: Basic behavior of fiber gratings. Fiber Bragg gratings (a) reflect light by Bragg reflection into identical counterpropagating modes. Long period gratings (b) couple forward propagating light to lossy cladding modes.

of the same mode, the attenuation occurs at the Bragg wavelength,

$$\lambda_B = 2n_{eff}\Lambda. \quad (2.9)$$

The reflections add constructively at this wavelength, similar to Bragg reflection in a crystal [20, 84]. Due to their effect on the incident light, FBGs are also known as reflection gratings or short-period gratings. They can achieve almost complete attenuation at λ_B with gratings only a few millimeters long. FBGs are most often used as temperature and strain sensors or as photonic components in fiber communications systems [84].

LPGs, also known as transmission gratings, have a period on the order of hundreds of micrometers and are usually one to a few centimeters long (Fig. 2.8b). They operate by coupling the fundamental mode (LP_{01}) to a forward-propagating cladding mode (LP_{0m}) at a resonant wavelength, λ_{LPG} . The cladding mode is rapidly dispersed by scattering at the cladding-air interface, resulting in strong attenuation at λ_{LPG} . The phase-matching relationship for an LPG is given by

$$\delta(\lambda) = \frac{1}{2} \left[\frac{2\pi}{\Lambda} - \beta_1(\lambda) - \beta_{2,m}(\lambda) \right], \quad (2.10)$$

where δ is the detuning parameter and is constant along the fiber axis, Λ is the grating

period, β_1 is the propagation constant of the fundamental mode and $\beta_{2,m}$ is the propagation constant of the m^{th} order cladding mode. The strongest coupling, and therefore the greatest attenuation, occurs when $\delta = 0$. In this case, the relationship reduces to the simpler form

$$\Lambda = \frac{2\pi}{\beta_1(\lambda) - \beta_{2,m}(\lambda)}. \quad (2.11)$$

By substituting $\beta = 2\pi n_{eff}/\lambda$, we find a relationship between the grating period and λ_{LPG} ,

$$\lambda_{LPG} = (n_1^{eff} - n_{2,m}^{eff})\Lambda, \quad (2.12)$$

where n_1^{eff} is the effective index of the fundamental mode and $n_{2,m}^{eff}$ is the effective index of the m^{th} cladding mode [99]. Increasing the surrounding refractive index, for instance, by applying high refractive index materials to the fiber surface, increases $n_{2,m}^{eff}$ because the evanescent tail of the cladding-mode field extends 100-200 nm outside the fiber [100]. The biosensor presented in this work detected attachment of DNA fragments through this dependence on external refractive index.

2.2.5 Phase-matching curves and turn-around point

The longer Λ for LPGs causes them to have attenuation at longer wavelengths than for FBGs. The wavelengths at which this attenuation occurs can be visualized with phase-matching curves (PMCs), which are plots of the resonant wavelength versus the grating period. To construct the PMCs, first the Sellmeier equation is used to find the refractive indexes in the core ($i=1$) and cladding ($i=2$) as a function of wavelength,

$$n_i(\lambda) = \sqrt{1 + \sum_{j=1}^3 \frac{A_{ij}\lambda^2}{\lambda^2 - B_{ij}^2}} \quad i = 1, 2, \quad (2.13)$$

Table 2.1: Sellmeier coefficients used for PMC simulations in this work, based on [1] and [2].

	A_{i1}	A_{i2}	A_{i3}	B_{i1}	B_{i2}	B_{i3}
i=1	0.68698290	0.44479505	0.79073512	0.078087582	0.1155184	10.436528
i=2	0.6961663	0.4079426	0.8974794	0.0684043	0.1162414	9.896161

where A_{ij} and B_{ij} are Sellmeier coefficients and are experimentally determined constants for the material. These expressions for $n(\lambda)$ can then be used to find the normalized frequency for the fiber,

$$V(\lambda) = \frac{2\pi a \sqrt{n_1(\lambda)^2 - n_2(\lambda)^2}}{\lambda} \quad i = 1, 2, \quad (2.14)$$

where a is the radius of the fiber core. The propagation constants in the core and cladding can then be found as

$$\beta_1(\lambda) = \sqrt{\left(\frac{2\pi n_1(\lambda)}{\lambda}\right)^2 - \left(\frac{u(\lambda)}{a}\right)^2}, \quad (2.15a)$$

$$\beta_{2,m}(\lambda) = \sqrt{\left(\frac{2\pi n_2(\lambda)}{\lambda}\right)^2 - \left(\frac{u_{0m}}{b}\right)^2}, \quad (2.15b)$$

where b is the cladding radius, u_{0m} represents the m^{th} zero of the zeroth order Bessel function of the first kind, and $u(\lambda)$ is given by

$$u(\lambda) = \frac{(1 + \sqrt{2})V(\lambda)}{1 + \sqrt[4]{4 + V(\lambda)^4}}. \quad (2.16)$$

These expressions for $\beta_1(\lambda)$ and $\beta_{2,m}(\lambda)$ can be used with equation (2.11) to generate PMCs. Example curves for a fiber a core radius of $3.2 \mu\text{m}$, a cladding radius of $59.2 \mu\text{m}$, and Sellmeier coefficients found in Table 2.1, are presented in Figure 2.9.

For lower-order modes (Fig. 2.9a), λ_{LPG} increases monotonically with Λ . For a fixed Λ , the grating can have multiple attenuations due to coupling with different mode orders, with λ_{LPG} at longer wavelengths for higher-order modes. Gratings with a long Λ may only

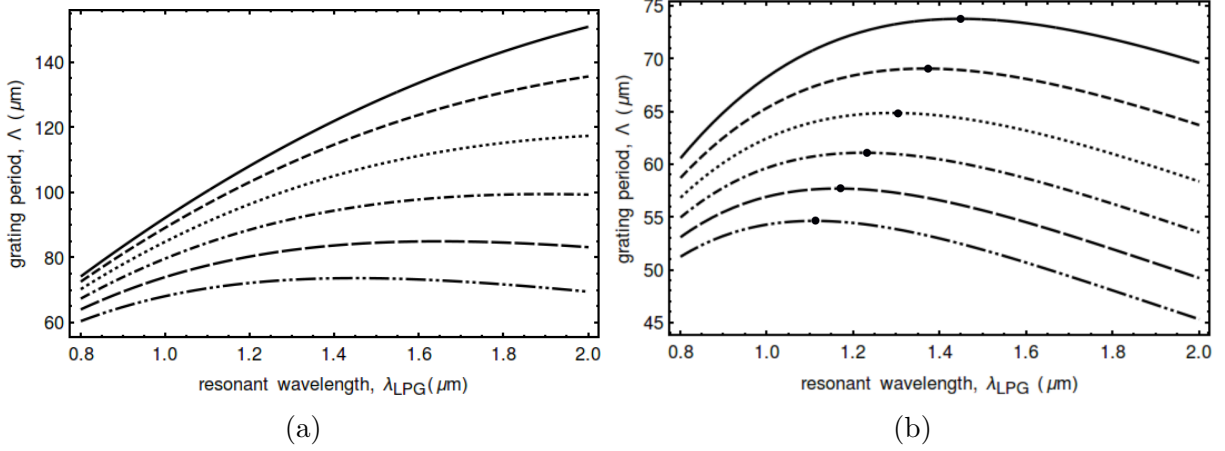


Figure 2.9: Simulated PMCs for coupling to (a) low-order modes and (b) high-order modes. Dots have been added to the higher-order modes indicate the local maxima, where TAP occurs. Generated in Mathematica using Sellmeier coefficient values for 93% silica, 7% GeO₂ glass, based on theory presented in references [1] and [2].

have coupling to a few low-order modes, while gratings with a shorter Λ can couple to many modes.

Following a single phase-matching curve, the slope $d\Lambda/d\lambda_{LPG}$ decreases with increasing wavelength. For high-order modes, $d\Lambda/d\lambda_{LPG}$ eventually goes to zero and $d\lambda_{LPG}/d\Lambda$ goes to infinity. As a result, LPGs coupling in this regime have very high sensitivity. As presented in Shu [23], the sensitivity of an LPG to the surrounding index of refraction is given by

$$\frac{d\lambda_{LPG}}{dn_3} = \lambda_{res}\gamma\Gamma_3, \quad (2.17)$$

where n_3 is the index of refraction of the surrounding material, γ is the waveguide dispersion,

$$\gamma = \frac{\frac{d\lambda_{LPG}}{d\Lambda}}{n_1^{eff} - n_{2,m}^{eff}}, \quad (2.18)$$

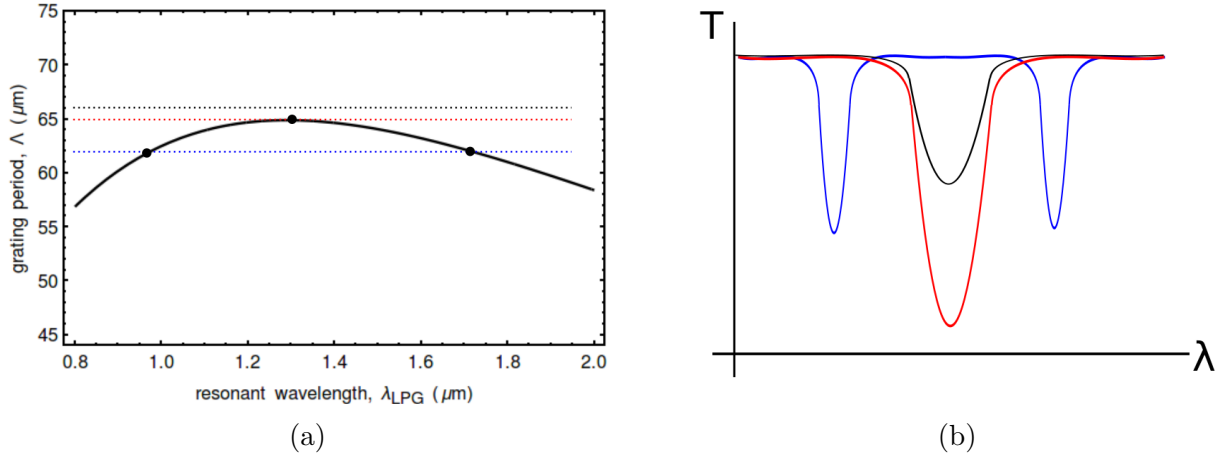


Figure 2.10: Behavior near the TAP. The PMC of the $LP_{0,15}$ mode is shown in (a), and a sketch of the transmission spectrum is shown in (b). Before the TAP (blue), the spectrum has a pair of resonant wavelengths. At the TAP (red), these combine into a single attenuation at λ_{TAP} . A little beyond the TAP (black) the coupling rapidly decreases in strength.

and Γ_3 describes the dependence of the waveguide dispersion on n_3 ,

$$\Gamma_3 = -\frac{u_m^2 \lambda_{LPG}^3 n_3}{8\pi b^3 n_2 (n_1^{eff} - n_{2,m}^{eff})(n_2^2 - n_3^2)^{3/2}}. \quad (2.19)$$

From these equations it can be seen that as $d\lambda_{LPG}/d\Lambda$ becomes large, the sensitivity of the fiber becomes very high. The local maximum where this occurs is called the turn-around point (TAP), and has interesting consequences for the transmission spectrum. For a given grating period, lower-order cladding modes have only one resonant wavelength. Sensors based on low-order LPGs monitor shifts in the central wavelength of this single peak. Modes with a TAP, meanwhile, can exhibit coupling at two wavelengths if Λ is a little smaller than the grating period at the TAP.

Changes in temperature, strain, or surrounding refractive index will cause these dual peaks to either shift closer together or farther apart. The longer wavelength peak exhibits a larger change in λ_{LPG} in these cases because, from equations (2.17) and (2.19), the sensitivity has a λ^4 dependence [23]. These wavelength shifts are more dramatic than those observed

in ordinary LPGs due to high near-TAP sensitivity, and several papers have been published demonstrating sensors which measure changes of λ_{LPG} in dual peak fibers due to external stimuli [101–109]. A variety of alternative terms are used for the TAP by these authors, including turning point, dual peaks, and phase-matching turning point.

As the fiber approaches the TAP, the dual peaks overlap and merge until they form a single deep attenuation at the TAP wavelength, λ_{TAP} (Fig. 2.10). Continuing past the TAP, the attenuation of the single peak decreases rapidly at a constant wavelength. Eventually, the peak disappears completely, as conditions now prevent coupling to this cladding mode. This behavior is experimentally demonstrated in Figure 5.2. By operating a sensor in the single-wavelength regime of a TAP-LPG, high sensitivity can be achieved while costs can be reduced by monitoring the transmitted power at λ_{TAP} rather than analyzing the whole spectrum.

Another consequence of equations (2.17)-(2.19) is that the sensitivity of the LPG to the external refractive index is higher for thinner claddings, due to the b^{-3} dependence of Γ_3 . The response of a sensor can therefore be improved by etching away the outer portion of the fiber, which can be accomplished with hydrofluoric acid. It has also been shown that higher sensitivity is achieved by coupling to higher order modes. A rapid increase in sensitivity is observed for the first few modes, which then levels off and approaches saturation for modes of index 20 or greater [23]. Through careful selection of fabrication parameters, a highly sensitive TAP-LPG sensor can be designed.

2.3 Optical biosensors

Biosensors are devices which make use of biological recognition elements to detect a species of interest, which may or may not itself be biological [110]. They may operate via a va-

riety of transduction methods, including mechanical, electrical, piezoelectric, thermal, and optical mechanisms. Optical biosensors are particularly popular because they can offer sensitive, real-time, non-destructive detection of biological and chemical materials [26]. Optical biosensors are broadly categorized as fluorescence-based, in which fluorescent tags are used to aid detection, and label-free, in which other approaches are used that do not require tagging. Both approaches can offer rapid, low-cost, sensitive, specific sensing in compact devices resistant to electromagnetic interference.

In label-based optical biosensors, either the biorecognition element or the target are bound to color-changing or fluorescent molecules that produce changes in the light profile of the system when detection occurs. Various properties may be analyzed, including emission intensity, decay time, polarization, anisotropy, and others [28]. A common type of label-assisted biosensor is enzyme-linked immunosorbent assay (ELISA). In ELISA, the wells of a multiwell plate are functionalized with antibodies or antigens, which bind to antigens or antibodies (respectively) from the sample. Enzyme-labeled secondary antibodies are then added, which bind to materials from the sample. Finally, a colorigenic enzyme substrate is added, resulting in a measurable color change. In general, label-based techniques are extremely sensitive, and have demonstrated the ability to detect single molecules [111]. However, the labeling process can be time consuming and complex, and can interfere with the normal functioning of the labeled biomolecules. Additionally, fluorescence signal bias can complicate quantitative analysis [29]. Alternatives without the need for labeling are therefore a subject of great interest.

Label-free optical biosensors produce a signal directly via the interaction between the analyte and the transducer itself, and leave the target molecules in their natural form [26]. They have the significant advantage of not requiring a separate labeling step. A wide variety of label-free biosensors have been investigated, including the TAP-LPG biosensor presented

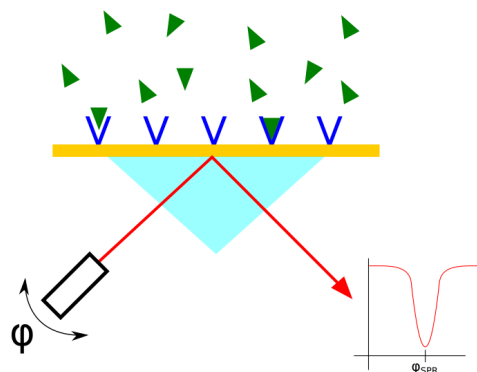


Figure 2.11: Kretschmann configuration of an SPR biosensor. Analyte (green) is flowed past receptor ligands (blue) immobilized on a gold film applied to the back of a prism. A light source is directed at the back side of the sensor surface, and reflection is monitored at different angles of incidence. The resonant angle, at which reflected light is attenuated by SPR absorption, varies when binding occurs.

in this work.

The most common label-free optical biosensor is the SPR biosensor. As discussed in Section 3.2, high absorption can occur when light incident on a metal induces resonant collective oscillations of free electrons, called plasmons. In SPR biosensors, light is directed through a prism coated with a gold film (Fig. 2.11). The incidence angle is varied to find the SPR angle, ϕ_{SPR} , where reflection is heavily attenuated by plasmon resonance. The gold film is functionalized with receptor ligands, usually by immobilizing proteins to a self-assembled monolayer of carboxymethylated dextran. The aqueous sample flows past the sensor surface and changes in ϕ_{SPR} due to binding of analyte are monitored. SPR biosensors can be extremely sensitive, and in some configurations can detect analytes as concentrations as low as 10 pM [29]. However, SPR instruments are expensive and bulky. They require very fine angle control, down to 0.001° , and they consequently have very sensitive alignment, which makes them non-portable. Additionally, preparing the sensor surface can be time consuming [26].

Due to the limitations of SPR biosensors and the advantages of label-free biosensors, multiple other approaches to label-free biosensing are being explored. In interferometric approaches, light is split into two paths. One of the paths interacts with the sample, while the other serves as a reference beam. Bioconjugation along the sample path causes a change in refractive index and a subsequent phase change that can be observed by comparison with the reference beam [112]. Alternatively, optical waveguide biosensors utilize waveguides in various geometries to detect binding by probing evanescent fields. These can include planar waveguides, microscopic optical ring resonators, and optical fibers [29].

2.3.1 Characterization of sensor performance

The effectiveness of a biosensor may be characterized by several different parameters. A good biosensor should be sensitive, specific, accurate, and reliable. Many of these terms have specific technical definitions which differ from their use in general speech, so it is worthwhile to note their meanings when describing sensors.

It is useful to know the minimum amount or concentration of analyte that can be detected by a sensor. The limit of detection (LOD) is the lowest amount of analyte that produces a positive result with reasonable certainty. The limit of quantification (LOQ) is similar, but refers to the lowest amount of analyte that can be reliably quantified. These limits can be determined by statistical analysis of the sensor's response to known samples. The LOQ is always higher than the LOD because quantification is more difficult than detection alone [113]. These properties are often confused with sensitivity, which is the magnitude of the change in transduction signal due to a change in the analyte [29]. It is possible for a sensor to be highly sensitive but to also have a poor LOD, for example, when the signal has high

background noise. More specifically, the percent sensitivity is defined in diagnostics as

$$\% \text{ sensitivity} = 100 * \frac{TP}{TP + FN}, \quad (2.20)$$

where TP is the number of true positives detected in the data set, and FN is the number of false negatives [114]. A sensor with 100% sensitivity would always generate a signal when the target is present, but could also suffer from a high rate of false positives.

Another important feature of a biosensor is its capacity to distinguish between the intended target and other materials. Specificity refers to the ability of the sensor to detect a specific analyte when that analyte is in an admixture with other components, as is the case in commonly collected samples such as blood, urine, or tissue [27]. In diagnostics, percent specificity is calculated as

$$\% \text{ specificity} = 100 * \frac{TN}{TN + FP}, \quad (2.21)$$

where TN is the number of true negatives that occurred in the data set, and FP is the number of false positives [114]. A test with 100% specificity, therefore, never generates a falsely positive signal. Good specificity can be achieved by blocking nonspecific binding and choosing appropriate receptor molecules. In many cases the sensor surface is functionalized with antibodies, which are produced by the immune system to bind to specific antigens. Enzymes, which are often specialized such that they only interact with certain substrates, are another common choice. DNA fragments with sequences selected to target the analyte, called hybridization probes, are also effective.

Other sensor properties refer to how predictable and dependable the sensor is. Reliability refers to the sensor's ability to produce the same results when exposed to the same stimulus. A good sensor should produce consistent, repeatable results. Another important

trait, accuracy, refers to the ability of a sensor to produce results consistent with reality. In quantitative testing, an accurate sensor should correctly identify the true amount of analyte present in a sample [113]. An accurate sensor should have a low rate of false positives and false negatives, both of which present significant problems depending on the application.

2.4 Bacterial detection

Bacteria are single-celled prokaryotic organisms that can be found almost ubiquitously around the globe. They have complex interactions with the larger-scale organisms with which they coexist, ranging from beneficial symbiotic relationships to deadly infections. Because many bacteria can be disease-causing, it is very important to be able to identify their species, and in some cases their subtype or strain, quickly, accurately, and sensitively in medicine, agriculture, food safety, preventing bioterrorism, and a plethora of other contexts.

2.4.1 Current techniques for bacterial identification

Techniques for identifying bacteria vary based on the setting. Clinicians are often able to make an informed guess of the pathogen in question based on signs and symptoms and can choose a small number of specific tests to confirm. This may also be the case in some laboratory settings, where contextual clues can suggest possible identities. In these cases, analysis of the phenotypical properties and susceptibility of the bacteria may be sufficient. In other cases, more extensive or sophisticated tests may be required to study the specific biomolecules or genetic code present. An overview of current approaches to bacterial identification is provided in this section.

Phenotypical tests, culture and susceptibility, and biochemical analysis

Traditional methods for identifying bacteria depend upon phenotypical tests studying cell morphology, colony growth, and biochemical characteristics. Different bacteria have different shapes, generally taking the form of rods (bacilli), spheres (cocci), commas, spirals, and corkscrews [115]. Therefore, simply observing the organisms under a microscope can provide clues toward identifying or ruling out their genera. Additional procedures, such as Gram staining, may be added to help obtain more information from microscopic observations.

Another major approach is to observe how the bacteria grow on plates. The usual morphology of the individual colonies varies with the genus, with some bacteria forming neat circular colonies while others may be branched or filamentous. Therefore, the appearance of the colonies can be used to narrow down the identities of the bacteria present. Additionally, more information can be obtained by subjecting the cultures to different nutritional, temperature, and oxygen-availability conditions. For example, a bacterium's ability to thrive in an anaerobic environment or in different growth media may be observed. Proliferation on a plate treated with an antibiotic can be used to indicate a strain that is resistant to that agent. For example, bacteria taken from an infected wound may be grown in the presence of antibiotics in order to distinguish between ordinary *Staphylococcus aureus* and methicillin-resistant *S. aureus* (MRSA). Culture and susceptibility assays are widely used in clinical settings, where a patient's signs and symptoms can be used to help determine possible bacterial candidates. However, while culture-based techniques are inexpensive and technically simple, they generally require 24 hours or more to obtain results due to the need to wait for colony growth. Long incubation times are problematic when attempting to diagnose an aggressive infection, and therefore more rapid tests are often desired.

In addition to observing bacteria directly and growing them on plates, further biochemical

tests can be performed. Biochemical analysis is used to determine whether the bacteria produces particular enzymes, which can be accomplished by introducing a color-changing enzyme substrate or by looking for physical evidence of the enzyme-substrate interaction. For example, many bacteria contain the enzyme catalase, which catalyzes the conversion of hydrogen peroxide into water and gaseous oxygen. If bubbles are produced when hydrogen peroxide is added to a small sample of a bacterial culture this indicates the presence of catalase. The catalase test can be used to distinguish between catalase-positive and catalase-negative species and genera, and because anaerobic bacteria are usually catalase-negative it can help differentiate aerobic and anaerobic bacteria [116]. Other forms of biochemical analysis involve subjecting the bacteria to various tests of their ability to metabolize certain sugars or carbohydrates. Cards containing miniature versions of many of these biochemical assays are commercially available, and are widely used for identification of commonly found bacteria in clinical environments. These cards, called analytical profile index (API) strips, allow multiple properties of the bacteria to be determined simultaneously. The results of these assays are then applied to a dichotomous key to identify the bacteria present [117].

While these tests are frequently sufficient, they suffer from some limitations. They can only be used to identify known bacteria, and in many cases may be unable to distinguish strains within a species when the strains are phenotypically similar. Phenotypical identification is usually restricted to bacteria that can grow *in vitro* under standard conditions, and can fail when more exotic bacteria are present [118]. Culture-based techniques and API analysis can be labor-intensive and slow due to the need to wait for bacteria to grow. For these reasons, more sophisticated molecular and DNA-based techniques may be required.

Molecular and DNA-based techniques

To combat the limitations of physical and biochemical identification, a number of molecular and DNA-based techniques have been developed. One widely applied technique is to observe the DNA amplification of a single gene by polymerase chain reaction (PCR) in real time. PCR is a process by which a single gene, targeted by short single-stranded DNA segments called primers, is amplified by thermocycling in the presence of excess nucleotides and the enzyme *Taq* polymerase. PCR multiplies the target gene exponentially, allowing for easier sequencing and further analysis. In one type of real-time PCR, molecules which fluoresce after binding with the amplification product are added and the samples are monitored by spectrofluorometry during the PCR process. By measuring the amount of fluorescence after each thermocycle for a range of dilutions of the sample, it is possible to quantify the amount of template DNA in the original sample [113]. Primers can be selected to be specific to a certain strain or species, allowing for rapid identification. When more general genes are targeted, further analysis by Sanger sequencing, pyrosequencing, reverse hybridization, or Luminex analysis is required [119]. Real-time PCR produces rapid results with high throughput, but can be susceptible to DNA contamination and requires additional strategies to distinguish between viable and dead cells [113]. The technique is also expensive and requires skilled personnel.

Another DNA-based technique is the use of oligonucleotide DNA microarrays. Here, fluorophore-labeled DNA probes for various species or strain-specific genes are immobilized in different regions of a solid substrate. Complementary DNA (cDNA) from the sample is extracted and applied to the chip, and regions where the cDNA hybridizes to the probes fluoresce. By analyzing which probes produce fluorescence, it is possible to identify the bacteria present in the sample [120]. A single chip may have hundreds of specific probes for simultaneous identification of multiple pathogens, allowing for high-throughput analysis.

Other molecular techniques exist which are not dependent on DNA. In fatty acid profiling, the relative amounts of different fatty acids in the bacteria are measured by performing gas chromatography and mass spectrometry or matrix-assisted laser desorption/ionization (MALDI) on the sample [121]. Adding time-of-flight (TOF) mass spectrometry to MALDI enables researchers to obtain a mass spectrum of the total protein profile of the subject. Currently, MALDI-TOF mass spectrometry is among the most common approaches to bacterial identification. Another technique is metabolic profiling or chemo-profiling, in which high pressure liquid chromatography and mass spectrometry are used to obtain a profile of the secondary metabolites produced by the microorganisms in the sample. Because the relative amounts of fatty acids in bacteria and the secondary metabolites produced by them differ from species to species, this provides a means of identification. However, these profiling techniques require expensive instrumentation.

In clinical settings, a practitioner can often narrow down the possible culprits by considering the patient's signs and symptoms and can use their suspicions to select the appropriate tests. In some cases it is practical to use a combination of techniques to ensure accurate diagnosis. For example, when a throat infection by group A *Streptococcus* (strep throat) is suspected, two types of test are typically performed on the throat swab. First, the sample is run through a rapid strep test, in which antigens for group A streptococci, if present, bind to labeled antibodies on a test strip. This test can provide a quick diagnosis while the patient is still in the office, allowing the antibiotic course to begin sooner if needed. However, because this assay has a high false negative rate, a throat culture is usually performed as well, the results of which are available the following day [122]. Combining methods of identification in this way can balance the disadvantages of some techniques with the advantages supplied by others and can lead to faster, more accurate, results.

Conventional techniques for identifying bacteria are often slow, expensive, or complex to

operate. There is therefore a need for more simple-to-use assays that are rapid, low-cost, and compact. As discussed in Section 2.3, optical biosensors are often able to combine the advantages of speed and sensitivity. TAP-LPG biosensors have the potential to offer sensitive and accurate bacterial detection in compact, rugged devices that could be operated by clinical staff. Chapter 5 presents the results of a TAP-LPG biosensor for *Brucella*.

2.4.2 Brucellosis

Brucella spp. are a group of bacteria that are responsible for brucellosis, a zoonotic infection that can cause chronic disease in agricultural animals including pigs, cattle, bison, sheep, and goats, as well as in marine mammals, rodents, dogs, and humans [123]. Most species of *Brucella* have a preferred host for which they are named, such as *B. suis* which preferentially infects pigs and *B. ovis* which favors sheep, although infection of other species is possible. In order to control risks and restrict the spread of brucellosis from infected herds, rapid assays are needed that can diagnose brucellosis and distinguish between *Brucella* species.

In general, infection occurs when *Brucella* comes in contact with the mucous membranes, which may occur when consuming contaminated materials. The bacteria cross the mucosal epithelium and are engulfed by mucosal macrophages and dendritic cells. Once inside these host cells the *Brucella* sequesters itself in a *Brucella* containing vacuole (BCV), where it adapts to its new environment and begins replication. The bacteria then disseminate and take up residence in their preferred tissues, such as in the placenta, fetal lungs, reproductive tract, and some connective tissues. Properties of the BCV help the bacteria evade the innate immune response. Meanwhile, the invading bacteria inhibit several cellular processes, including host cell apoptosis, dendritic cell maturation, antigen presentation, and activation of naive T cells, in order to ensure their survival. The combined evasion of the immune

system and persistence in infected cells enables *Brucella* to establish a chronic, systemic infection [123].

B. abortus is responsible for bovine brucellosis, which causes reproductive problems in cattle and bison due to its preference for placental, fetal, and reproductive tissue. Its effects can include low fertility, weak calves, abortion, retained placentas, reduced lactation, and male reproductive tract lesions. In addition, chronic infection can cause joint problems such as arthritis and bursitis [124]. Because brucellosis is economically prohibitive, the usual practice is to destroy infected animals, resulting in direct economic losses to agricultural producers.

Historically, brucellosis was endemic in a large fraction of livestock herds. Immunization schemes in the twentieth century significantly reduced infection rates in developed countries. For example, federal eradication programs in the United States lowered the incidence of *B. abortus* in US cattle from 15% in 1934 to zero in many parts of the country [124]. However, *B. abortus* remains endemic in many developing nations and is estimated to infect approximately 20% of cattle worldwide [123]. Additionally, *B. abortus* persists in natural reservoirs, including bison and elk in the US and African buffalo in south eastern Africa, from which it can be reintroduced to agricultural herds [125]. Particular attention is paid to the incidence of brucellosis in the greater Yellowstone area, where cattle ranching occurs in close proximity to large wildlife populations. Although *B. abortus* is present in wild bison, bison-to-cattle transmission has been relatively uncommon because of efforts to keep the species separated. In this region more spillover has been observed from elk, where changes in elk behavior patterns due to climate change, shrinking habitats, and the reintroduction of wolves have led to increased transmission events and heightened tensions between ranchers and conservationists [124].

While humans are not a preferred host for *Brucella*, brucellosis can be contracted through

the consumption of contaminated meat and dairy products. Infections due to inhalation of airborne *Brucella* have also been reported, and it is estimated that more than 500,000 new human infections occur annually [125]. In the United States, many cases of human brucellosis are laboratory acquired and have been linked to aerosolization of samples during routine handling [126]. Acute infection causes flu-like symptoms, including a high and variable fever, night sweats, and joint pain. Chronic brucellosis can cause persistent neurological problems, encephalomyelitis, hepatitis, orchitis, endocarditis, and other serious complications, the most common of which is arthritis [123, 127]. It also appears to increase the chance of adverse pregnancy outcomes [128]. While brucellosis is commonly viewed as an economic threat, its ramifications clearly extend into human health. Most efforts to control *Brucella* are restricted to vaccination and monitoring in the agricultural arena. However, because the bacteria can remain viable in aerosol and can cause infection with as few as 10 to 100 organisms, there is some concern that *Brucella* could be deployed as a bioterrorism agent. This is especially concerning because no human vaccine has been approved [123].

Because brucellosis is expensive to treat, it presents a considerable economic threat to agriculture through its effect on livestock fertility and its management via culling. Additional costs are incurred by the need to maintain testing programs and by regulations that regulate sales to certain markets. When possible, eradication programs are an effective means of reducing this cost. In one analysis of a program in Lazio, Italy, it was estimated that costs associated with *Brucella* management were reduced by 50% when the region achieved a disease-free status [129]. However, brucellosis remains harder to eliminate in regions where livestock may come into contact with wild reservoir species. Another challenge occurs in low to middle income countries, where it is more common for different livestock species to intermingle in small operations and where it may be more difficult to entice farmers to participate in eradication schemes [125]. Therefore, a sensitive, rapid, and portable assay

that can distinguish between species of *Brucella* is needed to monitor brucellosis incidence and to quickly establish the origin of new infections. In this dissertation, an ISAM-coated TAP-LPG biosensor for distinguishing between *B. abortus* and the non-bovine species *B. melitensis* and *B. suis* is presented.

Chapter 3

Background for plasmonic enhancement of second-harmonic generation

In this chapter, a review of topics relevant to the plasmonic enhancement of SHG is presented. These include a mathematical discussion of nonlinear optics, as well as an overview of nonlinear media, applications of second-order nonlinear effects, plasmonics, and the use of plasmonics to enhance nonlinear optics.

3.1 Nonlinear optics

An electric field applied to a dielectric causes molecular dipoles within the material to align, as well as induce dipoles in the material. This effect is referred to as the polarization. In most cases, the strength of the polarization is proportional to the strength of the electric field, as

$$\mathbf{P} = \epsilon_0 \chi_e \mathbf{E}, \quad (3.1)$$

where ϵ_0 is the permittivity of free space and χ_e is the electric susceptibility of the dielectric [130]. This equation holds true at ordinary field strengths. With more intense fields, such as

those found in electromagnetic radiation from a laser, some dielectrics exhibit other behavior. For lossless and dispersionless materials, equation (3.1) can be expanded in a Taylor series,

$$\tilde{P}(t) = \epsilon_0 \{ \chi^{(1)} \tilde{E}(t) + \chi^{(2)} \tilde{E}(t)^2 + \chi^{(3)} \tilde{E}(t)^3 + \dots \}, \quad (3.2)$$

where tilde ($\tilde{}$) indicates a value that varies rapidly in time. The linear relationship common at low field strengths is represented by the first term in the series, where $\chi^{(1)}$ (formerly χ_e) is known as the first-order susceptibility or linear susceptibility. The higher order terms represent nonlinear optical phenomena, which are classified according to their order in the series. Second-order nonlinear optics employ the second term and vary quadratically with the field strength. They occur in materials whose second-order nonlinear susceptibility, $\chi^{(2)}$, is sufficiently large, usually on the order of pm/V. Third-order nonlinear optics are represented by the third term and are governed by the third-order nonlinear susceptibility, $\chi^{(3)}$ [30]. Higher-order nonlinearities are less common, but are sometimes used for higher order harmonic generation. Second-harmonic generation, the focus of this work, is a second-order nonlinear process.

There are several types of second-order nonlinear processes. When the incident field has two frequencies,

$$\tilde{E}(t) = E_1 e^{-i\omega_1 t} + E_2 e^{-i\omega_2 t} + c.c., \quad (3.3)$$

the second-order induced polarization becomes

$$\tilde{P}^{(2)}(t) = \epsilon_0 \chi^{(2)} [E_1^2 e^{-i2\omega_1 t} + E_2^2 e^{-i2\omega_2 t} + 2E_1 E_2 e^{-i(\omega_1 + \omega_2)} + 2E_1 E_2 e^{-i(\omega_1 - \omega_2)} + c.c.] \quad (3.4)$$

$$+ 2\epsilon_0 \chi^{(2)} [E_1 E_1^* + E_2 E_2^*]. \quad (3.5)$$

The first two terms, which have frequencies $2\omega_1$ and $2\omega_2$, represent second-harmonic genera-

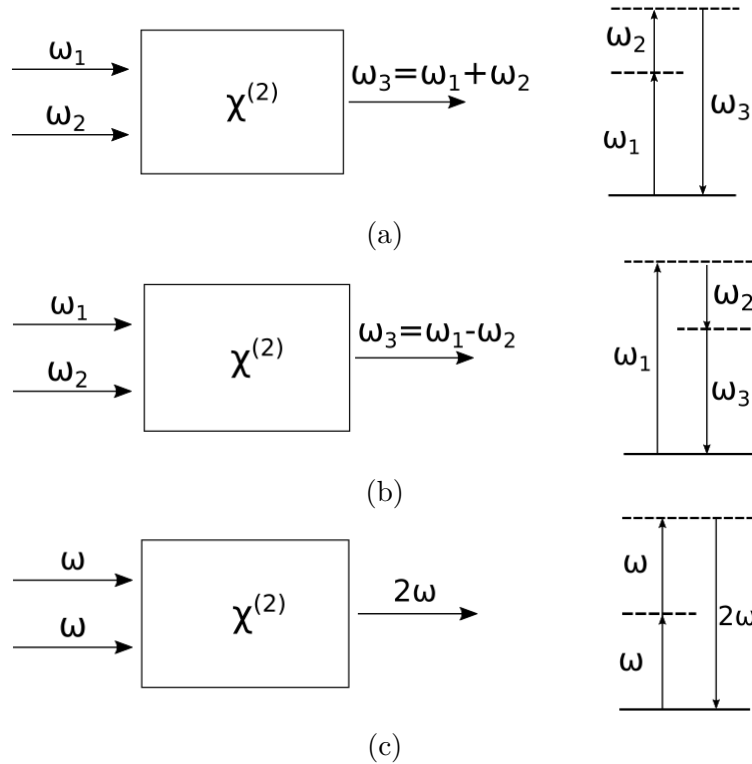


Figure 3.1: Schematics of second-order nonlinear optical processes. Sum-frequency generation produces an output wave with a frequency equal to the sum of the input frequencies (a). Difference-frequency generation produces an output wave with a frequency equal to the difference between the input frequencies (b). Second-harmonic generation produces an output wave with double the input frequency (c).

tion (SHG), in which two photons with the same frequency are destroyed and a single photon at twice the original frequency is simultaneously created in a single quantum mechanical process. The third term, with frequency $\omega_1 + \omega_2$, is sum-frequency generation (SFG). SFG is similar to SHG, but occurs when the two input photons are at different frequencies. It is used to fashion tunable UV radiation by applying a two visible wavelength lasers, one tunable and the other fixed-frequency, to a nonlinear crystal. The fourth term, with frequency $\omega_1 - \omega_2$, is difference-frequency generation (DFG). In DFG, a photon of frequency ω_1 is destroyed and photons at ω_2 and $\omega_1 - \omega_2$ are created. While this effect can occur spontaneously under exposure to ω_1 alone, it is significantly stimulated by an input field at ω_2 . Because it can be

used to amplify ω_2 , DFG can also be referred to as optical parametric amplification. DFG can be used similarly to SFG to make tunable IR light sources. The last two terms, for which ω is zero, represent the optical rectification, in which a static field is induced in the material, generating no radiation. While there are four different nonzero frequency terms, usually only one is produced at reasonable intensity due to restrictions caused by phase-matching conditions [30].

3.1.1 Noncentrosymmetry

An important property of second-order nonlinearity is that it is restricted to noncentrosymmetric media. Centrosymmetry, also known as inversion symmetry, is the property that the crystal structure appears the same from the point (x, y, z) as it does from $(-x, -y, -z)$ [131]. Centrosymmetry is a property of many crystal classes, as well as materials with randomized orientation such as liquids or gases. Therefore, the development of second-order nonlinear materials requires careful considerations to ensure a net order that will maintain noncentrosymmetry.

The limitation to noncentrosymmetric media is the result of fairly simple mathematical logic. From equation (3.2), the second-order nonlinear polarization in a material is given by

$$\tilde{P}(t) = \epsilon_0 \chi^{(2)} \tilde{E}(t)^2. \quad (3.6)$$

For a centrosymmetric material with an applied field of the form

$$\tilde{E}(t) = \mathcal{E} \cos(\omega t), \quad (3.7)$$

changing the sign of the incident field must change the sign of the induced polarization but

keep the magnitude fixed. The form for the polarization would become

$$-\tilde{P}(t) = \epsilon_0 \chi^{(2)} (-\tilde{E}(t))^2, \quad (3.8)$$

which, when the square is executed, simplifies to

$$-\tilde{P}(t) = \epsilon_0 \chi^{(2)} \tilde{E}(t)^2. \quad (3.9)$$

By comparing equations (3.6) and (3.9), it is clear that they imply $\tilde{P}(t) = -\tilde{P}(t)$. This is only possible for $\tilde{P}(t) = 0$, and because $\tilde{E}(t)$ and ϵ_0 are known to be nonzero, we find that

$$\chi^{(2)} = 0, \quad (3.10)$$

for centrosymmetric media. Therefore, centrosymmetric media are mathematically forbidden from exhibiting second-order nonlinear effects. It is worth noting, however, that second-order NLO can sometimes be observed from the surfaces and interfaces of centrosymmetric media due to symmetry breaking at their interfaces.

3.1.2 SHG theory

While the general case presented in equation (3.5) considered excitation by two frequencies, SHG is more often produced by a single light source at the fundamental frequency ω_1 . In this case, the incident electric field is given by

$$\tilde{E}(t) = E e^{-i\omega_1 t} + c.c., \quad (3.11)$$

and the nonlinear polarization is

$$\tilde{P}^{(2)}(t) = [\epsilon_0 \chi^{(2)} E_1^2 e^{-i2\omega_1 t} + c.c.] + 2\epsilon_0 \chi^{(2)} E_1 E_1^*. \quad (3.12)$$

Again, the terms at frequency $2\omega_1$ represent SHG, and the zero frequency term is the optical rectification.

The previous analysis has been for lossless, dispersionless materials. In materials with dispersion and/or loss, the Taylor series presented in equation (3.2) is no longer sufficient, and frequency-dependence and geometry must be considered. First, it is useful to alter the notation in order to reserve subscripts for summed indexes. A field at frequency n is now expressed as

$$\mathbf{E}_n = \mathbf{E}(\omega_n), \quad (3.13)$$

where

$$\mathbf{E}(-\omega_n) = \mathbf{E}(\omega_n)^*, \quad (3.14)$$

and the total field is the sum of the fields at each frequency,

$$\tilde{\mathbf{E}}(\mathbf{r}, t) = \sum_n \mathbf{E}(\omega_n) e^{-i\omega_n t}. \quad (3.15)$$

In this more general case, the relationship between the electric field and the polarization can be represented as

$$P_i(\omega_n + \omega_m) = \epsilon_0 \sum_{jk} \sum_{(nm)} \chi_{ijk}^{(2)}(\omega_n + \omega_m, \omega_n, \omega_m) E_j(\omega_n) E_k(\omega_m), \quad (3.16)$$

where ijk are the Cartesian components of the fields and ω_n and ω_m are allowed to vary but $\omega_n + \omega_m$ is held fixed. The second-order susceptibility, $\chi_{ijk}^{(2)}(\omega_n + \omega_m, \omega_n, \omega_m)$ is now a

third-rank tensor. There are 12 ways to combine the frequencies, six of which are given by:

$$\chi_{ijk}^{(2)}(\omega_3, \omega_1, \omega_2) \quad \chi_{ijk}^{(2)}(\omega_2, \omega_3, -\omega_1) \quad \chi_{ijk}^{(2)}(\omega_1, \omega_3, -\omega_2), \quad (3.17)$$

$$\chi_{ijk}^{(2)}(\omega_3, \omega_2, \omega_1) \quad \chi_{ijk}^{(2)}(\omega_2, -\omega_1, \omega_3) \quad \chi_{ijk}^{(2)}(\omega_1, -\omega_2, \omega_3), \quad (3.18)$$

and another six combinations where the sign of each frequency is reversed. Permuting over the Cartesian coordinates produces 27 possible combinations. The susceptibility tensor therefore has 324 elements. In practice, symmetry arguments can be used to reduce the number of independent elements that must be found.

For second-harmonic generation, $\omega_3 = 2\omega_1$. When the sum over the frequencies is executed in this case, this relationship becomes

$$P_i(\omega_3) = \epsilon_0 \sum_{jk} \chi_{ijk}^{(2)}(\omega_3, \omega_1, \omega_1) E_j(\omega_1) E_k(\omega_1). \quad (3.19)$$

3.1.3 Wave equation approach to SHG

The following derivation is based on Boyd's [30] treatment of an early theoretical analysis presented by Armstrong [132] in 1962. The basic approach is to begin by proposing forms for the electric fields and induced polarizations. These forms are then applied to the wave equation which, upon simplification, yields a coupled-amplitude relationship between the incident fields and the generated fields.

To begin, we consider a lossless material that is subject to dispersion, where the incident field is at frequency ω_1 and the second-harmonic field is at frequency $\omega_2 = 2\omega_1$. Each frequency component of the electric field must obey the wave equation for a lossless, dispersive

medium,

$$\nabla^2 \tilde{E}_j - \frac{\epsilon^{(1)}(\omega_j)}{c^2} \frac{\partial^2 \tilde{E}_j}{\partial t^2} = \frac{1}{\epsilon_0 c^2} \frac{\partial^2 \tilde{P}_j}{\partial t^2}. \quad (3.20)$$

The total electric field in the nonlinear material can be written as the sum of the electric fields at each frequency present. Because we have assumed an incident field at ω_1 and a generated field at ω_2 , the total field can be written as

$$\tilde{E}(z, t) = \tilde{E}_1(z, t) + \tilde{E}_2(z, t), \quad (3.21)$$

where \tilde{E}_1 and \tilde{E}_2 are the fields corresponding to ω_1 and ω_2 , respectively. Assuming the fields take the form of waves, we can separate the time dependence and spatial dependence into separate factors. Each of the fields can then be expressed in terms of a spatially-dependent complex amplitude, $E_j(z)$, and a time-dependent exponential factor, as

$$\tilde{E}_j(z, t) = E_j(z) e^{-i\omega_j t} + c.c., \quad j = 1, 2. \quad (3.22)$$

The spatial dependence can itself be broken into a slowly varying amplitude factor, $A_j(z)$, and a rapidly varying exponential factor. Each frequency component of the field can then be written as

$$\tilde{E}_j(z, t) = A_j(z) e^{ik_j z} e^{-i\omega_j t} + c.c., \quad j = 1, 2. \quad (3.23)$$

To account for dispersion, the propagation constant and refractive index are both allowed to vary with frequency as

$$k_j = \frac{n_j \omega_j}{c}, \quad n_j = \sqrt{\epsilon^{(1)}(\omega_j)}, \quad (3.24)$$

where $\epsilon^{(1)}$ is the dimensionless relative permittivity of the material, and is a frequency-independent tensor.

We perform a similar separation on the nonlinear polarization, which is written as

$$\tilde{P}^{NL}(z, t) = P_1(z)e^{-i\omega_1 t} + P_2(z)e^{-i\omega_2 t} + c.c. \quad j = 1, 2. \quad (3.25)$$

The magnitude of each polarization component, $P_j(z)$, can be determined from symmetry conditions. A degeneracy factor, d_{eff} , appears as a result of reducing the theory from tensor to scalar form. The form of d_{eff} varies based on geometry and crystal class, and has been derived by theorists for many solid-state systems. After this simplification, the polarization at frequency ω_1 takes the form

$$P_1(z) = 4\epsilon_0 d_{\text{eff},1} E_2 E_1^*, \quad (3.26)$$

which, when the expressions for the electric fields from (3.23) are applied, becomes

$$P_1(z) = 4\epsilon_0 d_{\text{eff},1} A_2 A_1^* e^{i(k_2 - k_1)z}, \quad (3.27)$$

where we assume the z -dependence of A_j is implicit for simplicity's sake. The polarization at the second-harmonic frequency is

$$P_2(z) = 2\epsilon_0 d_{\text{eff},2} E_1^2, \quad (3.28)$$

which likewise becomes

$$P_2(z) = 2\epsilon_0 d_{\text{eff},1} A_1^2 e^{2ik_1 z}. \quad (3.29)$$

Plugging these forms for E_j and P_j into the wave equation, one frequency at a time, yields

a set of equations relating the electric field amplitudes.

$$\frac{dA_1}{dz} = i \frac{2\omega_1^2 d_{\text{eff}}}{k_1 c^2} A_2 A_1^* e^{-i\Delta k z}, \quad (3.30a)$$

$$\frac{dA_2}{dz} = i \frac{\omega_2^2 d_{\text{eff}}}{k_2 c^2} A_1^2 e^{i\Delta k z}, \quad (3.30b)$$

where the wave vector mismatch,

$$\Delta k = 2k_1 - k_2, \quad (3.31)$$

is introduced to clean up the simplification. Because $\frac{dA_1}{dz}$ depends on A_1 and A_2 , and $\frac{dA_2}{dz}$ depends on A_1 , these equations are referred to as coupled-amplitude equations. Their coupling means they must be solved simultaneously.

If the SHG efficiency is low, as is often the case, then the undepleted-pump approximation can be applied. This approximation allows A_1 to be treated as a constant, significantly simplifying the solution. A constant amplitude for the fundamental field means equation (3.30a) is equal to zero, and equation (3.30b) can be easily integrated to obtain the spatial dependence of the second-harmonic radiation.

In the more general case, where A_1 is allowed to vary, the coupled differential equations must be solved simultaneously. Some clever manipulation of the coupled amplitude equations allows for easier visualization of their consequences. Several pieces of new notation are introduced to facilitate the solution. The total intensity, I , is the sum of the intensities of each wave, and is given by

$$I = I_1 + I_2 = 2n_1\epsilon_0|A_1|^2 + 2n_2\epsilon_0|A_2|^2. \quad (3.32)$$

By studying the spatial dependence of I_1 and I_2 , it can be shown that total intensity remains constant, which is consistent with our initial assumption of a lossless material. The equations

which support this are known as the Manley-Rowe relations, a derivation of which can be found in Boyd [30]. The intensity is used to express the field amplitudes in the form of complex numbers,

$$A_j = \sqrt{\frac{I}{2n_j\epsilon_0 c}} u_j e^{i\phi_j}. \quad (3.33)$$

The real quantities u_1 and u_2 are the normalized amplitudes of the fields. They are defined such that

$$u_1(z)^2 + u_2(z)^2 = 1. \quad (3.34)$$

Additional substitutions are introduced to describe distances and relative phases of the fields. A normalized distance parameter, ζ , is introduced, which is the distance into the medium, z , divided by the characteristic distance over which the fields interact, l ,

$$\zeta = \frac{z}{\frac{c}{2\omega_1 d_{\text{eff}}} \sqrt{\frac{2n_1^2 n_2}{\epsilon_0 c l}}} = \frac{z}{l}. \quad (3.35)$$

The relative phase of the interacting fields is written as

$$\theta = 2\phi_1 - \phi_2 + \Delta k z. \quad (3.36)$$

Finally, a normalized phase mismatch parameter is introduced,

$$\Delta s = \Delta k l. \quad (3.37)$$

Upon substitution, the coupled amplitude equations are transformed into the following

three equations:

$$\frac{du_1}{d\zeta} = u_1 u_2 \sin(\theta), \quad (3.38a)$$

$$\frac{du_2}{d\zeta} = -u_1^2 \sin(\theta), \quad (3.38b)$$

$$\frac{d\theta}{d\zeta} = \Delta s + \frac{\cos(\theta)}{\sin(\theta)} \frac{d}{d\zeta} (\ln u_1^2 u_2). \quad (3.38c)$$

Perfect phase-matching

Perfect phase-matching describes the case where individual dipoles in the material are phased such that their contributions add coherently to the generated wave. When perfect phase-matching occurs, the phase mismatch Δk , and hence the normalized phase mismatch Δs , are zero. As a consequence, the first term in equation (3.38c) vanishes, and the equation can be rewritten as

$$\frac{d}{d\zeta} \ln(u_1^2 u_2 \cos \theta) = 0, \quad (3.39)$$

which implies that the quantity in parentheses must be constant with respect to the normalized distance. This constant quantity is denoted by Γ :

$$\Gamma = u_1^2 u_2 \cos \theta. \quad (3.40)$$

Because Γ is unchanging, its value can be found using the properties at the front interface of the nonlinear medium. The values for u_1 , u_2 , and θ at $\zeta = 0$ are applied. Using the conserved quantities found in equations (3.34) and (3.40), it is possible to decouple and solve the set of equations in (3.38). The solutions take the form of Jacobi elliptic functions. The value for each u_j oscillates over the normalized propagation distance, indicating that the incident and second-harmonic fields interchange energy as they travel through the medium.

In the more specific case where $\Gamma = 0$, different behavior is observed. This occurs when the phase difference between u_1 and u_2 is such that $\cos \theta = 0$. Because cosine can be zero for two angles, we select the case where $\sin \theta = -1$, resulting in two important consequences. First, because we have specified a value for θ the relative phase of the fields remains fixed under propagation. Second, the coupled-amplitude equations simplify significantly to

$$\frac{du_1}{d\zeta} = -u_1u_2, \quad (3.41a)$$

$$\frac{du_2}{d\zeta} = u_1^2. \quad (3.41b)$$

If we assume that at the front interface all of the light is at the fundamental frequency and none is at the second-harmonic frequency, these equations produce the solutions

$$u_1 = \sinh(\zeta), \quad (3.42a)$$

$$u_2 = \cosh(\zeta). \quad (3.42b)$$

These solutions as plotted in Figure 3.2. As the distance into the medium increases, the fundamental field is depleted and the second-harmonic field gains in intensity. These changes are monotonic, and a complete conversion of radiation from ω_1 to ω_2 is observed as ζ approaches infinity. Therefore, improving phase-matching is an important strategy in optimizing non-linear devices.

Non-perfect phase matching

For cases with a non-zero phase mismatch, there is a lowered efficiency in converting the fundamental frequency to the harmonic frequency. For the related process SFG, where the phase mismatch is given by $k_1 + k_2 - k_3$, the sum-frequency intensity depends on the phase-

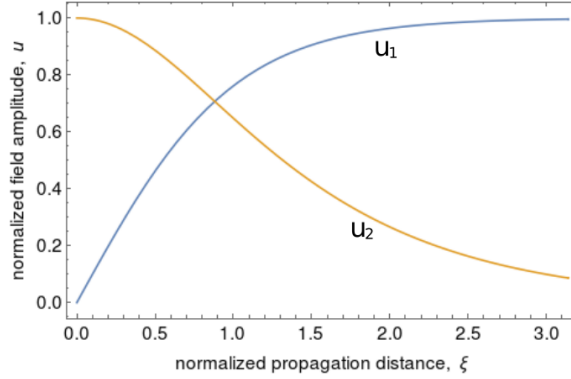


Figure 3.2: Relative intensity of normalized field amplitudes for the fundamental and second-harmonic fields as they propagate, for perfect phase-matching and $\Gamma=0$

mismatch as

$$I_3 = \frac{8d_{eff}^2\omega_3^2I_1I_2L^2}{n_1n_2n_3\epsilon_0c^2}\text{sinc}^2\left(\frac{\Delta kL}{2}\right). \quad (3.43)$$

This relationship is shown in Figure 3.3. The conversion efficiency depends on the product of the wave vector mismatch and the length of the crystal, and decreases rapidly as $|\Delta kL|$ increases. In non-phased matched materials that are much thinner than the coherence length, ΔkL is small and the phase-mismatch does not cause a significant decrease in the SHG efficiency. This was the case for the organic self-assembled films in studied in this work, which have a coherence length of about $10 \mu\text{m}$ while the films themselves are only a few nanometers thick. The phase-matching consequences of the thinness of ISAM films is discussed in more detail in Section 3.1.5. In this regime, the SHG intensity scales quadratically with increasing film thickness [5]. For materials with a nonzero phase mismatch and a longer crystal length, the detrimental effects of non-perfect phase matching are much more pronounced. Therefore, maintaining phase-matching is an important facet of developing effective nonlinear devices.

In reality, perfect phase-matching is difficult to achieve. Conservation of momentum requires that perfect phase-matching satisfies $k_1 + k_1 = k_2$. This implies that the material must have the property $n(\omega)=n(2\omega)$. However, real nonlinear materials are dispersive and

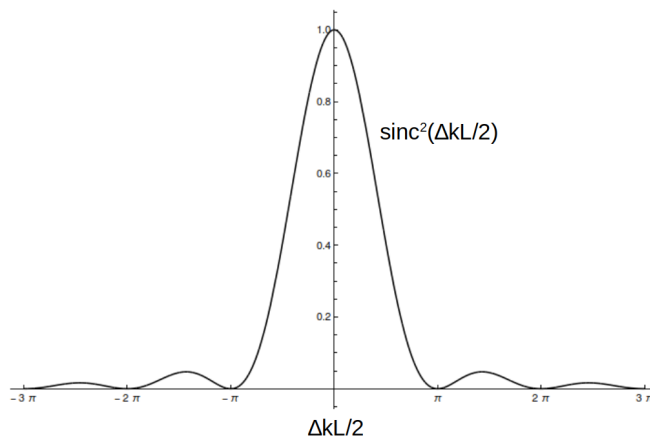


Figure 3.3: Plot of intensity versus phase mismatch for SFG. The conversion efficiency falls off rapidly away from $\Delta k = 0$.

have a monotonic relationship between the refractive index and the frequency, making it impossible to achieve the same refractive index at ω and 2ω . Although perfect phase-matching cannot generally be produced directly by nonlinear media, several engineering strategies can be employed to improve phase matching. In materials that are birefringent, the index of refraction depends on the polarization. With careful selection of material, its orientation, and the operating temperature, birefringent phase-matching can be exploited to improve the agreement between $n(\omega)$ and $n(2\omega)$. An alternative strategy, quasi-phase-matching, can be employed by inducing periodic changes in the nonlinear medium to interrupt regions which would normally produce out of phase light. It is used in materials such as periodically-poled lithium niobate. Because in this case all the radiation can be kept at the same polarization, quasi phase matching is governed by a different element of the d_{eff} tensor than birefringent phase matching. In some cases this means that for the same crystal type, stronger nonlinear effects can be observed from a quasi phase matched specimen than for birefringent phase matching in a homogeneous case [133].

3.1.4 Nonlinear optical materials

A variety of materials are used commercially for SHG, while more are in development. Any second-harmonic producing material must satisfy several requirements. Optically, materials used for SHG must lack a center of inversion symmetry in order to allow for second-order NLO, and should have a high $\chi^{(2)}$. They must also be transparent at the fundamental frequency, so that the pump beam can penetrate the material, and at the second-harmonic frequency, so the generated light is not reabsorbed. They need to have the right range of birefringence at the operating wavelengths in order to allow for phase-matching, or they should be able to accommodate other phase-matching strategies [134]. Additionally, mechanical properties such as a high laser damage threshold, durability, and long-term stability are important. Conventional materials for SHG are inorganic crystals, but a variety of alternative materials have been explored including organic crystals, thin films, and polymers.

Inorganic crystals

SHG was first demonstrated in quartz in 1961, when Franken et al. focused a pulsed laser onto a quartz crystal [135]. Inorganic crystals continue to be the most common media for frequency doubling. Today a variety of crystals are used which demonstrate strong SHG, including potassium dihydrogen phosphate (KH_2PO_4), potassium titanyl phosphate (KTiOPO_4), various borates, and most notably lithium niobate (LiNbO_3) [136, 137]. Inorganic nonlinear materials can have very high $\chi^{(2)}$, good mechanical strength, and long-term stability. Their main drawback is their cost. Nonlinear optical applications require defect-free single crystals of significant size, which are extremely difficult to grow. For example, successful growth of defect-free lithium niobate crystals with diameters exceeding 20 mm is noteworthy enough to be the subject of publications [138]. This makes inorganic crystals

very expensive optical components, generally costing hundreds to thousands of dollars.

One of the main crystals used for nonlinear optics is lithium niobate, which exhibits strong nonlinearities and a wide transparency range from 350 nm to 4 μm [139]. However, it suffers from difficulties in fabrication due to low thermal shock resistance, numerous light scattering centers, and local fluctuations in refractive index, which makes it expensive to produce good quality crystals [138]. Its use for frequency doubling is also limited by its tendency to sustain photorefractive damage. The resulting optically-induced inhomogeneities of refractive index can be useful for holographic applications, but are detrimental to harmonic generation. Photorefractive damage can be mitigated by doping with MgO [140] or by periodic poling. Periodic poling, in which a periodic reversal in the domain orientation is induced, is also useful for creating quasi-phase matching, which can be used to enhance nonlinear effects [139].

Another common crystal used in nonlinear optics is potassium titanyl phosphate (KTP) and other related titanyl crystals. KTP is a ferroelectric-superionic conductor. Like lithium niobate, KTP has a high nonlinear susceptibility and can be quasi-phase matched by periodic poling. Because of its high damage threshold and good crystal lifetime, KTP has widespread use in harmonic generation of Nd:YAG laser radiation and in optical parametric oscillators [141]. Its nonlinear susceptibility can be enhanced somewhat by substituting arsenic for phosphorus, or through partial substitution of titanium with niobium or zirconium. Other dopants have also been investigated in attempts to improve the nonlinearity of KTP [142].

A less expensive alternative is potassium dihydrogen phosphate (KDP), which has lower nonlinear susceptibility but is easier to grow at large sizes with good homogeneity. Additionally, it has a high damage threshold, making it useful for laser applications such as frequency doubling. Compared to other common nonlinear crystals, which are usually limited to dimensions of a few centimeters, KDP can be grown to sizes of half a meter. A large single

crystal of KDP was used as a Pockels cell in the National Ignition Facility laser system, which was the most powerful laser in the world at the time of its construction [143]. One limitation of KDP is that it is more hygroscopic than lithium niobate or KTP. Its hygroscopicity can result in etch pits on the surface due to condensation, which may damage antireflection coatings and permit excessive laser power to enter the crystal. Water droplets on the surface can also overly focus the pump beam in the crystal, resulting in damage. Consequently, KDP has a reduced lifetime in humid environments and requires careful moisture control or periodic replacement [144].

Borates constitute another class of nonlinear materials, particularly β -barium borate (BBO, β -BaB₂O₄). These incorporate a wide variety of compounds and exhibit NLO due to polarizable π electrons. Borate crystals are particularly attractive for UV generation because of their short wavelength absorption edge, which in some compounds occurs well below 200 nm. Their UV transparency, combined with their high damage threshold, make them good candidates for converting laser light to UV wavelengths [145]. New UV radiation sources are highly desirable for applications such as photolithography and attosecond pulse generation [146]. However, crystal growth for these materials is challenging and often requires very slow pulling rates [145].

In addition to crystals that already see widespread use, a wide variety of new crystals are in development. In some cases the goal is to find alternative crystals with even higher nonlinear susceptibility than in conventional materials. In other cases, reduced conversion efficiencies may be acceptable in order to cover new spectral regions or to develop improved radiation sources at wavelengths that can already be achieved by other methods. For example, as discussed in Section 3.1.6, alternative blue light sources are desirable because argon lasers, which are the usual source, are very energy inefficient. The development of new NLO crystals therefore continues to be an active area of research.

Organic materials for NLO

While inorganic crystals for NLO have advantages such as strong nonlinearity, good long-term stability, and a high laser damage threshold, limitations such as expensiveness and rigidity have led to the exploration of organic alternatives. Organic materials for NLO often combine the advantages of inorganic crystals with simpler synthesis and wider selection of molecular structure. They have gained popularity due to their ease of processing and affordability, and many organic alternatives retain the high laser damage thresholds and strong second-order effects found in inorganic media [137]. Because carbon is able to form several types of stable bonds with a variety of elements, organic synthesis methods allow for the development of a high diversity of nonlinear organic molecules [32]. Even when organic NLO materials do not attain or exceed the nonlinear susceptibilities of well established inorganic crystals, they offer the ability to significantly reduce the cost of optoelectronic devices and may introduce new features such as impact resistance and mechanical flexibility [147].

Most organic materials for nonlinear optics operate via the same general molecular structure, in which an electron donating group and an electron accepting group are located on opposite sides of a structure containing a series of π bonds. The molecular structure that produces NLO is referred to as the chromophore. Whereas σ bonds are formed by overlapping electron orbitals, π bonds are formed by orbitals that are adjacent and out of the molecular plane (Fig. 3.4). Electrons in π bonds are therefore freer to move around, allowing the overall polarization of the molecule to vary due to applied electric fields. This region of mobile electron density, when flanked by an electron donor and an electron acceptor, becomes hyperpolarizable, which means it exhibits nonlinear polarization. In practice these structures often take the form of benzene analogs, in which a single benzene ring provides the π electrons, or stilbene analogs, in which a pair of benzene rings is connected by a

bridge containing a double bond. The hyperpolarizability and other properties of organic NLO materials can be tailored by varying the electron donating/accepting groups used, the length of the molecular chain between them, and by attaching additional functional groups or atoms [32]. The second-order polarizability of nonlinear molecules is primarily determined

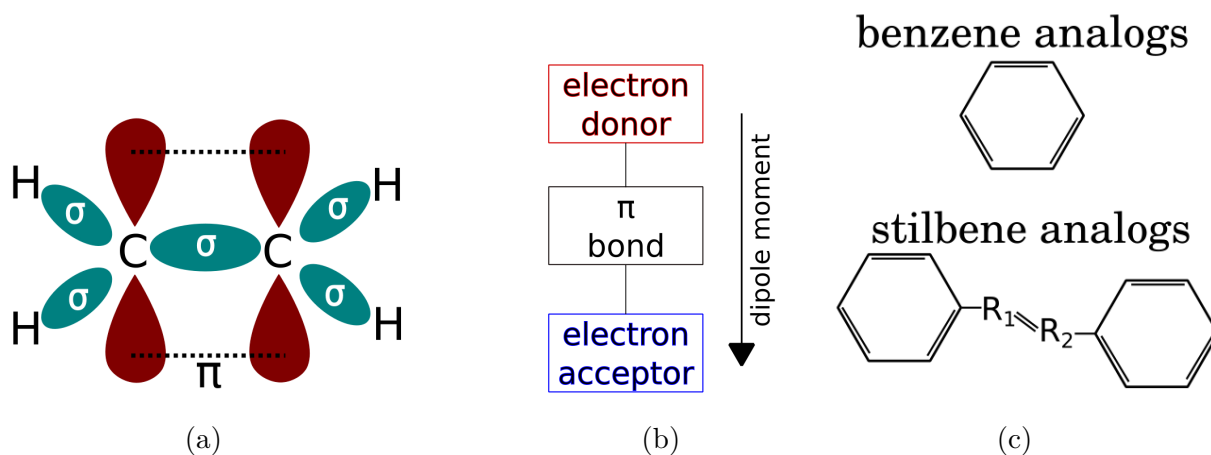


Figure 3.4: Configuration of organic chromophores. A diagram of electron orbitals in ethylene (a) demonstrates the difference between σ bonds (teal), which are formed by overlapping orbitals, and π bonds (red), which are formed by adjacent orbitals and thus have less localized electrons. Nearly all NLO chromophores are formed by an electron donor and acceptor linked by a π bond containing bridge (b). The π bond bridge is often a benzene or stilbene analog (c)

by low-energy electronic excitations in which charge is transferred between electron donor and acceptor groups. The polarizability can be shown to be proportional to the cube of the chromophore length using a theoretical approach known as the equivalent internal field model. An ideal nonlinear chromophore should have a long chromophore length, a low energy transition which facilitates absorption at long wavelengths, and a large dipole moment [32].

For second-order nonlinear effects, simply developing nonlinear molecules is insufficient due to the need to maintain net noncentrosymmetry in the material. In fact, dipole-dipole interactions between the chromophores tend to make them organize such that they have

inversion symmetry unless this is otherwise accounted for. Ensuring noncentrosymmetry can be accomplished in several ways, including using single crystal structures, thin film techniques, and several approaches to nonlinear polymers.

As in inorganic crystals, organic crystals can have a net order that eliminates centrosymmetry in certain lattice structures. The organic crystal approach is attractive because they can be highly ordered with lasting orientational stability. Additionally, single crystals can exhibit high nonlinearities due to high packing densities [148]. Several techniques are used to encourage noncentrosymmetric crystal structure. When forming crystals, molecules tend to become compacted and take on simpler, more symmetric shapes to accommodate close-packing. This can be prevented by using chiral molecules which are inherently nonsymmetric or by adding bulky substituents or rigid molecular core shapes to induce steric hindrance. Crystal formation can also be controlled by supramolecular synthesis, in which aggregates that tend to pack favorably are formed prior to growing the full crystal. Another challenge in growing nonlinear organic crystals is that dipolar chromophores will tend to arrange themselves centrosymmetrically due to Coulomb forces. Therefore, strategies to override this, such as the addition of strong counterions, can be helpful [32]. Although single optical crystals offer the potential for high hyperpolarizabilities, growing sizable crystals with the requisite optical properties is generally not straightforward. Solution based techniques are preferred for rapid and inexpensive growth, but vapor phase growth, which requires complex dedicated equipment, is usually needed to achieve crystals with sufficient optical quality [149].

Nonlinear thin films are a potential alternative to bulk crystals. In this area of research, polymers dominate the study of organic nonlinear thin films. Polymers are useful because they allow for several strategies for incorporating the chromophore into the material, and because they have well-developed design and processing technologies [148]. Optical polymers

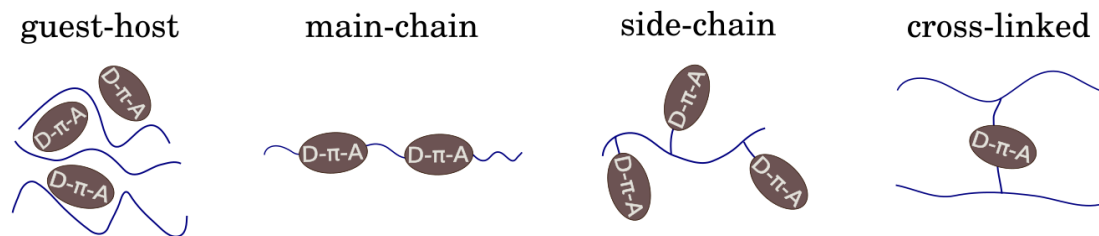


Figure 3.5: Different approaches to nonlinear polymers. In guest-host systems the chromophore is held in place by the polymer framework without covalent bonds. In main-chain and side-chain polymers the chromophore is part of the repeating monomer unit. In cross-linked polymers the chromophore forms part of the cross-linking bridge between separate polymer chains.

have been developed for applications including lenses, optical fibers, polarizing films, and light scatterers [150], due to their low weight, low cost, and ease of production. There are several approaches to accommodating the chromophore into the polymer (Fig. 3.5). In guest-host systems, the chromophore acts as the “guest” and is held in place by intermolecular forces from the polymer “host.” This can be done by adding nonlinear dyes to simple, inexpensive polymers, such as PMMA or poly(carbonate) [150]. Alternatively, the chromophore can be incorporated into the polymer molecules themselves, either along the polymer backbone (main-chain) or as part of a pendant structure (side-chain). Main-chain and side-chain polymers benefit from high chromophore density and thus have a good potential for strong nonlinear effects [137]. The chromophore can also be incorporated by crosslinking. In this case, individual polymer chains are covalently attached by a chromophore-containing bridge.

As with organic crystals, ensuring noncentrosymmetry is an important step toward achieving second-order nonlinear polymer materials. When the chromophore in use has a permanent dipole moment this can be accomplished by electric field poling. To pole a polymer, first it is raised above its glass transition temperature, T_g , to allow for increased mobility of the molecules. A strong electric field is applied and left in place as the material cools and regains its glassy state, freezing the dipoles in an ordered arrangement. Poled polymers can

have relatively good long-term orientational stability as long as they remain below T_g , so materials with a high T_g are preferable. In most cases, however, the optical nonlinearity decays on time scales of months to years, even below T_g [32]. Rigidity of main-chain polymers can make it difficult to achieve proper poling, however, these polymers are noted for their resistance to poled order relaxation [137].

In addition to polymers, other approaches can be used to fabricate nonlinear organic thin films. Langmuir-Blodgett films lend themselves readily to second-order NLO because they are formed by transferring ordered amphiphilic molecules from a liquid surface to a substrate. This net order imposed by the hydrophobic and hydrophilic ends of the molecules prevents centrosymmetry, but the technique is limited by its inherent requirement for amphiphilicity. Covalently bonded films have been demonstrated, but are likewise limited to molecules that are able to undergo reactions in order to form covalent bonds [147]. In other cases, organic thin films deposited with more sophisticated equipment have been investigated. Films grown by physical vapor deposition have also been demonstrated with large electro-optic responses [151], and molecular beam epitaxy can be used to fashion nonlinear ferroelectric thin films [32]. As discussed in Section 3.1.5, the environment produced by the alternating ionic layers in ISAM films can cause the chromophores to align with a net polar order. This was the strategy used for the nonlinear films reported in this dissertation, which consisted of the side-chain polymer PCBS assembled in ISAM films with PAH.

3.1.5 Nonlinear properties of ISAM films

The use of the ISAM technique to make nonlinear-active thin films has been studied extensively by this group. The chromophores in the film must have a net polar order in order for second-order nonlinear effects to occur. Electrostatic constraints inherent in the ISAM

technique tend to encourage the chromophores to orient themselves towards the substrate, but a fraction of the chromophores are likely to deposit in the reverse orientation, resulting in decreased nonlinear efficiency [152]. Therefore, techniques which help to preserve the polar order of the chromophores are a subject of interest. The degree of chromophore ordering can be determined by monitoring the amount of SHG produced by the films. The effect on the SHG due to different solution conditions during synthesis and environmental conditions subjected to the film have been studied previously by this group.

Chromophore orientation

Information about the orientation of chromophores in the ISAM films can be determined by tilt angle measurements, in which the relative amounts of p-polarized SHG produced by the film in response to s- and p-polarizations of the fundamental beam are compared. The average tilt angle of the chromophores away from the substrate normal (Fig. 3.6) can be shown to be

$$\bar{\psi} = \text{arccot} \sqrt{\frac{1}{2} \left(\sqrt{\frac{I_{2\omega}^{p \rightarrow p}}{I_{2\omega}^{s \rightarrow p}} \csc^2 \theta - 3 \cot^2 \theta} \right)}, \quad (3.44)$$

where $I_{2\omega}^{p \rightarrow p}$ and $I_{2\omega}^{s \rightarrow p}$ are the p-polarized SHG intensities due to a p- or s-polarized fundamental frequency and θ is the angle between the fundamental beam and the substrate normal. When the substrate is oriented at 45° to the fundamental beam, the ratio of the p-polarized SHG produced by a p-polarized fundamental beam, $I_{2\omega}^{p \rightarrow p}$, to that produced by an s-polarized fundamental, $I_{2\omega}^{s \rightarrow p}$, depends only on the average chromophore tilt angle, $\bar{\psi}$, as

$$\frac{I_{2\omega}^{p \rightarrow p}}{I_{2\omega}^{s \rightarrow p}} = \frac{1}{4} \left(3 + 2 \cot^2 \bar{\psi} \right)^2. \quad (3.45)$$

Using this approach, the average tilt angle of chromophores in a PCBS/PAH film was found to be 43° [153]. Another study found an average tilt angle of 35° for Poly S-119/PAH films

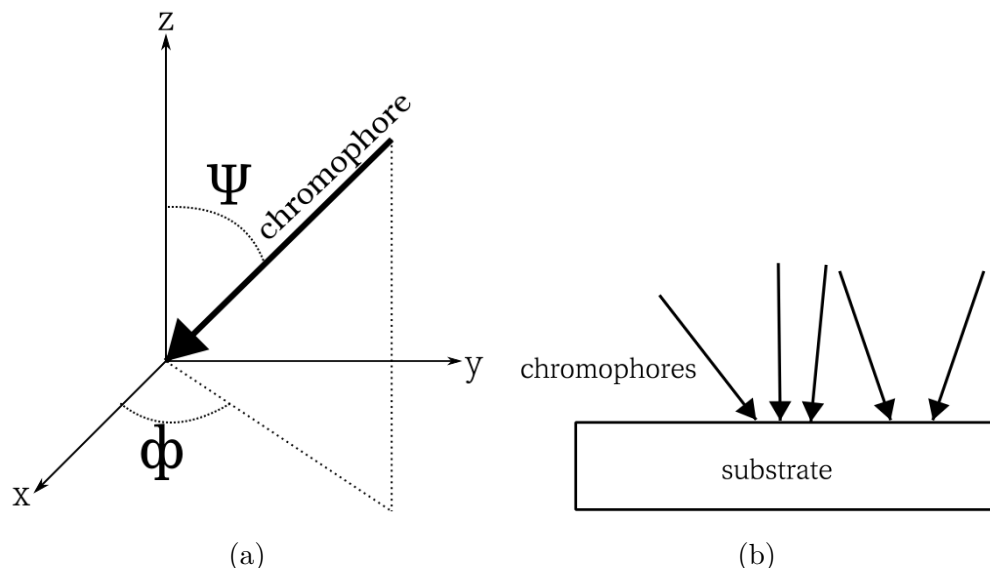


Figure 3.6: Diagrams showing the chromophore tilt angle, ψ , with respect to the substrate normal (a), and showing how a net polar order can still exist (b) when $\bar{\psi}$ is in the range of 30-40°, as has been observed experimentally for PAH/PCBS films.

[154]. While these tilts are significant, most of the chromophores point in the same direction with respect to the substrate (either towards or away), resulting in a net polar order.

Preservation of chromophore density and order with large numbers of bilayers

Many bilayers may be needed in order to accumulate enough material for a practical device. Therefore, it is important to ensure that the chromophore density and ordering continues to be the same in later added bilayers, and not only in those that are near the substrate. In several previous studies, it has been found that the peak wavelength absorbance from the chromophore increases linearly with the number of bilayers, showing that each additional bilayer has the same chromophore density as those added earlier [9, 154, 155]. SHG measurements have been used to determine whether the degree of chromophore orientation remained

constant as well. The second-harmonic intensity, I_{SHG} depends on the film thickness, l , as

$$I_{2\omega} \propto (l_c \chi^{(2)})^2 \sin^2\left(\frac{\pi l}{2l_c}\right) I_\omega^2, \quad (3.46)$$

where l_c is the coherence length and is typically on the order of about 10 μm , $\chi^{(2)}$ is the second-order nonlinear susceptibility from equation (3.2), and I_0 is the intensity of the fundamental beam. For films that are much thinner than the coherence length the small angle approximation applies, resulting in a quadratic relationship between I_{SHG} and l . If it was true that chromophore orientation decreases with increasing bilayer number, then sub-quadratic behavior would be observed. However, when Poly S-119/PAH films were tested with up to 100 bilayers, they showed a quadratic growth of I_{SHG} as the film thickness increased, demonstrating that the later bilayers continue to have a net polar order [154].

Nonlinear behavior of films with few bilayers

In one former study [156], in situ SHG was measured as PAH/PCBS ISAM films were deposited onto glass substrates. When PCBS at concentrations from 0.0025 to 0.5 mM was deposited onto a single layer of PAH, it was observed that the SHG signal plateaued within a minute, indicating complete adsorption of the PCBS monolayer. Less SHG intensity was observed for the lower concentrations of PCBS due to the presence of fewer deposited chromophores. Real time SHG was also monitored while applying 5 bilayers using 3 mM PAH and 0.11 mM PCBS at neutral pH. The deposition rate remained rapid and was unaffected by the bilayer number, but the SHG intensity remained about constant, rather than increasing as additional nonlinear PCBS layers were added. However, the theory of nonlinear optics predicts that for films whose thickness is much less than the coherence length, the SHG intensity should grow quadratically with film thickness [30]. It was concluded that for these

very thin films interface effects were the primary source of SHG, rather than a bulk nonlinear susceptibility. The expected quadratic behavior was obtained for films exceeding 20 bilayers. Another interesting observation of this study was the effect of “capping” the nonlinear film with a top layer of PAH. This was seen to decrease the SHG intensity compared to films with the same number of PCBS layers in which PCBS was the final layer. The lower SHG intensity from “capped” films was attributed to electrostatic interactions between the PAH and the chromophores. The chromophores ordinarily align themselves towards the substrate, but the presence of a top cationic layer may lead a fraction of the chromophores to flip. Oppositely oriented chromophores lead to a decrease in the net polar order, leading to a reduction in SHG. The effect became less severe as the number of bilayers increased due to increasing contribution of the bulk nonlinear susceptibility.

Influence of bilayer thickness on nonlinear performance

SHG was compared for films with the same number of bilayers whose thicknesses were varied by controlling the ionic strength of the polymer solutions [9]. The SHG intensity for a film whose thickness, l , is much less than the coherence length can be determined by applying the small angle approximation to equation (3.46), resulting in a quadratic dependence on the fundamental frequency:

$$I_{2\omega} \propto (l\chi^{(2)})^2 I_{\omega}^2. \quad (3.47)$$

In order to compare the contribution from each bilayer, the bilayer susceptibility $\eta^{(2)}$ was introduced to describe the effectiveness of the nonlinear response per bilayer deposition cycle. The SHG intensity can then be rewritten as

$$I_{2\omega} \propto (N_b \eta^{(2)})^2 I_{\omega}^2, \quad (3.48)$$

where N_b is the number of bilayers present. It was observed that films prepared with higher salt concentrations, which have higher ionic strengths and therefore form thicker films, had a higher $\eta^{(2)}$ but lower $\chi^{(2)}$. The reduced $\chi^{(2)}$ is attributed to chromophore orientation. At low ionic strengths, when the polymers adsorb in trains, the stretched out polymer chains force most of the chromophores to be located at the interfaces between the bilayers, where they are most exposed to electrostatic influences that cause them to align. At higher ionic strengths more of the chromophores are found in the middle of the nonlinear polymer layer due to curvature of the polymer backbone, where they are more sheltered from the charges of adjacent bilayers and therefore can have a more randomized orientation. Therefore, while films made with greater ionic strengths form thicker bilayers with higher chromophore density, the reduced order of the chromophores means that the net nonlinear susceptibility of the film is lower. The films used for the study of SHG in this dissertation consequently used neutral pH polyelectrolytes with no added salt.

Thermal stability of nonlinear ISAM films

One common approach to inducing noncentrosymmetry is known as poled polymers. Unfortunately, poled polymers suffer from poor thermal stability. In these materials a net chromophore order is induced by subjecting them to an electric field at a temperature above the glass transition temperature, T_g , where the molecules are free to reorient themselves in response to the field. The field is maintained while the polymer is cooled below T_g , “freezing” the chromophores in place. This induced ordering decays over time, particularly at elevated temperatures, and vanishes completely if the temperature ever exceeds T_g . To determine whether polymers deposited with the ISAM technique suffer from the same thermal limitations as poled polymers, SHG was measured from Poly S-119/PAH ISAM films while they were subjected to heating above the T_g [9]. The glass transition temperature of the films

was measured to be at 140 °C. As the temperature was increased to 150 °C over a period of three hours, a decrease in SHG intensity corresponding to a roughly 20% decrease in $\eta^{(2)}$ was observed. The SHG intensity remained about constant while the elevated temperature was maintained for 20 hours. When the sample was cooled back to room temperature, the SHG increased back to its original value, which is a significant departure from the behavior of poled polymer films. This behavior suggests that while at elevated temperatures some of the ionic bonds confining the chromophores are broken, these bonds are reestablished when the temperature is lowered again due to the electrostatic structure produced by the alternation between anionic and cationic layers. In another test, the ISAM film was exposed to a more severe heating cycle of 15 hours at 150 °C, 1 hour at 250 °C, and 20 hours at 200 °C. In this case, SHG data indicated that the nonlinear susceptibility after this heating cycle was only 70% of its original value. This change was accompanied by a similar reduction in extinction at the peak absorption wavelength of the chromophore, leading to the conclusion that chromophore decomposition, rather than reorientation, was the primary cause for SHG reduction after exposure to temperatures significantly above T_g .

3.1.6 Applications of second-order nonlinear effects

Nonlinear materials are currently deployed for applications in a variety of areas, including light generation, components in optical telecommunications systems, imaging, and information technology [157]. Harmonic generation and frequency-mixing processes are used to convert laser light to shorter wavelengths and can be used to make tunable light sources in spectral regions that are otherwise difficult to cover. Additionally, processes like Q-switching can be used to increase the intensity of laser pulses. Radiation sources employing nonlinear components can be used in other applications, such as micromachining, facilitating photo-mediated chemical reactions, and allowing high-resolution writing for high density optical

information storage. Devices such as electro-optic modulators, optical switches, Raman fiber amplifiers, Raman lasers, and wavelength-division multiplexers enable the development of sophisticated high-bandwidth telecommunications systems. In this section the major applications of SHG and the electro-optic effect will be discussed.

Frequency doubled lasers

Many IR lasers, including the one utilized in the optical setup for this project discussed in this work, include a nonlinear crystal to produce frequency doubled laser light. The harmonic generator may be located either inside or outside of the laser cavity, and both arrangements have been developed so that they have the potential to approach conversion efficiencies of 100%.

For many applications, frequency doubled lasers are preferable to other light sources available at similar wavelengths. Direct generation of green or blue laser radiation can be accomplished using argon lasers, in which gaseous argon is ionized and excited by an electrical discharge between two electrodes. However, producing significant laser power requires high electrical currents due to low quantum efficiency of the excitation process, meaning that argon ion lasers are very energy inefficient and can be costly to operate [86]. Converting light from a more efficient long-wavelength source into the blue/green region is therefore an attractive alternative. This is most often accomplished by pairing an Nd-based laser with a KTP or BBO crystal. Tunable UV light can be produced by frequency doubling dye lasers with BBO, which has extended transparency into the UV. In addition to high-powered laboratory systems, nonlinear frequency doubling has also seen widespread commercial use in the production of inexpensive green laser pointers. This has led to some concern that cheap models on the market may omit the filter required to prevent IR radiation from exiting the device [158]. IR radiation is invisible to the human eye and fails to trigger the blink reflex,

introducing the potential for unsuspecting consumers to sustain significant retinal damage.

Characterization of surfaces and interfaces

As previously discussed, second-order NLO processes are forbidden in materials with inversion symmetry. However, second-order effects can still occur at interfaces and at the boundaries of these materials, where symmetry is inherently broken. The study of SHG from these regions is second-harmonic surface spectroscopy. Spectroscopy utilizing SHG can be used to study interfaces buried within a sample and has the advantage that centrosymmetry requirements means that signal cannot be produced by the bulk, leading to low background signals [159]. This has been used to study effects such as strain at silicon-silica interfaces [160]. Second-harmonic surface spectroscopy can also be used to study colloids, which have a high surface area to volume ratio, or to monitor adsorption processes with high time resolution [159]. Details of the adsorption process, including molecular orientation and conformation, can be investigated by analyzing the second-harmonic signal [161]. In addition to monitoring the surface properties of solid substrates, second-harmonic surface spectroscopy can be used to study particles in solution. Charged particles and molecules in polar solvents exert an electric field that orients the solvent molecules. The ordered polar molecules can produce SHG, which can then be collected to deduce properties of the solution or of monolayers formed at the liquid-air interface [159, 162].

Second-harmonic imaging microscopy

One major application of SHG is in second-harmonic imaging microscopy, in which samples are illuminated with long wavelength light and emission at the second-harmonic frequency is recorded. This produces an image of the sample based on spatial variations in its second-order

nonlinear susceptibility, and can reveal features with negligible change in refractive index that would remain invisible in ordinary optical microscopy. Second-harmonic microscopy is therefore capable of revealing details of molecular order or lattice structure [163]. Perhaps surprisingly it is particularly useful for imaging biological samples, due to significant SHG produced by certain biological macromolecules.

Second-harmonic imaging microscopy was first demonstrated by Hellwarth and Christensen in 1974 to probe the physical structure of a ZnSe crystal, where it enabled them to identify 500 nm-thick monocrystalline platelets interspersed amongst larger grains [164]. The first application to biological samples was introduced about a decade later by Freund and Deutsch, who used it to study polar structures in rat tail tendons [163]. These structures had proven difficult to study using conventional methods because the preparation steps required, including freezing and drying the sample, disrupted these polar structures. They were able to perform second-harmonic microscopy on fresh, wet samples, however, enabling them to get a better picture of the tendon structure.

Since its first demonstrations, second-harmonic microscopy has been used extensively in materials science and biology because it offers several advantages over other techniques. The ability of second-harmonic microscopy to reveal structural details is helpful in characterizing physical samples and investigating the function of biological structures. Unlike other microscopy techniques, second-harmonic microscopy does not require the addition of stains or fluorescent dyes because samples with noncentrosymmetric features can produce SHG directly [157]. Adding dyes is an additional preparation step that can highlight certain features while obscuring others, so the ability to bypass it is beneficial. Additionally, because SHG is a parametric process in which photons are excited to a virtual level and no actual absorption occurs, second-harmonic microscopy is less susceptible to photobleaching and phototoxicity than fluorescence based techniques [165]. As in the case of the rat tail

tendons, second-harmonic microscopy does not require damaging sample preparation steps such as freezing or drying, and can even be performed *in vivo* to image live cells [166]. Live cell imaging is an important tool in studies of cellular propulsion, intercellular trafficking, and other features of cell biology [167]. Additionally, because tissue is transparent to IR light, the excitation can penetrate into thick samples to allow for three dimensional imaging. Second-harmonic microscopy is especially useful in diagnostics, because many pathologies induce structural changes to the tissues which can be revealed by SHG produced in collagen, a noncentrosymmetric molecule abundant in the extracellular matrix [165, 166]. Due to its numerous advantages in imaging substructures of materials, second-harmonic microscopy is widely used in a variety of fields.

Electro-optic modulators

Electro-optic effects are processes in which the application of a static or low-frequency external electric field alters the refractive index of a material. Different varieties of electro-optic effects are possible, depending on the material. In noncentrosymmetric materials only the linear electro-optic effect, or Pockels effect, can occur. This phenomenon is governed by the second order susceptibility, $\chi^{(2)}$, of the material [30], and can be described as

$$P_i(\omega) = \epsilon_0 \sum_{jk} \chi_{ijk}^{(2)}(\omega = \omega + 0) E_j(\omega) E_k(0). \quad (3.49)$$

Because the linear electro-optic effect and SHG are both dependent on $\chi^{(2)}$, the electro-optic effect generally scales with the SHG efficiency of a material. Materials that demonstrate strong second-harmonic effects, such as the organic self-assembled films studied in this work, may also be applied in electro-optic devices.

Electro-optic modulators utilize the electro-optic effect in order to alter the phase, po-

larization, intensity (amplitude), or frequency of light [168]. For example, Pockels cells are used in Q-switched solid state lasers to increase the pulse power by using an applied voltage to control the release of the population inversion. Electro-optic modulators can be rapidly switched on and off, making them important components in many photonic and optical communications devices. However, the conventional crystals used for electro-optic modulation require large applied voltages of hundreds to thousands of volts, and must be on the order of centimeters long to allow for interference effects to occur [169]. In order to compete with or exceed the performance of semiconductor technologies, electro-optic modulators for computing applications must be much more compact and less energy demanding [170]. Nanophotonic electro-optic devices are key elements in optoelectronic integration, and may be constructed using nanostructures composed of semiconductors [171] or nonlinear crystals, such as lithium niobate [172], or through the development of organic alternatives [168, 173]. SHG offers a relatively simple means of probing the nonlinear behavior of novel materials, and nonlinear media studied using SHG could have the potential to be used in electro-optic applications.

3.2 Plasmonics

An electric field incident on a conductor will exert a force on the free electrons, causing them to move around within the confines of the material. When electrons in a metal are subject to a time-varying electric field, such as light, they are driven to oscillate as a group as the electric field changes. These collective oscillations are known as plasmons, and are divided into three major types depending on the geometry of the host material and the location of the electron oscillations. Collective oscillations in the bulk of the conductor are called volume plasmons. In more confined geometries, surface plasmon polaritons (SPPs) and localized

surface plasmons (LSPs) occur. In this section, SPPs and LSPs will be discussed in more detail.

SPPs are plasmons at the interface between a metal and a dielectric. They typically occur at the external surface of the conductor, where the dielectric takes the form of air or vacuum. SPPs are confined to the interface, decaying exponentially with increasing distance into each medium, and are essentially two-dimensional. This confinement results in an enhancement of the electromagnetic field which is highly sensitive to changes at the surface, making them excellent for sensing applications [174]. For example, the SPR biosensors discussed in Section 2.3 utilize SPPs to detect binding of low concentration analytes to a functionalized gold film. In addition to sensing applications, SPPs are also attractive for waveguiding. In 1997, two papers suggested that SPPs could guide light at much smaller scales than allowed by usual diffraction limits. Takahara [175] proposed that a light beam could be reduced to nanometer diameter using SPPs in a cylindrical waveguide, while Nerkararyan [176] showed that light could be superfocused to a few nanometers using a wedge-like metal structure. The possibility of sub-wavelength guiding has attracted much attention since then, as nanophotonics and optical circuits have the potential to allow for miniaturization beyond the limits present in semiconductor technology [177].

LSPs, unlike SPPs, are non-propagating collective oscillations that occur in sub-wavelength sized conductive nanoparticles. Electrons within the nanoparticle oscillate under excitation by incident light, but experience a restoring force when they encounter the edges of the particle. When LSPs are excited at the resonant wavelength, localized surface plasmon resonance (LSPR) occurs. Nanoparticles exhibit strong absorption at the LSPR wavelength and cause strongly enhanced electric fields in a range of a few nanometers. The properties of the LSPR depend on the size and shape of the particle, the interparticle spacing, and the dielectric properties of the particle and its environment [178].

The following discussion of the quasi-static approximation for a spherical nanoparticle is based on its presentation by Maier [33]. An electromagnetic plane wave at wavelength λ , incident on a metal nanoparticle with radius a , can be treated as a uniform field if $a \ll \lambda$ (Fig. 3.7). This is known as the quasi-static approximation. The electric field induces a

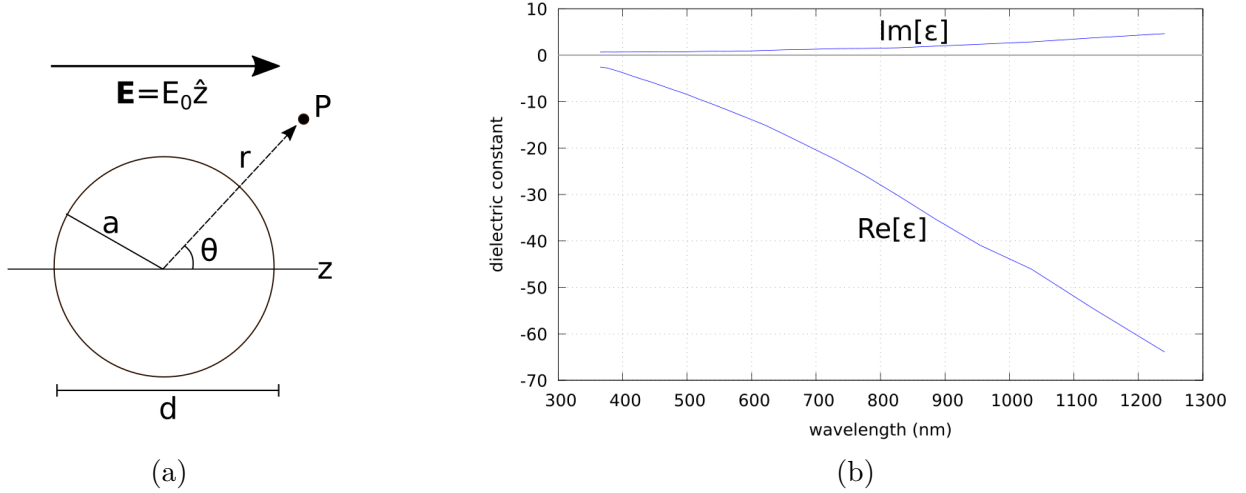


Figure 3.7: For a sufficiently small nanoparticle ($d \ll \lambda$), the field can be treated as uniform across the sphere, which is known as the quasi-static approximation (a). The dielectric function for silver [3] (b) has a small imaginary component and a large negative real component, allowing the Frölich condition to be satisfied.

dipole moment in the nanoparticle,

$$\mathbf{p} = \epsilon_0 \epsilon_m \alpha \mathbf{E}_0, \quad (3.50)$$

where ϵ_m is the dielectric function of the surrounding medium. The polarizability, α , is given by

$$\alpha = 4\pi a^3 \frac{\epsilon - \epsilon_m}{\epsilon + 2\epsilon_m}, \quad (3.51)$$

where ϵ is the complex dielectric function of the metal. The dipole exhibits resonance when the magnitude of the denominator in equation (3.51) is minimized. If $\text{Im}(\epsilon)$ is small or slowly

varying near the resonant frequency, the resonance condition can be written as

$$\text{Re}[\epsilon(\omega)] = -2\epsilon_m, \quad (3.52)$$

which is known as the Frölich condition. The mode associated with this relationship is the dipole surface plasmon mode. Due to $n = \sqrt{\epsilon_r \mu_r}$, increasing the external index of refraction increases ϵ_m . This means that resonance occurs at larger $|\text{Re}(\epsilon)|$, which is satisfied in noble metals at lower frequencies. The LSPR can therefore be redshifted by coating nanoparticles with a high refractive index material. Localized surface plasmon resonance (LSPR) therefore requires a dielectric function with a large and negative real part and a small positive imaginary part [33]. This property is satisfied in several metals, including Ag (Fig. 3.7), Au, Cu, Pt, Pd, Li, Na, Al, In, and Ga. Recently, plasmonic nanoparticles made of heavily doped semiconductors and metal oxides have also been investigated [179]. However, many of the materials which exhibit LSPR suffer from instability or undergo rapid surface oxidation, making them poor candidates for practical applications [178]. For this reason, gold and silver nanoparticles continue to dominate LSPR studies.

When an electrostatic field is incident on a particle that can be treated with the quasistatic approximation, the total fields inside and outside the particle are given by

$$\mathbf{E}_{\text{in}} = \frac{3\epsilon_m}{\epsilon + 2\epsilon_m} \mathbf{E}_0, \quad (3.53a)$$

$$\mathbf{E}_{\text{out}} = \mathbf{E}_0 + \frac{3\hat{\mathbf{r}}(\hat{\mathbf{r}} \times \mathbf{p}) - \mathbf{p}}{4\pi\epsilon_0\epsilon_m r^3}. \quad (3.53b)$$

Since $|\mathbf{p}| \propto \alpha$, the large polarizability obtained at resonance results in enhancement to both the internal and external fields. If a time-dependent electric field varying as $e^{-i\omega t}$ is present instead of a static field, the oscillating dipole will scatter the incident electromagnetic wave. In this case, the net electric and magnetic fields near the nanoparticle ($kr \ll 1$) can be shown

to be

$$\mathbf{E}(t) = \frac{3\epsilon_m}{\epsilon + 2\epsilon_m} \mathbf{E}_0, \quad (3.54a)$$

$$\mathbf{H}(t) = \frac{i\omega}{4\pi} (\hat{\mathbf{r}} \times \mathbf{p}) \frac{1}{r^2}. \quad (3.54b)$$

Here, the magnetic field is smaller than the electric field by a factor of about $kr\sqrt{\epsilon_0/\mu_0}$. Therefore, in the region very close to the nanosphere, the enhanced electric field dominates over the magnetic field. The magnitude of the electric field enhancement depends on the type of metal the nanoparticle is composed of and on its shape, and can be modeled for arbitrary particle shapes by computational methods.

The distinctive extinction spectra observed for plasmonic nanoparticles can be described by the extinction cross section, $C_{ext} = C_{sca} + C_{abs}$, where C_{sca} and C_{abs} are the cross sections for scattering and absorption, respectively. These are given by

$$C_{sca} = \frac{k^4}{6\pi} |\alpha|^2 = \frac{8\pi k^4}{3} \left| \frac{\epsilon - \epsilon_m}{\epsilon + 2\epsilon_m} \right|^2 a^6, \quad (3.55a)$$

$$C_{abs} = k \text{Im}(\alpha) = 4\pi k \text{Im} \left(\frac{\epsilon - \epsilon_m}{\epsilon + 2\epsilon_m} \right) a^3. \quad (3.55b)$$

The scattering cross section has a^6 dependence, compared to an a^3 dependence for the absorption cross section, indicating that scattering becomes the more important process as the particle size increases. For smaller particles with $a \ll \lambda$, absorption dominates over scattering. When the Frölich condition is satisfied, both cross sections become large, resulting in high extinction at the LSPR frequency. After simplification, the extinction cross section becomes

$$C_{ext} = 9 \frac{\omega}{c} \epsilon_m^{3/2} V \frac{\epsilon_2}{(\epsilon_1 + 2\epsilon_m)^2 + \epsilon_2^2}. \quad (3.56)$$

Particles with larger diameters have their LSPR peaks at longer wavelengths. This is demon-

strated particularly well by gold, which forms visibly different colored solutions at different particle sizes.

While the above approaches work well for moderate sized nanoparticles, particles that are larger suffer from retardation effects and are better modeled using Mie theory. Introduced by Gustav Mie in 1908, Mie theory involves solving Maxwell's equations analytically by expanding the internal and scattered fields into a set of normal modes described by vector harmonics [180]. Mie theory successfully describes the redshifting of the LSPR with increasing particle size and predicts the higher order modes, such as quadrupolar resonances, that appear in larger nanoparticles. However, Mie theory can only be applied to spheres, spheroids, and infinite cylinders. An alternate approach is required to describe particles with other geometries.

The discrete dipole approximation (DDA) is typically used to determine optical properties of nanoparticles with arbitrary shapes or for closely spaced nanoparticles. The DDA is a finite-element method for predicting scattering and absorption of targets computationally. In this approach, the particle is modeled as an array of individual polarizable cubes in which dipole moments are induced by a local electric field. Each dipole exerts its own electric field, and the results of the interactions of all the dipoles in the array are calculated [181]. The DDA provides great flexibility but quickly becomes computationally expensive at higher resolutions. In general, the DDA predicts multiple resonances for nonspherical particles due to oscillations along different axes, as well as intense fields near tips and points. Particles that are close together can form dimers, which are predicted to have extremely strong electric field enhancement in the small gap between them.

3.2.1 Optical properties of silver nanoprisms

This section describes results obtained by Hao et al. [37] in using the DDA to model the extinction spectra and electric field enhancements of silver nanoprisms. Silver nanoprisms are shaped like thin triangular plates, with thicknesses of about 10 nm and edge lengths of 30-200 nm. In their simulations, Hao et al. determined that silver nanoprisms exhibit several different resonances. The longest wavelength and strongest extinction was attributed to an in-plane dipole resonance, while weaker extinction peaks at shorter wavelengths were attributed to quadrupole resonances. For 12 nm thick nanoprisms with an edge length of 60 nm, their simulations showed the in-plane dipole resonance at 700 nm, the in-plane quadrupole at 434 nm, and the out-of-plane quadrupole at 340 nm. They also demonstrated that the in-plane dipole resonance would redshift with increasing edge length, decreasing thickness, and increasing sharpness of the points. They found similar E-field ($|\mathbf{E}|^2$) enhancements for silver prisms (3500), rods (4500), and spheroids (4700).

Larger enhancements can be achieved by closely packing the nanoparticles such that they lay within a few nanometers of each other. For silver nanoprisms, Hao et al. found that the field between dimers separated by 2 nm was as much as 57,000 times the applied field ($|\mathbf{E}|^2$), about an order of magnitude larger than the enhancement for isolated prisms. They found that the extinction spectra for the dimer was dependent on the polarization of the incoming light. The in-plane dipole peak showed a redshift of nearly 300 nm when the incident light was polarized parallel to the interparticle axis. Light polarized perpendicular to this axis produced extinction that was similar to the lone particle. The enhancement magnitude was similar for tip-to-tip and tip-to-edge configurations, however, the underlying behavior differed. Smaller enhancements were seen for edge-to-edge arrangements (11,000), however, the E-field enhancement occurs over a larger area [37].

3.2.2 Synthesis of silver nanoprisms

Silver nanoprisms can be synthesized using physical techniques, such as lithography, or by growing the nanoprisms colloiddally in solution. In this section both approaches are described, as well as their advantages and limitations.

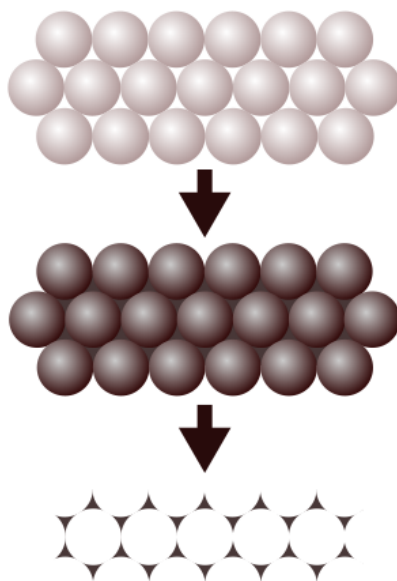


Figure 3.8: Process of making silver nanoprisms via nanosphere lithography. A monolayer of polystyrene nanospheres is deposited, then a thin silver film is evaporated onto the surface. When the nanospheres are removed silver nanotriangles remain in the interstices.

Nanosphere lithography is a simple, low-cost method for depositing two-dimensional nanoparticle arrays on a substrate. It reliably produces monodisperse arrays with good control over nanoparticle size, shape, and interparticle spacing [182]. In a typical procedure, a colloidal crystal mask is produced by spin- or drop-casting monodisperse polystyrene nanospheres onto a smooth substrate such that they form a monolayer. The spheres assemble as a hexagonal close-packed monolayer, forming an array of triangular gaps. Next, silver is deposited onto the substrate using a technique allowing for thickness control, such as thermal evaporation, electron beam deposition, or pulsed laser deposition. Finally, the

original colloidal layer is removed by sonication in a solvent. The silver that deposited in the interstitial spaces between the colloids remains on the surface. Nanosphere lithography allows for easy control of nanoprism size, thickness, and spacing, simply through the selection of the polystyrene sphere size and the evaporation time. Additionally, it has been demonstrated that the nanoprisms can be lifted from the surface and into solution, allowing for synthesis of a highly monodisperse colloidal solution [183].

In contrast to the physical approach supplied by nanosphere lithography, many wet-chemistry synthesis procedures have been developed to grow silver nanoprisms in solution. These techniques can be divided into two main types: photomediated approaches, where light exposure facilitates the transformation of spherical particles to triangles, and seed-mediated approaches, where the prisms grow in triangular shapes due to selective reduction onto the triangle edges.

In photomediated methods for silver nanoprism synthesis, a solution of small (<10 nm) silver nanoparticles in the presence of poly(vinylpyrrolidone) (PVP) or Bis(*p*-sulfonatophenyl) phenylphosphine dihydrate dipotassium salt (BSPP) is irradiated with visible wavelength light [184]. A variety of light sources have been employed, including conventional fluorescent lighting [184], lasers [185], xenon arc lamps [185], and halogen lamps [186]. The original nanoparticles appear to be consumed and a reasonably monodisperse solution of silver nanoprisms is obtained, although the underlying mechanism has been the subject of some debate [187]. It appears that a multistep reaction occurs, involving the breakdown of silver particles into Ag^+ by oxygen, the formation of BSPP- Ag^+ complexes, and reduction of Ag^+ onto other silver particles that is anisotropic due to dipole plasmon excitation by the light source [186]. In other photoinduced methods, citrate-capped silver nanoparticles in the presence of excess silver ions are grown via visible-wavelength irradiation. An interesting feature of photomediated approaches is that the irradiation wavelength has been shown to

control the final particle size, with longer wavelength light sources resulting in larger prisms [186].

Alternatively, a variety of chemical reduction processes have been developed without the need for photointervention. In general these involve the use of a reducing agent and a capping agent to encourage silver ions to preferentially reduce onto certain faces of small silver nanoparticles. The reactant concentrations and the reaction time and concentration are typically used to control the final morphology of the nanoprisms. However, many of these approaches result in a wide distribution of prism sizes or produce prisms alongside a high concentration of particles in other morphologies. Techniques that produce uniform prisms with sharp tips are highly desirable. For the nanoparticles used in this work a seed-mediated synthesis was used, in which a stock solution of small silver nanospheres is injected into a second reaction to produce the nanoprisms. The procedure used by Dr. Liu's group for the prisms used in this work was based on the seed-mediated method reported by Aherne et al. [4]. In brief, seed particles are first produced by gradually adding silver nitrate to a stirred solution of trisodium citrate, poly(sodium styrenesulphonate) (PSSS), and sodium borohydride. Nanoprisms are then prepared by gradually adding a higher concentration of silver nitrate to a solution of water, ascorbic acid, and seed solution, with trisodium citrate added at the end to stabilize the particles. The final prism size can be controlled by varying the amount of seed solution added in the second step. Colloidal synthesis procedures can produce nanoprisms with controllable edge length, however, the thickness of the prisms tends to be more or less constant. For prisms produced by the seed-mediated method, Aherne proposes that this is due to different energies for different planes of the crystal lattice. As shown in Figure 3.9, a defect-rich hexagonal-close-packed (hcp) region is sandwiched between two large hexagonal face-centered cubic planes. Each edge has a pair of diagonal faces, one of which is $\{100\}$ and the other $\{111\}$, that link the top and bottom planes to a small exposed

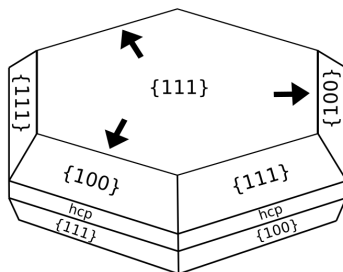


Figure 3.9: Process of seed-mediated silver nanoprism formation, as proposed by Aherne [4]. Growth is preferred at the exposed hcp faces and the three edges where the $\{100\}$ face dominates due to starting asymmetry in the crystal. These edges grow faster, resulting in a triangular shape.

hcp layer. Silver atoms preferentially attach to the unstable hcp faces, allowing for lateral growth. If the hexagon is perfectly symmetrical, it will continue to grow in a hexagonal shape. In practice, most of these tiny crystals are asymmetrical. In these cases the edges with a larger $\{100\}$ face and a smaller $\{111\}$ face will grow faster, due to the higher stability of $\{111\}$ faces.

3.2.3 Enhancement of nonlinear optics by LSPR

The strong electric fields produced by plasmonic enhancement within a few nanometers of a metal nanoparticle can be used to produce the conditions necessary for nonlinear optics, and is generally studied in one of two main regimes [33]. In one, the metal nanostructures themselves produce the nonlinear behavior. Despite having a centrosymmetric cubic lattice structure, metals can exhibit some second-order NLO due to symmetry breaking at the surface. Strategies to improve this effect by creating interesting nanostructured metals are the subject of widespread investigation. The second regime, and the one focused on in this section, is the use of plasmonic effects to enhance NLO from a host material with an independent nonlinear susceptibility. These strategies may take the form of embedding plasmonic nanoparticles into nonlinear host materials, assembling or constructing metal nanostructures

onto the surface of a nonlinear material, or by assembling structures where a nanoparticle of nonlinear medium is brought in close contact with a plasmonic nanoparticle to form dimers or concentric geometries.

One approach to using LSPR to enhance nonlinear effects is to embed conductive nanoparticles directly within a nonlinear host material. This can be accomplished by ion implantation, in which a beam of metal ions is accelerated at the target, followed by annealing to facilitate nanoparticle growth and repair damage due to the ion beam. This process can be used to create nanocomposites with a high degree of purity and stability in a variety of substrates. In one case, gold nanoparticles were inserted into Nd:YAG crystal, resulting in a five order of magnitude enhancement to the nonlinear absorption coefficients over non-embedded crystals [188]. Plasmonic gold and silver nanoparticles have also been implanted into lithium niobate. Pang et al. have investigated lithium niobate with embedded gold and silver nanoparticles as saturable absorbers in Q-switched laser cavities operating at visible and near infrared wavelengths, and observed an output power three times higher for silver than for gold. However, they found that the changes in nonlinear absorption due to the embedded nanoparticles were unpredictable, which they attributed to competition between the effects of plasmonic enhancement by the nanoparticles versus interruptions to the host crystal lattice [189, 190]. In general, enhancements achieved by embedding nanoparticles in nonlinear bulk materials are relatively small and difficult to control, leading most studies to focus on other approaches.

An alternate strategy for plasmonically enhancing SHG is to leave the host material intact and to place the plasmonic materials on its surface. This can be accomplished by fabricating metallic nanostructures on the surface using epitaxial techniques, or by depositing colloiddally grown nanoparticles onto a nonlinear substrate. Prior work by this group, discussed in more detail in Section 6.1, demonstrated SHG enhancements of up to 1600 times from

nonlinear ISAM films due to silver nanotriangles deposited by nanosphere lithography [152] and enhancements of up to 100 times by the adsorption of colloidal gold nanorods [5]. In a similar project, Ishifuji et al. [191] reported enhancement of SHG from nonlinear-active LB films with added gold nanoparticles. Compare to a single nonlinear polymer sheet, an 8 times enhancement in SHG intensity was observed after adsorption of gold nanoparticles, and an enhancement of 288 times was achieved when a two layer sandwich structure was assembled. Adsorbing colloidal plasmonic nanoparticles onto nonlinear media is procedurally simple, but because the field enhancements extend only a few nanometers from the nanoparticle relatively little of it may penetrate vertically into the nonlinear material.

Other approaches to decorating nonlinear media with plasmonic surface structures use more sophisticated techniques to control the geometry of the surface structures. In one case, a lithium niobate substrate was etched into 120 nm diameter pillars by character projection electron beam lithography and ion beam enhanced etching, which were then coated with a 40 nm thick gold layer by physical vapor deposition. Gold was removed from all horizontal surfaces by ion beam etching, leaving behind an array of lithium niobate-filled gold nanorings. An enhancement of about 20 times was achieved with tilted illumination, which matched with theoretical predictions [192]. Another group used a similar geometry, in which GaAs posts penetrated through holes in a gold film. The resulting structure had SHG similar to that observed for a lithium niobate control [193]. In another case, periodic arrays of silver nanoparticles were synthesized on the surface on Nd³⁺-doped lithium niobate patterned with ferroelectric domain structures by a photochemical growth method, in which the patterned crystals were immersed in a silver nitrate containing solution and illuminated with 254 nm light. At domain boundaries, chains of 40-70 nm silver nanoparticles with an average spacing of 20 nm were obtained, which enhanced SHG by up to 20 times [194].

Nonlinear effects can also be plasmonically enhanced by forming structures in which

nanoscale nonlinear crystals are placed in proximity to plasmonic structures. This can be accomplished by arranging them side-by-side or by forming concentric arrangements. In one case, dimers of 100 nm BaTiO₃ and 80 nm gold nanoparticles were formed by sequential capillarity-assisted particle assembly, resulting in 15 times enhancement compared to isolated BaTiO₃ spheres [195]. In another case, individual 25 nm indium tin oxide (ITO) nanoparticles were fabricated by lithography and flanked by gold nanorods, such that the ITO particle laid in a gap between the nanorod tips. Third harmonic generation was enhanced by up to 10⁶ compared to the single ITO nanoparticle, depending on the spacing between the nanorods [196]. In another case, gold seeds were deposited onto 100 nm tetragonal BaTiO₃ spheres and were grown into a 10 nm thick gold film by reaction with a gold chloride solution. The resulting BaTiO₃-Au core/shell nanoparticles exhibited a second-harmonic scattering cross section several hundred times larger than observed for uncoated BaTiO₃ spheres [197]. Another group studying BaTiO₃ cores with gold shells added an additional step to coat the core-shell structures with an 80 nm thick silica layer to help protect them from laser damage and to prevent interparticle interactions. Enhancements to DFG were predicted and observed to be a factor of about 100 better than for the bare BaTiO₃ particles [198].

Chapter 4

Methods

This chapter describes the experimental techniques used in the projects presented in this dissertation. Both projects utilized ISAM films deposited by aqueous polymer solutions, the preparation of which is discussed in Section 4.1. The procedures associated with our biosensor experiments are discussed in Section 4.2. The general steps of the assay were to coat the fiber grating with ISAMs and bioreceptor molecules, then to expose the functionalized sensor to various lysed bacteria. These techniques, the apparatus used for them, and additional steps to prepare and clean the optical fiber are described. Section 4.3 presents the setup and procedures used for our fabrication of LPGs by CO₂ laser. Our sample fabrication techniques for the nonlinear optical plasmonic enhancement experiments are discussed in Section 4.4. These include the methods for cleaning the substrates and depositing the ISAM films, applying silver nanoprisms, and adding additional coatings to try to improve the SHG enhancement. Our methods for characterizing the plasmonic enhancement samples are described in Section 4.5. Properties of the samples were primarily monitored by extinction and thickness measurements. The apparatus and procedures for SHG measurements are also described.

4.1 Polymer preparation

Aqueous solutions of PAH and PCBS were used in both projects for the application of ISAMs to glass surfaces. PAH was obtained from Alfa Aesar (91 g/mol, product number 4309209) and PCBS was obtained from Sigma-Aldrich (369 g/mol, product number 346411). Dry powder was added to RO water such that the final concentration was 10 mM monomer. The solutions were left to stir overnight before being adjusted to pH 7 using 0.1 M HCl or NaOH, as needed. Before adjustment, PAH typically had a pH of about 4 and PCBS of about 9. The pH of both polymer solutions showed a tendency to slowly drift toward more basic pH over time, not exceeding pH 8. The pH of polymers was therefore measured and readjusted every few weeks.

For the biosensing experiments the polymers were transferred to sterile 15-mL centrifuge tubes and stored at 4° C in order to retard bacterial growth. The tubes were inverted several times before use in order to redistribute the contents. The polymer solutions used for the plasmonics experiments were left on stir plates to ensure long-term homogeneity.

4.2 Optical fiber preparation and biosensor assay

TAP-LPGs were fabricated by UV laser by Siddarth Ramachandran at OFS Laboratories and later Boston University. The transmission spectrum through the fiber was monitored using a broadband light source and an optical spectrum analyzer (OSA). The light source used was a Fiberlabs SLD-1310/1400/1480/1600, which uses four superluminescent diodes to generate wideband output from 1250 nm to 1650 nm. The transmission spectrum was monitored with an Ando AQ6317 optical spectrum analyzer, which measured attenuation in the transmission with respect to wavelength.

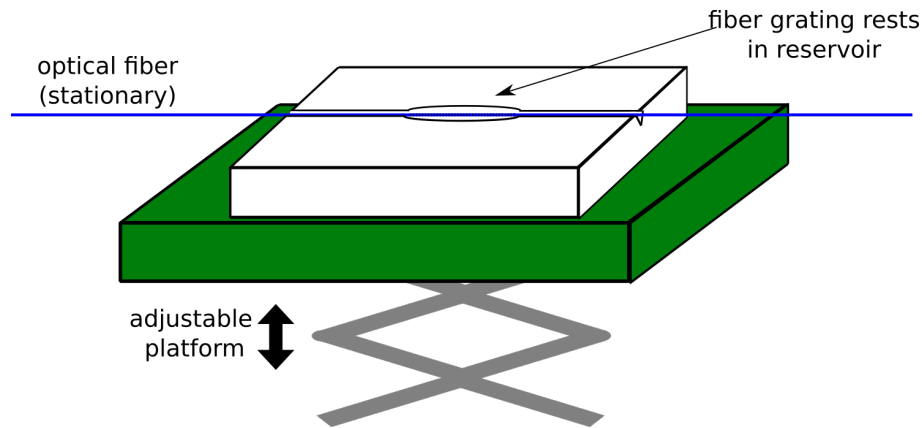


Figure 4.1: Setup for applying liquids to the fiber grating. The grating was held fixed, and the height-adjustable stage was raised under it such that the fiber nestled in the groove along the length of the block and the grating was located in the larger rounded cavity. Liquids were dropped into this reservoir by pipette and remained in place due to surface tension.

4.2.1 Initial fiber preparation: tuning the LPG to TAP

As received, the TAP-LPGs exhibited dual peaks that moved away from each other when the surrounding refractive index was increased, such as by applying ISAM layers. Therefore, it was necessary to fine-tune the cladding thickness such that the sensor could operate in the single-peak regime. This was done using hydrofluoric acid to etch away the outer portion of the glass, as described by Biswas et al. [109]. For the fibers used in this work, which had a TAP peak attenuation of about -10 dB, the sensor retained a single peak with a reasonable number of ISAM bilayers when the bare fiber in phosphate buffered saline (PBS) had a peak attenuation of about -1 dB.

In order to etch the fiber, the fiber grating was held taut and the fiber ends were connected to the light source and OSA in order to monitor the spectrum. A polytetrafluoroethylene (PTFE) block with a groove was raised below the fiber such that the sensing region of the fiber rested in the groove, as seen in Figure 4.1. A solution of 1% v/v HF was prepared in a PTFE beaker. The solution was dripped into the reservoir in the block, submerging the

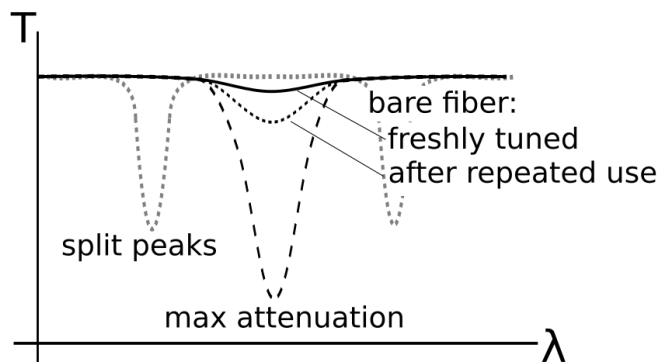


Figure 4.2: Diagram of change in the bare fiber spectra after repeated cleaning cycles. Over the course of weeks of experiments, the attenuation of the bare fiber would increase, meaning there was less dynamic range available before reaching the TAP. This could be corrected by retuning with HF acid etching.

fiber grating. The transmission spectrum of the fiber was monitored while the cladding was etched. When the attenuation peak reached about -2 dB, the fiber was removed from the HF and was rinsed copiously with DI water. The attenuation in PBS was then checked to see if the desired level had been achieved. This process was repeated if further etching was required.

The peak of the bare fiber tended to drift towards the TAP over time (Fig. 4.2), and after several months the sensor would no longer be able to accommodate sufficient ISAM layers to functionalize the surface without splitting the peaks in later steps. This drift may be due to accumulated exposure time to the cleaning solution, which may have caused small changes to the silica. Because the ability to operate in a single wavelength regime is an important advantage of TAP-LPGs, it was desirable to conduct the complete assay without splitting the peaks. Drift toward TAP was corrected by retuning the fiber with HF. In general, this correction was only required once or twice over the lifetime of the fiber grating. These changes could be avoided in a practical device by mass-producing compatible TAP-LPGs such that they could be replaced more often. The fibers could potentially be single-use, thus allowing the device to operate without a cleaning cycle.

4.2.2 Running the biosensor test

Mounting the fiber

To test the biosensor, the fiber was mounted in an apparatus similar to the one used for HF etching. The fiber ends were connected to the light source and the OSA. The grating section of the fiber was held taut between two posts, and suspended over a stage that could be raised or lowered. A plastic block, with notches on the end to accommodate the fiber and a groove in the center to hold liquids, was placed on a height-adjustable stage under the fiber. To apply liquids to the fiber, the stage was raised so the fiber rested in the notches and groove, and liquids were dropped into the groove using a micropipette or transfer pipette. To remove liquids from the fiber, the stage was simply lowered and the liquid was discarded.

Applying ISAMs to the fiber

Clean glass has a negative surface charge in solution due to the dissociation of the terminal silanol groups of the silica [71]. Therefore, the first layer applied to the bare glass fiber was the polycation. The grating was submerged in 10 mM PAH (pH 7) for 3 minutes. The PAH was then removed and discarded, and the fiber and the plastic block were rinsed separately by flowing DI water over them with a wash bottle. The grating was then submerged in 10 mM PCBS (pH 7) for 3 minutes, then rinsed again. At this point, one bilayer had been applied.

Layers continued to be added, alternating between PAH and PCBS, until the desired attenuation was achieved. For the -10 dB fiber used for most of these experiments, ISAMs were added until the transmission spectrum in PCBS had an attenuation of -4 to -5 dB, which typically required two to three bilayers depending on how close the bare fiber transmission

was to the TAP. This allowed the sensor to operate in the highly sensitive near-TAP regime while still being able to bind further biological molecules without pushing the spectrum past TAP and splitting the peak.

The choice of the final polymer layer depended on the chemistry required for binding the receptor molecules. When amine groups were required, PAH was the final layer; whereas when carboxyl groups were required, PCBS was the final layer. For most of the experiments in this work, the ISAM films ended with PAH in order to accommodate binding to N-hydroxysuccinimide (NHS) functionalized biotin.

Measuring the transmission spectrum

Transmission spectra for the fiber were recorded using an optical spectrum analyzer, which reported the attenuation of light through the fiber in decibels over a range of wavelengths. Decibels compare the measured value to some reference value, and are calculated logarithmically as

$$I(dB) = 10\log_{10}\left(\frac{I}{I_0}\right). \quad (4.1)$$

Therefore, the reduction of intensity in the transmitted light is actually much larger than the number value in decibels. For example, a decibel value of -10 dB, typical of the maximum attenuation for the TAP-LPGs used in this work, corresponds to a 90% reduction in transmission.

To measure the transmission spectrum, the fiber was submerged in phosphate buffered saline (PBS) at pH 7.2, which had concentrations of 0.1 M sodium phosphate and 0.15 M sodium chloride. PBS was chosen, rather than air or water, to provide a stable, repeatable, environment in which to perform measurements and to avoid damage to the biological molecules. The sensor was incubated in PBS for 3 minutes prior to measurement to allow

interactions between the adsorbed material and the salts in the solution to stabilize. The transmission spectrum was recorded at the end of this stabilization period. The fiber was then rinsed with water and the measurement step was repeated to check the stability of adsorbed material. In the final rinsing step before the application of biological materials, the grooved block was treated with 70% ethanol for about one minute to disinfect the reservoir.

Applying the receptor molecules

For the majority of the biosensor experiments, DNA probes were used as the sensor's receptor molecules. DNA, or hybridization, probes are single strands of a selected DNA or RNA sequence. The selected sequence, usually about 20 to 100 bases long, is chosen to be specific to the species being detected. When a complementary sequence, such as from the target organism, is present, the strands hybridize. This binding event can be measured by sensitive biosensors, such as the optical fiber sensor in this work.

A common technique for attaching receptor molecules to amine or carboxyl groups is to use carbodiimide cross-linking with 1-ethyl-3-(3-dimethylaminopropyl)carbodiimide-HCl (EDC) and NHS. This approach was used to covalently bind antibodies to the ISAM film in prior work by this group [24]. However, EDC hydrolyzes rapidly when exposed to moisture and becomes inert. It was found that repeated exposures to room air were sufficient to degrade the EDC, and because the biosensor required only about 1 mg of EDC per test, this approach was wasteful and impractical.

In order to circumvent the need for EDC, a combination of NHS, biotin, and streptavidin were used. Biotin (Fig. 4.3), known nutritionally as vitamin B_7 , is a small water-soluble molecule. Streptavidin is a larger (52 kDa) tetrameric protein capable of binding up to four biotin molecules. Biotin and streptavidin are well known for binding extremely well with

with each other due to a combination of multiple hydrogen bonds, van der Waals interactions, and structural changes that secure the biotin within the streptavidin [199]. Due to their very small dissociation constant ($K_d = 10^{-15}$ M) the strong attachment between biotin and streptavidin is widely used for a variety of applications in biomedical science. In this project, commercially available NHS-functionalized biotin was attached to the PAH top layer of the ISAMs, streptavidin was attached to the biotin, then biotinylated DNA probes were attached to the streptavidin layer.

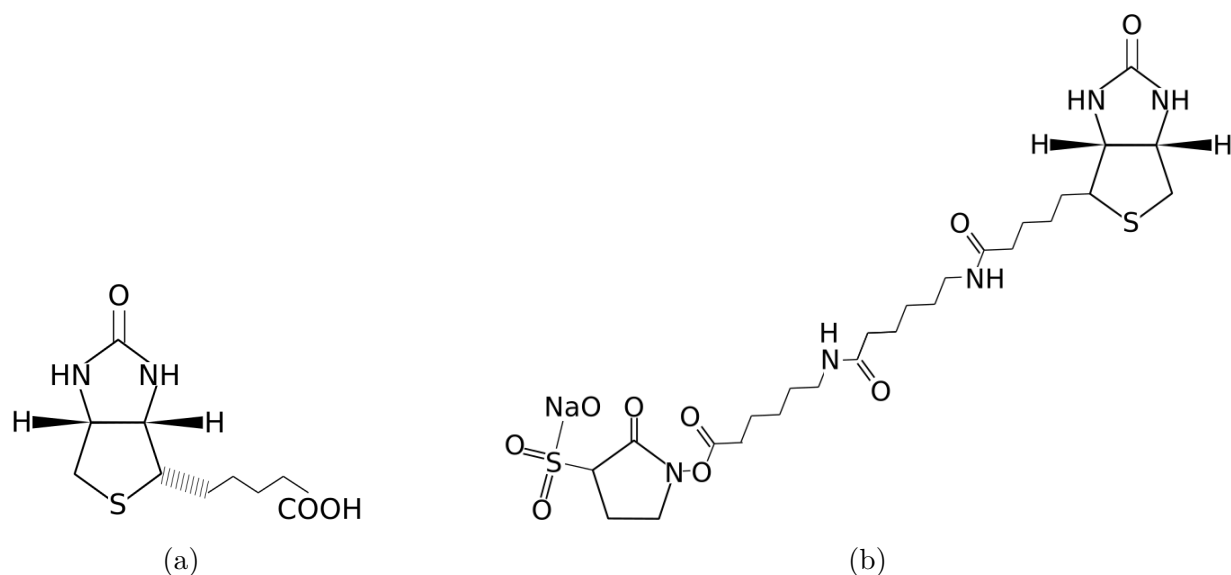


Figure 4.3: Chemical structures for (a) biotin, and (b) NHS-LC-LC-biotin

Sulfo-NHS-LC-LC-biotin (Fig. 4.3) consists of NHS at one end and biotin at the other, with a 3 nm spacer arm between them to reduce steric hindrance. A solution was prepared by dissolving 1 mg of sulfo-NHS-LC-LC-biotin (Thermo Scientific 21338) in 10 μ L of DMSO by vortexing. This small volume of DMSO was chosen due to poor solubility of NHS-LC-LC-biotin in water. PBS was added to dilute the mixture to 1 mg/mL (1.76 μ mol/mL). The resulting biotin solution was applied to the fiber for 60 minutes and was stirred by pipette every 15 minutes to redistribute settled materials. The solution was then removed and the fiber was rinsed and measured in PBS as described above. The fiber was rinsed with water,

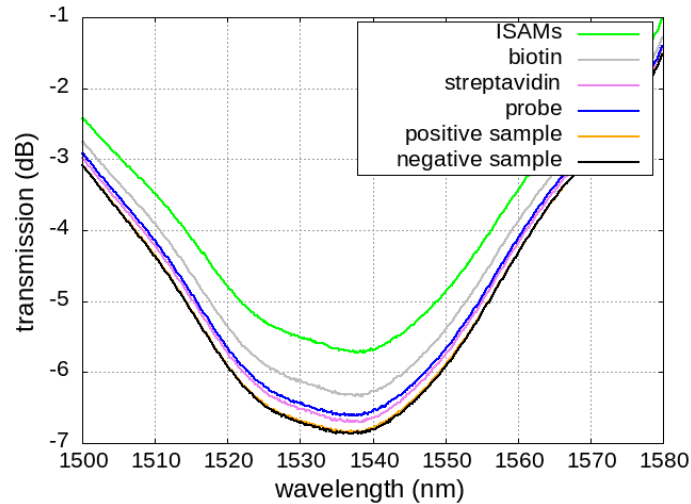


Figure 4.4: Typical development of the transmission spectrum after each step of the assay. The attenuation increased significantly due to application of the biotin and streptavidin layers. A slight backward change was consistently observed after adding the hybridization probe. Exposure to the positive control increased the attenuation, while exposure to the negative control had almost no effect on the attenuation.

fresh PBS was applied, and the transmission was measured again to monitor losses of loosely bound material.

Next, a layer of streptavidin was applied by binding to the deposited biotin molecules. Streptavidin was prepared at 0.05 mg/mL (0.095 nmol/mL), from 1 mg/mL stock stored at 4 ° C, in PBS and vortexed. Like the biotin solution, the streptavidin solution was applied for 60 minutes, with stirring every 15 minutes, then measured repeatedly in PBS. The NHS-LC-LC-biotin and streptavidin concentrations used for these steps were based on guidelines provided by the suppliers [200].

Finally, the biotinylated DNA probes were applied. To limit repeated freeze/thaw cycles of the high-concentration DNA probe stock, 0.5 mL aliquots at 1.2 nmol/mL in 0.5 mL were prepared and refrozen in advance. For each assay, an individual aliquot was thawed, mixed by pipetting, and immersed onto the fiber. As in previous steps, the sensor was incubated for 1 hour, with stirring every 15 minutes, then measured repeatedly in PBS. At this point, the

sensor was fully functionalized with receptor molecules and ready for exposure to bacterial samples. An example of how the transmission spectrum develops over each step of the procedure is shown in Figure 4.4.

Testing for bacteria

For the bulk of the biosensor experiments, cultures of known bacterial species were used. These were provided by our collaborators in the group of Professor Thomas Inzana in the College of Veterinary Medicine. The bacteria were killed prior to being transferred to our lab and were kept frozen until use. The cultures were provided at 10^9 cfu/mL and diluted to 10^4 to 10^7 cfu/mL for testing.

In order to maximize access to the DNA within the cells, it was necessary to lyse them to rupture the cell membranes and expose their contents. This was done by submerging a Parafilm-sealed microcentrifuge tube containing a 0.5 mL aliquot of the bacteria solution in a boiling water bath for 10 minutes to break open the cells and to dehybridize the DNA. The tube was then transferred to an ice bath for five minutes to rapidly chill the solution and prevent immediate rehybridization of the DNA strands. The lysed and chilled solution was then applied to the biosensor, and ice blocks were placed beside the plastic block to keep the system cold. The solution was incubated for 30 minutes and stirred by pipette every 15 minutes. The ice blocks were then removed to give the fiber sufficient time to return to room temperature, due to the sensitivity of LPGs to temperature changes. Incubation and stirring was continued for an additional 30 minutes before the solution was removed and the transmission spectrum was measured. In some cases, the application of bacteria was repeated for additional samples.

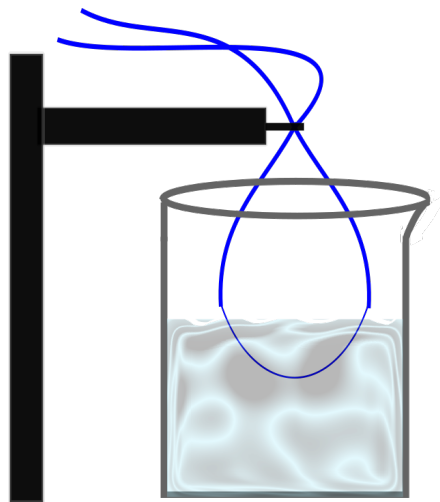


Figure 4.5: Apparatus for cleaning the fiber by sulfonitric acid. The fiber was secured in a loop shape using a simple alligator clip so the jacketless grating was submerged in slowly stirred steaming sulfonitric acid.

4.2.3 Cleaning the fiber

After the bacterial tests were completed, it was necessary to remove the polymers and biological molecules from the fiber in order to prepare it for the next experiment. As seen in Figure 4.5, the fiber was mounted on a stand such that the sensing region formed the bottom of a loop. The sensing region was then carefully lowered into a steaming solution of 90% sulfuric acid and 10% nitric acid by volume. The fiber was left in the cleaning solution for 1 hour, then removed and rinsed with DI water. The solution was stirred with a magnetic stir bar during cleaning to keep the mixture homogeneous, but a slow stir speed was used to avoid damage to the delicate jacketless portion of the fiber.

4.3 LPG fabrication by CO₂ laser

Because the biosensor assay was limited by the sensitivity of the available TAP-LPG fibers, fabrication of TAP-LPGs was attempted with the assistance of Dr. Ziwei Zuo in the lab of Dr. Anbo Wang at the Virginia Tech Center for Photonics Technology.

4.3.1 Fabrication setup

Radiation was supplied by a Synrad J48-2 CO₂ laser operated with a Synrad UC-2000 laser controller. This laser model produces a Gaussian beam with a maximum power output of 25 W at 10.6 μm , and can be operated at pulse frequencies of 5 kHz, 10 kHz, or 20 kHz. The output power can be reduced by pulse width modulation, in which the length of time the system stays at high voltage during a given pulse is varied. A power of about 10 W was typically used for LPG writing. When operating at 5 kHz, 10 W can be achieved with a 40% duty cycle, in which each 200 ms pulse period consists of 80 ms of high voltage and 120 ms of low voltage.

A diagram of the LPG writing setup is presented in Figure 4.6a. First, the beam was directed toward the fiber by a mirror and then focused using a 50 mm focal length cylindrical lens. This resulted in an elliptical spot 150 μm wide and 3 mm long. The spot was aligned with the long axis perpendicular to the fiber as shown in the Figure 4.6b. Because the mid infrared light from the CO₂ laser is invisible, a HeNe laser along the same beam path was used to check the alignment and to ensure that the fiber was centered in the ellipse. The mirror and lens were enclosed within a beam guidance tube to both maintain consistent alignment and to reduce the danger of stray reflections from the high-powered laser. A fire resistant block was placed beneath the fiber to absorb unused laser radiation.

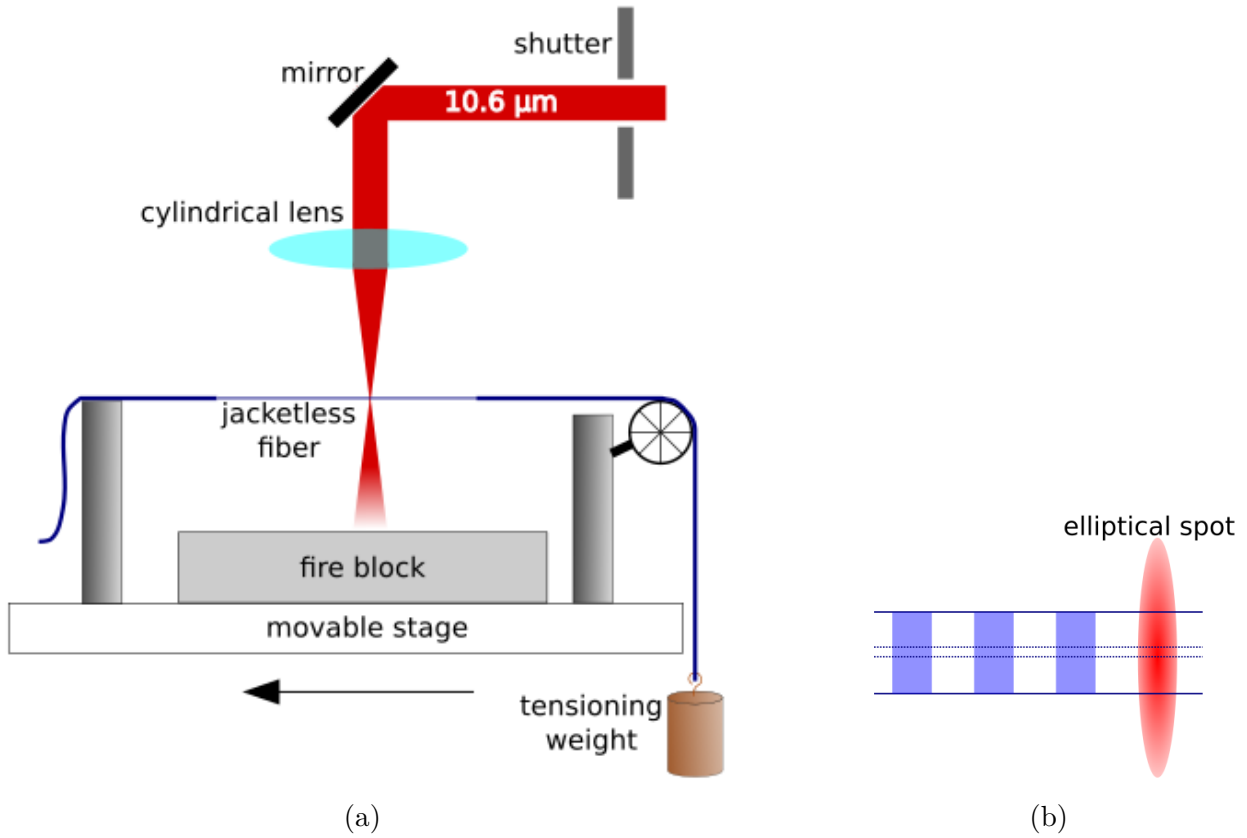


Figure 4.6: Diagram of the CO₂ writing setup (a). Alignment of the elliptical laser spot on the fiber (b).

The fibers used were Corning[®] SMF-28e[®] and SMF-28r[®] fibers. These are standard single-mode step-index telecommunications fibers and differ slightly in their doping characteristics. The SMF-28R was observed by a previous student to require slightly higher laser powers, by about 0.1 W [201]. To prepare the fiber, a roughly 1 m length was cut from the spool. The jacket was removed from a few centimeters of the middle using a stripping tool, then the bare fiber was wiped clean with a Kimwipe and isopropyl alcohol to remove loosely attached jacket remnants. The prepared fiber was then loaded into the writing setup. One end of the fiber was secured with a fiber clamp, while the other was draped over a pulley and attached to the tensioning weight.

Applying a prestrain to the fiber enables the gratings to be written with lower incident

powers. For example, Liu et al. found that for their setup, the minimum energy density required to write a grating was reduced from about 5 to 2.5 J/mm² when the tensioning weight was increased from 10 to 300 g [202]. They attributed this increase in writing efficiency to a change in the required thermal penetration depth. For an unstressed fiber, the core must be heated to a sufficient temperature to allow for residual stress relaxation. In contrast, they suggest that a fiber with prestrain may only require heating at the surface to induce viscoelastic strain in the cladding. Previous work on our setup indicated that deleterious physical deformations occurred with tensioning weights above 50 g [201]. Typical hanging masses used in this project were between 1 to 20 g. The posts supporting the clamp and pulley were on a UTS100CC linear translation stage so that the fiber could be moved under the laser spot between exposures. The translation stage had a range of 100 mm and had on-axis accuracy of 100 nm, and it was operated using a Newport ESP300 motion controller/driver. The entire apparatus was assembled on a stable optical bench and was controlled using a Matlab program developed by Bo Liu and adapted for LPG fabrication by Dr. Ziwei Zuo.

4.3.2 Fabrication procedure and typical parameters

Gratings were written in a point-by-point fashion by holding the laser fixed and moving the fiber beneath it. Parameters were selected on the advice of Dr. Ziwei Zuo, who contributed to developing the setup and was also working on LPG fabrication. A more detailed description of the Matlab program, including features that were not used in this work, are available in his Master's thesis [201].

The power behavior at each position could be controlled by choosing the writing power, exposure time, and the times used to ramp up to the writing power at the beginning of the exposure and to return to zero at the end. In the fibers explored in this work, the writing

power was typically around 10 W, the writing time was 27 ms, and the rising and falling times were always 5 ms. The program also allowed for the inclusion of an additional delay between periods to give thermal effects time to dissipate. The time step used was 1 ms.

Several parameters were available to control the motion of the fiber between exposures. The program allowed for the selection of the grating period to within 0.1 μm and the number of periods to include. This work mainly concerned gratings with periods around 200 μm that were 30 to 45 periods long. Additionally, the setup could be assigned to return to the first grating period and repeat the writing process on an individual fiber over multiple iterations. Writing the grating using multiple short pulses, instead of long single exposures, allowed the fiber to recover between exposures so that it could withstand more laser energy without significant physical deformations. Doing multiple passes over the fiber, rather than rewriting the same spot repeatedly, was done to reduce the impact of slow-changing laser fluctuations. Fully writing a typical grating required about 20 minutes. Thus, if the laser power was falling gradually during operation, repeated moving over the fiber meant that each grating iteration was done at a fairly constant power over a shorter period of time. The fibers reported in this work typically used 7 writing iterations. The power per area and energy delivered to the fiber with the typical parameters can be calculated and is useful for comparing to literature values. When the laser is operating at 10 W, the elliptical spot has a power density of 2833 W/cm². For a standard 27 ms exposure, the energy density is therefore 0.76 J/cm². The spot intersects the fiber with a 150 by 125 μm rectangular cross section, meaning that the fiber receives 0.0143 J in each exposure. After seven iterations, the total energy supplied to an individual period is 0.100 J. In comparison, Lan et al. [203] reported successful TAP-LPG fabrication in SMF-28e using a laser power of 6.8 W, 100 ms exposures, and 200 points with a period of 226 to 228.3 μm . For their spot size, this corresponds to an energy density of 4.33 J/mm², which is significantly higher than ours (which was 0.76 J/cm²). However, they

did not report using prestrain, which improves writing efficiency.

4.3.3 Grating evaluation

The fabricated LPGs were primarily evaluated by observing the transmission spectrum under different conditions. The same fiber mount, light source, and OSA were used as for the biosensor experiments, as described in Section 4.2.2. The transmission spectrum through an optical fiber exhibits several attenuations due to inherent properties of the glass, such as an OH- absorption peak at 1385 nm. Therefore, it was necessary to compare the spectra of the LPGs to a baseline to separate the inherent attenuations from those due to the gratings. However, the baseline spectra for the bulk SMF-28e and SMF-28r were unreliable, possibly due to differences in how the fiber ends cleaved. In order to obtain a clean spectrum, the fiber end must be smoothly cut perpendicular to the axis so that it can interface properly with the internal fiber optic components of the light source and OSA. Special tools exist for accomplishing this. Our lab utilized a manual splicer, which is dependent on operator technique. Several attempts were often required, and it is possible that some of the cleaves obtained may have been tilted or subject to surface defects such as cracks, chips, or lips (Fig. 4.7). Some of the fabricated LPGs were also observed with an optical microscope to inspect for physical deformations due to the laser exposure. Because the baseline spectrum had poor reliability, attenuations due to the grating were therefore searched for by recording the spectrum from a single fiber under different conditions. All spectra for an individual fiber were taken without disconnecting the fiber from the light source and OSA in order to eliminate variables due to poor connections. Because LPGs are sensitive to tension, the spectrum was measured with the fiber loose and pulled taut, then compared. The refractive index sensitivity was probed by immersing the taut fiber in phosphate buffered saline and comparing it to the taut fiber in air. It should be noted that while the spectra shared similar

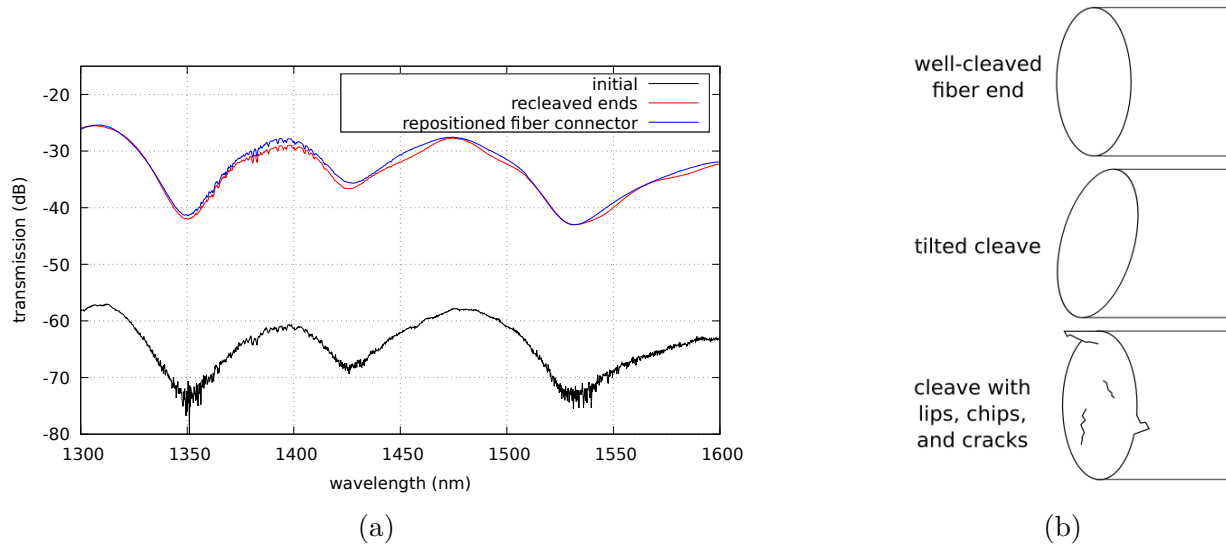


Figure 4.7: (a) Variable transmission spectra obtained a single length of SMF-28e. The initial transmission (black) was very low, so the ends were recleaved. This improved the transmission strength, but details of the spectrum remained sensitive to the orientation of the fiber connectors attached to the light source and OSA. (b) Possible cleaving flaws that can lead to unpredictable scattering and reflections at connections.

large-scale features, they often appeared at different positions on the y-axis due to differences in connection quality. In order to make it easier to compare the spectra, each data trace was normalized by shifting it up such that its maximum value occurred at 0 dB.

4.4 Sample fabrication for plasmonic enhancement of SHG

In general, the SHG experiment was performed by applying PAH/PCBS ISAM films to clean microscope slides, depositing silver nanoprisms onto a region of the ISAM film, and comparing the SHG produced by the ISAM film alone to the SHG produced by the combined prisms/ISAM film. In some cases the deposition order was inverted, or further treatment was applied after the ISAMs and prisms were deposited. These procedures are explained in

more detail in this section.

4.4.1 Preparation of glass slides

Glass microscope slides (Fisherbrand Premium Plain, Fisher 12-544) were used as the substrate for these experiments. In order to ensure uniform and repeatable thin films it was necessary to start with a surface that was as clean as possible. The slides were first solvent cleaned to remove large-scale organic deposits leftover from manufacturing. First, the slides were rinsed with acetone. Immediately afterwards the slides were rinsed with isopropanol to prevent the acetone from drying on the slide and leaving behind residue. The slides were then rinsed thoroughly in water and transferred to a glass Coplin jar in the fume hood for the next cleaning step.

The second step of slide preparation was piranha cleaning. A 3/1 piranha solution, composed of 25 mL of hydrogen peroxide added to 75 mL of sulfuric acid, was mixed in the Coplin jar to strip all remaining organic materials from the surface of the slides. The piranha solution was allowed to react for 30 minutes, after which the slides were removed and rinsed thoroughly in water. The clean slides were stored in beakers of water until ready to use, for up to a few hours.

4.4.2 Applying ISAM films to the slides

ISAM films were applied to the clean slides using a StratoSequenceTM Mark VI automated dipper machine (nanoStrata Inc.). Four clean slides were fitted into slots in a round mount that was held stationary but was free to rotate. The mount was suspended over a circular platform supporting beakers of the appropriate solutions. The platform could rise such that the glass slides were immersed in the solutions when the platform was elevated. The slide

mount was rotated by a motor while the slides were immersed, effectively stirring the solution. At the end of each immersion, the platform lowered and rotated such that the next beaker of solution was aligned below the slides. Using the automated machine ensured repeatable and homogeneous films. Each polymer layer was applied in a 5 minute dip, followed by rinsing in two beakers of water for one minute each.

Polymer solutions of PAH and PCBS were prepared as described in Section 4.1. Due to the negative surface charge of clean silica, PAH was the first polymer deposited. Likewise, because the silver nanoprisms have a negative surface charge, PAH was also used as the final layer. Because plasmonic effects only extend a few nanometers beyond the nanoparticle, enhancement is lower for thick films where only a few of the total layers have access to the plasmonically enhanced E-fields [152]. Therefore, a thickness of 3.5 bilayers was used for the base ISAM film.

4.4.3 Applying nanoprisms to the slides

The silver nanoprisms had a negative surface charge in solution, and were therefore deposited onto microscope slides with a top layer of PAH. The primary methods used to deposit the nanoprisms were the immersion method and the dropcast method (Fig. 4.8). Both were compatible with the aqueous suspensions of nanoprisms produced by the seed-mediated synthesis process and are described below. The immersion method involves submerging the lower portion of the glass slide in the nanoparticle solution. This can be done simply on a lab bench, or by using the dipper machine to allow for stirring and hence more rapid and even depositions. The immersion method has the advantage of coating both sides of the slide, resulting in higher SHG signals due to enhancement on both faces. However, in this project it often resulted in better deposition onto single layer PAH films than onto the PAH/PCBS

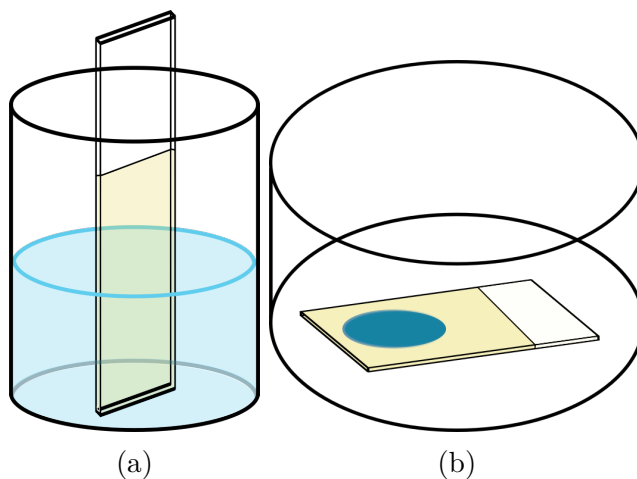


Figure 4.8: Setup for applying nanoprisms to ISAM-coated slides using the (a) immersion method and (b) dropcast method. In both cases the top was sealed with Parafilm to prevent contamination and excess evaporation.

films required for SHG.

In the dropcast method, the slide was placed horizontally in a crystallization dish and a droplet of nanoparticle solution was placed on top. The system was covered with Parafilm and allowed to incubate for up to 24 hours. A small dish or beaker of water was sometimes placed in the container with the slide to provide an alternate source of water vapor and prevent evaporation of the nanoparticle droplet, when desired. While the immersion method generally requires at least 15 mL of solution to coat a reasonable portion of the slide, the dropcast method can be used for volumes of less than 1 mL. It can therefore be used for highly concentrated solutions of nanoparticles. However, the dropcast method can result in nonuniform depositions and “coffee ring” effects, and only enhances the SHG from one face of the slide.

4.4.4 Spincasting

In some cases, additional polymers were spincast onto the deposited prisms in order to redshift their LSPR. A Chemat Technology Spin Coater KW-4A was used. PMMA solutions for spincasting were prepared by dissolving solid PMMA in chloroform by sonication for 60 minutes, and were spincast onto the samples at 3000 rpm for 60 seconds, as recommended by Dr. Liu's group. PCBS spincasting solutions were prepared in methanol and would dissolve on their own after several hours. PCBS solutions were prepared in methanol and were spincast at 4000 rpm for 60 seconds, following the procedures outlined by Goldenberg et al. [204].

4.5 Characterization of samples and measurement of plasmonic enhancement

4.5.1 Sample characterization

In order to study the density and LSPR wavelength of the nanoparticles after deposition, optical extinction data was recorded using a Filmetrics F10-RT. The device was calibrated using a fused silica reference material. The transmittance and reflectance from both the prism-decorated and prism-free regions of the ISAM film were measured, and extinction for each area was calculated as

$$A = -\log_{10}\left(\frac{T}{100 - R}\right), \quad (4.2)$$

where T is the transmittance and R is the reflectance. The extinction of the nanoparticles was determined by subtracting the extinction of the prism-free region from the extinction of the region with the nanoprisms.

For spincoated polymers, the film thickness was measured with a Veeco Dektak[®] 150 Surface Profiler, which measures surface height and roughness by dragging a stylus across the surface. To determine the thickness of the spincoated films, a thin scratch was inscribed using a clean plastic tweezer and the depth of the scratch was measured in several locations and averaged.

4.5.2 Optical setup for SHG measurement

SHG was measured using the apparatus shown in Figure 4.9.

The light source used in these experiments was a Q-switched Spectra-Physics Quanta-Ray INDI pulsed Nd:YAG laser, with a pulse width of 11 ns and a frequency of 10 Hz. In an Nd:YAG laser, electrons in triply ionized neodymium are excited by a xenon flash lamp. The pulse width of the resulting laser light is shortened and its power is increased by a process known as Q-switching. A Q-switch controls the release of the laser light pulse, allowing a large population inversion to build up before emission. The laser used in these experiments also contained a second-harmonic crystal which could be used to emit 532 nm laser radiation by frequency doubling. Even with this feature disabled, it proved necessary to physically block leakage of the 532 nm beam from the second laser aperture with a screen to prevent it from reaching the detector. Several centimeters after the output from the laser head, the beam was passed through a 2 cm hole in a second screen to eliminate more stray light.

After passing through this aperture, the beam was redirected and the power was stepped down by a mirror which reflects 1064 nm light at about 10%. It was necessary to reduce the power of the fundamental beam in order to avoid damaging the nanoparticles and to reduce 532 nm light produced by SHG in the lenses and polarizers in the beam path. This mirror also transmitted 532 nm light, helping to eliminate any stray second-harmonic light produced by the laser. The transmitted light was captured in a beam dump (Blackhole Model 510).

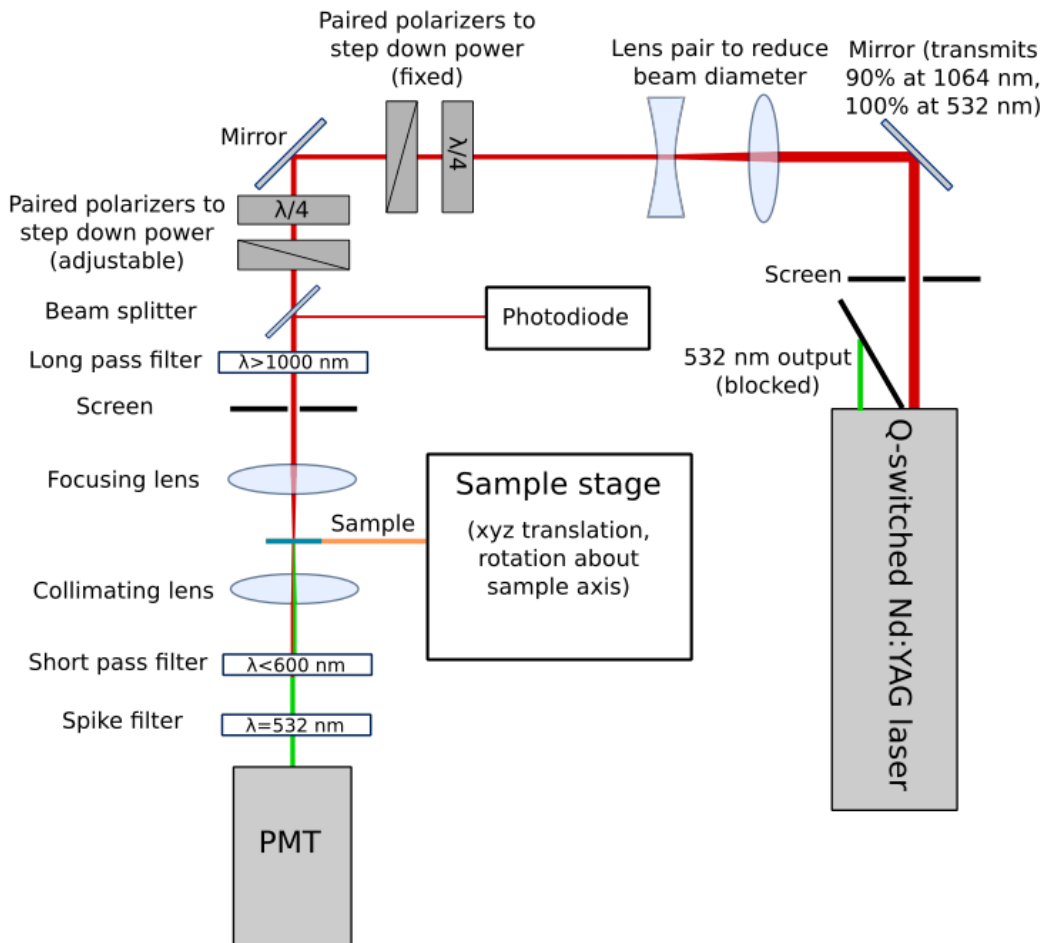


Figure 4.9: Optical setup used to measure SHG. A Q-switched Nd:YAG laser provided excitation at 1064 nm, and SHG light produced by the sample at 532 nm was detected by a PMT. The sample was mounted in a movable sample stage to allow the sample to be positioned accurately and undergo automated rotation during measurement. Electronic components are omitted from this diagram, but their attachments can be seen in [5].

Next, it was necessary to reduce the beam diameter in order for the beam to pass through smaller sized optics. A convex ($f=300$ mm) and concave ($f=-150$ mm) were arranged to form a Galilean telescope to reduce the beam diameter from 10 mm to 5 mm. A quarter waveplate and a Glan-Taylor polarizer were then used to further attenuate the beam power. The quarter waveplate converts the linearly polarized laser emission to circularly polarized. The Glan-Taylor polarizer consists of a pair of prisms aligned so that only p-polarized light is transmitted, while s-polarized light is totally internally reflected and discarded. By varying the angle between these two components, the level of attenuation could be controlled. The angle was kept constant throughout these experiments to reduce the power by a consistent amount.

The beam was next passed through another aperture to block back reflections, and was directed towards the sample by a mirror (Thorlabs BB1-EO3). A second quarter waveplate and Glan-Taylor polarizer were used to further reduce the power and to ensure that the polarization at the sample was vertical. In this case, the angle of the polarizers was adjusted between experiments to control the power reaching the sample. Measurements of ISAM films and films with prisms were typically performed at $700 \mu\text{J}$ and $25 \mu\text{J}$, respectively. A long-pass filter which transmits wavelengths longer than 1000 nm was used to block any second-harmonic light generated by the polarizers. Next, a glass slide was used as a beam splitter to direct a portion of the beam to a photodiode (PIN10D BIAS Box 45V, built by the physics electronics shop at Virginia Tech). The output from the photodiode was connected to channel 1 of the oscilloscope (Textronix TDS 2022B), allowing power stability to be monitored during measurements.

The beam was passed through one final aperture in order to block stray back reflections from prior optics before being focused onto the sample by a converging lens ($f=300$ mm). When required, the power was measured shortly after this converging lens using an Ophir

PE9-C pyroelectric energy meter. The sample was located at the beam focus, which had a spot size of about 1 mm^2 . The sample stage was constructed from three stepper-motor linear translation stages (Aerotech 50SMC2N-HMK) with $2 \mu\text{m}$ resolution to allow for fine control over the three-dimensional position of the sample. In addition, a rotational stage with $1/27^\circ$ resolution was used to rotate the sample over the course of the measurement, as described in the following section. The stepper motors were controlled by a Joerger SMC-R motor controller, which was itself controlled by a KineticSystems 1510-P2C CAMAC (computer automated measurement and control) minicrate. After passing through the sample, the diverging beam was recollimated by a converging lens ($f=200 \text{ mm}$). Two additional filters were used to eliminate the fundamental wavelength so that only second-harmonic light would reach the detector. A short-pass filter was used to block wavelengths longer than 600 nm , and a spike filter centered at 532 nm was used to transmit second-harmonic light while blocking other wavelengths.

To detect the second-harmonic light, a PMT (Hamamatsu R1924) was powered by a high voltage power supply (Bertran 230-03-R) operating at 1.2 kV . In practice, the efficiency of SHG is usually quite low, with only $10^{-9}\%$ of incident photons undergoing conversion [205]. Therefore, a highly sensitive detection scheme was required to pick up the second-harmonic signal. The signal from the PMT was amplified to a gain of $10,000$ by a variable-gain high speed current amplifier (Femto DHPA-100) and sent to channel 2 of the oscilloscope. The oscilloscope signals were sent to a computer and analyzed by a Labview program, as described in a prior dissertation from this group [5].

In previous SHG work by this group, it was found that the SHG signal was so small that it was easily lost in the electrical noise. Therefore, several physical and analytical noise-reduction strategies were implemented. The PMT and the current amplifier were connected to an electrical ground in a surge protector by a grounding braid, and were shielded by

a Faraday cage built by the Virginia Tech physics machine shop. The Faraday cage had the additional benefit of providing a dark environment for the PMT, which was sufficiently sensitive that it could be burned out by unintentional exposure to ambient room light. Shorter BNC cable lengths were selected where possible, and ferrite beads were used to reduce high-frequency noise in the signals. Finally, the frequency bandwidth of the oscilloscope was set to 20 MHz to reject higher frequency noise components. The oscilloscope was set to average mode so that the mean of the previous 120 acquisitions were displayed, increasing the stability of the signal recorded.

Despite these efforts to reduce noise, the low power used to measure the prisms meant that their SHG signal was often too small to be visibly obvious over the noise. Ensemble averaging was used to improve the signal quality. At each angle step the channel 2 waveform was recorded multiple times. On each iteration the DC signal bias, obtained from the portion of the screen before the laser pulse, was subtracted from the waveform to ensure a uniform baseline. The waveforms were then added together and divided by the total number of waveforms in order to obtain the ensemble average for that angle step. The sample was then advanced to the next angle and the process was repeated. In general, ISAM measurements were done with 20 ensemble averages and prism measurements were done with 40 or more ensemble averages. Fewer averages were required for the ISAMs because they could be measured at much higher pump powers, and thus generated a stronger raw signal.

4.5.3 SHG measurement procedure

In order to determine the SHG enhancement due to adding the nanoparticles to the PCBS film, it was necessary to measure the SHG of the film with and without nanoparticles to compare the SHG produced in each case. The comparison was done for each microscope slide

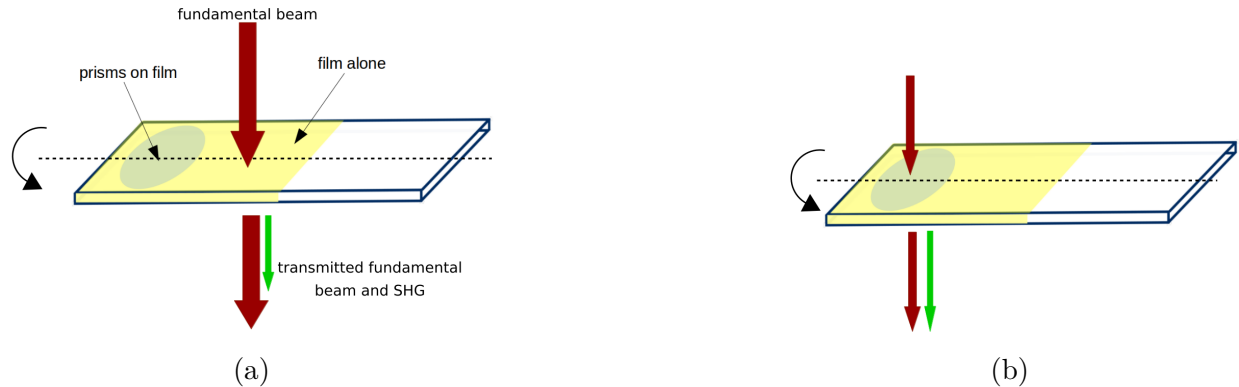


Figure 4.10: Procedure for measuring SHG enhancement. The undecorated ISAM film is measured at a range of angles as a control (a). Next, the nanoprism region of the sample is measured at a lower power to avoid damage to the nanoparticles (b).

by applying the nanoparticles to a smaller area than the total ISAM film (Fig. 4.10), then measuring each region separately. It is worth noting that it was not possible to measure the two regions with the fundamental beam at equal powers because the nanoparticles are easily damaged by intense laser light, while the unenhanced SHG from the bare films requires a higher input power to produce a measurable signal. In previous work, gold nanorods were found to degrade to dogbone-shaped at laser fluence above $0.07 \mu\text{J}/\text{cm}^2$ [5]. For this reason, the ISAM films were measured at a pump power of $700 \mu\text{J}$ to produce a clean and readable signal, while the silver nanoprisms were measured at about $25 \mu\text{J}$. This difference was accounted for by dividing by the square of the pump power to normalize the SHG data.

Maker fringe method

SHG was measured using a technique related to the Maker fringe method. The Maker fringe method was developed shortly after the first demonstration of SHG in quartz by Franken [206], and was described in more detail by Jerphagnon and Kurtz in 1970 [207]. In this technique the effective distance through a nonlinear material is varied, either by rotating the sample or by adjusting the polarization of the fundamental beam on a birefringent material.

Second-harmonic light generated in different regions of the crystal have a phase-mismatch and may interfere constructively or destructively depending on the effective length of the crystal. As the length changes a distinctive Maker fringe pattern is produced. By comparing the observed fringes to theoretical predictions, it can be possible to determine elements of the $\chi^{(2)}$ tensor.

In the simplest case, Maker fringes can be observed for a single slab of isotropic, non-absorbing, nonlinear material. For a continuous slab of a lossless nonlinear material with thickness L and coherence length $l_c(\theta)$, the Maker fringe pattern produced as the sample rotates is given by

$$P_{2\omega}(\theta) = P_{env}(\theta) \sin^2\left(\frac{\pi L}{2l_c(\theta)}\right). \quad (4.3)$$

The oscillating interference pattern is contained within a more slowly varying amplitude or envelope, $P_{env}(\theta)$. The envelope function has a complicated form and involves a number of factors, including a correction factor accounting for the presence of multiple reflections, a projection factor governed by the nonlinear coefficient tensor and the angle between the nonlinear polarization and the plane of incidence, the sample thickness, and additional factors determining transmission based on polarization for both frequencies [207]. The coherence length, $l_c(\theta)$, is a function of the angle between the fundamental beam and the plane of incidence and is given by

$$l_c(\theta) = \frac{\pi}{\Delta k} = \frac{\lambda}{4|n_\omega \cos(\theta'_\omega) - n_{2\omega} \cos(\theta'_{2\omega})|}, \quad (4.4)$$

where n_ω and $n_{2\omega}$ are the indexes of refraction in the nonlinear material of the fundamental and second-harmonic frequencies, and θ'_ω and $\theta'_{2\omega}$ are the transmission angles of each frequency. In its basic form, the Maker fringe method requires that the thickness of the nonlinear material be much longer than its coherent build-up length. For thin films, such as

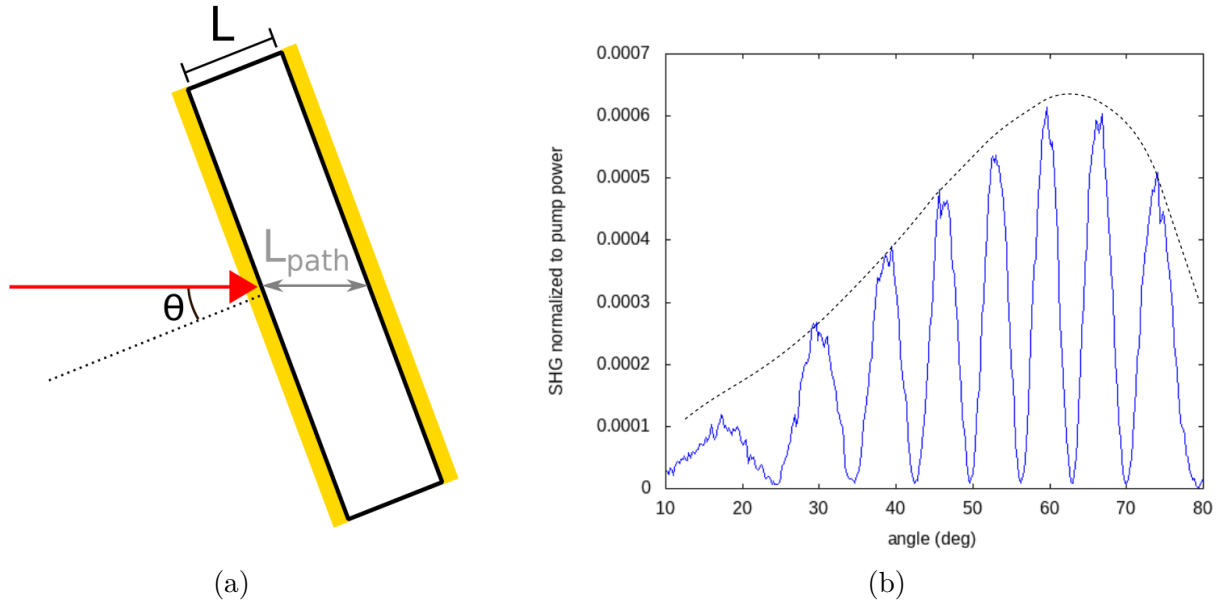


Figure 4.11: Fringes observed from plane-parallel substrates coated on both sides with nonlinear thin films. (a) Variation in path length as the sample angle changes results in an interference pattern. (b) Typical fringe pattern enclosed in an envelope for an ISAM coated slide.

those studied in this work, it is still possible to produce interference fringes by coating both sides of a plane-parallel centrosymmetric substrate (glass) with a nonlinear film, and observing the interference pattern produced by second-harmonic light generated on both faces of the slide (Fig. 4.11). The appearance of fringes in the SHG data results in some inherent error when a single SHG value is required to characterize the film. In nearly all cases the value selected is the maximum observed. However, when the maximum of the envelope fails to line up with the maximum of one of the fringes, the recorded SHG value will be less than the maximum SHG of the film.

SHG from the sample was measured with the fundamental beam at a range of angles with respect to the normal, in order to observe the fringe pattern and/or envelope produced. Due to the shape of the envelope, very little SHG is produced when the angle of incidence is near 0° or 90° . Therefore, in most cases data was recorded from 10° to 80° to obtain a full

picture. However, because the maximum SHG typically occurred between 40° to 70° , shorter data sets in this range were sometimes taken as a time-saving measure. At each angle step, the sample was held stationary while the desired number of data points was collected for ensemble averaging. The stepper motor then advanced the sample to the next angle step to repeat the process.

Chapter 5

TAP-LPG biosensor results and discussion

In this chapter our results relating to the TAP-LPG biosensor are presented and discussed. First, section 5.1 presents the results of work with *Histophilus somni*, which was primarily performed by Dr. Ziwei Zuo. The remaining sections concern our novel work. Section 5.2 shows the typical evolution of the transmission spectrum through the fiber as ISAM layers are added, as a demonstration of the dynamic range of the fiber and of the general function of the sensor. Section 5.3 describes several studies that were undertaken to help optimize the functionalization procedure for the sensor surface. Section 5.4 presents our results when using the TAP-LPG sensor to detect bacteria at known concentrations grown in culture, while Section 5.5 presents our results for samples taken from the tissues of *Brucella* infected mice. Finally, Section 5.6 presents the results of our CO₂ fabrication attempts.

5.1 Prior work with *Histophilus somni*

Previous work with the sensor system was focused on the detection of *Histophilus somni*, a bacterium that is present in the normal mucosal fluids of sheep and cattle but is also among the primary bacteria responsible for bovine respiratory disease (BRD). BRD is a major cause of economic losses in the cattle industry through lost production, treatment

and labor costs, and increased mortality [208]. Because the symptoms of *H. somni* derived infections are similar to those observed from other bacteria, it is not often identified at autopsy. Serological techniques, which detect antibodies, can produce false positives if there has been previous infection or colonization. Techniques which rely on culture growth can fail if there are other pathogens present because *H. somni* is slow-growing and has specific nutritional needs. The TAP-LPG biosensor was therefore investigated as a means to identify *H. somni*.

Initial assays studying the response of the sensor to different concentrations of *H. somni* 2336 used a -27 dB fiber. In these tests, 4 ISAM bilayers were applied. The biotinylated nucleotide probes were attached directly to the ISAM surface by cross-linking with EDC and NHS as described in Section 4.2.2. In this crosslinking procedure, 60 pmol of probe was added to a freshly prepared solution of EDC and NHS, both at 0.17 M, and applied to the fiber 30 minutes at room temperature. In a separate step, the sensor was then exposed to killed, lysed cells of *H. somni* 2336 suspended in PBS.

As can be seen in Figure 5.1, the attenuation increased with increasing *H. somni* concentration. This trend occurred rapidly at low concentrations. The sensor was clearly able to distinguish between samples with and without *H. somni*. The negative control, which contained 50,000 cfu of *E. coli*, produced a signal of 1.6%, while only 100 cells of *H. somni* produced a signal of 9.4%. Diminishing returns were observed at higher concentrations. Between the two highest concentrations the signal increased by about 25%, compared to an increase in concentration of 625%. The sensor also demonstrated high repeatability, with a low standard deviation at each concentration. The large changes in attenuation, and the high repeatability of the measurement, can be attributed to using a -27 dB TAP-LPG with a high sensitivity to external refractive index changes.

Additional *H. somni* tests were performed to determine whether attaching streptavidin to

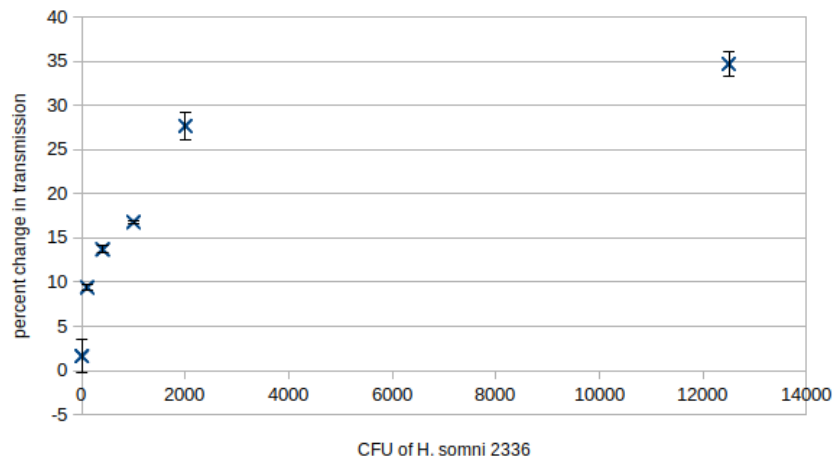


Figure 5.1: Results for tests of *H. somni* 2336 cells at 100, 400, 1000, 2000, and 12500 cfu in 0.5 mL. Each assay was run three times and averaged, with error bars representing the standard deviation. Samples containing 0 cfu of *H. somni* were completed using 50,000 cfu of *E. coli* DH5 α . These assays utilized a higher sensitivity fiber with a maximum attenuation of -27 dB.

the ISAMs in order to later attach the biotinylated probes was more effective than attaching the nucleotide probes directly to the ISAMs. The sensor was tested with *H. somni* 2336 as the positive control and *E. coli* DH5 α as the negative control at four different concentrations. Each concentration was tested with and without the intermediary streptavidin step. The addition of streptavidin was observed to increase the signal observed when the sensor was exposed to *H. somni* cell cultures. Further details of the *H. somni* assays are available in a prior dissertation from this group [24] and in a recent publication [25].

5.2 Typical ISAM deposition

Sections 5.2-5.5 will focus on using the TAP-LPG biosensor to identify the presence of *Brucella* bacteria. The TAP-LPGs used in the biosensor projects were fairly fragile, due to the removal of the plastic jacket over the grated portion of the fiber. Additionally, the fibers

became increasingly brittle after several months of use, eventually breaking due to stresses during transfer between the measurement apparatus and the cleaning solution. In one case, the delicate jacketless fiber broke simply due to surface tension when being removed from an incubation solution. While prior work by this group used fibers with a dynamic range of about -30 dB, which corresponds to a maximum decrease in transmission by a factor of 1000, the only surviving LPGs available for the remaining biosensor tests had a maximum attenuation of about -10 dB, which only reduced the transmission by up to a factor of 10. The smaller dynamic range meant that the fibers were less sensitive, making it more difficult to detect small binding events at the surface.

The ISAM deposition was highly repeatable. A typical progression of the transmission spectrum of the fiber when adding ISAMs is shown in Figure 5.2. As can be seen, the grating region of the fiber has been tuned by etching with HF such that the bare fiber has a small attenuation of about -2 dB while submerged in PBS. The attenuation of this single peak increases with each ISAM bilayer added to the fiber. The TAP occurs near four bilayers, after which the peaks split and begin to move apart. Furthermore, the change in attenuation between bilayers increases as the transmission approaches the TAP, especially at the wavelength of maximum attenuation. While each bilayer is about 1.2 nm thick, the later bilayers have a larger impact on the attenuation than the initial ISAM layers. This occurs because the fiber becomes more sensitive near the TAP. The biosensor experiments were designed such that the functionalized fiber operated in this sensitive near-TAP regime when exposed to the analytes.

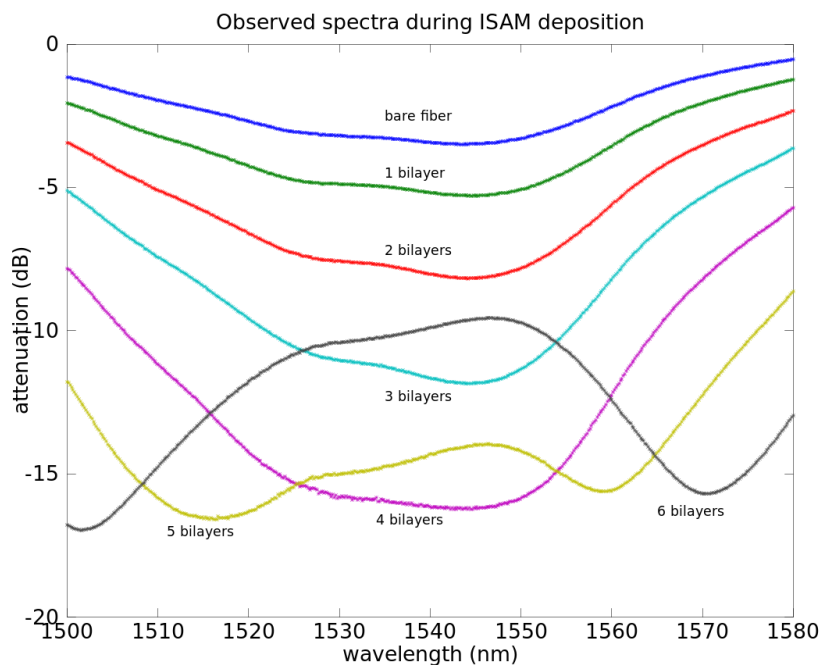


Figure 5.2: Typical evolution of transmission spectrum in PBS between ISAM deposition steps. The single peak deepens as the coating thickness is increased, achieving a maximum attenuation at the TAP before splitting into dual peaks.

5.3 Determination of biological functionalization parameters

After ISAM application, functionalizing the biosensor with receptor molecules was a multi-step process. As discussed in Section 4.2.2, the hybridization probes were not cross-linked directly to the ISAM film due to rapid hydrolyzation degradation of one of the reagents (EDC) required for cross-linking. Instead, a three-step procedure was used in which NHS-LC-LC-biotin was attached to the film. Streptavidin was then attached to the biotin-coated sensor in order to create binding sites for the biotinylated hybridization probes. The concentration of the first NHS-LC-LC-biotin solution applied to the fiber was calculated using guidelines provided by the manufacturer based on the geometry of the substrate surface [200].

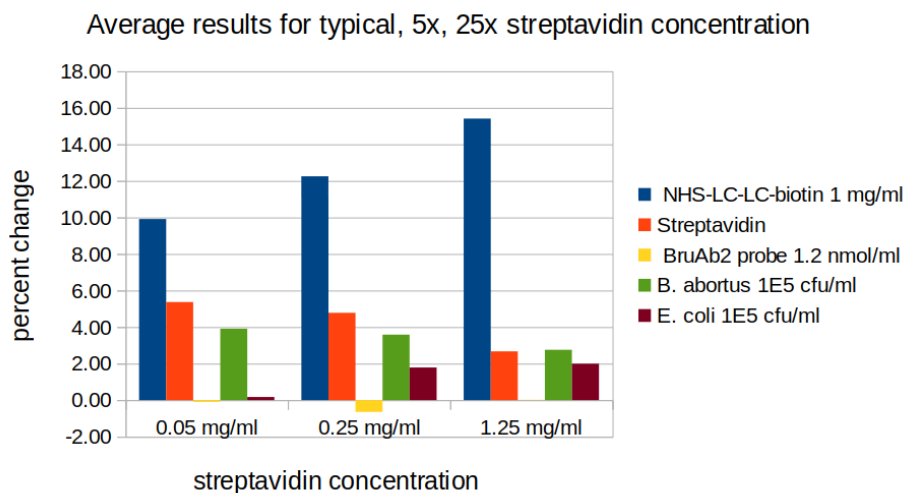


Figure 5.3: Results for tests comparing the sensor’s performance with different concentrations of streptavidin. Each streptavidin concentration was tested twice and the results were averaged. Higher concentrations of streptavidin did not increase streptavidin deposition or improve the sensor’s ability to detect and distinguish bacterial samples at 10^5 cfu/mL.

Therefore, 1 mg/mL was used for the initial biotin application in all experiments. The optimum concentrations for the remaining functionalization steps were estimated based on the expected concentration of biotin of the surface, but were also investigated experimentally.

5.3.1 Streptavidin concentration

To study the ideal concentration of streptavidin to use for the second biological layer, the biosensor test was performed with streptavidin at the typical concentration used in prior work, 0.05 mg/mL, and at elevated concentrations. The results of these tests are presented in Figure 5.3. Unfortunately, because these tests were performed in order of increasing concentration, there is a distinct trend in the attenuation change due to the first biotin layer, which should have been the same for all of the tests. This trend may be due to changes in the glass structure of the fiber due to repeated exposures to the sulfonitric cleaning solution. As discussed previously, the bare LPG tended to drift towards the TAP with repeated use.

This would mean each individual step of the functionalization would occur closer to the TAP, where the fiber is more sensitive to changes at its surface. This change in behavior can be counteracted by retuning the fiber with HF, but this was not done over the course of the streptavidin concentration experiments.

Looking at the change in attenuation due to the streptavidin deposition, it appears that higher streptavidin concentrations did not result in increased streptavidin attachment. This is clear despite the systematic error evident in the NHS-LC-LC-biotin step. Additionally, the tests at 0.25 and 1.25 mg/mL did not exhibit a higher signal when exposed to the positive sample, *B. abortus*, and in fact showed a higher signal when exposed to the negative sample, *E. coli*. While the small sample size and poor randomization make it difficult to draw conclusions about these changes, it is clear that increasing the streptavidin concentration did not improve the function of the sensor. The remainder of the biosensor experiments therefore continued to use 0.05 mg/mL streptavidin.

5.3.2 Varying concentration of second biotin layer

The sensor surface was assembled by binding biotin to the ISAM surface, which then bound streptavidin, which then bound biotin from biotinylated DNA probes. To investigate the ideal concentration of DNA probe to use, the biotin-streptavidin functionalized sensor was exposed to different concentrations of NHS-LC-LC-biotin. Biotin, rather than DNA probe, was used for initial tests in order to conserve the more expensive DNA probes. Exposures to biotin at 0, 10, and 100 nmol/mL were tested. The 0 nmol/mL sample consisted of PBS and DMSO without NHS-LC-LC-biotin. The usual probe concentration, 1.2 nmol/mL, was omitted from this study of biotin, but was compared with elevated probe concentrations in later experiments (Section 5.3.3). Each biotin concentration was tested twice, and the

averaged results are presented in Figure 5.4. The attenuation due to the second biotin

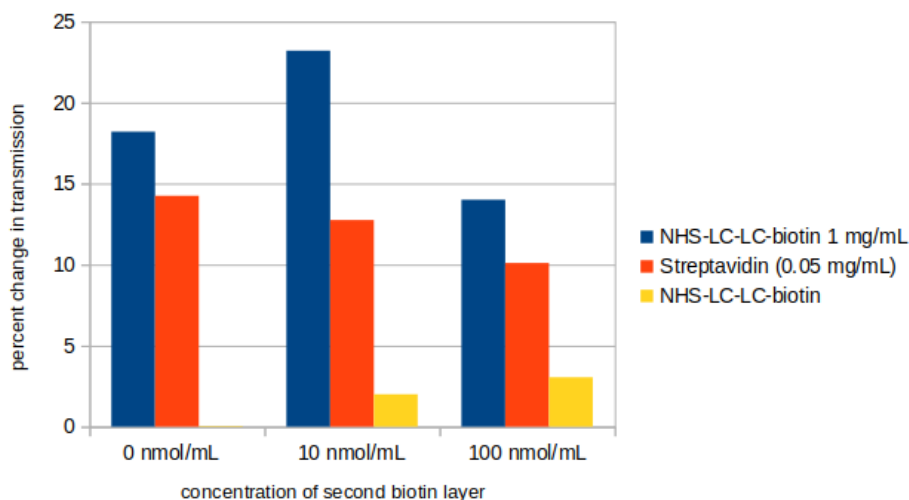


Figure 5.4: Results for tests comparing different concentrations of the second biotin layer. Because tests with bacteria utilize biotinylated hybridization probes attached to streptavidin immobilized on the fiber, biotin was used as a stand-in to economically investigate the benefits of using higher probe concentrations. A negative control consisting of PBS and DMSO, without NHS-LC-LC-biotin, was also tested (0 nmol/mL). The standard 1.2 nmol/mL probe concentration was omitted from these tests with biotin, but was examined in a later comparison of probe concentrations (Section 5.3.3).

layer increased with increasing concentration, as expected. However, in all cases the change in transmission at this step remained quite small, at less than 5%. This could in part be attributed to the small size of biotin when compared to streptavidin, although the initial LC-LC-biotin was able to produce a large signal. Furthermore, when the biotin concentration was increased ten-fold, the change in transmission increased by only a factor of about 1.5. Because of the limited benefits of increasing the concentration at this step, the concentration of the DNA probes was not increased and they were typically applied at 1.2 nmol/mL.

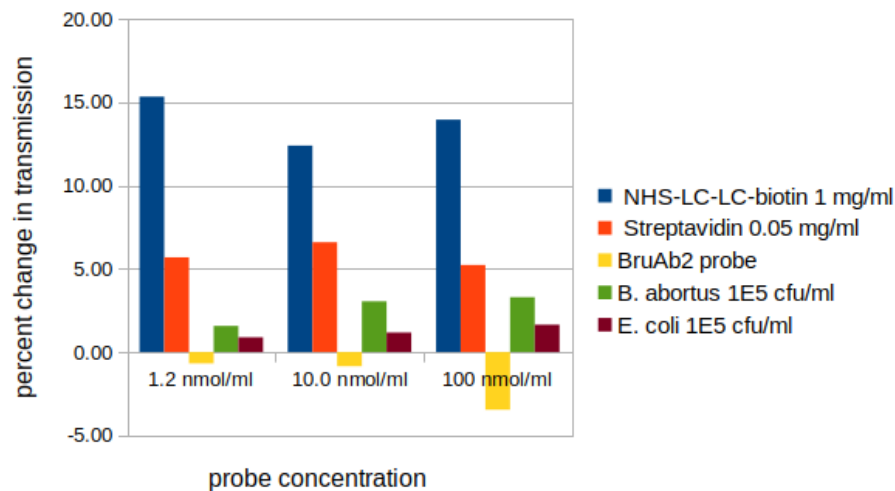


Figure 5.5: Results for tests of the sensor at the typical probe concentration (1.2 nmol/mL), as well as two elevated concentrations. The probe attachment resulted in a negative change in attenuation, for reasons that remain unclear. Higher probe concentrations resulted in slightly higher signals for both the positive (*B. abortus*) and negative (*E. coli*) controls.

5.3.3 Probe concentration

To try to improve the performance of the bacterial sensor, and to confirm the results of the previous biotin concentration tests discussed in Section 5.3.2, tests were performed at the standard DNA probe concentration and at two elevated concentrations. Each concentration was tested twice, and the average results are presented in Figure 5.5.

In all cases, the application of the DNA probe resulted in a negative percent change in transmission compared to the previous steps. The effect was stronger with higher probe concentrations. The mechanism behind this behavior is unclear, however, it was observed consistently over the many tests performed. It is possible that an additional chemical found in the concentrated DNA probe stock, which was obtained commercially, could have been the cause. Another explanation could be an effect due to the geometry of the DNA probe molecules. Increases in attenuation occur for the TAP-LPG when the effective external refractive index increases. This change in refractive index is usually accomplished by binding

materials to the outer surface of the fiber. However, because the single stranded DNA in the probes are long and thin and therefore extend further into the surrounding liquid, it is possible that steric effects occurred which caused different behavior from molecules with a lower aspect ratio.

The lowest concentration tested was the typical concentration used in prior work by our group. Increasing the probe concentration to 10 nmol/mL approximately doubled the signal from the positive bacterial control, but further increasing to 100 nmol/mL failed to produce significant enhancements beyond this. A small increase in signal from the negative control was also observed with increasing probe concentration. This effect was less pronounced than for the positive control, exhibiting only about 1.3 times more percent change in transmission compared to the previous step.

5.4 Experiments using bacterial cultures

In the field or in a clinical setting the LPG biosensor would need to be compatible with samples taken directly from tissues of infected hosts. However, such samples can contain a multitude of additional materials that can make the sensor performance more complex. Therefore, to first study the sensor performance under controlled conditions, simpler samples consisting of bacterial cultures of known concentrations were used.

5.4.1 Sample concentration

In characterizing a biosensor, it is important to determine its response at a range of ligand concentrations. This allows the sensitivity and dynamic range to be quantified. *B. abortus* cultures ranging from 10^4 to 10^7 cfu/mL were tested with the biosensor to study how it re-

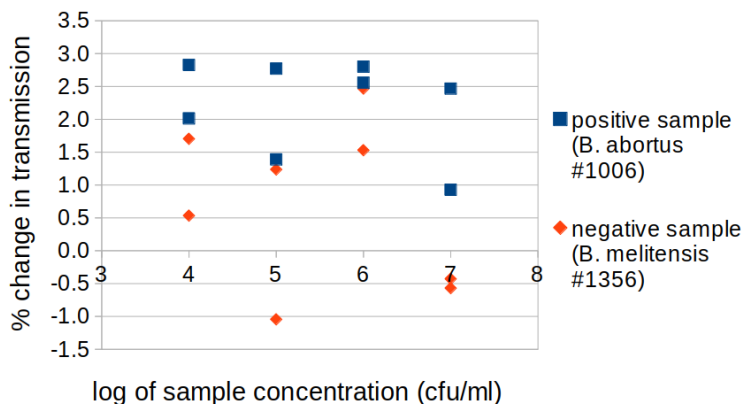


Figure 5.6: Results from exposing the biosensor to *Brucella* samples at 10^4 to 10^6 cfu/mL. The change in transmission was only slightly higher for positive controls than for negative controls, and no correlation with concentration was observed.

sponded to different concentrations of bacteria. In order to determine whether the biosensor could distinguish between similar species, *B. melitensis* was used as the negative control. Each concentration was tested twice, using the positive sample before the negative control, and the results are presented in Figure 5.6. The usual procedure of functionalizing the sensor using biotin/streptavidin/probe was used, but these initial steps are omitted for clarity. As can be seen in Figure 5.6, higher bacterial concentrations did not improve the sensor's performance. More problematically, while the positive controls consistently produced a higher signal than the negative controls at individual concentrations, the difference between them is very small. In some cases, the average negative sample falls within one standard deviation of the average positive sample signal, and vice versa. Looking at all of the measurements together, some of the negative controls produced a higher signal than some of the positive controls. Although both samples were *Brucella* species, the DNA probe used was composed of a sequence specific to *B. abortus*. *B. melitensis* samples should have shown no binding to the DNA probes because this strain does not have the correct complementary DNA sequence. These weak results could possibly be due to insufficient sensitivity of the TAP-LPG used, which inherently had a low change in transmission due to binding of analyte. It is also

possible that nonspecific binding was the cause. While the sensor was designed to detect binding of single stranded DNA to the hybridization probes, materials such as cell membranes miscellaneous cellular contents were also present in the solutions. If these materials were able to attach to exposed PAH, biotin, or streptavidin, a false signal would be observed. It appears that the sensor was unable to distinguish between positive and negative bacterial controls in a statistically significant way. Nonetheless, further tests were performed using alternate strains of *Brucella* or different bacterial species as the negative controls, and by substituting mouse tissue samples for the bacterial cultures.

5.4.2 Tests using miscellaneous bacterial species as negative controls

A larger set of trials was run using *Brucella* samples as the positive controls and various bacterial species as the negative controls, all at a concentration of 1×10^7 cfu/mL. The *Brucella* species *B. abortus*, *B. melitensis*, and *B. suis* were used as the positive samples, with DNA probes specific to the corresponding species. For each *Brucella* species, five different bacterial species were tested as the negative controls. Each combination was repeated once to check for consistency. These thirty tests were performed in a randomized order to minimize influences from system changes over time. The results of these tests are presented in Figure 5.7.

The results from tests using *B. abortus* as the positive sample showed a particularly low signal from the positive sample. Because all of the DNA probes attached to streptavidin on the fiber via their attached biotin molecules, all of the probes should have deposited equally well onto the fiber surface. The lower signal from *B. abortus* may indicate that the DNA sequence chosen for this probe was less effective than for *B. melitensis* or *B.*

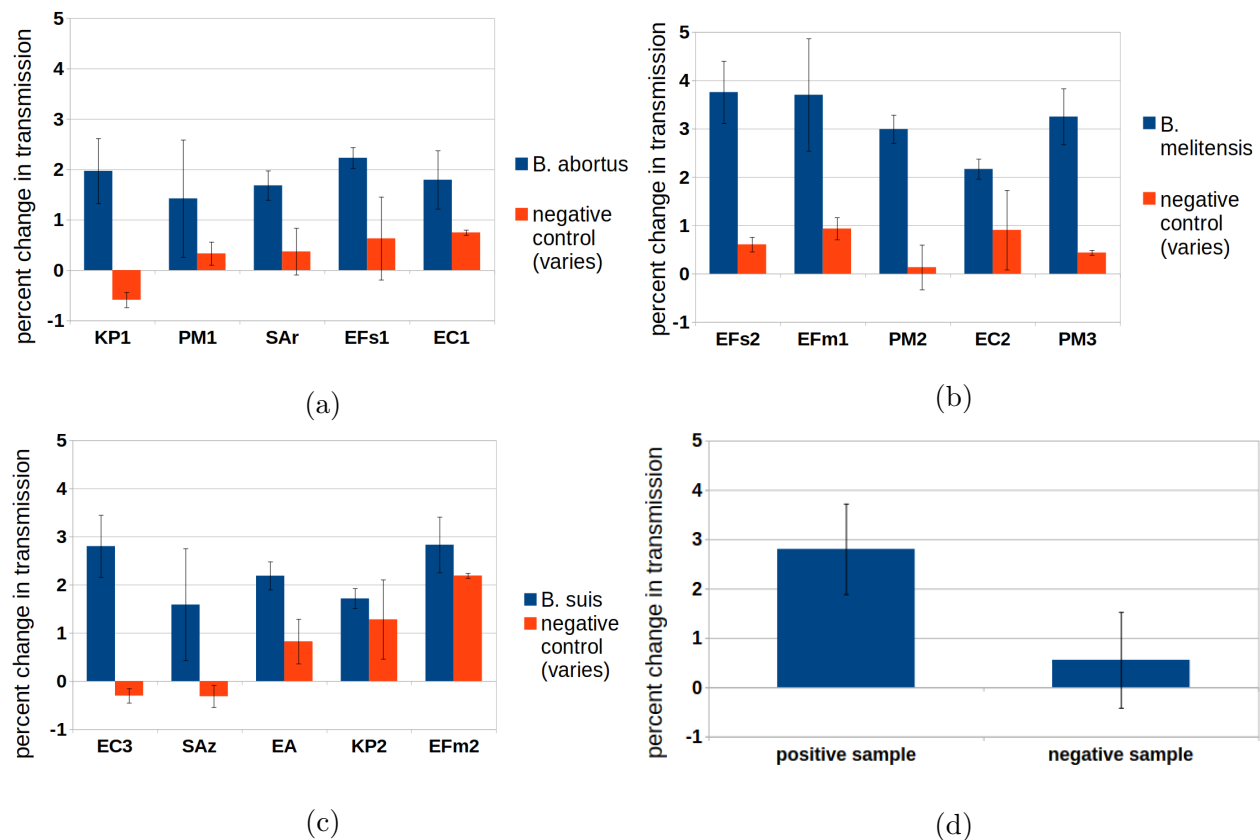


Figure 5.7: Results for tests using species specific DNA probes to distinguish individual species of *Brucella* from other non-*Brucella* negative controls. The positive controls were (a) *B. abortus*, (b) *B. melitensis*, or (c) *B. suis*. Each *Brucella* strain was tested versus five non-*Brucella* bacterial samples. While some negative control species were repeated, each of the fifteen negative bacterial strains were from unique batches (Table 5.1). Each test was repeated and the results were averaged. The average results of all thirty assays is presented in (d). Error bars indicate the standard deviation between the repeated measurements. The transmission change was always larger for the positive controls, but in many cases the standard deviations for positive and negative controls overlapped.

Table 5.1: Abbreviations used for negative control samples when attempting to distinguish *Brucella* species from other genera of bacteria, as presented in Figure 5.7.

Abbreviation	Sample species and name
EA	<i>Enterobacter aerogenes</i> 13-2329-2
EC1	<i>Escherichia coli</i> 2174
EC2	<i>Escherichia coli</i> 13-2401
EC3	<i>Escherichia coli</i> Top10
EFm1	<i>Enterococcus faecium</i> 13-2248-2
EFm2	<i>Enterococcus faecium</i> 13-2174-C
EFs1	<i>Enterococcus faecalis</i> 2174
EFs2	<i>Enterococcus faecalis</i> 13-2321-2
KP1	<i>Klebsiella pneumoniae</i> 2237
KP2	<i>Klebsiella pneumoniae</i> 2237-133
PM1	<i>Proteus mirabilis</i> 2172B
PM3	<i>Proteus mirabilis</i> 13-2401
PM2	<i>Proteus mirabilis</i> 13-2319
SAr	<i>Staphylococcus aureus</i> 29213
SAz	<i>Salmonella arizonae</i> 13-2453

suis. As in previous tests, the difference between positive and negative samples was small, but in all cases the positive samples produced a higher signal than the negative samples. In some cases, the standard deviation of the positive samples overlaps with the standard deviation with the negative samples. Looking at the overall data set (Fig. 5.7d), one standard deviation less than the average positive sample (1.89%) is only slightly higher than one standard deviation above the average negative sample (1.53%), however, they do not overlap. These results indicate that the sensor in its current configuration is not a reliable means of distinguishing between *Brucella* and other bacterial species. However, the results suggest that a real difference is present between the positive and negative responses, which could be improved upon by altering the functionalization procedure, using a fiber with a greater dynamic range, or taking steps to block nonspecific binding.

Table 5.2: Samples tested to distinguish *B. abortus* from *B. melitensis* and *B. suis*, using samples provided by the USDA. Results are presented in Figure 5.8

Experiment Name	Positive sample	Negative sample
M1	<i>B. abortus</i> 1001	<i>B. melitensis</i> 1253
M2	<i>B. abortus</i> 1009	<i>B. melitensis</i> 1254
M3	<i>B. abortus</i> 1003	<i>B. melitensis</i> 1255
M4	<i>B. abortus</i> 1005	<i>B. melitensis</i> 1355
M5	<i>B. abortus</i> 1006	<i>B. melitensis</i> 1356
S1	<i>B. abortus</i> 1008	<i>B. suis</i> 1736
S2	<i>B. abortus</i> 1007	<i>B. suis</i> 1737
S3	<i>B. abortus</i> 1002	<i>B. suis</i> 1738
S4	<i>B. abortus</i> 1011	<i>B. suis</i> 1739
S5	<i>B. abortus</i> 1013	<i>B. suis</i> 1740

5.4.3 USDA samples

Because *B. abortus* presents a severe risk to livestock (Section 2.4.2), a practical sensor should be able to distinguish between it and less threatening species. Ten tests were performed using *B. abortus* as the positive sample and various strains of *B. melitensis* or *B. suis* as the negative control. Each bacterial sample used was a unique subtype of the strain, and none were repeated. The specific combinations used can be seen in Table 5.2. The tests were run in a randomized order. As is clear in Figure 5.8, the sensor proved unable to distinguish between *B. abortus* and other *Brucella* species. The *B. abortus* samples, which should have supplied the correct DNA to hybridize to the DNA probes on the sensor surface, failed to produce a significant signal. It is possible that there were problems either with the sensor functionalization or with the bacterial samples themselves. However, the greatest challenge was the low LPG sensitivity compared to those used in prior work by this group. Meanwhile, while the negative samples generally produced negative or small positive signals, the highest signal observed throughout the data set came from one of the negative controls, *B. suis* 1739. The average signal for the positive samples was nearly identical to

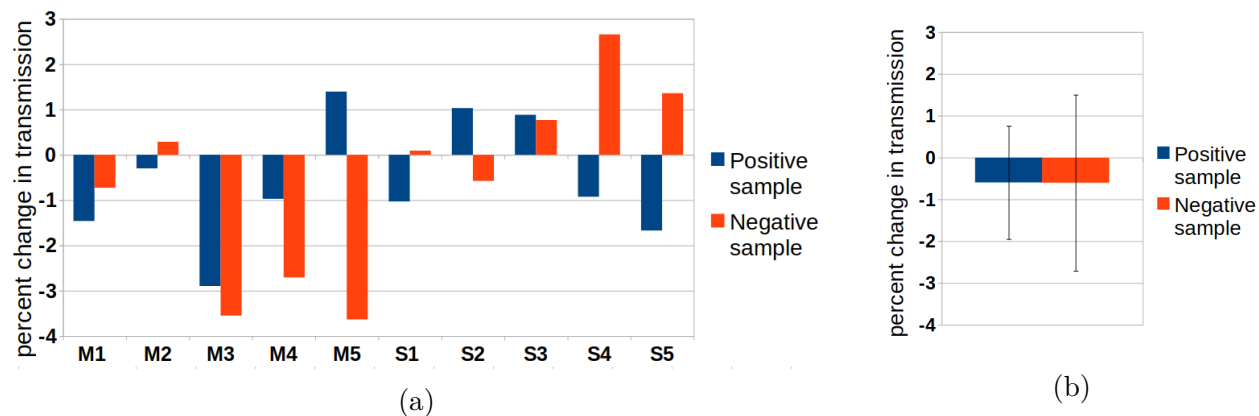


Figure 5.8: Results of tests distinguishing *B. abortus* from *B. melitensis* and *B. suis*, using samples provided by the USDA (Table 5.2). Individual assays (a) often resulted in a negative change in attenuation, which was the opposite of what was expected. The mean signal of all tests (b) was about the same for positive and negative samples, due to the high variability of the individual assays.

the negative samples, although the negative samples had more variation. While the assays using miscellaneous bacteria as the negative controls produced a noticeable, if statistically weak, difference between positive and negative signals, the assays using *Brucella* species as the negative controls failed to distinguish between *B. abortus* and less harmful species.

5.5 Mouse tissues

Most of the tests discussed in this work dealt with pure cultures of bacteria. However, to fully take advantage of the speed of the optical fiber biosensor in real-world applications, it would have to function using samples taken directly from infected wildlife, livestock, or clinical patients. To provide a more realistic test of the biosensor, tissue samples from the organs of mice infected with *Brucella* were used. Two mice were infected with *B. abortus*, two mice were infected with *B. melitensis*, two mice were infected with *B. suis*, and two negative control mice were injected with PBS. Spleen and liver tissues were harvested from the mice and suspended in PBS. Each organ from each infected mouse was tested once using the

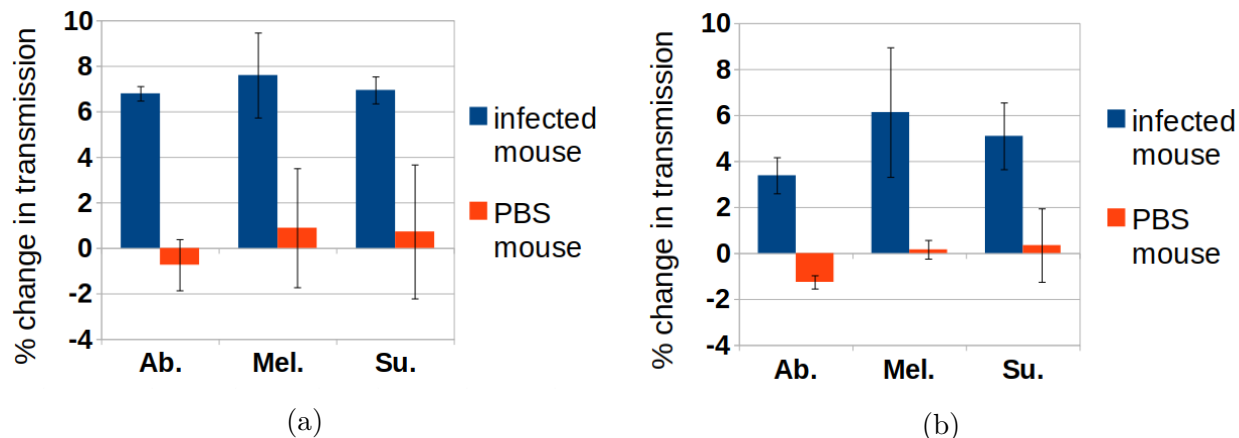


Figure 5.9: Results obtained from tissues of mice infected with different *Brucella* species. The change in attenuation was slightly greater for spleen samples (a) than for liver samples (b).

TAP-LPG biosensor, and the results for each *Brucella* species are averaged and presented in Figure 5.9. Overall, the results from the mouse tissues were much better than for the pure bacterial cultures. For all species, the signal from the infected mice was higher than for the mice injected with PBS. This was especially true for the spleen tissues, where the average positive signal was 7.1% and the negative sample was 0.3%. The standard deviation from the positive sample never overlapped with the standard deviation from the negative samples. It is possible that these samples contained more bacteria than those discussed in prior sections of this chapter, or that their DNA was in better condition. Interestingly, the DNA in the tissue samples was at its original concentration and had not been amplified by PCR. While more testing would need to be done to rule out contributions from nonspecific binding, ensure repeatability, and better randomize the sample order, it appears that the sensor could be effective at identifying *Brucella* infection in animals.

5.6 TAP-LPG fabrication by CO₂ laser

5.6.1 Initial attempts using recommended parameters

Initial attempts to fabricate LPGs by CO₂ laser used parameters recommended by Dr. Ziwei Zuo, as shown in Table 5.3. It was found that the laser operation was most stable when its output was near 10 W. Consequently a shorter exposure time was used, compared to literature reports with lower laser powers. The exposure time was 27 ms, with 5 ms each of rising and falling time, and 7 iterations of the writing were performed. The LPG was 45 periods long with a period of 204.5 μm . Transmission spectra were recorded when the fiber

Table 5.3: Default parameters used for writing LPGs, based on advice from a fellow researcher.

power	exposure	rise/fall	period	length	iterations	fiber	mass
10 W	27 ms	5 ms	204.5 μm	45 periods	7	SMF-28e	6.7 g

was loose in air and when it was pulled taut and exposed to both air and 70% ethanol. It was initially thought that this LPG was promising due to differences in the loose and taut spectra, especially in the peak near 1450 nm (Fig. 5.10). However, these measurements were subject to significant instability. The spectrum for each set of conditions was recorded again after a 60 s interval and showed significant changes, even when the fiber was not moved. This time-varying behavior was not attributed to the light source or the OSA, because both components were used without similar problems during biosensor assays performed amidst the CO₂ fabrication studies. Later attempts to establish a baseline in the bulk fiber exhibited similar instability. It was concluded that imperfect connections were causing instability in the spectra. These connection issues were not apparent in the biosensor work because once a good cleave was obtained on the TAP-LPG the ends were installed into well-functioning fiber connectors and kept covered to protect them from damage. The well-cleaved fiber ends could

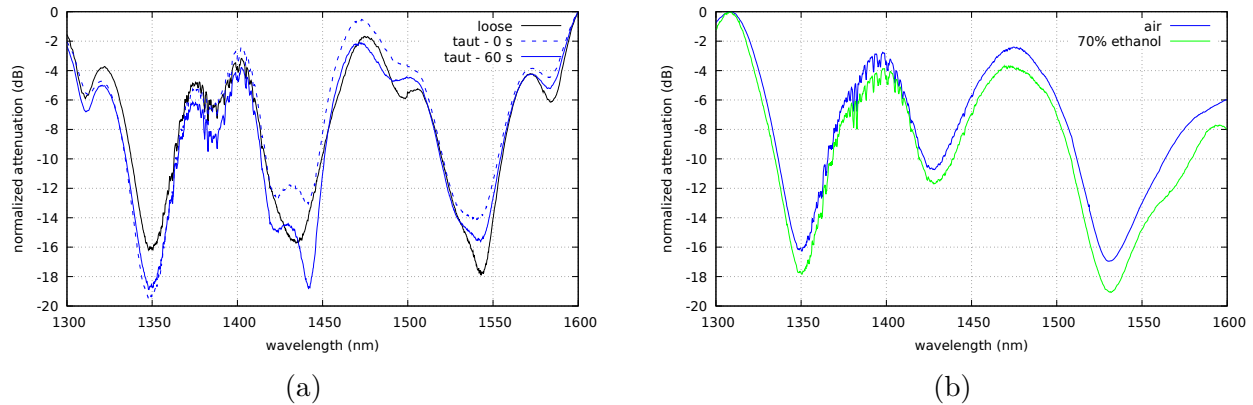


Figure 5.10: Transmission spectra of the first fabricated LPG comparing its behaviors under different tensions (a) and surrounding refractive indexes (b). Apparent changes in the spectra were later attributed to poor stability due to low quality cleaves, rather than mode coupling due to the grating.

be preserved in this way for months. In contrast, when testing fibers for the CO₂ fabrication work, fibers might be cleaved and inserted into fiber connectors multiple times in a single day, leading to variable connection qualities. Additionally, the fiber connectors were of varying quality. Several were functional but were partially clogged or had poorly aligned mechanical components, and were used nonetheless in order to not disturb the better connectors already installed on the biosensor. These damaged fiber connectors may have exerted pressures on the fiber ends that would have caused changes in the transmission spectra.

Attempts were made to fabricate additional fibers using the same parameters, including two other fibers made on the same day as the one presented in Figure 5.10. Many of these procedures failed before they were completed due to software errors. The incomplete gratings were discarded, as the grating length and the number of iterations could not be determined. Those that were completed successfully failed to exhibit grating behavior. Spectra for a grating fabricated with the same parameters about a month after the one presented in Figure 5.10 are shown in Figure 5.11. The spectrum remained essentially unchanged despite changes in tension and external refractive index, to the degree that the three spectra are

almost completely overlapped.

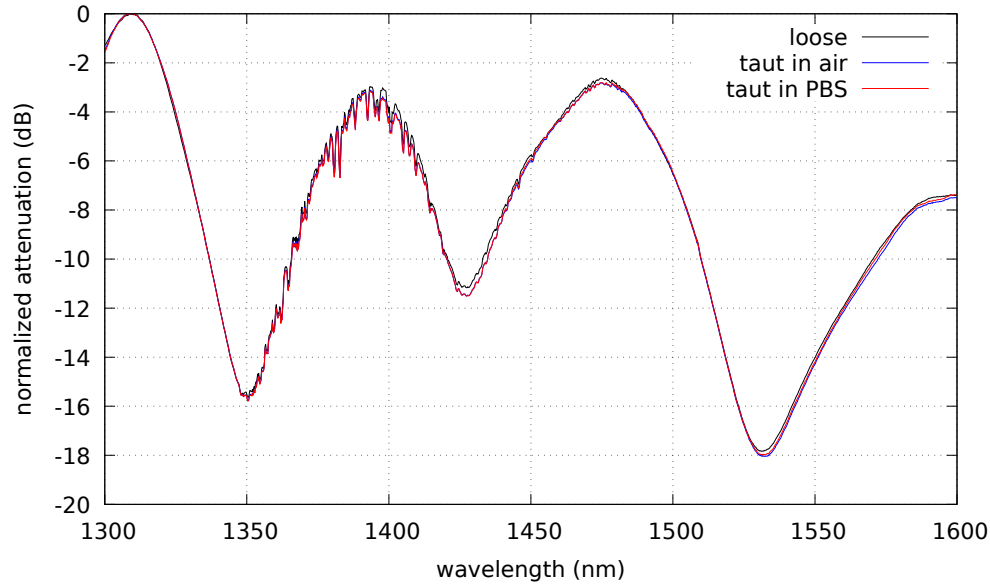


Figure 5.11: Transmission spectra for an LPG fabricated using the recommended parameters, fabricated about a month after the initial attempts. This fiber exhibited no sensitivity to tension or surrounding refractive index, which further supports the hypothesis that the apparent response of the first fiber was an error due to poor connections at the fiber ends.

5.6.2 LPG fabrication with altered parameters

While previous work using the same fabrication setup was successful using the parameters presented in Table 5.3, the same settings failed to result in LPGs in this work. Minor deviations from the suggested settings were therefore investigated to try to find a grating period or a writing power that would produce LPGs.

Different grating periods

Several sets of LPGs were fabricated using different grating periods in the vicinity of $204.5 \mu\text{m}$, which was the recommended period. First, four fibers were made using the standard

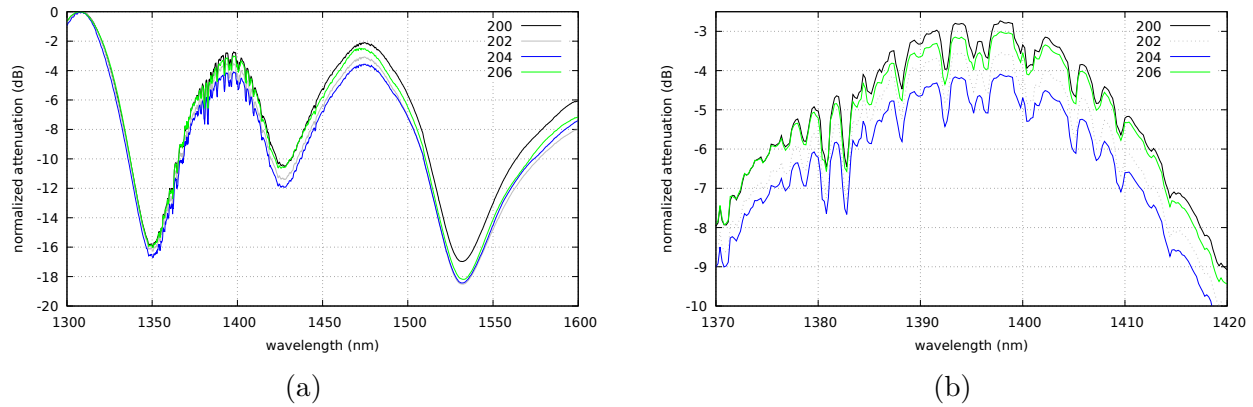


Figure 5.12: Transmission spectra of LPGs fabricated with grating periods from 200 to 206 μm (a), with a cutout of the peak near 1400 nm (b). The spectra for all four fibers were recorded with the fiber held taut in air. No resonant attenuation was observed.

exposure conditions presented in Table 5.3, but with periods of 200, 202, 204, and 206 μm . In order to accommodate higher throughput these gratings were shorter than the earlier LPGs, consisting of 30 periods rather than 45. When coupling occurs, having fewer grating periods will result in weaker coupling and a broader, shallower attenuation peak. At this point the focus of the work was only to find the presence of LPG resonance. Once a set of parameters which would generate an LPG were found they could be fine-tuned to improve the peak quality, so shorter gratings were acceptable in the search for any resonant attenuations. As shown in Figure 5.12, all four gratings produced basically identical transmission spectra. On close inspection, the fine details on the 1400 nm peak, which look as though they could be disguising some variation, are also the same in all four cases. The spectra were insensitive to tension and external refractive index. It was concluded that the procedure used to modulate these fibers failed to produce LPGs. Another set of fibers was fabricated using slightly longer grating periods. Periods from 205.5 to 208 μm were tested, while all other parameters were restored to the default values used in Section 5.6.1. Another set was made with periods from 204 to 205 μm , this time using SMF-28r as the base fiber. The resulting transmission spectra while taut in air are shown in Figure 5.13. The spectra all appear similar and no new peaks

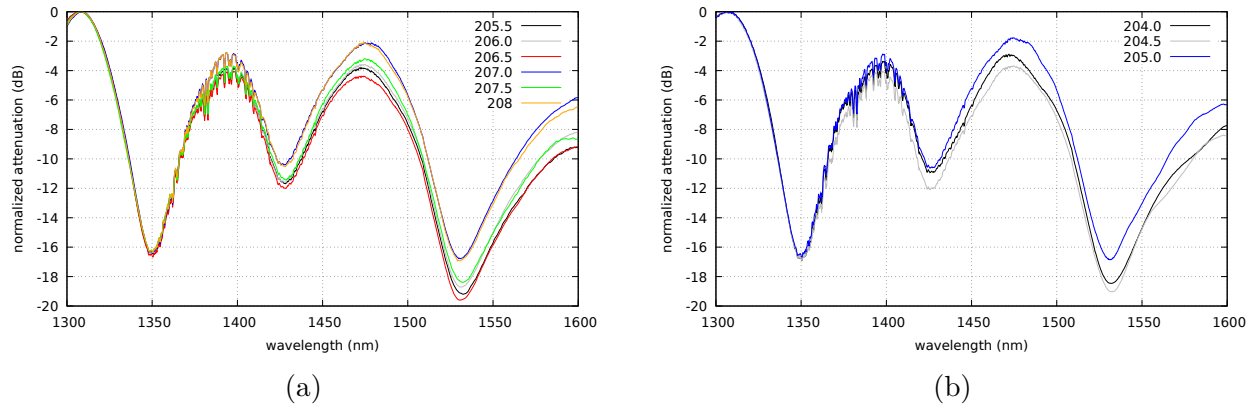


Figure 5.13: Transmission spectra of LPGs fabricated with standard settings and grating periods from 205.5 to 208 μm in SMF-28e (a), or with periods of 204 to 205 μm in SMF-28r. All spectra recorded with the fiber held taut in air. No resonant attenuation was observed.

appeared, so it was concluded that the procedure was unsuccessful. This was confirmed by the failure of the fibers to respond to changes in tension or surrounding refractive index.

Gratings with different writing powers

It was initially recommended that gratings be written with the laser operating at about 10 W, due to reports that this particular laser unit had better stability at that power. However, none of the gratings fabricated at 10 W exhibited an LPG resonant peak. Additionally, there was no visible evidence that the fiber had been modified, either with the naked eye or under an optical microscope. Higher powers were therefore investigated as a means of increasing the refractive index modulation and producing a grating. A set of gratings were written using powers ranging from 10.1 to 11 W in 0.1 W steps. All of the LPGs were written into SMF-28R fiber. Besides the writing power and the fiber type, all other parameters were identical to those in Table 5.3. Again, all of the spectra appeared similar and none exhibited peaks that were sensitive to tension or external refractive index (Fig. 5.14). The 11 W fiber was also observed under an optical microscope to look for signs of physical deformations. The

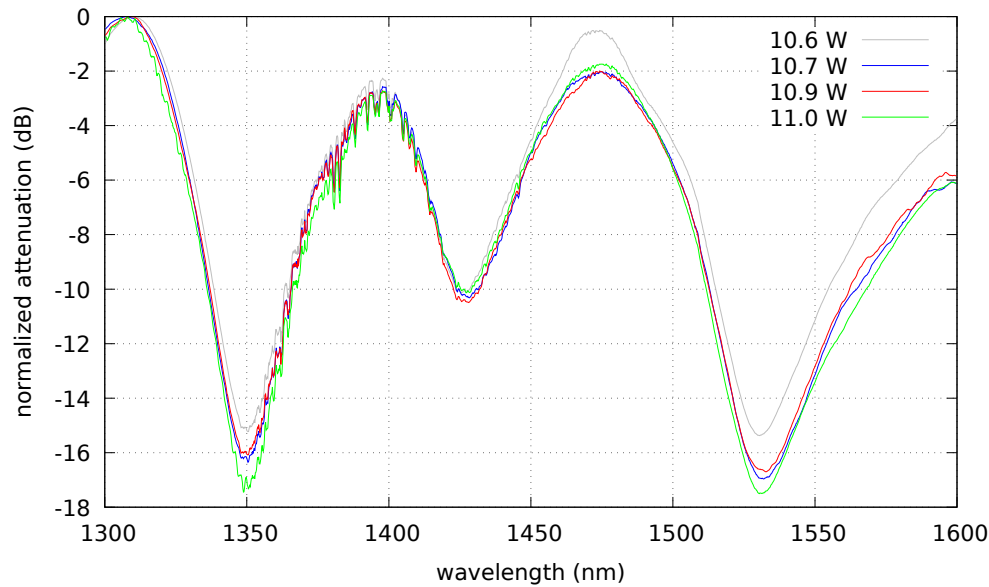


Figure 5.14: Selected transmission spectra for an LPGs fabricated at different powers between 10 and 11 W. No significant departures from the bulk spectrum was observed.

fiber appeared unaltered, which led to concerns that the laser may not have been affecting the fiber at all. These concerns were addressed by exposing fibers to even higher powers until visible tapers could be observed (Section 5.6.3).

While reports of LPGs fabricated by CO₂ laser are fairly common, fewer groups have reported TAP-LPGs [6, 209, 210]. Of these, only the group of Xinwei Lan provided sufficient experimental details to allow us to approximate their procedure [6, 211]. They presented TAP-LPGs with dynamic ranges of about -10 to -15 dB, which had a linear response to refractive indexes from 1.33 to 1.37 and separately from 1.41 to 1.42. These LPGs were fabricated in SMF-28e using 100 ms exposures of 6.8 W irradiation to form a 4.5 cm long grating with a period around 230 μm . The spot size was unspecified, and they appear to have written their grating without the application of a prestrain. Using our setup, an LPG was fabricated using the same laser power, exposure time, and grating period (228 μm) and length. The usual elliptical spot and 6.7 g weight were used. As seen in Figure 5.15, the

grating was completely insensitive to changes in tension or surrounding refractive index. It is possible that differences in laser power density or prestrain contributed to this failure to match the results found in the literature. However, because none of the strategies attempted produced even non-TAP or weakly coupled LPGs, it appears that there may have been an inherent problem with the setup.

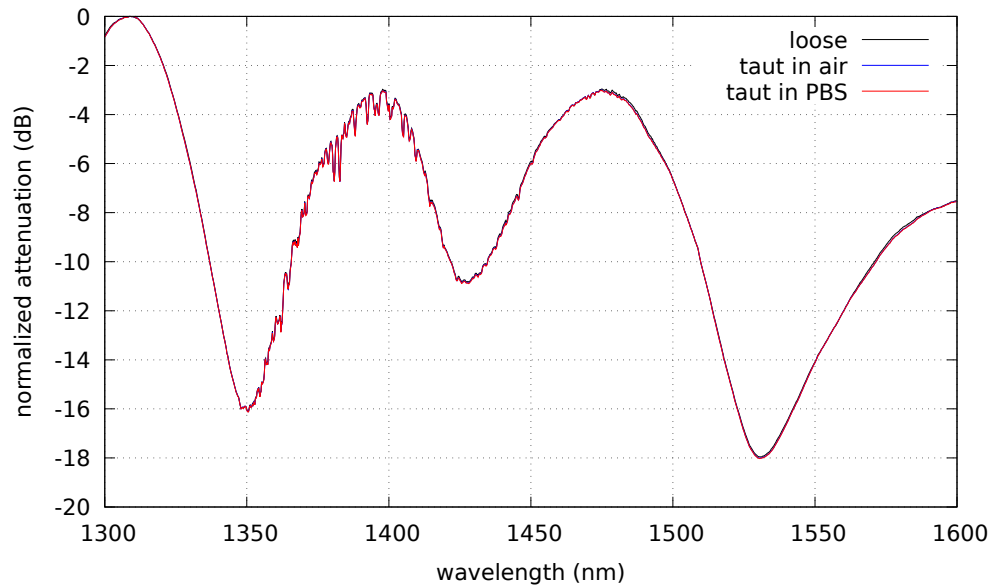


Figure 5.15: Transmission spectra for an LPG written using 6.8 W, 100 ms, and a period of $228.3 \mu\text{m}$, based on parameters from literature [6]. The fiber was insensitive to changes in tension and external refractive index.

5.6.3 Study of physical deformations at high writing powers and longer exposure times

Because none of the previous attempts provided any obvious indication that the fiber had been altered, a series of experiments were performed using higher laser powers than advised to deliberately produce visible deformations in the fiber. This was done to explore the upper limits of the power the fiber could withstand, and to determine if the writing powers used

previously were likely to be sufficient.

The first attempt kept the laser power at 10 W, but varied the energy delivered to the fiber by using longer exposures or additional writing iterations. Observed under an optical microscope, there were no visible changes in the fiber when increasing the exposure time from 27 ms to 54 ms or when increasing the iterations of the writing procedure from 7 to 10. When the modifications were combined to do 10 iterations of 54 ms exposures, thin vertical lines were observed perpendicular to the fiber axis and corresponding to the grating period, although no tapering appeared to have occurred. No such lines were present when a grating fabricated with the settings in Table 5.3 was observed at the same magnifications.

Another fiber was exposed to higher laser powers in an attempt to deliberately break the fiber. In this case a 17 g weight was used, and a single writing iteration of 100 ms exposures was performed. After every five grating periods the power was increased by 0.5 W. Slight deformations occurred below 11 W, but were intermittent and did not appear for every grating period. At 11 W the deformations became more pronounced, and the fiber clearly began to taper. At 11.5 W the first 3 periods were strongly tapered, while the next 2 were noticeably less affected. The first 2 periods at 12 W were similarly unaffected, the third was very long and thin, and last two periods had intermediate tapering. Teardrop-shaped tapers were visible even without the aid of the microscope. The fiber broke while exposing the fourth period at 12.5 W. The three periods before the break were tapered irregularly, as was seen for the previous regions exposed at 11-12 W. These irregularities were attributed to variations in the laser power during operation. Specifications for the Synrad 48-2 indicate that it may have a power fluctuation of plus or minus 5 percent. It was also suspected that the particular laser used in this setup was prone to overheating, possibly due to its age or its location in a small room with poor circulation, which may have decreased its stability beyond the ideal specifications [201].

Next, a fiber was prepared to investigate the effects of high power exposures when performing repeated writings with a smaller prestrain, making the conditions more similar to those in Table 5.3. The fiber was irradiated in 100 ms exposures with 7 iterations while it was strained by a 6.7 g mass. Powers from 11.5 to 14 W were tested with ten 200 μm periods at each power step. Images of the fiber are presented in Figure 5.16. The region written

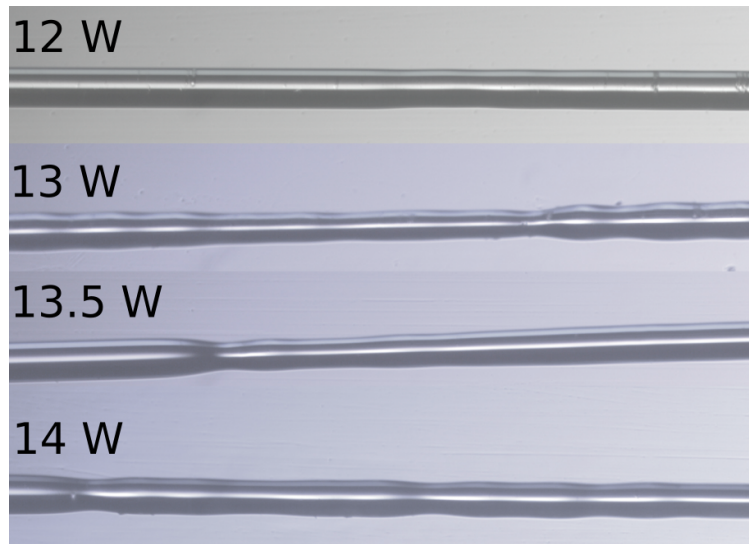


Figure 5.16: Images of a fiber written with 100 ms exposures, 7 iterations, 6.7 g prestrain mass, and 10 periods at each power. These powers were sufficient to taper the fiber. The physical deformations of the fiber are irregular, which may indicate that variations in the refractive index modulation from period to period prevented successful grating fabrication.

with 12 W showed slight deformations. The tapering was much more significant at 13 W, and it is almost possible to identify each individual period. However, it is clear that the tapers are irregular. For the three periods on the left and right side of the image the fiber returns to its original diameter between exposures, while in the center of the image there is an extended thin zone where the individual modulations are less apparent. The irregularity of the tapering is also apparent in the 13.5 W and 14 W regions. If the gratings written at lower powers had similar levels of irregularity they would have reduced periodicity, which may explain why they failed to show mode coupling. The poor quality of the gratings was

attributed to poor stability of the laser power. If the exposure conditions were identical at each writing location, and thermal effects allowed to dissipate between each exposure, a uniform periodicity should have been observed. If the wait time between periods was insufficient to allow thermal effects in the prior spot to cool, the first few periods should have always appeared different than later periods, resulting in a noticeable pattern. Neither of these cases were observed, and instead the modulation at each position appears to be randomized. The poor quality of the gratings is surprising, as it was thought that fluctuations in the laser power would be accounted for by the procedure of rewriting the grating multiple times. It is possible that tapers formed on earlier iterations lengthened the fiber, resulting in an offset between the prior writing position and later locations. For a stable laser output this would have resulted in wider modulated regions than intended, but could still have produced a uniform grating as each period would be widened by the same amount. For the fluctuating power, the offsets would have varied in severity and reduced the periodicity of the grating. This may be responsible for the regions which appear to be smoothly thinned out for a few periods rather than more sharply tapered, as in the central portion of the 13 W region of the fiber.

5.6.4 Other factors contributing to fabrication failure

The failure to produce LPGs with the CO₂ laser setup was attributed primarily to laser power fluctuations. As described in the previous section, these fluctuations became apparent when the laser power was increased sufficiently to produce visible tapers in the fiber. It is possible that vibrations in the fiber may have also contributed to the irregularity of the gratings. The prestrain mass was attached to the end of the fiber, and was thus free to swing in response to the movement of the translation stage. If the hanging mass was not stationary when the fiber was exposed, this would caused a time-varying tension in the fiber. Fibers subjected

to higher levels of strain are known to be more susceptible to refractive index modulation. Therefore, variable prestrain due to movement of the hanging mass could have contributed to the failure to obtain periodic modulations.

Software bugs were another major challenge with this project. The most prominent issues were related to the motion controller, which often interrupted the fabrication due to hardware communication timeout errors. This occurred in about half of fabrication attempts, significantly inhibiting throughput. The errors appeared to have been related to incompatibilities of the initialization behavior of the equipment and the Matlab program. On startup, the motion controller set the current position of the translation stage to zero, regardless of where it was physically located. When the Matlab program was launched, it would move the stage backwards slightly such that the new position read by the motion controller was -0.1 mm. The stage was then manually controlled to position the prepared fiber under the laser spot. If the system happened to encounter a negative position during the writing process errors would occur that aborted the writing in the middle of the grating, resulting in gratings of unknown length. A more rigorous study of CO₂ fabrication would require modifications to the software to make it more robust.

5.7 Summary of TAP-LPG biosensor results

Overall, this project demonstrated that TAP-LPG biosensors could be used for identifying the presence of *Brucella*, but that the effectiveness of such a sensor is heavily dependent on having a TAP-LPG with sufficient dynamic range. Prior work by this group using a TAP-LPG with a dynamic range of -27 dB to detect *H. somni* resulted in a 9.4% change in transmission due to exposure to 100 cells of *H. somni*, but only a 1.6% change due to exposure to 50,000 cells of a negative control. In contrast, the largest transmission changes

observed using the -10 dB TAP-LPG available during the *Brucella* assays were around 6%, and occurred after exposure to much higher bacterial concentrations. Attempts to optimize the functionalization of the sensor surface showed that elevated concentrations of streptavidin and biotinylated probe failed to improve the sensor's performance. In one set of tests using *B. abortus* as the positive control and *B. melitensis* as the negative control, mean signals of $2.2 \pm 0.7\%$ for positive samples and $0.7 \pm 1.3\%$ for negative samples were obtained, suggesting a statistically weak ability to distinguish *Brucella* species. In another set of assays attempting to distinguish between *Brucella* species, both the negative and positive controls caused a change in transmission of about -0.6%. It was found that increasing the bacterial concentration from 10^4 to 10^7 cfu/ml had no effect on the sensor's behavior, showing that the sensor could not function quantitatively. Better results were obtained when distinguishing between *Brucella* and other species. In this case, the change in transmission was $2.8 \pm 0.9\%$ for positive controls and $0.6 \pm 1.0\%$ for negative controls. Slightly higher signals were observed when using samples taken from the spleens and livers of mice, possibly due to higher bacterial concentrations in these samples. The mean transmission change was $6.0 \pm 1.4\%$ for *Brucella*-infected mice but only $0.5 \pm 2.0\%$ for mice injected with saline. In all cases the signals from positive and negative controls were fairly close together, sometimes with overlapping standard deviations.

Because the dynamic range of the available TAP-LPGs was a significant limitation for this project, attempts were made to fabricate new TAP-LPGs using the CO₂ laser technique. No changes in the transmission spectra were observed after writing the gratings into the fibers, despite using parameters reported to be effective in prior work on the same setup and in the literature. After observing irregular physical deformations at different grating periods in LPGs written at higher powers, it was concluded that fluctuations in the CO₂ laser were preventing sufficient periodicity to develop in order for coupling between the core and

cladding modes to occur.

Chapter 6

Results of plasmonic enhancement of ISAM film SHG by silver nanoprisms

This chapter presents our results of SHG enhancement by silver nanoprisms. First, Section 6.1 presents prior SHG enhancement of ISAM films by this group, focusing on nanosphere lithography experiments performed by Dr. Kai Chen and colloidal gold nanorods studied by Dr. Jeong-Ah Lee. The remaining sections present our novel work with colloidal silver nanoprisms synthesized by Assad Ullah Khan. First, our results are discussed for nanoparticles deposited by immersion while stationary (Section 6.2) and using the dipper machine (Section 6.3), including SHG results and various attempts to improve deposition density. Next, our results obtained by dropcasting concentrated nanoprisms onto ISAM films are discussed in Section 6.4. Finally, our attempts to improve SHG enhancement by deposited prisms are presented in Section 6.5. The results detailed in the preceding sections are summarized in Section 6.6.

6.1 Prior SHG enhancement by this group

This group has previously investigated the enhancement of SHG from PAH/PCBS ISAM films by plasmonic nanoparticles, including silver nanotriangles and gold nanorods, on the surface of nonlinear films. The results of those studies are summarized in this section.

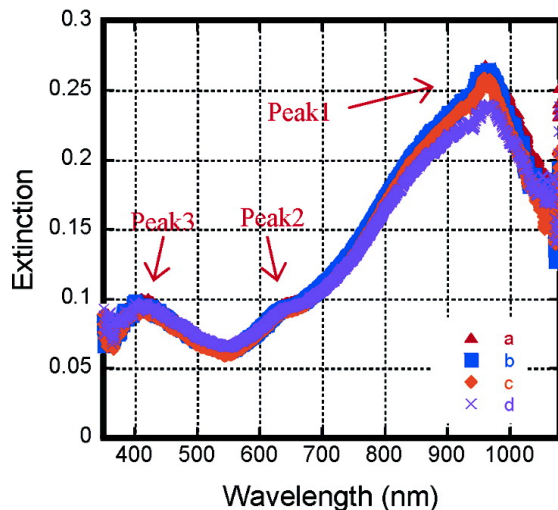


Figure 6.1: Extinction results from the nanosphere lithography project [7]. The in-plane dipole resonance caused an extinction of 0.25 (a) for 50 nm thick nanotriangles, when observed at four different locations on the same sample (traces a-d). Reprinted with permission from *Nano Letters* 7:254-258 [7]. Copyright 2007 American Chemical Society.

6.1.1 Silver nanoprisms applied by nanosphere lithography

One prior project by this group used nanosphere lithography to create a pattern of silver nanotriangles on one side of a PAH/PCBS ISAM-coated microscope slide. As described in Section 3.2.2, nanosphere lithography is performed by applying a thin layer of silver onto a close-packed monolayer of uniform nanospheres. When the nanospheres are lifted off, an ordered array of nanotriangles is left behind due to the silver that was deposited in the interstices between the spheres. In a former project, polystyrene spheres with a diameter of 720 nm were used as a template to make an array of triangles with an edge length of about 200 nm, and a 50 nm thick layer of silver was applied. For the resulting particles the in-plane dipole resonance had an extinction of about 0.25 at a wavelength of about 950 nm (Fig. 6.1). Increasing the thickness of the nanotriangles decreased their aspect ratio, and the in-plane dipole resonance was blueshifted as expected [7, 152].

For another sample, SHG was measured for an array of 72 nm thick silver nanoprisms

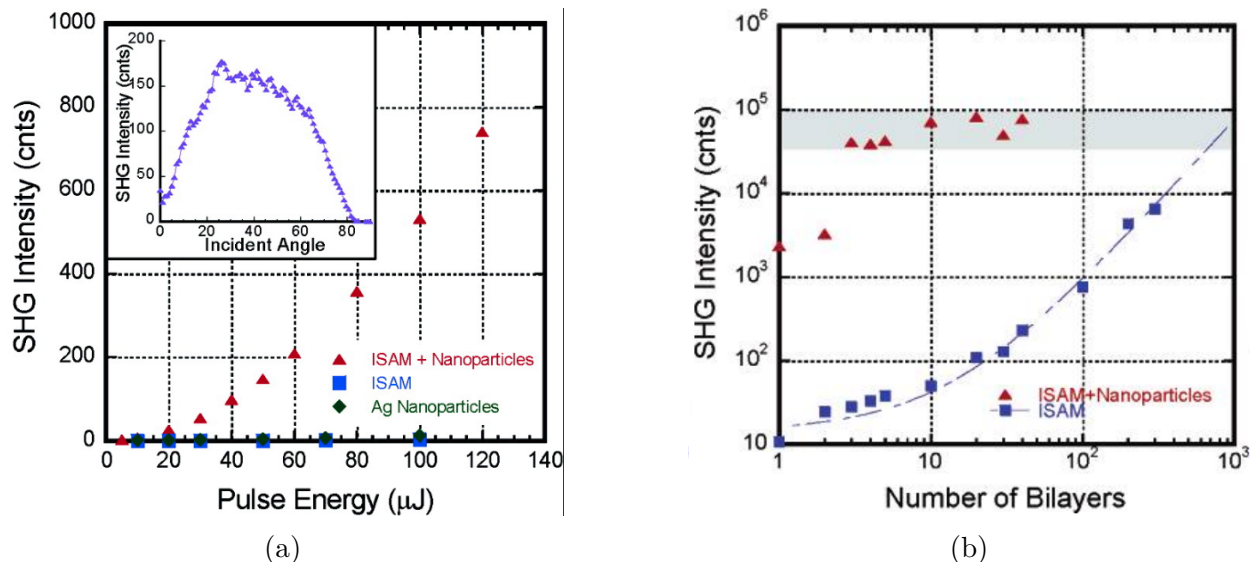


Figure 6.2: SHG results from the nanosphere lithography project [7]. For 72 nm thick nanotriangles on 3 bilayers of PAH/PCBS, the SHG intensity (a) was much larger for the ISAM film with nanoparticles than for a bare 40 bilayer film, or for nanotriangles in the absence of PCBS. The SHG had a quadratic relationship with the power of the fundamental beam, as expected. When increasing the numbers of bilayers (b) the SHG intensity of the bare film increases quadratically, but the intensity for films with nanoparticles saturates as the film thickness exceeds the penetration depth of the plasmonic field enhancements. Reprinted with permission from *Nano Letters* 7:254-258 [7]. Copyright 2007 American Chemical Society.

on a three bilayer PAH/PCBS film. SHG was measured from a region of the film without the ISAMs, and from a region where there were nanotriangles on the ISAMs. For the nanoparticle-ISAM films, the bulk of the signal comes from the side of the slide with the nanoparticles amplifying the SHG. Prior to comparing the two regions, the ISAM-only signal is divided by four to account for this. This sample exhibited a 1600 times enhancement to SHG, corresponding to a 40 times increase in $\chi^{(2)}$ (Fig. 6.2b). The nanoparticles on a 40 bilayer film showed an enhancement of 200 times. For larger numbers of bilayers, the SHG intensity from the bare film increases quadratically, while the SHG intensity from films with silver nanotriangles remains roughly constant (Fig. 6.2c). The SHG signal from the hybrid film did not continue to increase because the plasmonic field enhancements only extend a few nanometers from the nanoparticle. Therefore, the largest SHG enhancements are observed

when the ISAM films do not extend beyond the reach of the plasmonic fields. Because the silver nanotriangles are similar in composition and dimensions to the colloidal silver nanoprisms reported in this work, these prior results were promising.

6.1.2 Colloidal gold nanorods

Like silver nanoprisms, gold nanorods can exhibit strong plasmonic field enhancements with LSPRs at long wavelengths. For nanorods, these enhancements are strongest at the tips of the rod. Their extinction spectra feature a weak transverse resonance in the visible range, and a strong longitudinal mode in the NIR part of the spectrum. The position of the longitudinal extinction depends heavily on the aspect ratio of the nanorods. The aspect ratio can be controlled by varying reactant concentrations in well-reported seed-mediated synthesis methods [212, 213]. In prior work by our group, gold nanorods with a longitudinal resonance near 1064 nm were synthesized and deposited by immersion onto PAH/PCBS ISAM films [5]. Initial tests used poly(sodium-4-styrenesulfonate) (PSS) -coated gold nanorods supplied by the Murphy group at UIUC. The PSS coating was applied to give the nanoparticles a negative surface charge and stabilize the solution. Very low deposition density was observed after immersion for 16 hours, and the SHG intensity was actually slightly lower for the hybrid film than for the bare film. It was proposed that the poor enhancement observed in these tests might be because relatively little of the plasmonic field enhancement was penetrating the ISAM film. The nanorods were about 10 nm in diameter, compared to the ISAM films which were only about 4 nm. To account for this, an additional three bilayers of PAH/PCBS were applied on top of the gold nanorods. This improved the SHG enhancement by about a factor of two. Another approach to improving the SHG enhancement was to wrap the nanoparticles themselves in NLO active ISAM layers. Gold nanorods were functionalized with 0, 1, 2, and 3 bilayers of PAH/PCBS deposited onto 3 bilayers of PAH/PCBS. The

functionalized nanoparticles showed SHG enhancements of about 1/2, 100, 65, and 8 times, respectively. Another important observation from this project was that the nanoparticles were easily damaged due to the intensity of the fundamental beam. At higher pump powers, the nanorods took on a dogbone shape, as a first step towards becoming spherical. It was determined that the fluence threshold for damage was $0.07 \mu\text{J}/\text{cm}^2$. Therefore, it was necessary to measure the nanorod-enhanced SHG at a lower pump power than was used for measuring the undecorated films.

6.2 Colloidal silver nanoparticles applied by stationary immersion

The silver nanoprisms used in this project were prepared by Dr. Liu's group using a seed-mediated colloidal synthesis method [4, 36]. Initial attempts to apply nanoprisms that were large enough to have the correct LSPR wavelength (1064 nm) proved unsuccessful due to large nanoprism size and low concentration, as discussed below. Further studies were done using smaller nanoprisms in conjunction with strategies to redshift or broaden the LSPR peak.

6.2.1 Early results using 1140 nm peak wavelength particles

Initial attempts to plasmonically enhance SHG with colloidal silver nanoprisms used particles with their LSPR peak at 1140 nm while suspended in water. As can be seen in Figure 6.3, the sample consisted of a large fraction of triangles with edge lengths of 200-250 nm, with some imperfect hexagonal shapes. The solution appeared slightly iridescent but was mostly clear and colorless due to the low nanoparticle concentration and infrared extinc-

tion peak. Two slides with 3.5 bilayers PAH/PCBS were immersed in about 15 mL of the solution in a small beaker. A second beaker was set up with two slides with 3.5 bilayers PAH/PSS. Both immersion setups were sealed with Parafilm and protected from light by foil-wrapped containers. The slides were immersed for 2 days. Because the LSPR blueshifts

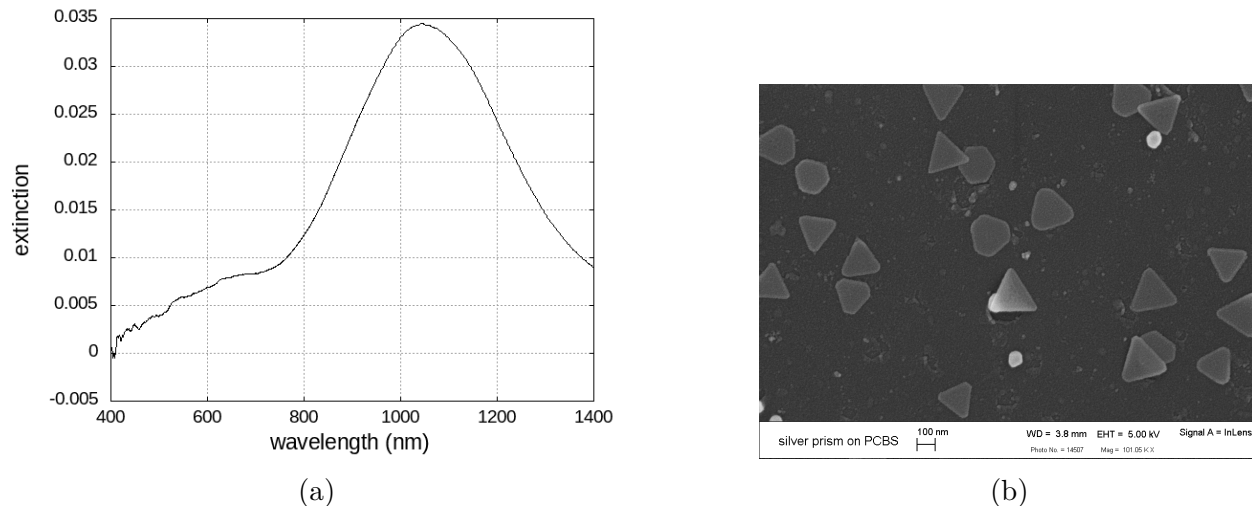


Figure 6.3: Deposition results for initial attempts to deposit 1140 nm wavelength particles onto 3.5 bilayers PAH/PCBS by immersion. The extinction (a) is low, and an SEM image (b) reveals that the nanoprisms were sparsely distributed.

when nanoparticles are deposited on a surface, the final absorption peak was very close to the 1064 nm wavelength of the fundamental beam. As can be seen in Figure 6.3, the peak extinction occurred at 1043 nm. This is very close to the wavelength of the fundamental beam and should be ideal for inducing plasmonic enhancement. However, it is also apparent from the SEM image and from the extinction that the nanoprisms were adsorbed onto the ISAM film at a very low density. This was clear from the visible appearance of the slide, which showed only a very slight white film where the nanoparticles were applied. The peak extinction was only 0.03. The poor deposition density was attributed to the low concentration of the nanoprisms in solution, which is a consequence of their size. The nanoparticles had to be quite large (>200 nm) in order to have an LSPR that would match the wavelength of the fundamental beam. However, for the synthesis procedure used, the particle

concentration decreases with increasing nanoparticle size.

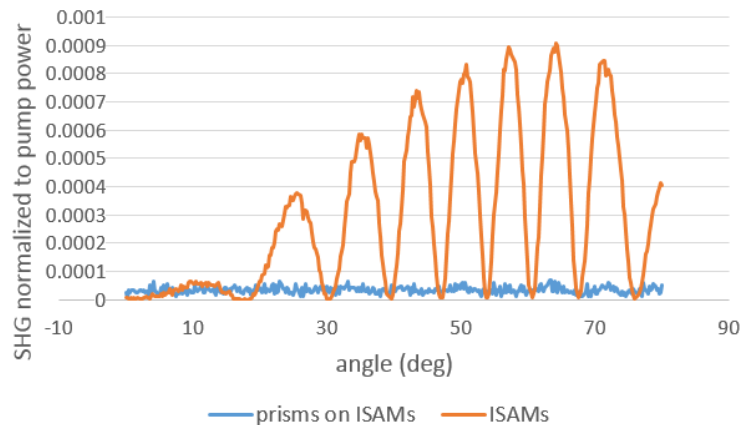


Figure 6.4: SHG results for initial attempts to deposit 1140 nm wavelength particles onto 3.5 bilayers PAH/PCBS by immersion. Due to low prism density, essentially no SHG was observed from the prism decorated film at the low pump power required to avoid damage to the nanoprisms.

SHG results for this sample are presented in Figure 6.4. The pump power for the prism portion of the slide was $25 \mu\text{J}$, and the pump power for the no-prism portion was $700 \mu\text{J}$. Essentially zero SHG was detected from the prism portion of the slide. While SHG enhancement may have occurred locally near the individual prisms, the effect was insufficient to overcome the noise. Therefore, subsequent efforts focused on attempts to increase the density at which the 1140 nm wavelength nanoprisms attached to the ISAM layers.

A repeat attempt to apply the 1140 nm particles by immersion was performed several months after the initial immersion setup. At this point, the nanoparticles had been diluted by a factor of two with ultrapure water, in order to accommodate attempts with the dipper machine which required larger beaker sizes. The decision to dilute was also based on previous gold nanorod results that suggested that lower concentrations can sometimes improve deposition by limiting “jamming” [5]. A glass slide was cleaned by wiping with isopropyl alcohol, then 3.5 bilayers PAH/PCBS were applied and the sample was immersed in the 1140 nm nanoprism solution for a period of 2 days. While the diluted solution failed to deposit

well onto prior samples, some of which are discussed elsewhere (Sections 6.2.3, 6.3.1), for reasons that remain unclear, this deposition was surprisingly successful, as can be seen in Figure 6.5. The sample exhibited a peak extinction of 0.2 near 1043 nm. This was quite similar to the extinction observed in the nanosphere lithography project. However, an important difference in this case is that the prisms are on both sides of the slide, while the nanotriangles produced by nanosphere lithography are on only one side. It can be concluded that the prisms were less dense for this immersion test than they were for the nanosphere lithography experiments. SHG was measured on this slide using 40 μJ as the pump power for the prism portion. An enhancement of 2.3 times was observed.

6.2.2 Attempts to improve deposition

A variety of strategies were investigated to improve deposition. Smaller prisms with an LSPR near 600 nm were used for testing purposes, as they are easier to produce in large quantities than larger prisms. The resulting extinction spectra are presented in Figure 6.6. The techniques employed to try to enhance deposition included the following:

- The anion in the underlying 3.5 bilayer ISAM film was changed from PCBS to PAA to investigate whether PCBS had a role in limiting deposition. Although the anionic layers should be screened by the top PAH layer and should not have a major role in determining deposition success, much denser nanoprism coverage was observed for PAA than for PCBS. PAA has a much smaller side-chain than PCBS, so the underlying ISAM layers may have been thinner or smoother than with PCBS. The nanoprism density was sufficient to significantly broaden the LSPR peak due to interparticle interactions. Peak-broadening was used as a later strategy to try to get SHG enhancement from nanoprisms whose LSPR peak was at a shorter wavelength than the fundamental

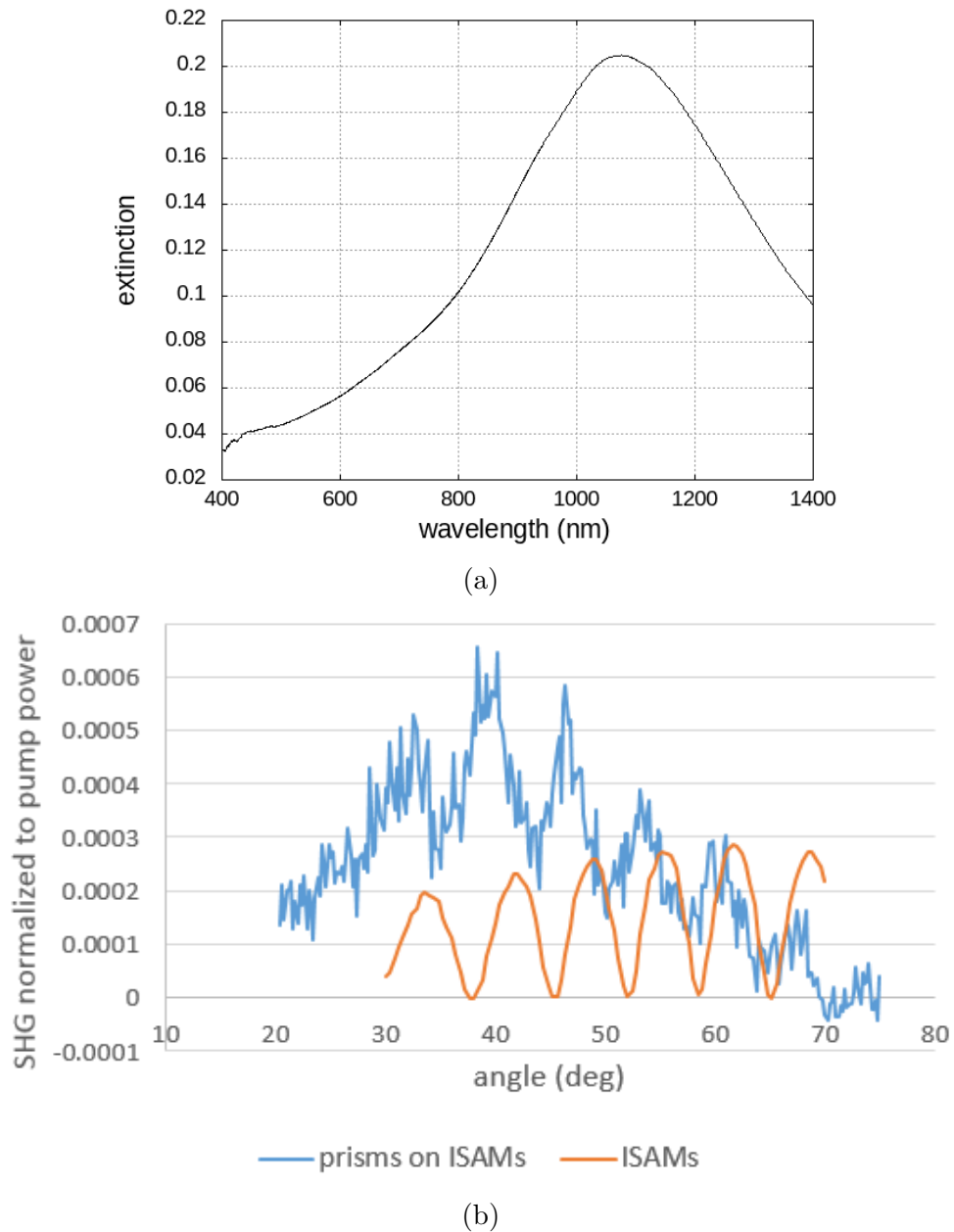


Figure 6.5: Results from a later attempt to deposit 1140 nm wavelength nanoprisms onto 3.5 bilayers PAH/PCBS by immersion, after diluting the nanoprisms. For unknown reasons, higher extinction (a) was achieved in this case than in previous attempts with the same solution. The SHG enhancement (b) compared to the bare film was 2.3 times.

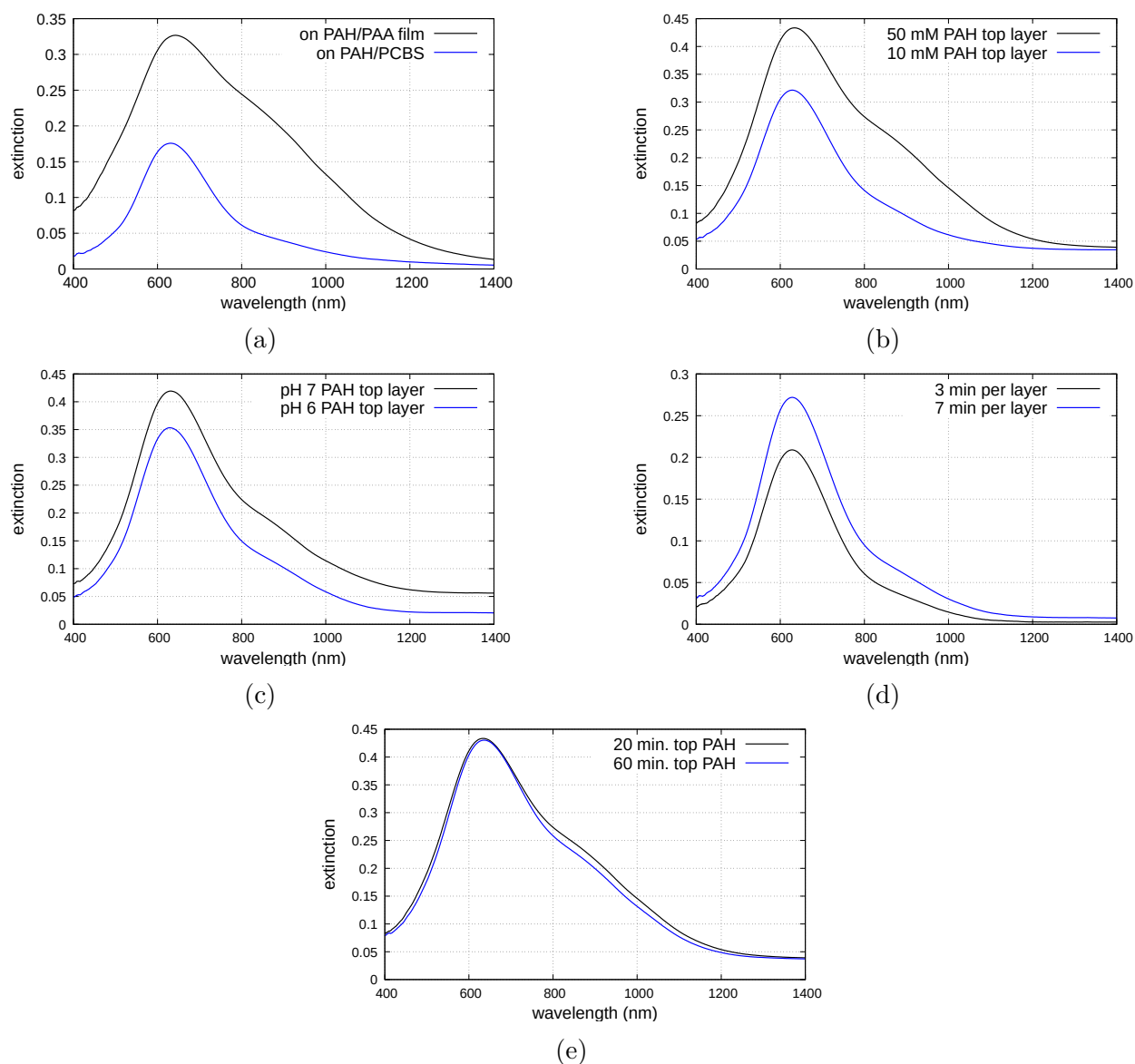


Figure 6.6: Attempts to improve nanoparticle deposition by varying the underlying ISAM layers. Replacing PCBS with PAA (a) resulted in significant improvement. The concentration (b) of the final PAH layer was increased, which also improved the deposition density. Smaller changes were observed when varying the pH (c) of the final PAH layer and when increasing the dip duration (d) for each polymer layer in the underlying film. Using longer soak times (e) for the final PAH layer produced almost no change in extinction.

beam.

- The concentration of the final PAH layer was increased from 10 mM to 50 mM. While the lower concentration PAH should have been sufficient to form a monolayer on the top surface, a nontrivial improvement was observed when the PAH concentration was increased.
- The pH of the final PAH layer was lowered slightly from 7 to 6 to increase its protonation. Because the nanoprisms were attracted to the top PAH layer of the ISAM film by their negative surface charge, it was hoped that making a stronger positive charge on the surface would improve deposition density. A small improvement in extinction was observed.
- The procedure for applying the underlying ISAM layers was altered to lengthen the time spent in each polymer from 3 minutes to 7 minutes. This was done to ensure that each additional layer had the chance to reach saturation. A small improvement was observed with this change.
- The length of time the slide was immersed in the final PAH layer was increased. The base time was 20 minutes, while the 50 mM time was extended to 1 hour and the 10 mM time was extended to 3 hours. The 50 mM samples showed essentially no difference, indicating that the polymer deposition had saturated within 20 minutes. The 10 mM samples showed a slight improvement due to extending the final PAH time.

Of the strategies tested to improve deposition with the immersion technique, the most effective was to replace the PCBS with PAA. This was consistent with early results observed when depositing the 1140 nm prisms onto PAH/PSS films, which had about 2-3 times higher

extinction than the prisms on PAH/PCBS films. While this provided some information regarding the poor attachment of the molecules, it did not constitute a useful strategy because PCBS, as the NLO-active polymer, was a vital component of our SHG experiments. Using a higher concentration of PAH for the top layer was also effective and was employed for later tests. Dip time and pH had only small effects and were thus left unchanged from their default values.

6.2.3 Attempts with long immersions (>1 week)

Initially, immersions were performed for 1-3 days on the assumption that after this length of time the deposition would have reached saturation. Because this strategy was failing to produce sufficient deposition onto PAH/PCBS films, longer immersions were attempted to try to increase the nanoprism density.

In an initial test, the 2x diluted 1140 nm prisms were applied to an ISAM-coated slide for 12 days. This was done prior to the surprisingly good deposition done with this solution presented above in Figure 6.5, so the nanoprisms were not yet depleted at this point. The resulting extinction was essentially zero. As the preparation of this sample was similar to that used for the later, more successful sample, it is unknown why the nanoparticles failed to absorb in this case. Due to poor deposition, SHG was not measured for this sample. Further attempts at immersion abandoned the 1140 nm prisms in favor of shorter wavelength prisms with higher concentrations.

An extinction of about 0.2 was achieved on several PAH/PCBS slides by immersing them in a solution of nanoprisms with an LSPR of about 900 nm for one week (Fig. 6.7). This was similar to the extinction reported for the 2x enhancement slide previously described, albeit at a shorter wavelength. After the deposition, the LSPR blueshifted to about 850

nm. SHG was not measured for these slides because the extinction at 1064 nm was still quite low. However, these slides suggested that using smaller nanoprisms could be a viable strategy going forward.

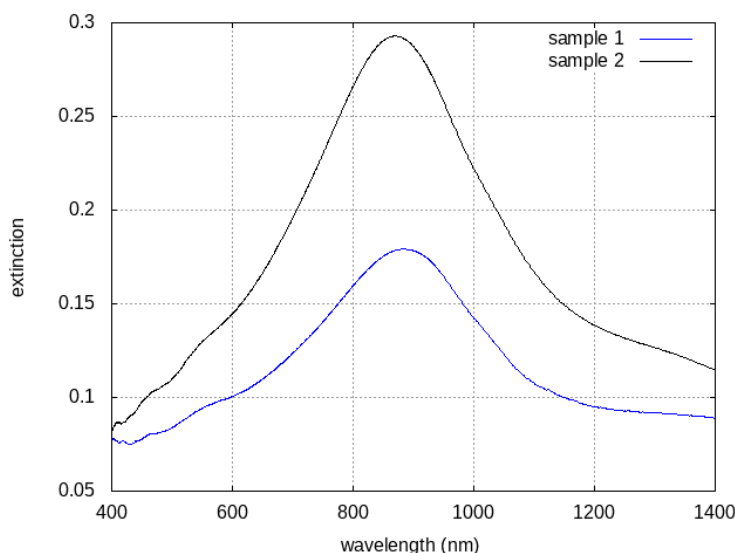


Figure 6.7: Absorbance of ISAM-coated slides immersed in 900 nm silver nanoprisms for about 1 week. The two samples shown came from different batches but the procedure used was the same.

Better results were obtained using a solution of 950 nm prisms. Although it would be expected that this solution would have a lower concentration after synthesis than the 900 nm solution, it is possible that the prisms in the 900 nm solution were depleted by previous efforts to deposit them. Two samples were immersed in a fresh solution of 950 nm silver nanoprisms for two weeks. Very good deposition was observed. The slides appeared dark blue in color where they had been exposed to the nanoparticles and the extinctions exceeded 0.7, as shown in Figure 6.8a. As can be seen in the SEM image presented in Figure 6.9, there was sufficient density for interparticle interactions to broaden the peak, allowing the extinction to remain high at 1064 nm. SHG was measured for these samples (Fig. 6.8b). The enhancement to the SHG due to the prisms was found to be 19 times for sample 180918-2 and

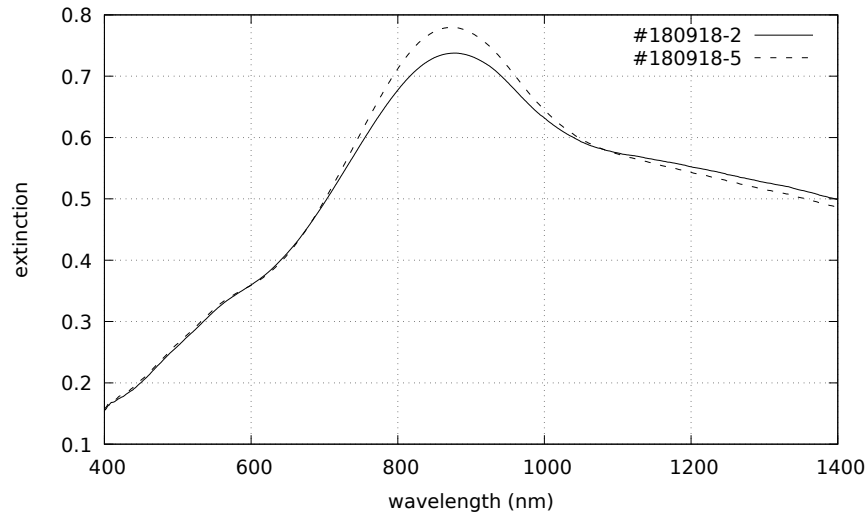
35 times for sample 180918-5. The difference in the two may be due to local variations in the nanoparticle density, as the two samples were prepared together and should have been quite similar. These enhancements are lower than might be expected at such a high extinction, but are better than those observed for other samples prepared by stationary immersion. As can be seen in Figure 6.8b, the SHG signal for these samples had an unusual shape, where Maker fringes are visible but fail to go to zero between the fringes. In prior work, this has been attributed to burning on the nanoparticles [5]. Another possibility is that absorbance at the second-harmonic wavelength may be a factor.

6.3 Immersion while stirring with the dipper machine

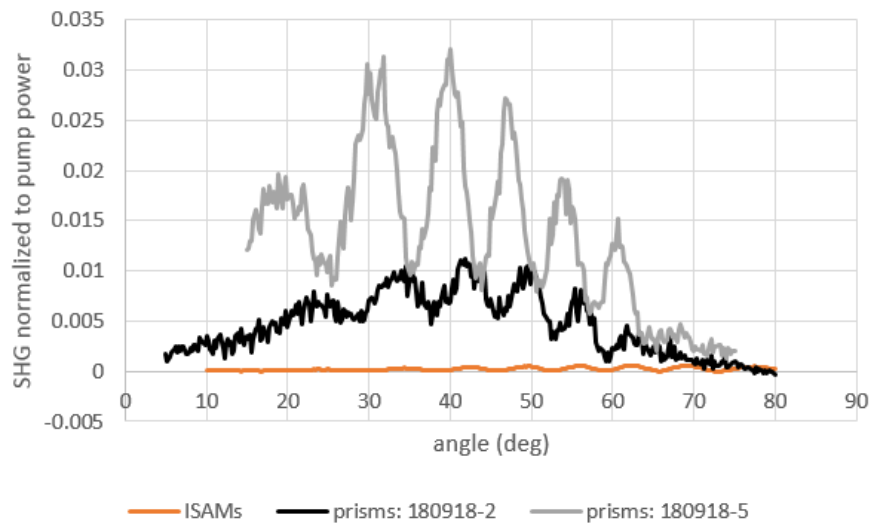
Dr. Liu's group reported good results when using the dipper machine to apply their nanoprisms to PAH layers on glass slides. The dipper machine rapidly rotates the slides in the solution, effectively "stirring" the nanoparticles. This agitation was reported to accelerate the deposition and improve uniformity. Deposition onto nonlinear ISAM films by dipper immersion was attempted for the 1140 nm prisms and for smaller prism sizes.

6.3.1 Initial attempts with 1140 nm prisms

The dipper machine was first used to try to improve deposition of the 1140 nm particles onto 3.5 bilayers PAH/PCBS. As previously discussed, these prisms were at a very low concentration and only yielded an extinction of 0.03 when deposited at the original concentration via stationary immersion. However, because the LSPR of these nanoprisms was very close to the wavelength of the Nd:YAG laser, it was highly desirable to improve their attachment rate. Due to the dimensions of the dipper machine, it was necessary to dilute the nanopar-



(a)



(b)

Figure 6.8: Results for two samples prepared by immersing slides coated with 3.5 bilayers PAH/PCBS in an unused solution of 950 nm nanoprisms for two weeks. The extinction (a) exceeded 0.7 and was significantly broadened. SHG enhancements (b) of 19 and 35 times were observed.

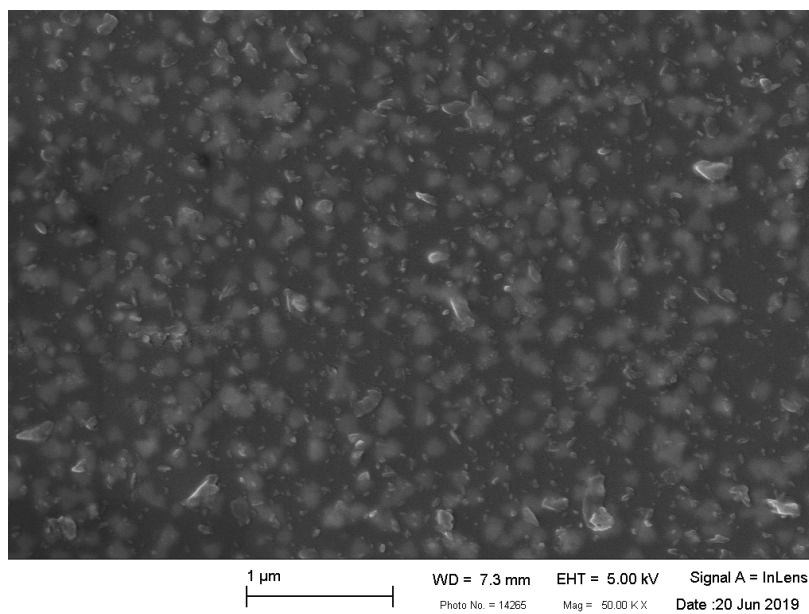


Figure 6.9: SEM image at 50,000 times magnification of sample 180918-5, which exhibited 35 times SHG enhancement. The prisms appear blurry due to an additional layer of PCBS that was later spincoated onto them as part of the experiments discussed in Section 6.5. The absorbance and SHG prior to the spincoating treatment are presented in Figure 6.8.

ticles to increase their volume. The original solution had a volume of about 30 mL, but the dipper machine is designed to be compatible with 150 mL beakers. Ultrapure water was added to double the volume of the nanoparticle solution in order for the solution to reach a sufficient height in the 150 mL beaker to submerge a significant portion of the substrate. Glass slides coated with 3.5 bilayers PAH/PCBS were immersed in the nanoparticle solution while stirring for 6 hours. The resulting extinctions were similar to those observed for 1 day stationary immersions.

It was suggested by Dr. Liu's group that in some cases deposition is maximized for immersions a few hours long, and that some of the nanoprisms can detach during longer immersions. Therefore, a new batch of PAH/PCBS slides was prepared and immersed using the dipper machine for 90 minutes. Extinction was measured on these slides and found to be only about 0.01. Because shorter immersions produced less deposition, it was hypothesized

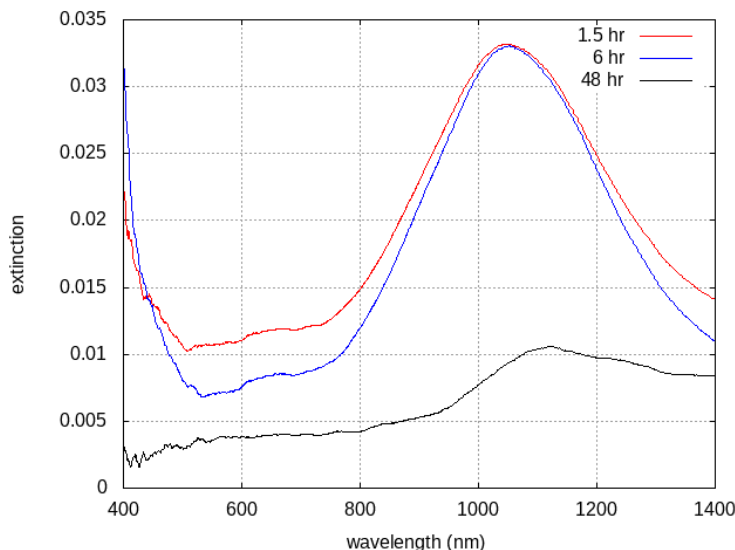


Figure 6.10: Extinction from slides with 3.5 bilayers PAH/PCBS immersed in 2 times diluted 1140 nm silver nanoprisms in the dipper machine for different durations. Because extending the immersion to 48 hours failed to improve the nanoprism density, it was concluded that the nanoparticle solution was too dilute.

that a longer immersion may be beneficial. The nanoprisms were applied to 3.5 bilayers PAH/PCBS using the dipper machine while stirring for 48 hours. The resulting extinctions remained very small, all being less than 0.01. The extinctions of the 90 minute, 6 hour, and 48 hour slides are shown in Figure 6.10. It was therefore concluded that the concentration of these nanoprisms would have to be increased.

6.3.2 Prisms (800 nm LSPR) applied to PAH instead of 3.5 bilayers PAH/PCBS

The good depositions obtained by Dr. Liu's group were achieved while applying prisms to a single PAH layer using the dipper machine. To confirm their results and study the poor adsorption onto the nonlinear films, an immersion onto a single PAH layer was attempted. Plain microscope slides were immersed in PAH for several minutes, rinsed well, then im-

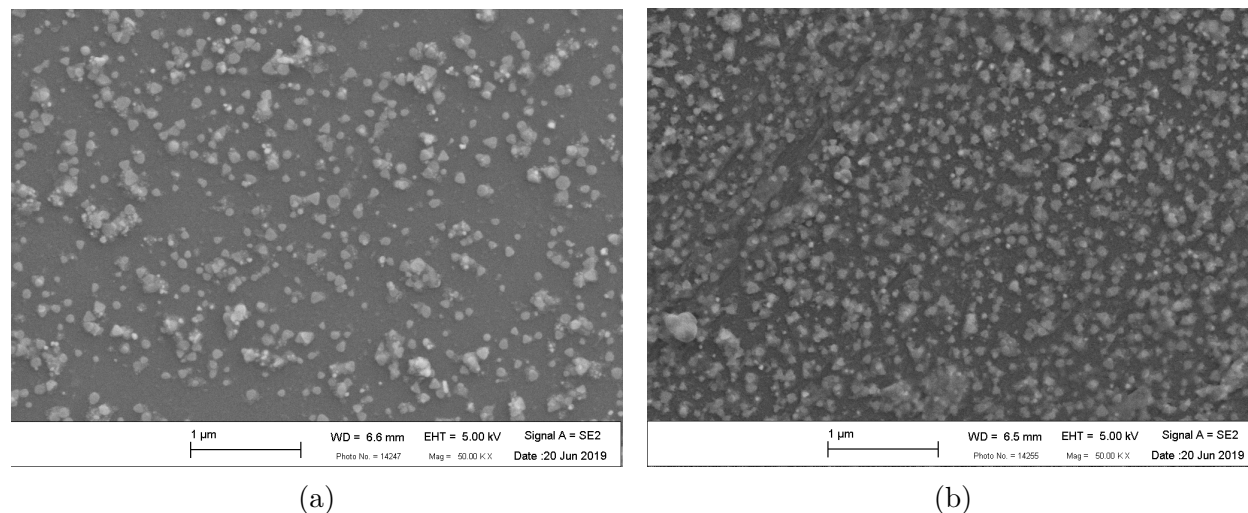


Figure 6.11: SEM images at 50,000 times magnification for 800 nm wavelength prisms deposited onto PAH-coated slides by immersing in the dipper machine while stirring. The samples immersed for 5 hours (a) had less nanoprism density than samples immersed for 10 hours (b).

mersed in 800 nm LSPR nanoprisms in the dipper machine while stirring. Four slides were immersed for 5 hours, then a second batch of slides was immersed for 10 hours. As can be seen in SEM images of these slides (Fig. 6.11), significant prism densities were achieved, with more prisms on the slides that had longer immersions. Strong extinctions, greater than 0.5, were observed (Fig. 6.12).

Despite the absence of PCBS in these ISAM films, a small amount of SHG is produced by the interfaces of the PAH layer. As discussed in Section 3.1.1, second-order nonlinear effects are forbidden in centrosymmetric media but can occur at interfaces due to symmetry breaking at the surface. Additionally, SHG can be produced by silver nanoparticles independent of a nonlinear host material [214]. The strength of the SHG signal observed for silver nanoprisms on a single PAH layer was smaller than that typically recorded for 3.5 bilayers of PAH/PCBS by about a factor of one hundred. The prisms deposited for 300 minutes and 600 minutes produced SHG signals that were larger than the PAH alone by 129 times and 135 times, respectively (Fig. 6.12). In order to compare the shape of the SHG fringes

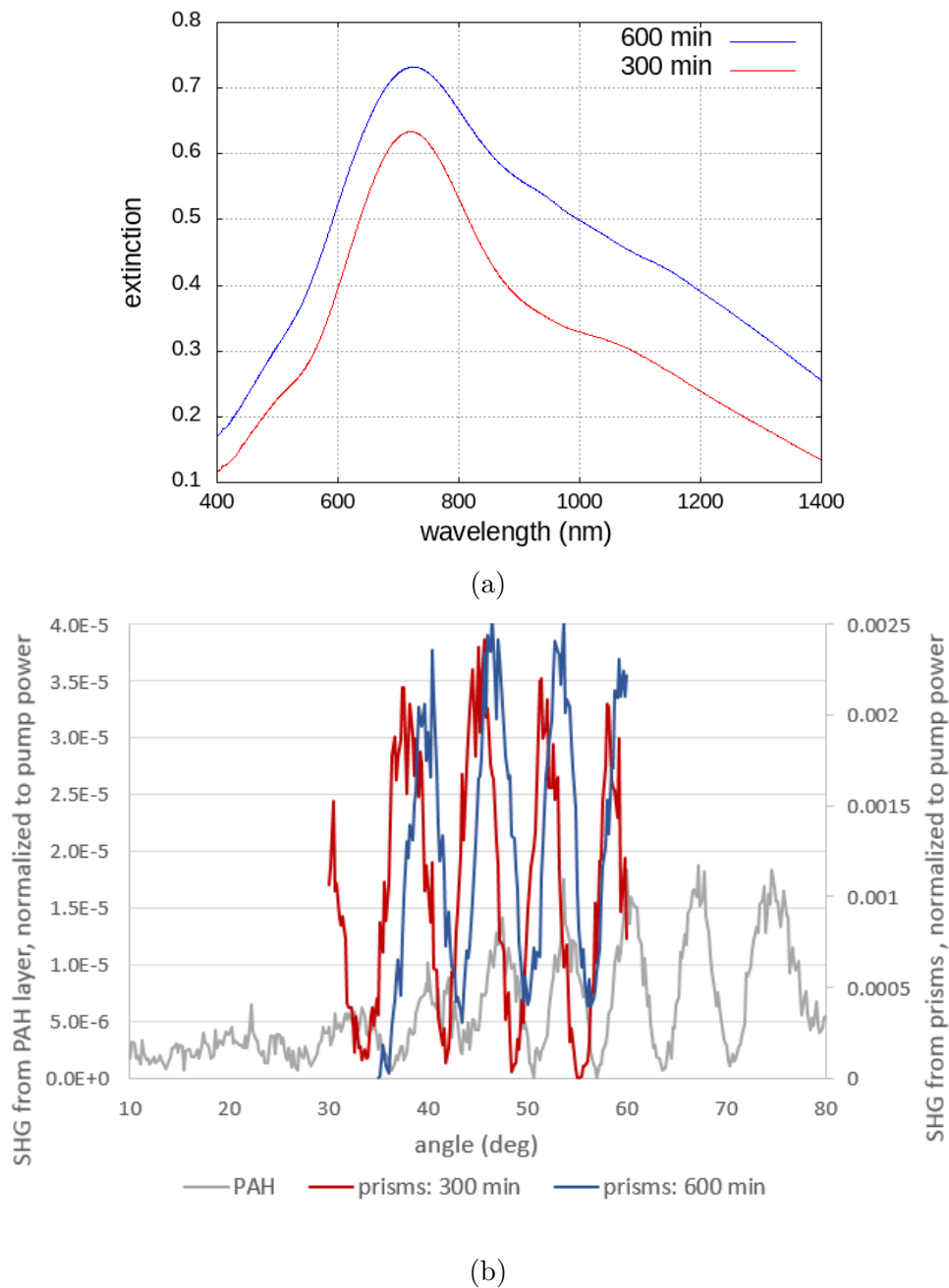


Figure 6.12: Absorbance and SHG results for 800 nm wavelength prisms deposited onto PAH-coated slides by immersing in the dipper machine while stirring for 300 minutes and 600 minutes. This resulted in high nanoparticle densities with extinctions (a) exceeding 0.6. Normalized SHG intensity for these samples (b) is plotted, with different axes for the regions with and without nanoprisms due to the enhanced signal from the hybrid films. The SHG for the 300 minute and 600 minute samples was 129 times and 135 times, respectively, larger than the SHG produced by the single PAH layer without added nanoprisms.

with and without the prisms, the data are plotted together but with different axes. Some attempts were later made to exploit the tendency of the nanoprisms to adsorb well to single PAH layers by applying nonlinear films on top of nanoprisms deposited in this way (Section 6.5.1). However, due to concerns that exposure to the polymer solutions could damage the nanoprisms, procedures in which the nanoprisms were adsorbed onto pre-existing nonlinear films were preferred.

6.3.3 Prisms (950 nm LSPR) applied to 3.5 bilayers PAH/PCBS

Based on the success of the procedure used to deposit prisms onto PAH, the same approach was used to deposit prisms onto 3.5 bilayers of PAH/PCBS. Because the top layer is PAH the deposition should be similar to that observed on PAH alone, although prior results indicated that the nanoprisms had less affinity for thicker films. Prisms were applied to slides coated with 3.5 bilayers PAH/PCBS in the dipper for two hours. As can be seen in Figure 6.13, the extinction after deposition was about 0.35, which was less than the extinction for prisms on PAH alone but is still fairly strong. The peak extinction occurred at about 830 nm, which is over 200 nm away from the wavelength of the fundamental beam. Despite the nonideal peak absorption wavelength, SHG was measured for these samples and is presented in Figure 6.13. After normalizing to the pump power, there was significantly more SHG observed from the films with the nanoprisms than from the bare ISAM films. The SHG enhancements for slides #180703-6, #180703-7, and #180703-8 were 20, 19, and 34 times, respectively. Interestingly, these enhancements are similar to the enhancements observed for prisms applied by stationary immersion for 2 weeks (Section 6.2.3), although the extinction for these is about half as much as it was for those.

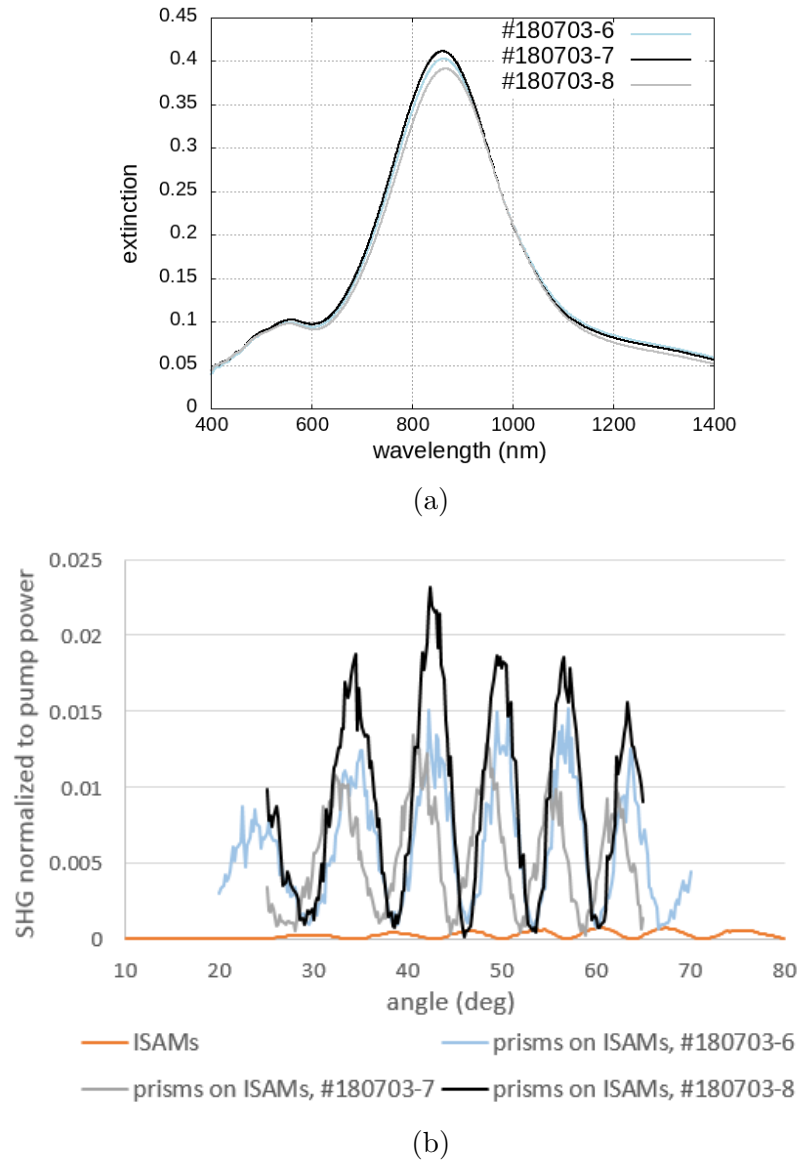
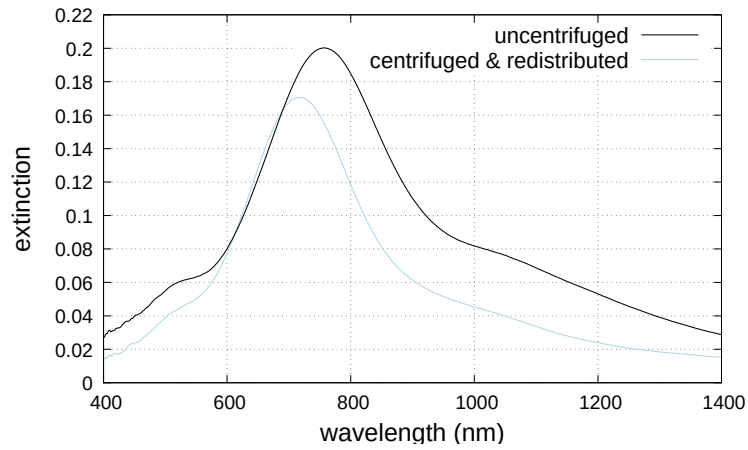


Figure 6.13: Results for 950 nm wavelength prisms applied to 3.5 bilayers PAH/PCBS for 2 hours in the dipper machine. All three slides were prepared with the same procedure, and the extinctions (a) were similar for all three samples. The SHG enhancements (b) ranged from 19 to 34 times.

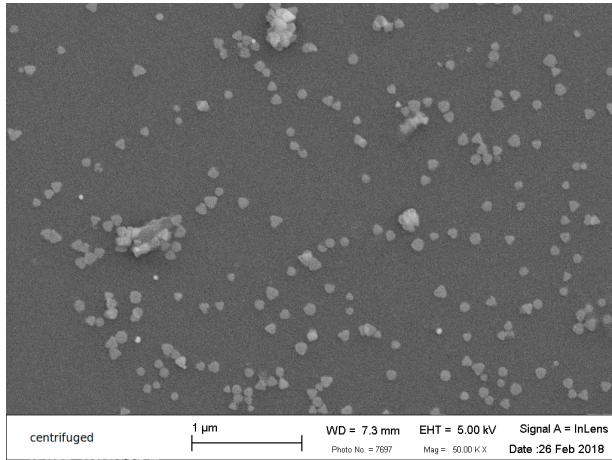
6.4 Prisms applied by centrifuging and dropcasting

Due to the difficulties in obtaining sufficient deposition by immersion, alternatives were explored. One approach was to increase the particle concentration via centrifugation. This approach was recommended against by Dr. Liu's group due to concerns about deforming or agglomerating the nanoprisms. It was pursued nonetheless in light of continuing difficulties in getting sufficient deposition with the nanoprisms at the provided concentrations. In a typical experiment, a 2 to 6 mL volume of nanoparticle solution was centrifuged at 5000 rpm for 10 minutes. The supernatant was removed, leaving a dense nanoparticle solution of less than 0.5 mL. Because the resulting volume was too small to allow for immersion, the nanoprisms were applied to the substrates by dropcasting instead. In general, dropcasting is not preferred because drying effects can lead to non uniform deposition. Also, dropcasting only applies the particles to one side of the slide, which means that the enhanced SHG must be generated by only half of the available film.

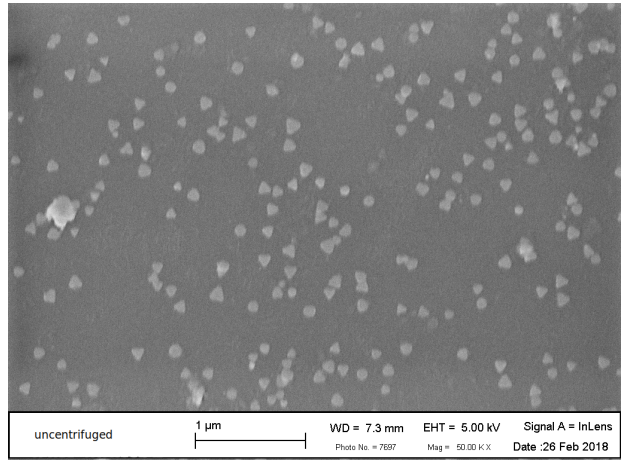
To test whether prisms were damaged by centrifugation, SEM images of centrifuged and uncentrifuged nanoprisms were compared. These tests were performed with 600 nm prisms to preserve the harder to produce long wavelength prisms. One aliquot was centrifuged, the supernatant was removed, and it was redistributed to its original concentration. A second aliquot from the original, uncentrifuged stock solution was used for comparison. Despite the small change in extinction, the 600 nm nanoprisms do not appear to have suffered any ill effects from centrifugation. There appears to be a similar fraction of triangular nanoparticles, which retain their pointed tips. Relatively few agglomerations were observed. Another sample was similarly prepared using a small amount of concentrated 1140 nm particles. As can be seen in Figure 6.15, in this case the nanoprisms appear damaged. It is unclear whether this is the result of centrifugation. These particles had been in solution for over a year by



(a)



(b)



(c)

Figure 6.14: Comparison of centrifuged and uncentrifuged 600 nm wavelength prisms. The extinction (a) of the nanoparticle solution was slightly lower after centrifuging and redistributing, which may indicate that some of the prisms were lost in the process. SEM images of the redistributed prisms (b) and stock solution (c) show that the nanoparticles retain their triangular shape after centrifugation.

the time of this test and had been used in multiple attempts at deposition, so it is possible that other factors were at play.

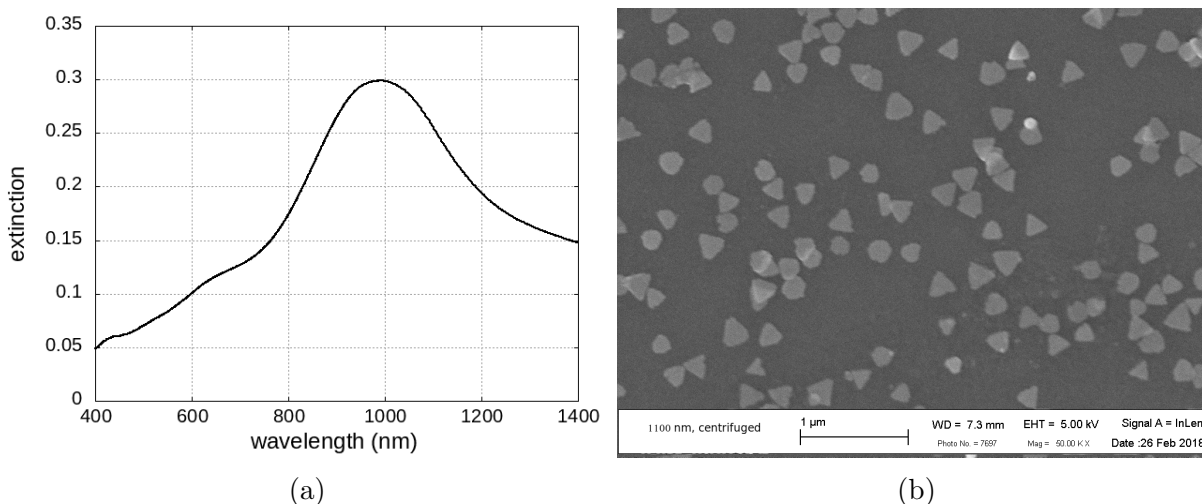


Figure 6.15: Deposition results of year-old 1140 nm prisms, centrifuged and dropcast onto PAH. The peak extinction (a) was 0.3, which was an order of magnitude larger than what was typically observed in attempts prior to concentrating this solution. An SEM image (b) reveals that the particles remain triangular but appear somewhat damaged, possibly due to age.

To study SHG enhancement from dropcast silver nanoprisms, a set of three samples was prepared. Each slide was piranha cleaned and coated with 3.5 bilayers PAH/PCBS. The clean substrates were soaked in PAH for about 15 minutes, rinsed thoroughly, and dried, immediately before dropcasting. While the substrates were soaking, the concentrated nanoprisms were prepared. A solution of 900 nm LSPR nanoprisms was separated into 4 mL aliquots. The aliquots were centrifuged for 15 minutes at 5000 g. Then, as much supernatant was removed as was possible without disturbing the nanoprism pellet at the bottom. The remaining dense nanoparticle solutions were about 30 μL in volume. These solutions were dropcast onto the ISAM coated slides for about 24 hours while preventing evaporation as described in Section 4.4.3. Finally, the slides were rinsed in water and dried.

SEM images for two samples prepared in this way are presented in Figure 6.16. The

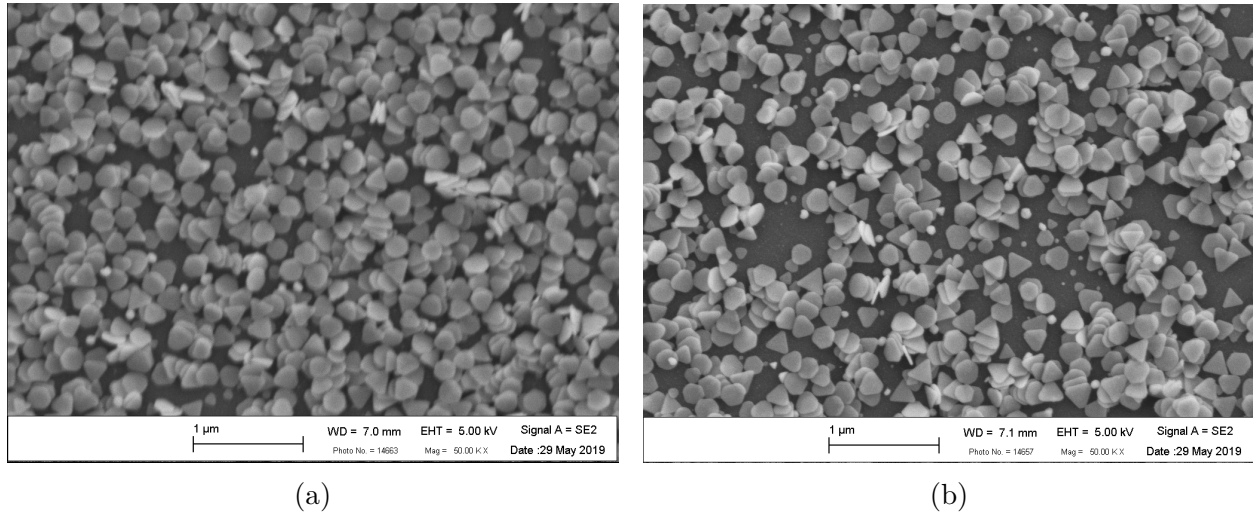


Figure 6.16: SEM images at 50,000 times magnification for 900 nm wavelength prisms dropcast onto 3.5 bilayers PAH/PCBS at high concentration. The images correspond to samples 180528-3 (a) and 180528-4 (b) in Figure 6.17. Much higher density was achieved than for samples prepared by immersion.

prisms are arranged much more densely than was achieved for samples prepared by immersion. Although some empty space remains, the prisms are beginning to stack and overlap. Interestingly, it is apparent from the points of overlap that the prisms are somewhat transparent under SEM. This may be due to the thinness of the nanoprisms, which were only about 12 nm thick. The extinction and SHG results for these samples is presented in Figure 6.17. All three samples showed high extinctions with very broad peaks and significant enhancement over the ISAM SHG. Because the prisms were only on one side of the slide, and the nonlinear ISAM film was on both sides, the prism signal was multiplied by 4 when determining enhancement. A wide range of enhancements was observed. Slides 1, 3, and 5 had enhancements of 113 times, 1380 times, and 797 times, respectively. Due to the significant SHG enhancement, the normalized SHG from regions with and without nanoprisms are plotted together on different axes to allow the fringe shapes for both regions to be compared. Higher extinctions were correlated with higher enhancements, although the intended concentrations for all three samples should have been similar. The differences in extinction

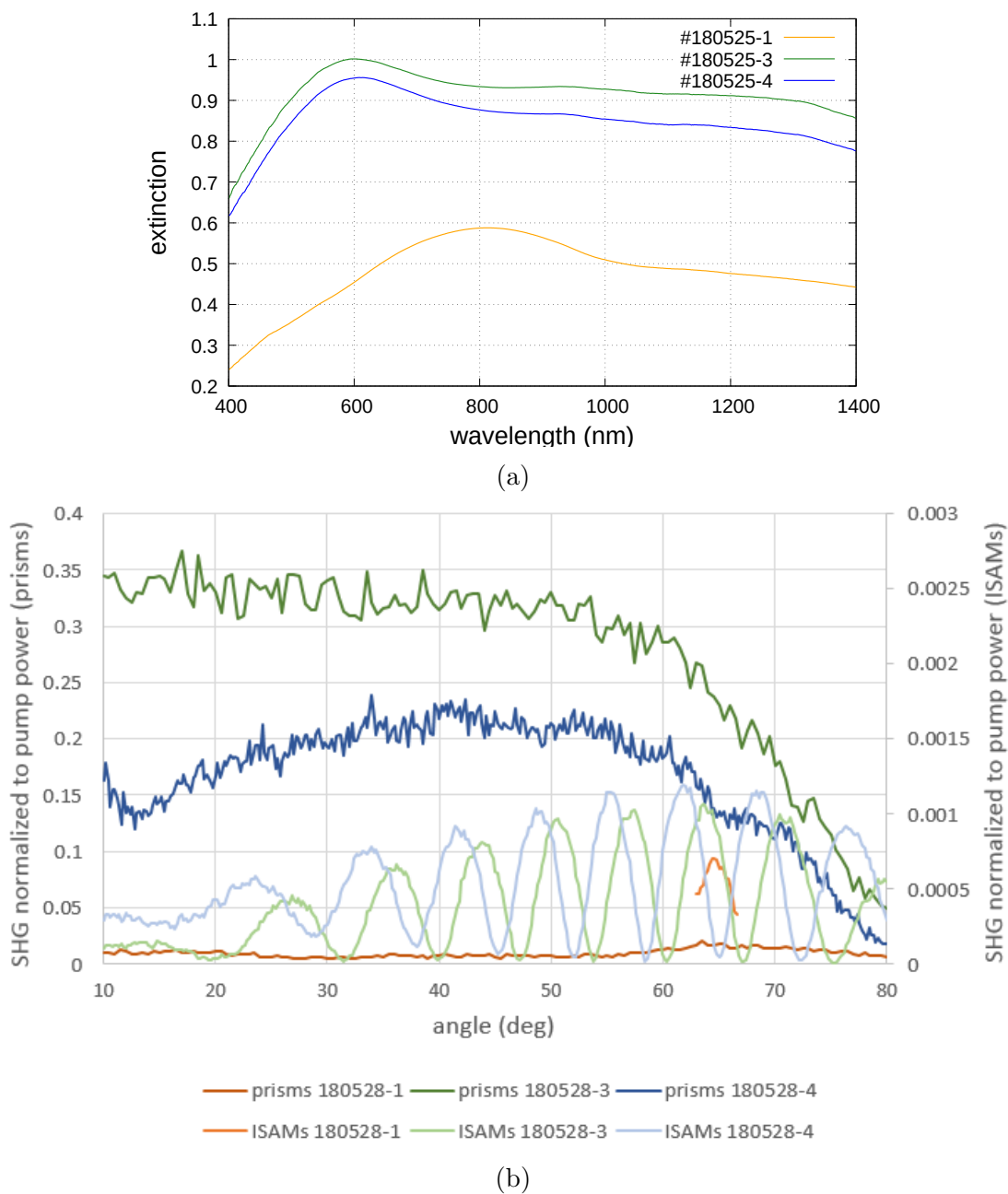


Figure 6.17: Results for 900 nm wavelength prisms dropcast onto 3.5 bilayers PAH/PCBS at high concentration. The extinction (a) is high and very broad for all three samples. A wide range of enhancements to SHG (b), from 113 to 1380 times, was observed. The normalized SHG is plotted on different axes for the regions with and without nanoprisms, in order for fringe shapes from both regions to be discernible.

and enhancement may be due to variability in density due to the dropcasting method or accidental removal of nanoprisms along with the supernatant for some aliquots. It can be seen in the SEM images that the sample with the best enhancement (Fig. 6.16a) had a denser layer of nanoparticles than the sample with intermediate enhancement (Fig. 6.16b), with less empty space.

The above technique was performed again to make three samples using prisms with different LSPR wavelengths. Silver nanoprisms with LSPRs in solution near 600 nm, 800 nm, and 950 nm were used. SEM images of these samples are presented in Figure 6.18. Dense depositions with a single layer of nanoprisms were achieved in each case. The SEM image of the 800 nm wavelength prisms (Fig. 6.18b) was taken after the sample had been spin-cast with PCBS as part of later work. The nanoprisms are blurry but visible beneath this polymer layer, and are obscured by a layer of particles that are much smaller. The origin of these small particles is uncertain, but it is possible that they are excess seed particles left over from the synthesis procedure. The extinction is presented in Figure 6.19. In all cases, a very broadened extinction peak was observed, consistent with the close arrangements visible in the SEM images. The SHG from these samples is presented in Figure 6.20. The enhancements observed were 257 times for 600 nm prisms, 405 times for 800 nm prisms, and 230 times for 950 nm prisms. These significant enhancements help to confirm that using prisms with the “incorrect” LSPR wavelength at high enough densities to broaden the peaks can be a viable strategy for improving SHG enhancement.

The above experiments showed that good SHG enhancement could be obtained by drop-casting nanoprisms at the highest achievable concentration. However, the actual enhancements were somewhat erratic. It was suspected that these fluctuations could be due to variations in the nanoprism density. To investigate this, samples were prepared at a range of concentrations and SHG was measured. Three sets of samples were prepared on different

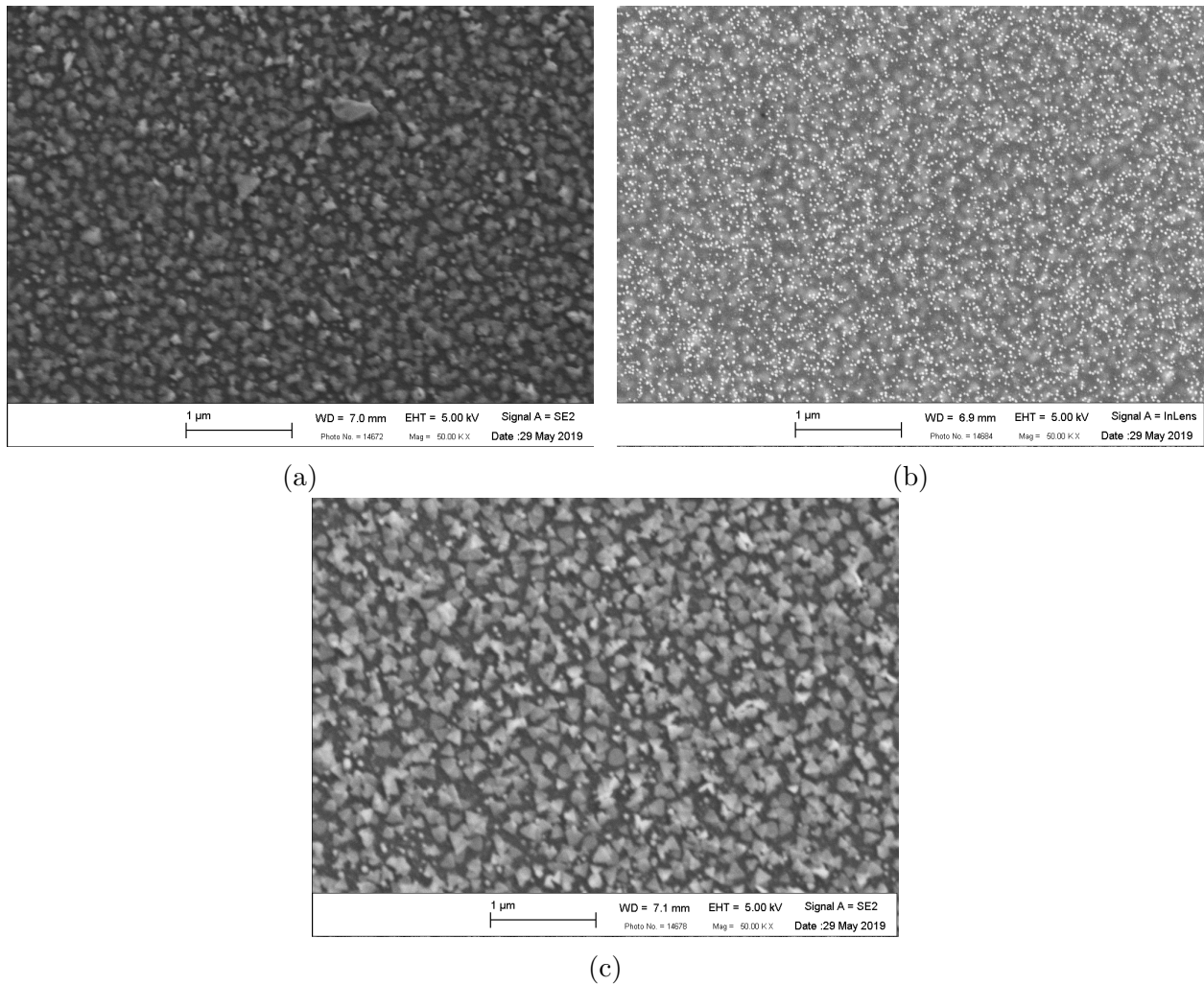


Figure 6.18: SEM images taken at 50,000 times magnification for high concentration prisms with LSPR wavelengths of (a) 600 nm, (b) 800 nm, and (c) 950 nm, dropcast onto 3.5 bilayers of PAH/PCBS using the same procedure in all three cases. The 800 nm prisms were later spincast with PCBS as part of the work described in Section 6.5, leading to their obscured appearance in the SEM image.

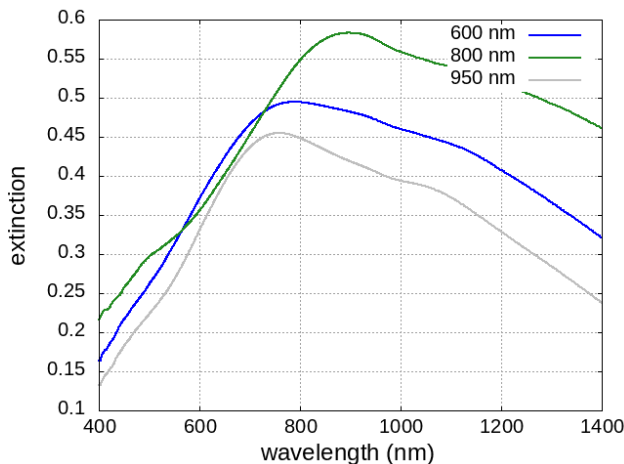
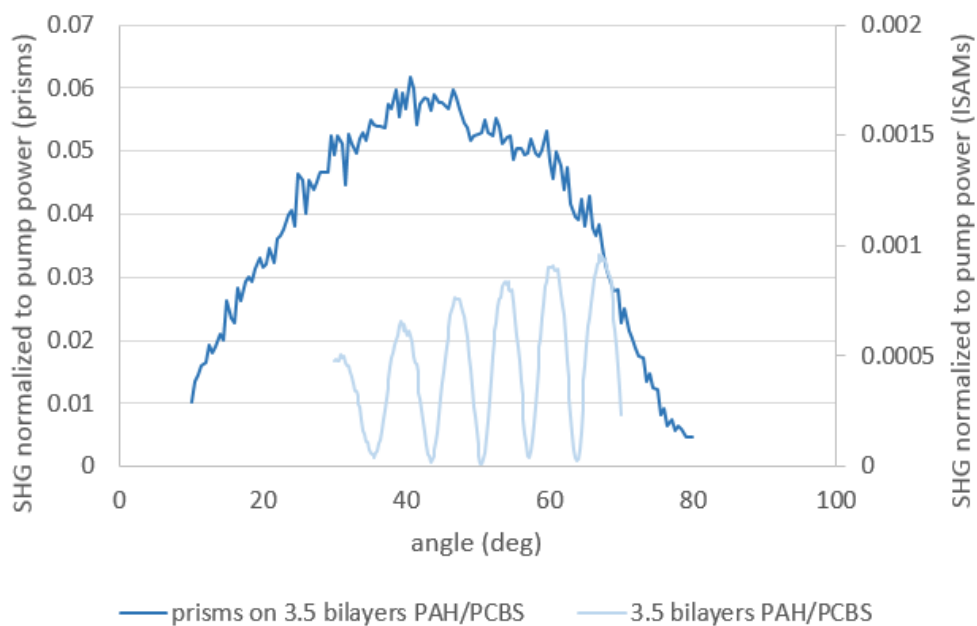


Figure 6.19: Extinction for high concentration prisms with LSPR wavelengths of 600 nm, 800 nm, and 950 nm dropcast onto 3.5 bilayers of PAH/PCBS, using the same procedure in all three cases. All three samples show significant broadening on the LSPR peak.

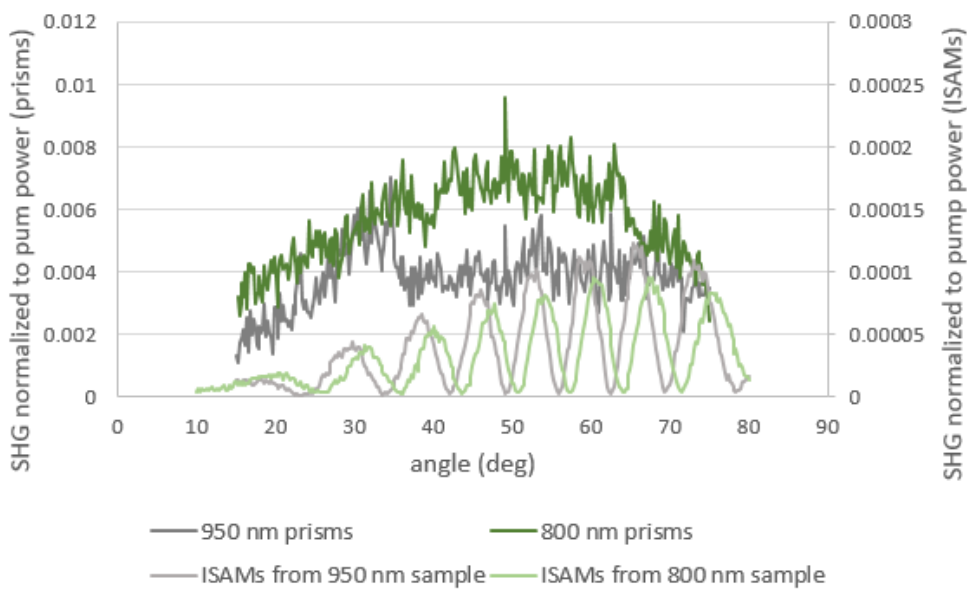
occasions, and the results are discussed below.

Initially, a set of dropcast slides was prepared with nanoprism solutions at 33 to 240 times the original stock concentration. SEM images of samples prepared at 33, 67, 100, and 240 times the stock concentration are presented in Figure 6.21. At 33 times the stock concentration most of the nanoprisms occur close together, with empty spaces separating the clusters. The empty spaces are reduced at 67 times the stock concentration, and are basically gone at the higher concentrations. At 100 and 240 times the stock concentration, significant numbers of the prisms are no longer laying flat on the ISAM film but are tilted due to space constraints.

The large aggregate observed at 67 times is one of many that were distributed over the sample, which were also present in the 240 times concentrated sample but absent at 33 times and 100 times. The distribution of the aggregates on the samples on which they appeared is presented in Figure 6.22. It is surprising that the appearance of the aggregates was not correlated with the concentration. However, the slides at 67 and 240 times the stock concentration were centrifuged separately from those at 33 and 100 times. Although the



(a)



(b)

Figure 6.20: SHG results for high concentration prisms with LSPR wavelengths of 600 nm, 800 nm, and 950 nm, dropcast onto 3.5 bilayers of PAH/PCBS using the same procedure in all three cases. The 600 nm wavelength prisms (a) had an enhancement of 257 times. The 800 nm and 950 nm wavelength prisms (b) had enhancements of 405 times and 230 times, respectively.

centrifugation parameters were identical in both sets, it is possible that some unintentional difference occurred that contributed to the aggregation.

In all cases, the extinction peak was very broad (Fig. 6.23a). There was a loose correlation between concentration and extinction; the highest concentration produced the highest extinction, and the lowest concentrations produced the lowest extinctions, but some concentrations in the middle failed to follow the trend (Fig. 6.23b). Most of the enhancements were between about 50 and 115 times. The two samples that were 67 times concentrated had much higher enhancements: 851 times for one and 1107 times for the other. It was hypothesized that there might be an optimum concentration, high enough to take advantage of interparticle effects and low enough to avoid problems due to burning or absorption. Additional batches of variable concentration dropcast samples were prepared in an attempt to pinpoint the optimum deposition density.

Two follow-up attempts were made to further study the influence of concentration, the results of which are presented in Figure 6.25. Each consisted of four samples that were prepared together as a batch to minimize the chance that unconscious synthesis differences could occur. The first batch was done at concentrations from 22 to 67 times, but produced quite low enhancements, from only 10 to 23 times. The second batch used concentrations from 28 to 67 times. In this case the enhancements were higher, from 81 to 100 times. In both cases, higher enhancements were observed with higher concentrations, although the trend was weaker than expected. More than doubling the concentration only changed the enhancement by a factor of about 1.2. Additionally, while dropcasting at 67 times the stock concentration produced very high enhancements in the first enhancement vs. concentration test (Fig. 6.23), it failed to do so here.

Because previous attempts to relate concentration to enhancement suggested that there might be a trend or an optimum concentration, a final set of samples was prepared to

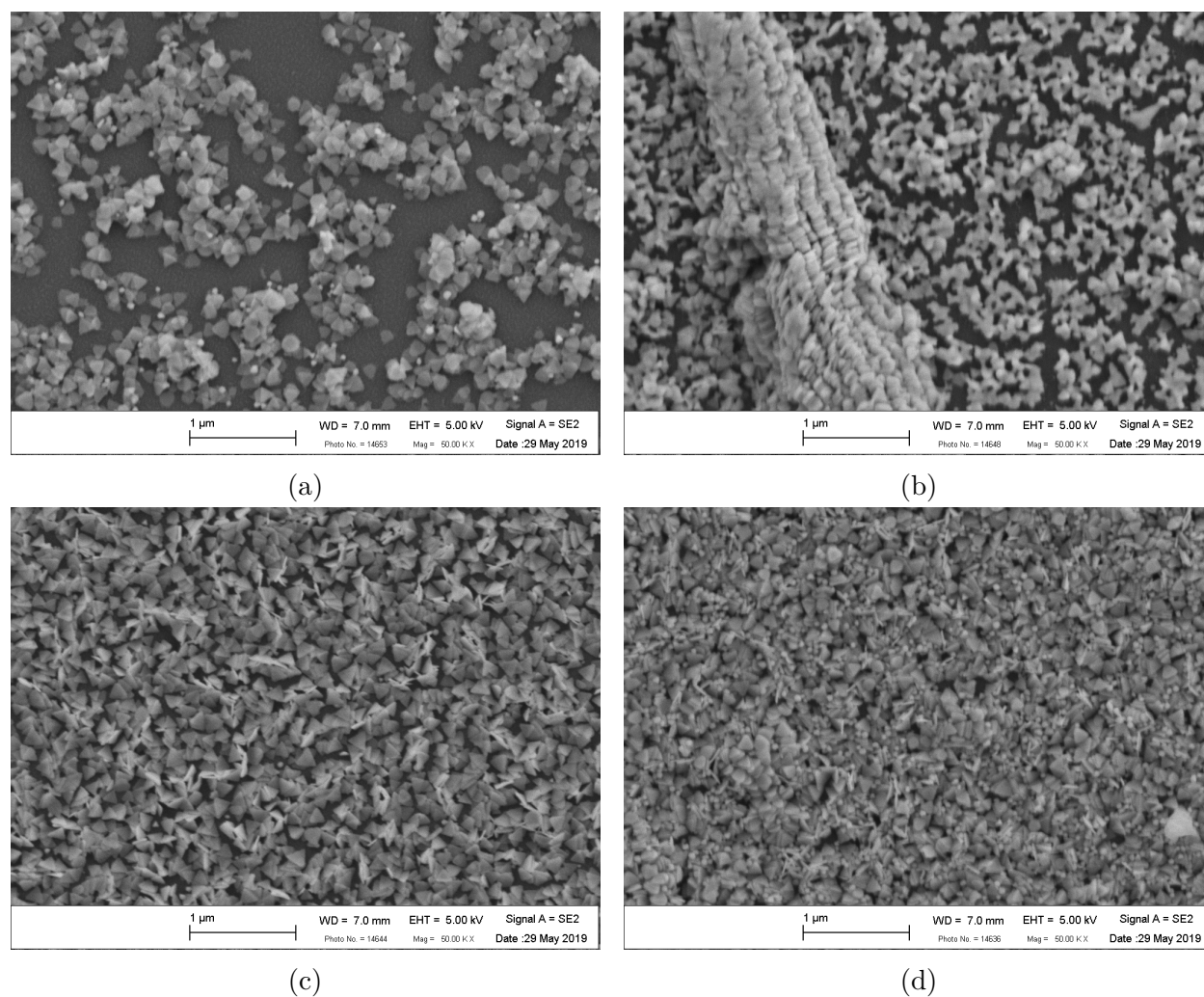


Figure 6.21: SEM images taken at 50,000 times magnification for nanoprisms dropcast at (a) 33, (b) 67, (c) 100, and (d) 240 times the stock concentration. The type of aggregate present at 67 times the stock concentration was also observed at 240 times, but was absent at 33 and 100 times.

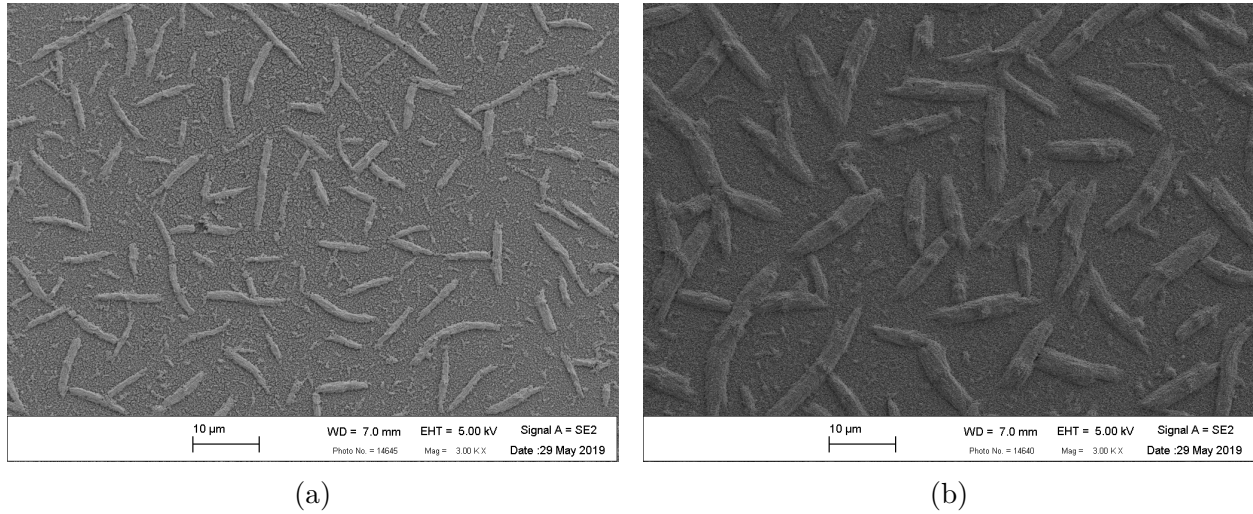
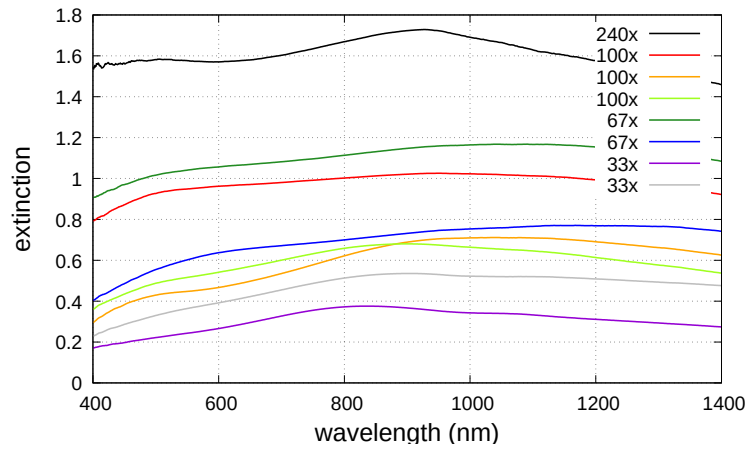


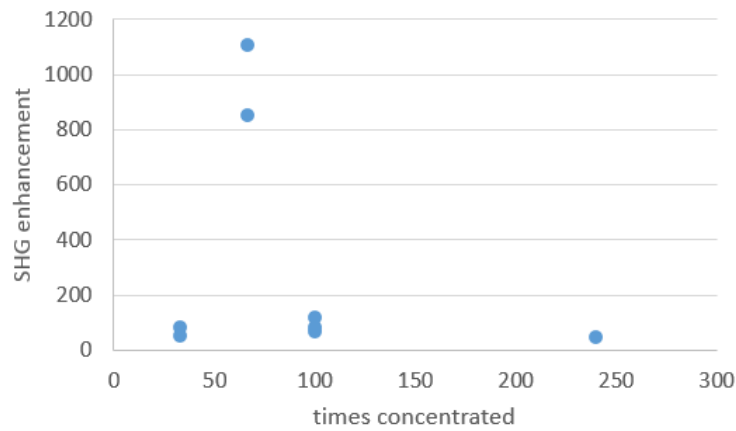
Figure 6.22: SEM images taken at 3000 times magnification for samples prepared at 67 (a) and 240 (b) times the stock concentration. Large aggregates were distributed across the surface in both cases.

more definitively determine the relationship. In this case, a larger number of samples and a higher range of concentrations were used to try to eliminate uncertainties in the previous studies. Eight samples were prepared with concentrations from 50 to 200 times the stock concentration using 950 nm prisms. SEM images of samples dropcast at 67 and 200 times the stock concentration are presented in Figure 6.26. Small aggregates are observed in both of these samples, and the higher concentration sample has more complete coverage of the surface. Absorbance and SHG results for this set of samples are presented in Figure 6.27. As in previous experiments with dropcast nanoprisms, broad extinctions were observed, with a general trend of higher extinctions for higher concentrations. However, there are some violations of this trend at intermediate concentrations. There does not appear to be a trend linking enhancement with concentration. However, the highest SHG enhancement was 108 times from the 62 times concentrated nanoprisms, which happened to be near the most successful concentration (67 times) observed in the first concentration dependence test.

Based on the results of the experiments presented in this section, it was concluded that



(a)



(b)

Figure 6.23: Results for samples dropcast at different concentrations. This first attempt to study the influence of concentration on enhancement used nanoprism solutions concentrated by 33 to 240 times. All of the samples had very broad extinction peaks (a). The SHG enhancements (b) appeared to be optimized for a 67 times concentrated solution, for which the enhancements were about 1000 times.

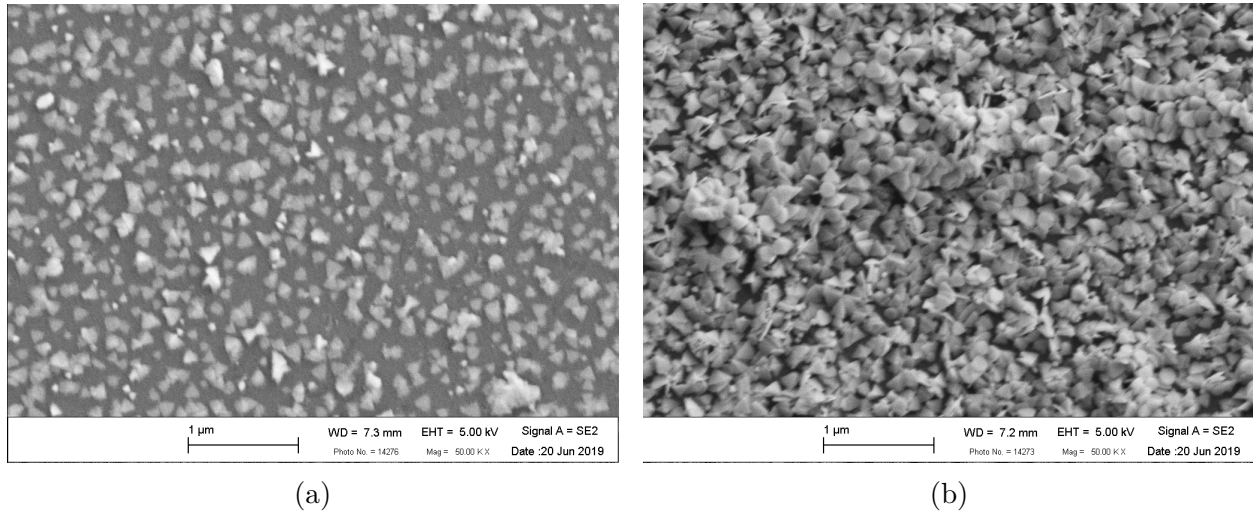
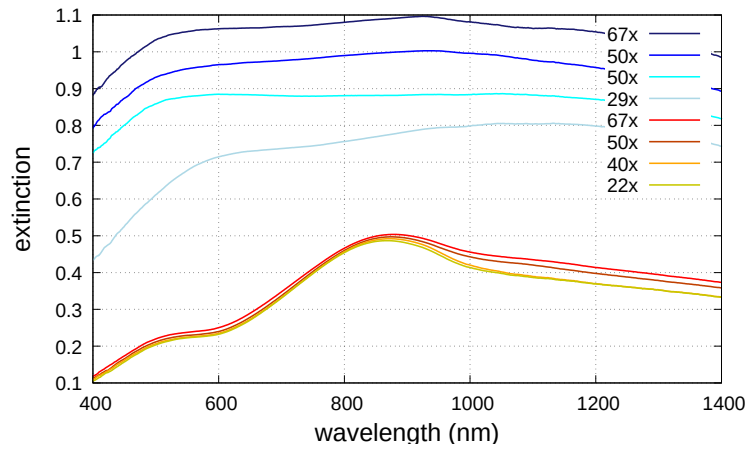


Figure 6.24: SEM images at 50,000 times magnification of samples prepared at 22 (a) and 67 (b) times the stock concentration from batch 181115 presented in Figure 6.25. The density of the deposited nanoprisms is clearly higher at higher concentrations, although both of these samples failed to achieve enhancements above about 20 times.

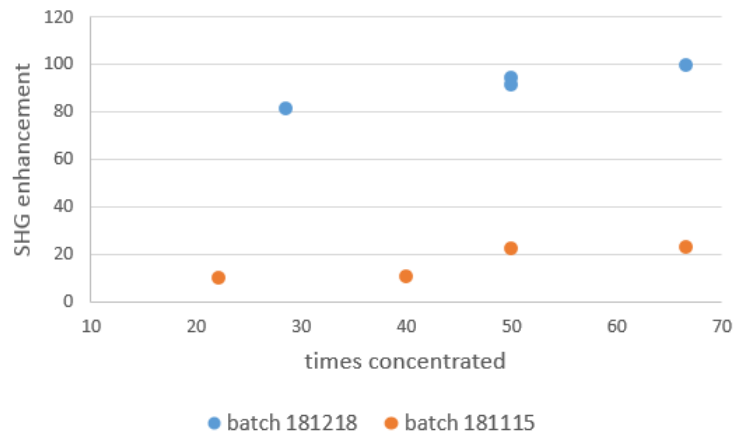
concentrating the nanoprisms results in higher extinction and enhancement than was observed when using the stock concentrations. However, once the nanoparticles were concentrated by a significant factor (greater than about 20 times), attempts to study the effect of varying the exact concentration were mostly inconclusive. It is possible that the benefits of concentrating the nanoprisms primarily derive from broadening of the extinction peak, which was achieved in all cases. It is also possible that poor uniformity due to the use of the dropcasting method was responsible for local variations in deposition density, which made trends in enhancement difficult to observe.

6.5 Further treatments to deposited nanoparticles

In addition to trying to increase the deposition density of the silver nanoprisms, attempts were made to improve SHG by applying additional polymer coatings on top of the deposited prisms. These strategies included applying nonlinear ISAM films onto the deposited



(a)



(b)

Figure 6.25: Results from two further attempts to study concentration versus enhancement. One set of samples was prepared at concentrations from 22 to 67 times and is shown in shades of orange in both images, while a second was at 29 to 67 times and is shown in shades of blue. All of the extinction peaks (a) were very broad. The enhancement (b) appeared to be weakly correlated with the nanoprism concentration.

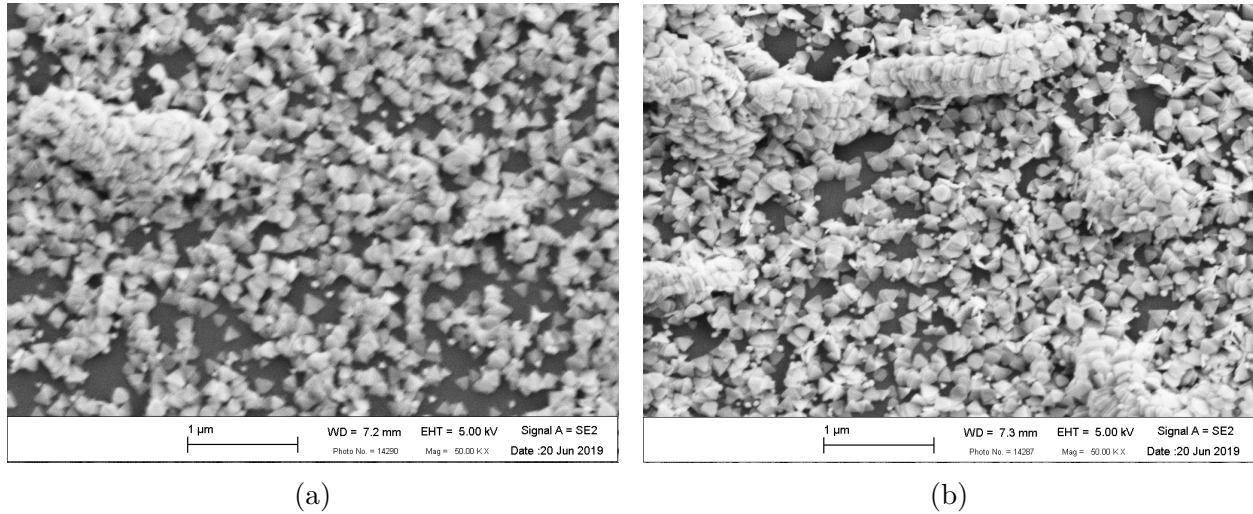
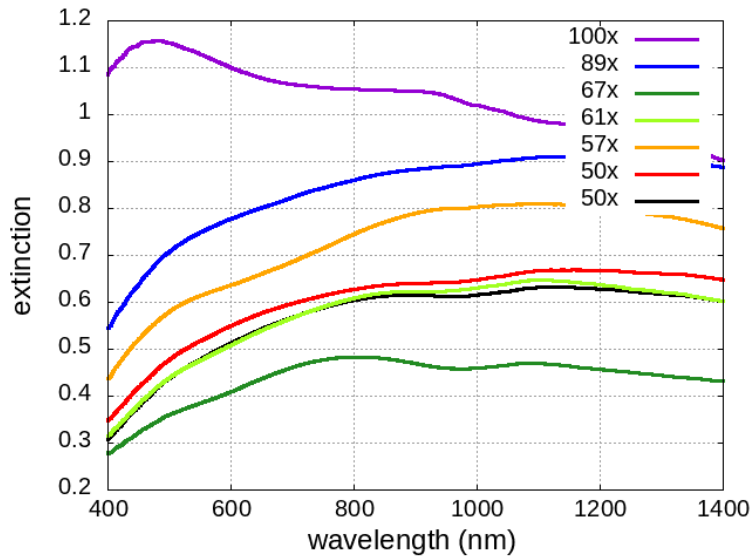


Figure 6.26: SEM images at 50,000 times magnification of samples dropcast at 67 times (a) and 200 times (b) the stock concentration, corresponding to the data presented in Figure 6.27.

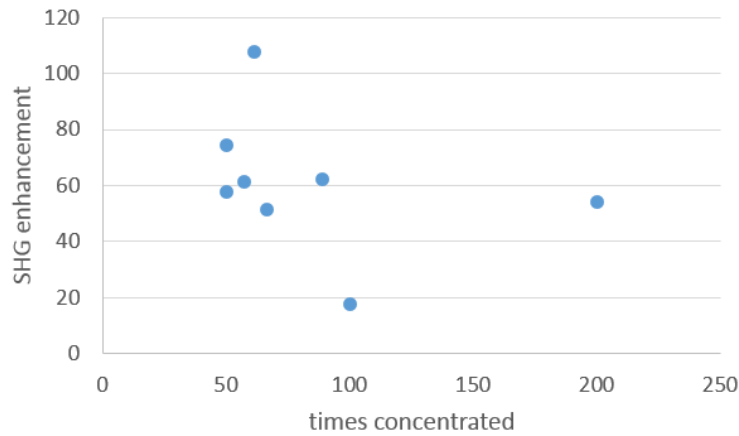
nanoparticles and using spincoat polymers to alter their LSPR wavelength. When using the shorter wavelength particles it was desirable to redshift them closer to the wavelength of the Nd:YAG laser used for excitation in order to optimize their resonance with the fundamental beam. As discussed in Section 3.2, the LSPR of metal nanoparticles can be redshifted by increasing the refractive index of the surrounding medium. Polymer coatings were applied to deposited prisms by the ISAM technique and by spincoating.

6.5.1 Applying ISAMs on top of prisms

It was expected that applying nonlinear ISAM films on top of the deposited nanoprisms would be a viable strategy to both redshift the LSPR peak and to increase the amount of ordered PCBS exposed to plasmonic field enhancements. Regions in-plane with and above the nanoprisms have plasmonic electric field enhancements that are unutilized when the nanoprisms are simply deposited on top of the nonlinear films. Top ISAM layers were applied to samples with and without the foundational PAH/PCBS bilayers underneath the



(a)



(b)

Figure 6.27: Results from a final attempt to study concentration versus enhancement using a larger sample set. Concentrations from 50 to 200 times were tested. Extinctions (a) were very broad in all cases, but could not be obtained for the 200 times concentrated sample due to saturation. The relationship between concentration and enhancement (b) appears randomized.

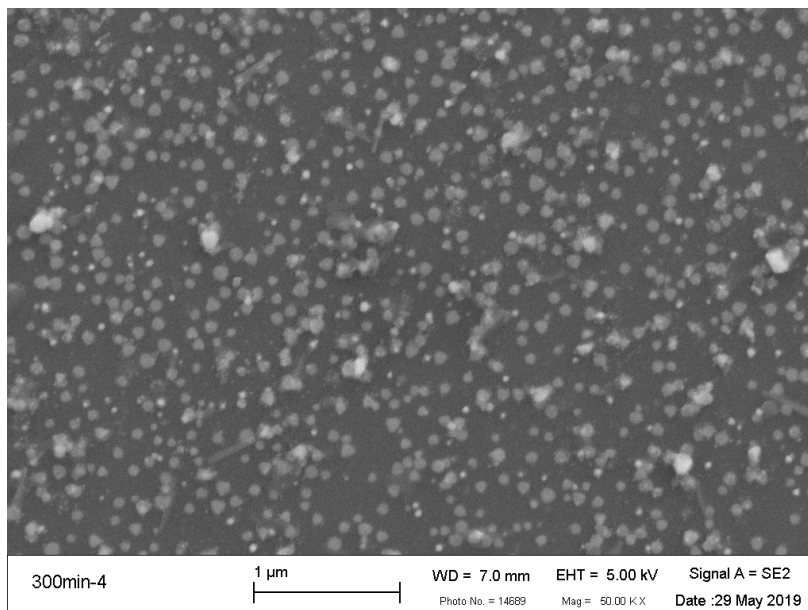


Figure 6.28: SEM image at 50,000 times magnification of a sample prepared by immersing a PAH coated slide in 800 nm LSPR nanoprisms in the dipper machine for 300 minutes, with PAH/PCBS ISAM layers applied on top. The absorbance and SHG for this sample can be found in Figures 6.29 and 6.30a.

prisms.

First, 3.5 bilayers of PAH/PCBS were applied to slides which had prisms deposited onto PAH alone, because more prisms deposited onto PAH than onto PAH/PCBS bilayers. The previously-discussed slides which had been in the dipper for 300 and 600 minutes were used because they had very good density, with extinctions above 0.6.

An SEM image taken of the 300 minute sample after top ISAM layers had been applied is presented in Figure 6.28. Many of the nanoprisms appear to have lost their triangular shape and become rounded. However, this blunting was also widespread in the SEM image of a 300 minute sample which did not have top ISAMs applied (Fig. 6.11a), and may not be due to the application of the additional ISAM layers. The extinction and SHG results are shown in Figures 6.30a and 6.30. Applying the top ISAMs resulted in a very small redshift of the peak wavelength, with little change in the peak extinction. The extinction at

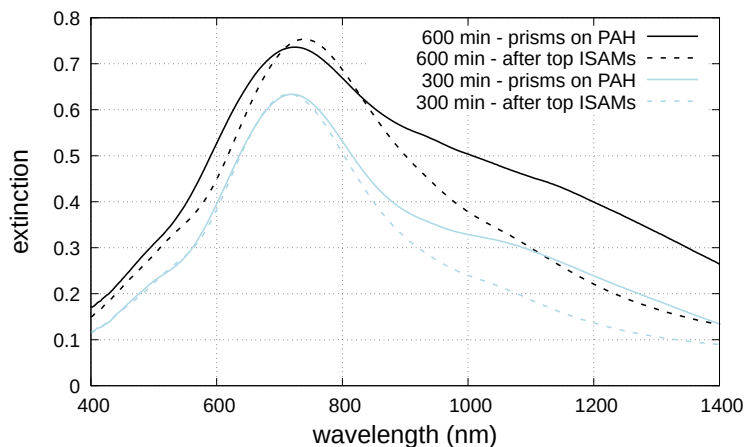
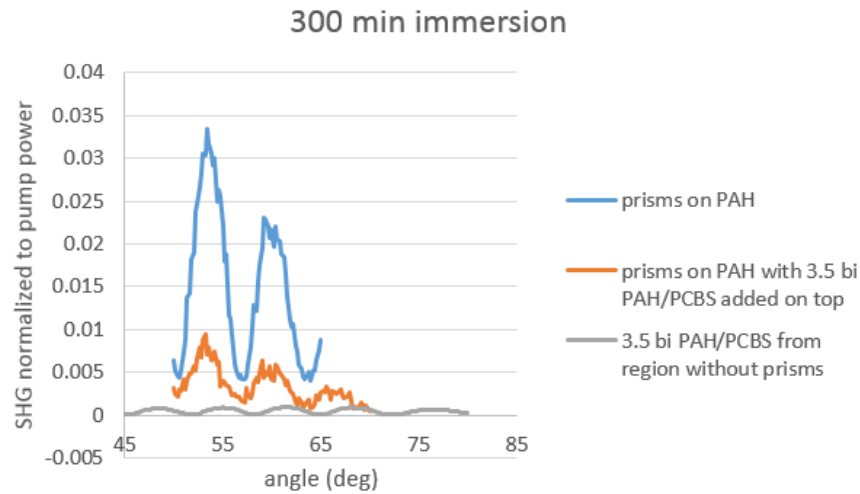


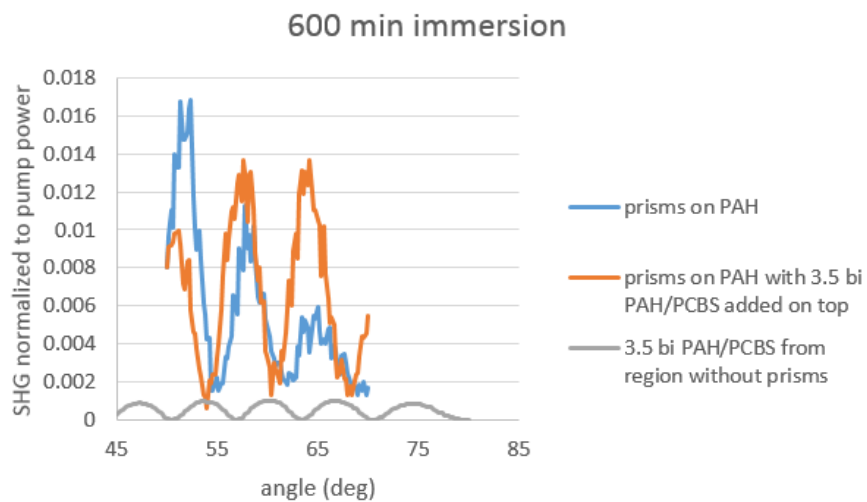
Figure 6.29: Extinction before and after applying ISAMs onto prisms deposited on PAH with the dipper for 300 minutes and 600 minutes. The additional ISAM layers had little effect on the peak extinction but did reduce the extinction at 1064 nm.

1064 nm, however, was greatly reduced. This could explain the SHG results observed. For the 300 minute slide, the prism SHG dropped significantly after the top ISAMs were added, while for the 600 minutes slide the prism SHG remained about the same. Meanwhile, the SHG from regions without prisms increased due to the additional ISAM layers, resulting in similar or lower enhancements than were observed without the new layers. From these results, it was concluded that inverting the deposition order of the nonlinear films and the nanoprisms was not a useful means of improving SHG enhancement. Prior work by this group has shown that interface effects dominate SHG at small numbers of bilayers, and in some cases increasing the number of bilayers can reduce the total SHG produced [152]. In this case, it was suspected that SHG produced by some layers was out of phase with SHG produced in other parts of the sample, resulting in an overall lower signal. It is possible that a similar effect is at play here, and could explain the failure to produce more SH light after adding ordered chromophores to the sample.

Another approach was to “sandwich” deposited prisms between ISAM films by applying additional ISAM layers onto a sample which already had nanoprisms deposited onto 3.5



(a)



(b)

Figure 6.30: SHG results before and after applying ISAMs onto prisms deposited on PAH with the dipper machine. The additional ISAM layers caused a substantial decrease in SHG for the prisms deposited for 300 minutes (a), while the SHG remained about the same for the prisms deposited for 600 minutes (b).

bilayers of PAH/PCBS. In one such case, additional ISAM layers were applied to a sample which had 900 nm prisms applied to 3.5 bilayers PAH/PCBS by immersion for 8 days, and the extinction was measured after each additional polymer layer in order to monitor the consequent redshift. Consistent with the extinction results for prisms on PAH, the change in LSPR wavelength was quite small, amounting to a shift of less than 20 nm for an additional 2.5 bilayers applied on top of the nanoprisms (Fig. 6.31). This may be because relative to the size of the nanoprisms, the ISAM layers are quite thin. The additional ISAM layers had a thickness of about 3 nm, while the nanoprisms are about 10 nm thick and have an edge length of over 100 nm. Unfortunately, SHG was not measured for this slide until after additional polymers had been spincoated onto the sample, so enhancement changes due to the additional nonlinear film layers are not known.

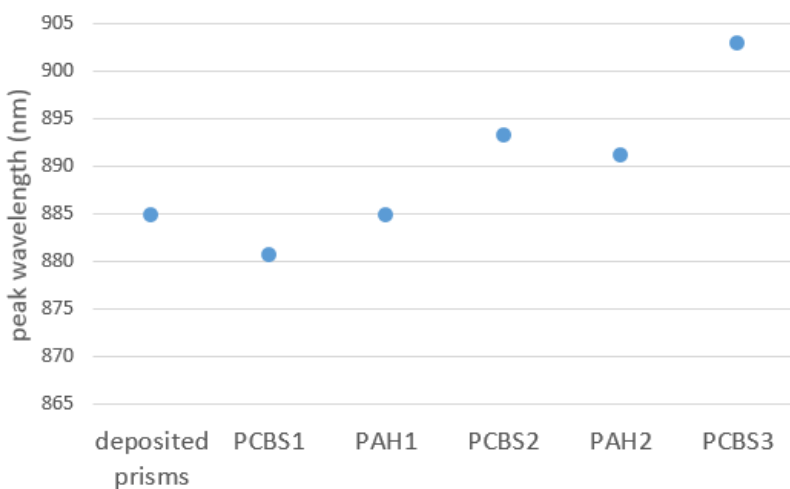


Figure 6.31: Change in peak extinction wavelength due to ISAM layers applied on top of deposited prisms.

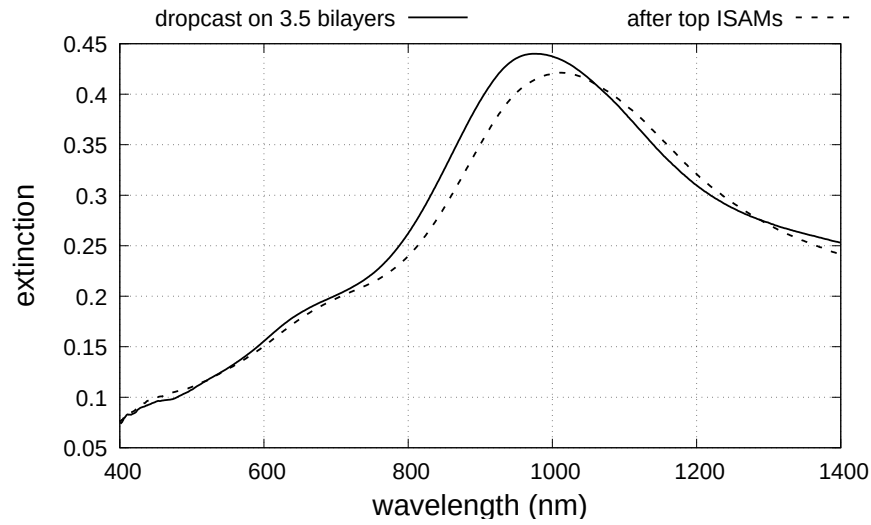
Another sample was prepared by dropcasting high concentration 1140 nm prisms onto 3.5 bilayers PAH/PCBS and applying an additional 3.5 bilayers on top. Again, the additional ISAM layers resulted in a small change in the peak extinction, with a reduction in extinction at 1064 nm. The SHG enhancement for the prisms with 3.5 bilayers above and below them

was only 12.8 times. Unfortunately, SHG was not measured prior to applying the top ISAMs to this sample, so the change in enhancement due to the top ISAMs cannot be determined. However, based on previous results for samples in which the prisms were adsorbed on PAH and the nonlinear film was applied on top, it is likely that the top ISAMs had only a small effect and may have been detrimental, which could explain the low enhancement.

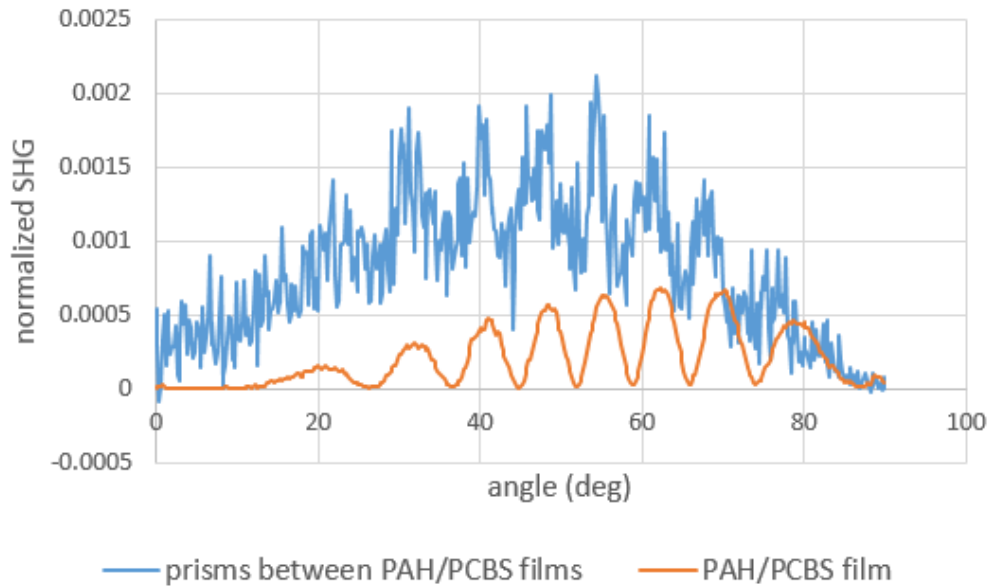
6.5.2 Spincasting polymers on top

After it was decided to focus on nanoparticles with shorter wavelengths due to their easier synthesis, it was proposed that the deposited particles be coated with a dielectric to redshift them closer to the excitation wavelength of 1064 nm. As discussed in Section 3.2, LSPR peaks are sensitive to the refractive index of the surrounding material. The condition for resonance, found in equation (3.52), indicates that the LSPR shifts to longer wavelengths if the refractive index of the surrounding medium is increased. This was accomplished by spincasting additional polymers onto the deposited prisms. The polymers investigated were PMMA, which is NLO-inactive, and PCBS, which is the NLO-active polymer in the ISAM layers.

For the PCBS spincasting, it was important to investigate how much additional SHG would be coming from spincast layer. As previously discussed, SHG requires noncentrosymmetry. Noncentrosymmetry is preserved for PCBS in ISAM layers because the electrostatic forces present create ordering in the film. However, for spincast PCBS, the orientation of the chromophores is randomized. It was therefore expected that the contribution to SHG from the spincast PCBS layer would be minimal. To experimentally determine the amount of SHG produced by the spincast PCBS layer, PCBS at concentrations ranging from 0.1 to 2.0 wt% in methanol was spincast onto plain blank microscope slides for 60 s at 4000 rpm. The



(a)



(b)

Figure 6.32: Results for 1140 nm wavelength prisms “sandwiched” between ISAMs. The prisms were deposited onto 3.5 bilayers PAH/PCBS, then an additional 3.5 bilayers was applied to the sample. The additional ISAM layers had little effect on the extinction (a). The SHG enhancement (b) was 12.8 times.

slides with higher PCBS concentrations were more visibly orange. This observation was supported by thickness measurements made with the profilometer, which showed that there was an approximately linear relationship between the polymer concentration and the thickness of the spincoated film (Fig. 6.33). SHG from these slides was measured at a pump power of 700 μJ . As can be seen in Figure 6.33, SHG was produced from these slides. However, the signal was about two orders of magnitude smaller than the signal from 3 bilayers of PAH/PCBS. This happens to be similar to the normalized SHG signal observed for nanoprisms deposited on PAH with no PCBS present, where the SHG was attributed to interface effects (Section 6.3.2). While the SHG signal from each spincoated PCBS film was phase-shifted differently, the magnitude of SHG produced was about the same. Because the amount of SHG produced was independent of the thickness of the spincoated layer, it was concluded that SHG was only being produced at the interfaces.

The goal of spincoating was to improve the match between the LSPR wavelength and the wavelength of the pump beam. It was therefore useful to determine how the redshift depends on the concentration of the spincoated solution. Dr. Liu's group reported that redshifts of about 100 nm could be achieved using PMMA of 1 percent by weight, but that distortions in the shape of the extinction spectrum occurred above 0.5 wt%. Therefore, 0.5 percent by weight was used initially as the default PMMA concentration. PCBS at concentrations of 2.3, 1.7, and 0.5 percent by weight was applied to deposited 900 nm prisms, yielding redshifts of 186, 147, and 133 nm, respectively. Because the prisms typically had LSPR peaks at less than 900 nm after deposition, and the target wavelength was 1064 nm, 2 percent by weight was preferred in order to sufficiently redshift the peak.

To investigate the contribution to SHG from spincoated PCBS, slides with spincoated PCBS and PMMA were compared. Two slides were prepared by immersing prisms onto 3.5 bilayers PAH/PCBS for 2 hours using the dipper machine. SHG and extinction were measured.

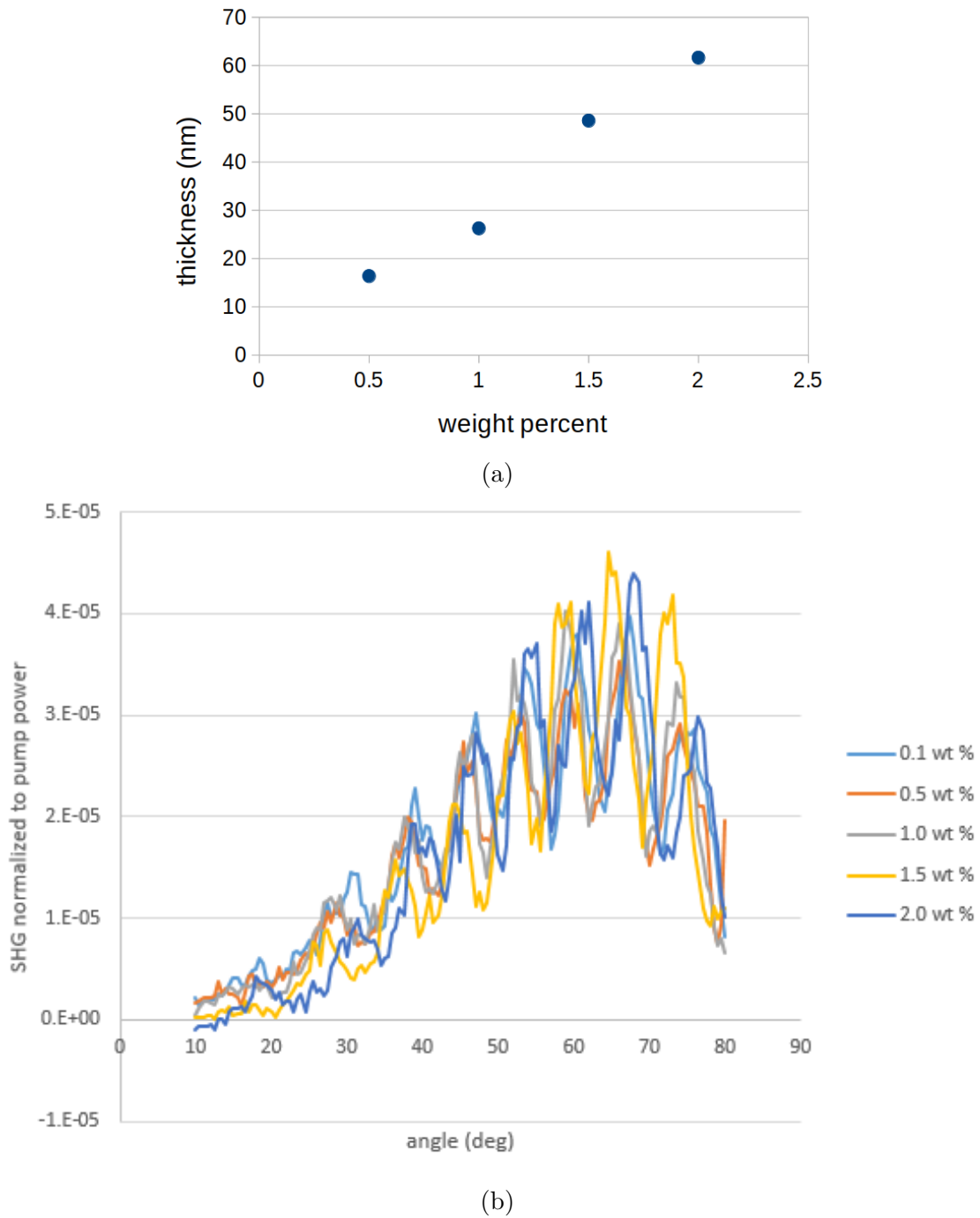


Figure 6.33: Results for PCBS spincast onto glass. Thickness was measured with the Dektak (a) and was found to vary proportionally with concentration. The SHG intensity (b) was of similar magnitude for all the samples tested, indicating that bulk PCBS did not contribute to the SHG.

Afterwards, one slide was spincoated with 2 percent by weight PMMA and the other was spincoated with 2 percent by weight PCBS. In both cases, a drop in overall extinction was accompanied by a significant redshift of the peak wavelength. The SHG from the non-prism film remained essentially unchanged after spincoating with PMMA. For the PMMA coated sample, the SHG enhancement due to the prisms was 32.4 times before spincoating and dropped slightly to 31.0 times after spincoating. For the PCBS sample, the spincoating increased the SHG from the non-prism film by about a factor of two, and a substantial increase in the prism SHG was observed. The SHG enhancement for the PCBS slide was 19.3 times before spincoating and 140.1 times after spincoating.

The effect that the volatile spincoating solvents had on the nanoprisms was a concern. Dr. Liu's group reported that the nanoprisms were largely unharmed by a short exposure to the PMMA spincoating solution, which was made with chloroform. Following the spincoating procedure reported by Goldenberg [204], the PCBS spincoating solution was made with methanol as described in Section 4.4.4. A third slide, similar to the PMMA and PCBS slides reported above, was prepared in a similar manner. This slide was meant to compare the effects of 0.5 percent by weight PCBS to 2 percent by weight PCBS, but in this case the PCBS solution was unintentionally allowed to sit on the slide for about 2 minutes prior to spincoating. The resulting extinction spectra are shown in Figure 6.35. A dramatic drop in the prism extinction was observed after the spincoating step. In the previously discussed PCBS slide, where spincoating was done immediately after the solution was applied, only a small drop in extinction occurred. These results, as well as SEM images taken of other immediately spincoated samples, led to the conclusion that methanol was harmful to the nanoprisms but that the effects could be minimized by limiting the exposure time.

Further tests were performed using PCBS as the spincoated polymer. When spincoating, only one face of the slide is coated at a time. Therefore, extinction and SHG were measured

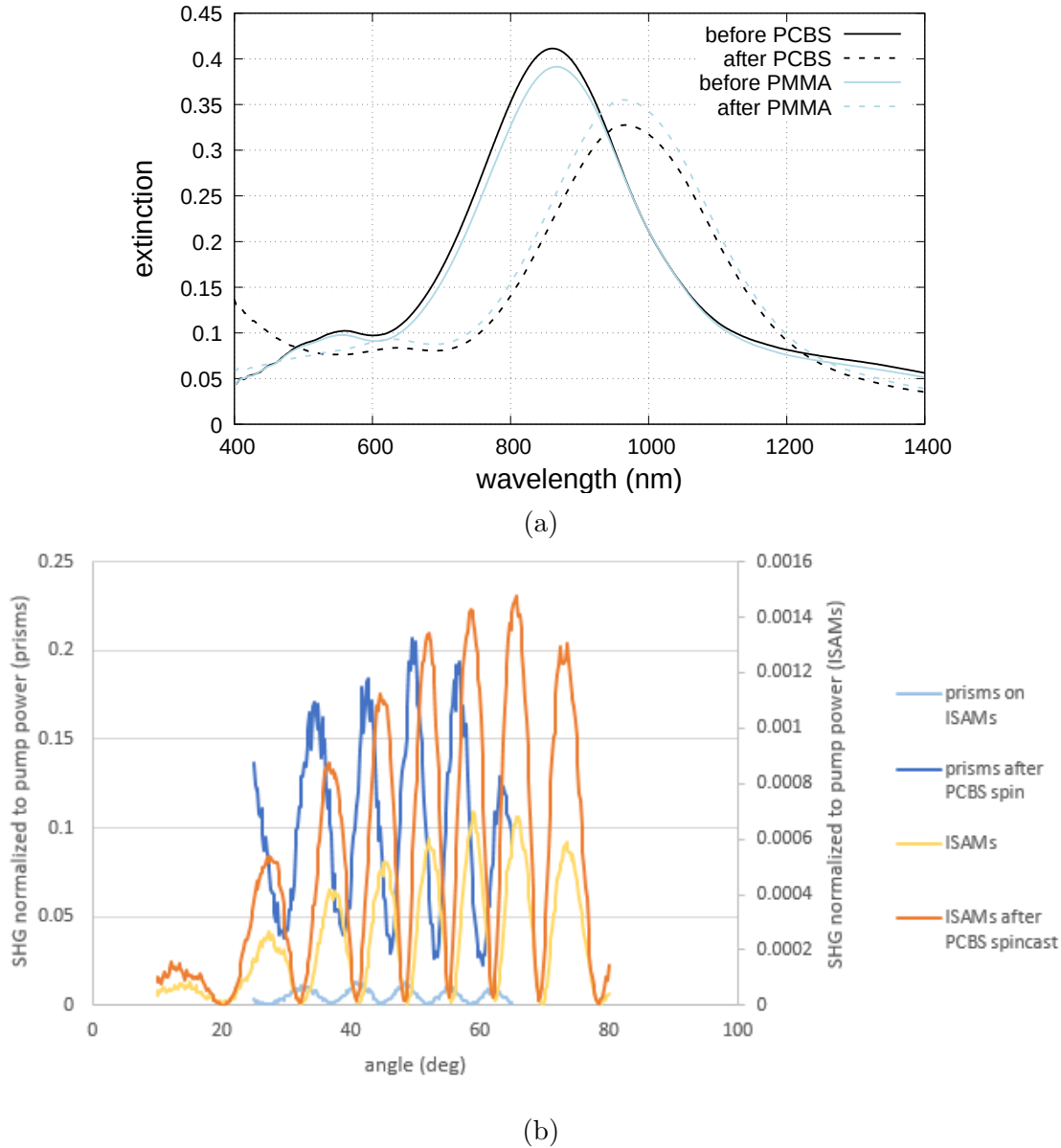


Figure 6.34: Results for prisms deposited onto 3.5 bilayers PAH/PCBS using the dipper and then spincast with equal concentrations of PMMA and PCBS. The peak extinction (a) was significantly redshifted by both polymers. The SHG (b) for the PMMA coated slide remained about the same before and after spincasting, but the enhancement for the PCBS coated slide increased from 19.3 times to 140.1 times. The SHG from the regions with and without the nanoprisms is shown on different axes due to the differing magnitudes of normalized SHG.

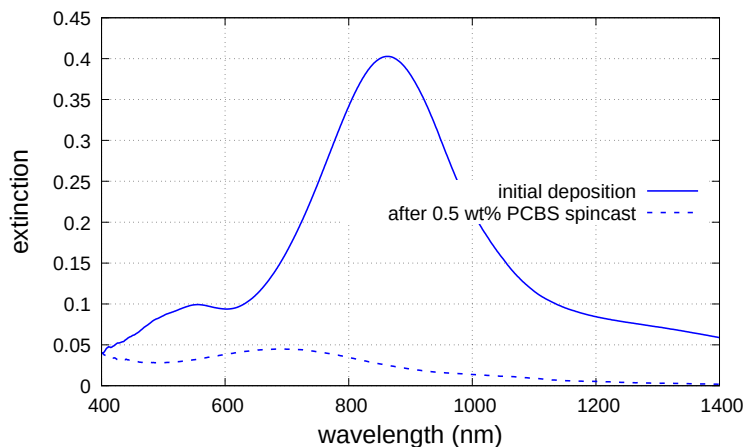


Figure 6.35: Drop in extinction of deposited prisms due to a 2 minute exposure to the methanol-PCBS solution prior to spincasting. Methanol was found to be harmful to the nanoprisms, so their exposure was minimized in later experiments by performing the spincasting immediately after applying the methanol solution.

after each face was spincast in order to observe changes after each step. First, samples with 950 nm prisms deposited by immersion and by dropcasting were studied. An ISAM-coated slide was immersed in a solution of 950 nm prisms for two weeks, resulting in surprisingly high extinction (Fig. 6.36). A second sample was prepared by dropcasting the same prisms at 80 times concentration onto an ISAM-coated slide. An SEM image of the immersion slide was presented in Figure 6.9. This slide initially had 35 times enhancement to SHG (Fig. 6.37). After spincasting one side of the slide, the enhancement remained about the same. After the second slide was spincast, the enhancement dropped to only 15 times. The drop in enhancement after spincasting could be due to damage to the nanoprisms, or due to an increase in the signal from the region without the nanoprisms. The dropcast slide initially had 84 times enhancement. After spincasting the side of the slide with the prisms, the enhancement increased to 135 times. After spincasting the back side of the slide the enhancement dropped to 63 times, because there was an increase in the ISAM signal but little change in the prism signal.

Another set of slides was prepared by dropcasting 900 nm prisms at different concentra-

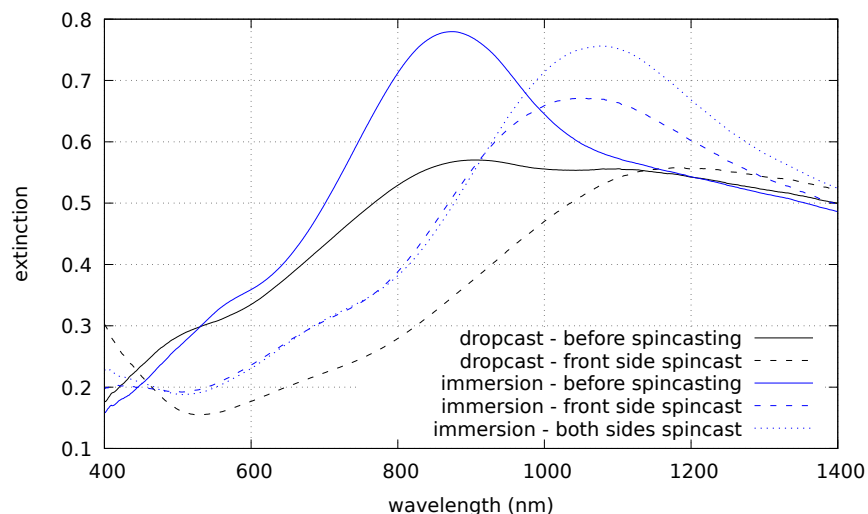
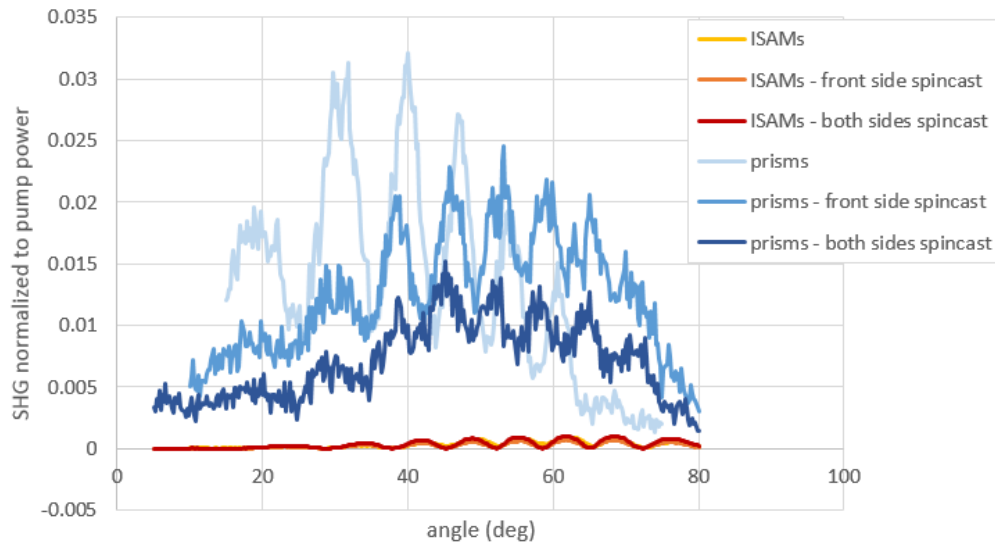
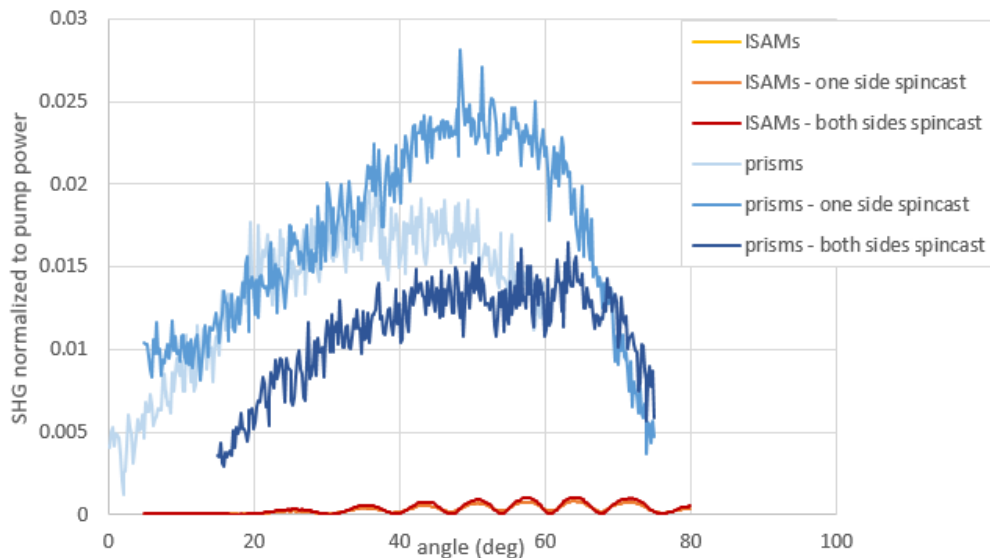


Figure 6.36: Extinction for 950 nm wavelength prisms applied via immersion and by dropcasting, before and after spincasting with 2 percent by weight PCBS. In both cases, spincasting redshifted the LSPR wavelength and decreased the peak extinction.

tions. Four milliliter aliquots of prisms were centrifuged at 5000 rpm for 15 minutes. As much supernatant as possible was pipetted out of each centrifuge tube without disturbing the isolated nanoparticles, leaving approximated $100 \mu\text{L}$ of solution at the bottom of the tubes. Three of the aliquots were redistributed with ultrapure water to achieve concentrations of 1, 2, and 4 times the original concentration. No water was added to the fourth pellet, and allowing it to remain at high concentration. The solutions were applied via dropcasting onto glass slides with 3.5 bilayers PAH/PCBS. Care was taken to limit evaporation. At the end of 24 hours, excess liquid was removed and the slides were rinsed and dried. There was a marked difference in the deposition density of the four slides. The nanoparticles applied at the stock concentration produced a light blue transparent spot. The nanoparticles at 2 and 4 times the original concentration produced significantly darker, though still transparent, spots. The nanoparticles dropcast at the maximum concentration produced a spot that was shiny, opaque, and metallic in appearance. The differences in deposition success were quantified by their extinction spectra and by SEM (Fig. 6.38). The extinction spectra for the four



(a)



(b)

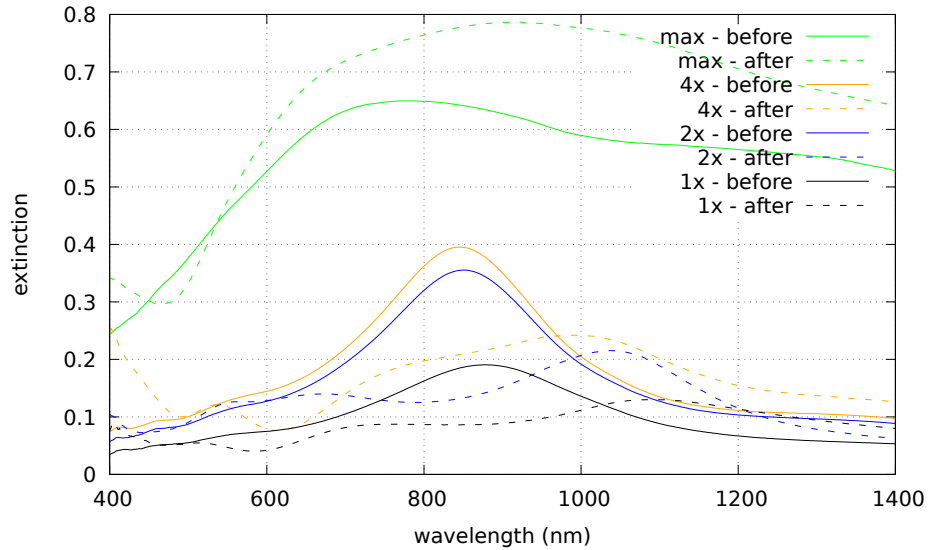
Figure 6.37: SHG for deposited 950 nm wavelength prisms before and after spincasting with 2 percent by weight PCBS. SHG was collected for slides prepared by immersion (a) and dropcasting (b). Spincasting did not increase the enhancement for the immersion slide, which started at about 35 times. Spincasting onto the prism side of the dropcast slide increased the enhancement from 84 times to 135 times.

samples clearly show the range of deposition densities achieved. The sample produced by dropcasting at the original concentration has the lowest extinction, about 0.2 near 850 nm. The intermediate slides, at 2 and 4 times the stock concentration, had higher extinctions, although these two intermediate concentrations were surprisingly similar despite differing in concentration by a factor of two. The slide produced by dropcasting only the centrifuged pellet had a significantly higher extinction than the others, of more than 0.6. The shape of the spectrum also broadened substantially, especially at longer wavelengths. This broadening is attributed to interparticle interactions due to the high density of the deposition. The inferred nanoprism densities are supported by SEM images of the samples with the highest and lowest dropcast concentrations (Fig. 6.38b,c). For the high concentration slide, the nanoparticles cluster and overlap. For the stock concentration slide, they are much sparser, and there is little to no opportunity for interparticle interactions.

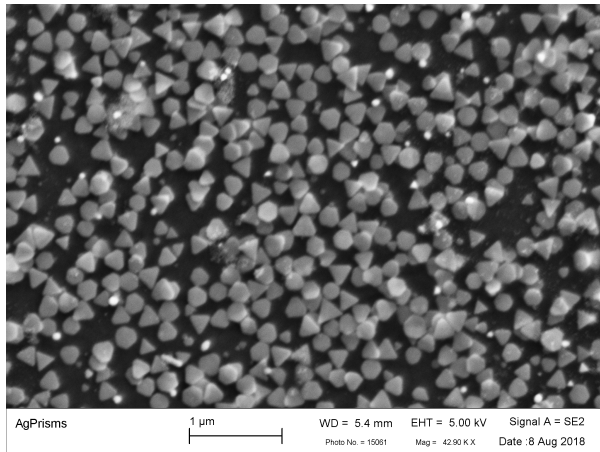
SHG results for these four slides are shown in Figure 6.39. The SHG for the stock concentration sample had a 9 times enhancement to SHG. The samples at two and four times the stock concentration performed much better but showed the inverse of the expected trend, with enhancements of 232 and 126 times, respectively. The sample at the highest concentration had by far the best enhancement, at 2368 times.

6.6 Summary of plasmonic enhancement results

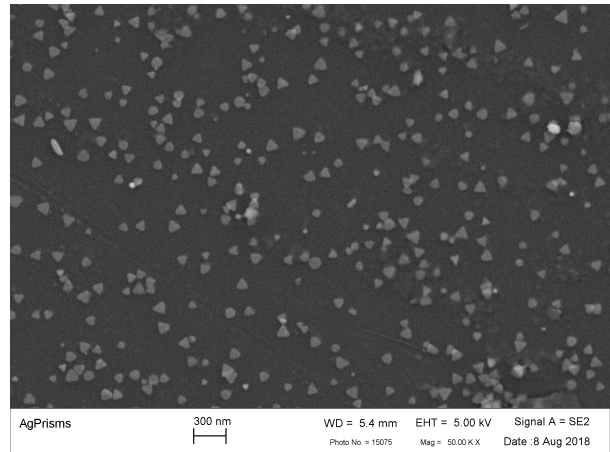
Overall, the results of this project show that SHG from self-assembled films can be significantly enhanced by the addition of silver nanoprisms. When using prisms whose LSPR wavelength after deposition matches the 1064 nm fundamental wavelength, the large size and dilute concentration of these long wavelength nanoparticles made it difficult to deposit them at sufficient densities. Despite investigating strategies to increase the adsorption of



(a)

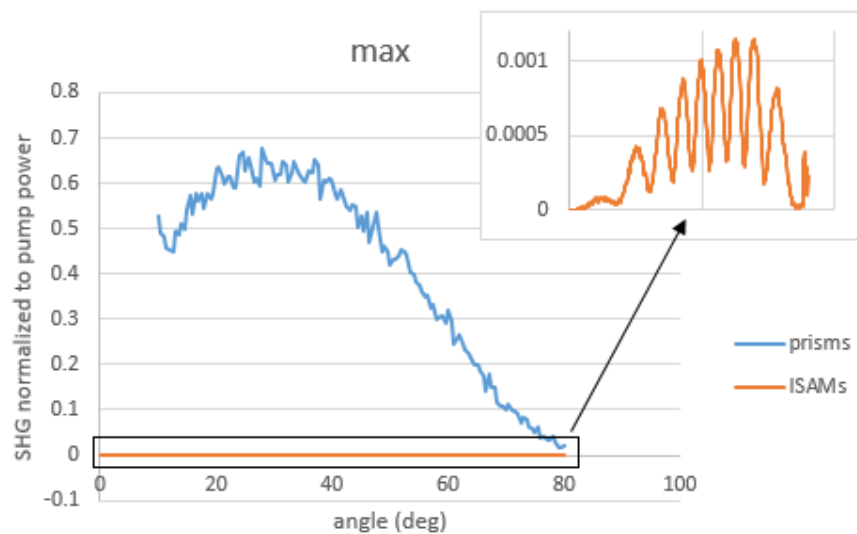


(b)

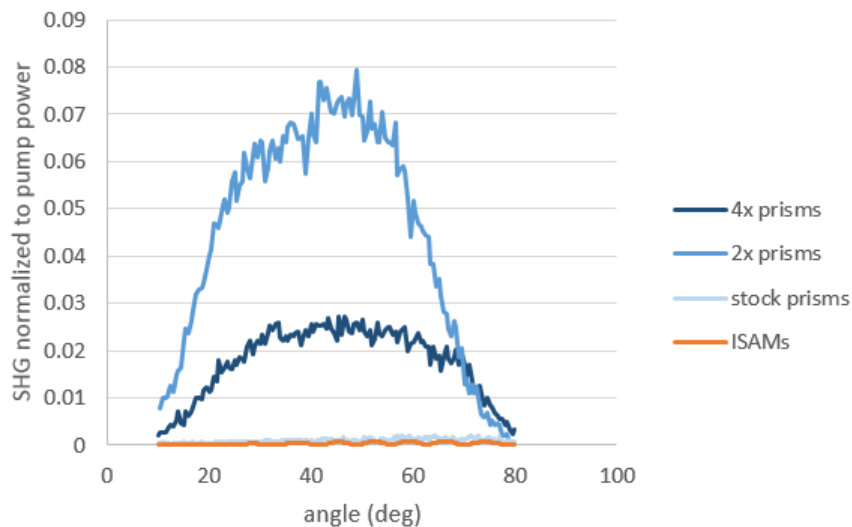


(c)

Figure 6.38: Deposition results for 900 nm wavelength prisms dropcast at high concentrations. The extinctions (a) for slides prepared with concentrated nanoprisms were high and the peaks were broadened substantially. An SEM image (b) of the sample prepared at the highest achievable concentration for this aliquot volume shows close particle spacing, in contrast to the sparse density (c) observed on a sample prepared with the stock concentration.



(a)



(b)

Figure 6.39: SHG results for slides with prisms dropcast at high concentrations. The highest concentration (a) is shown separately from the samples at and at four times, two times, and one times the stock concentration (b) due to its large normalized SHG. An inset shows the normalized SHG for a region without prisms, which was about the same for all four samples.

these particles onto the underlying ISAM films, the best SHG enhancement observed for these nanoprisms was by a factor of about two. Nanoprisms with shorter wavelength resonances are smaller in size and easier to synthesize in larger quantities and concentrations. Therefore, the focus of the work shifted to using nanoprisms with 800-950 nm wavelengths. When smaller nanoprisms were deposited at high enough densities to allow for interparticle interactions, the LSPR peak broadened toward 1064 nm, allowing them to remain compatible with the 1064 nm excitation used in the optical setup for measuring SHG. An SHG enhancement of up to 35 times was observed for 950 nm wavelength prisms deposited via stationary immersion. When the dipper machine was used to stir the solutions during immersion, higher extinctions were obtained but the SHG enhancements remained about the same. The enhancement to SHG was significantly improved by increasing the nanoprism concentration by centrifugation and dropcasting the resulting solution onto the ISAM films. There appeared to be some correlation between the concentration and the enhancement, but the effect was unpredictable. Enhancement on the order of 10-100 times were observed routinely, with a few samples exceeding 1000 times enhancement. The largest enhancement observed for this procedure was 1380 times, for a sample using 900 nm wavelength prisms where as much supernatant was removed as possible without disturbing the pellet and the resulting high-concentration nanoparticles were dropcast.

Further strategies were investigated to improve the SHG enhancement. One of these was to invert the deposition order, by applying the nanoprisms to a single layer of PAH and then adding PAH/PCBS layers on top of the deposited prisms. While this strategy led to better deposition rates when using immersion techniques, the SHG produced by the films with underlying nanoprisms was actually lower than the SHG produced by the interfaces of the nanoprisms on PAH prior to adding PAH/PCBS. Sandwiching the prisms between PAH/PCBS films also failed to improve the SHG enhancement. Better results were obtained

by spincoating additional polymers onto samples with prisms on PAH/PCBS ISAM layers. This was initially proposed as a means of redshifting the 800-950 nm wavelength nanoprisms closer to 1064 nm. The best results were obtained by spincoating polymers onto concentrated nanoprisms deposited by dropcasting. In one case this procedure increased the SHG enhancement from 19.3 times to 140.1 times. The highest SHG enhancement observed was from a sample where 4 mL of 900 nm wavelength prisms was centrifuged, as much supernatant as was feasible was removed, the high concentration solution was dropcast onto 3.5 bilayers PAH/PCBS, and the sample was later spincoated with 2 weight percent PCBS. The final enhancement for this sample was 2368 times.

Overall, the largest SHG enhancements were observed in cases where the nanoprisms were deposited at sufficient densities to have highly broadened LSPR spectra. SHG enhancements on the order of hundreds, and occasionally thousands, of times were observed. While further work would be required to improve predictability of the enhancements, this work shows that high density silver nanoprism depositions can be used to significantly enhance the nonlinear behavior of organic self-assembled films.

Chapter 7

Conclusions

An optical fiber biosensor was investigated for its ability to detect and differentiate species of *Brucella* bacteria. *Brucella* has serious deleterious effects on the health and reproduction of livestock, resulting in the potential for significant economic losses in agriculture. *B. abortus* primarily affects cattle and other bovines, while *B. melitensis* is more implicated in sheep and goats and *B. suis* in swine. Although *B. abortus* has been largely eliminated in domestic herds, it remains endemic in wild cervid populations such as deer and elk. A rapid, compact, and durable sensor is desirable to allow *B. abortus* to be diagnosed in the field in order to monitor threats from adjacent wildlife.

The optical fiber biosensor project showed that a TAP-LPG fiber could be used to detect bacteria, however, the sensitivity of the fibers available for the work in this dissertation was a major limitation. This group previously demonstrated the ability to detect as few as 100 cells of *H. somni* using a TAP-LPG with a dynamic range of about -27 dB, corresponding to a maximum attenuation of transmission of about a factor of 1000. Unfortunately, the fiber gratings are fragile due to their exposed sensing region, and become increasingly brittle after repeated cleaning cycles. When subject to daily use, the optical fibers used in our lab were found to have a typical lifetime on the order of months. Consequently, the experiments reported in this work were performed using surviving TAP-LPGs with a dynamic range of about -10 dB, which had a smaller change in transmission due to binding events than the earlier fibers.

Fabrication of TAP-LPGs by CO₂ laser was attempted with on a setup managed by Dr. Anbo Wang at the Virginia Tech Center for Photonics Technology. Despite multiple attempts to fabricate gratings using parameters from literature and recommended by other students using the setup, none of the LPGs produced showed modifications to their transmission spectra consistent with coupling between the core and cladding modes. When the power was increased in order to produce visible tapering, it was found that the tapers were uneven and that the gratings lacked periodicity. This was attributed to power fluctuations in the laser, which may have exceeded predicted levels due to the age of the device and its poor temperature regulation. Uneven tension due to movement of the hanging mass used to exert prestrain may also have contributed. The work was also hindered by inherent limitations of the CO₂ laser technique, which is known to suffer from poor reliability and repeatability [89]. Fabrication techniques using UV lasers are therefore preferable. Ideally, a reliable supply of identical TAP-LPGs could be established by developing a fabrication technique using a UV laser with a phase mask. This would allow for high-throughput fabrication of sensitive TAP fibers with predictable behavior. Because the gratings can be written into inexpensive telecommunications fibers, a practical device could be developed using single-use fiber gratings, eliminating the need for a cleaning step.

In this work, the results of studies varying the concentrations of the functionalization materials are presented. It was found that elevating the concentrations of streptavidin or hybridization probe failed to improve the sensor's performance. The sensor also did not show an increase in signal when exposed to higher analyte concentrations, which indicated that the dynamic range was insufficient to effectively quantify the concentration of bacteria present. The sensor was able to distinguish between cultures of *Brucella* and other bacteria genera, although with a low level of statistical significance. Attempts to distinguish between *B. abortus*, *B. melitensis*, and *B. suis* using species specific probes was less successful. While

the mean signal from positive controls was larger than the signal from negative controls, they were within one standard deviation of each other, and in some individual runs the negative control produced a larger signal than the positive control. Better results were obtained using samples obtained from mice, where the transmission change was $6.0 \pm 1.4\%$ for samples from mice infected with *Brucella* and $0.5 \pm 2.0\%$ from mice injected with saline. This was possibly due to the tissue samples having higher bacterial concentrations than were used in the culture experiments, although it is expected that the tissue samples would have lower concentrations. Alternatively, differences in how the various sample types were treated may be responsible for some of the trends observed in the results. For example, the USDA samples (Section 5.4.3) were killed more aggressively than other cell cultures, which may have degraded their DNA and resulted in the poor results observed. In contrast, the mouse tissues (Section 5.5) had comparatively gentler treatment prior to transfer to our lab, and may have arrived with their DNA in better condition.

In order to further develop the biosensor, further testing would be necessary to establish a definite ability to distinguish between positive and negative controls. While most of the tests presented here exposed the sensor to the positive sample first, it would be important to vary the order and determine how many exposures could be reliably tested with sensor before cleaning and refunctionalizing the fiber. This was not done in this work because of poor performance of the available sensor. The sample order was kept fixed in order to collect results without the confusion of additional variables, and because it was expected that more rigorous tests could be performed with superior LPGs in the future. The sample order is a serious limitation on the work presented here, and should be addressed in similar projects in the future. Once these properties are established with bacterial cultures, more samples from living specimens should be tested to ensure that the assay still behaves well when other materials are in the solution. It may be necessary to add additional steps to help protect

the sensor from nonspecific binding.

The second project presented in this dissertation concerns the plasmonic enhancement of SHG from nonlinear ISAM films by colloiddally grown silver nanoprisms. Nonlinear optics has a variety of useful applications in optoelectronics, sensing, light generation, and other fields. SHG in particular is used for frequency doubling of radiation sources, second-harmonic surface spectroscopy, and second-harmonic microscopy. However, the inorganic crystals typically used for nonlinear optics are difficult to grow with sufficient optical quality and are consequently expensive. Organic alternatives are often easier to synthesize and offer additional benefits and features such as wider choice in molecular structure and mechanical flexibility. Polymers are particularly popular due to the availability of well-established processing techniques. However, because organic nonlinear media often have a lower nonlinear susceptibility than their inorganic counterparts, strategies for increasing their nonlinear behavior are important. Because nonlinear effects occur in the presence of strong electric fields, they can be amplified by the presence of plasmonic structures, which produce strong enhancements to the electric field within a range of a few nanometers. These enhancements are especially strong for noble metal nanoparticles with high aspect ratios or sharp tips and edges.

In previous work by this group, SHG enhancements from PAH/PCBS ISAM films of up to 1600 times and 100 times was observed due to silver nanotriangles created by nanosphere lithography and colloidal gold nanorods, respectively. In this dissertation, enhancement due to colloidal silver nanoprisms fabricated in the group of Professor Guoliang (Greg) Liu in the Department of Chemistry was studied. Nanoprisms with an LSPR near 1140 nm were studied initially because their LSPR after adsorption was near the wavelength of the fundamental beam. However, these nanoprisms were quite large and were synthesized at low concentrations.

Despite several attempts to alter the deposition procedure, the number of adsorbed nanoprisms on the ISAM film was not significantly improved, and the maximum enhancement observed with these prisms was 2.3 times. Better results were observed when using nanoprisms with shorter LSPR wavelengths. Although these were not matched as well with the wavelength of the Nd:YAG laser, some SHG enhancements were observed. Using basic immersion to deposit the nanoprisms, the highest enhancement obtained was 35 times for 950 nm wavelength prisms on 3.5 bilayers PAH/PCBS for two weeks, compared to the bare PAH/PCBS film. The nanoprisms deposited more readily onto a single PAH layer. Compared to the SHG produced by the glass/PAH/air interfaces, SHG enhancements of up to 135 times were obtained for 800 nm wavelength nanoprisms immersed while stirring with the dipper machine. More pronounced SHG enhancements were obtained when additional strategies were employed to increase the absorption at 1064 nm. Nanoprisms that were centrifuged to increase their concentration exhibited peak broadening due to interparticle interactions, which when combined with the high nanoparticle density was able to produce large SHG enhancements. High enhancements were possible using this strategy, but the degree of enhancement was unpredictable. In one set of three samples prepared using the same procedure, the SHG enhancements varied from 113 to 1380 times. Further strategies investigated to increase the SHG included applying additional polymers to the deposited prisms. Surprisingly, applying PAH/PCBS layers failed to increase the SHG enhancement, and in some cases decreased it. Spincasting polymers onto the prisms in order to redshift their LSPR peak was more successful. The best enhancement observed in this work occurred for a sample of 900 nm wavelength prisms dropcast at high concentration onto 3.5 bilayer of PAH/PCBS and then spincast with 2 percent by weight PCBS, resulting in an SHG enhancement of 2368 times.

Several questions remain which could be elucidated by future work. While increasing

the nanoprism concentration by centrifugation was successful in improving the SHG enhancement, attempts to determine the optimum concentration has so far been inconclusive. Further experiments to determine the concentration and dropcasting parameters that optimize SHG enhancement would be beneficial. Additionally, further investigation could be done into the surprisingly poor results obtained when applying nonlinear ISAM films onto deposited prisms. It was expected that by locating more of the nonlinear film in close proximity to the plasmonically enhanced fields the SHG could be increased substantially, however, this was not observed. Because a practical device would likely require repeated layers of ISAMs and plasmonic particles in order to attain sufficient conversion efficiency, the reasons for the low SHG observed for top ISAMs should be determined. Another concern that should be addressed is the SHG contribution from the spincast PCBS in samples where this step was performed. Although the SHG results for spincast films of different thicknesses suggest that this was not a major contribution, a more rigorous study should be conducted. Finally, stability of the samples over time should be established. The silver nanoprisms used in this work were photosensitive and could be subject to tarnishing, both of which may alter the LSPR peak and the performance of the samples produced in this work.

Bibliography

- [1] Zhiyong Wang. *Ionic Self-Assembled Multilayers Adsorbed on Long Period Fiber Gratings for Use as Biosensors*. PhD thesis, Virginia Polytechnic Institute, Blacksburg, VA, 12 2005.
- [2] Tiffanie Gabrielle D'Alberto. Long-period gratings as immuno-diagnostic biosensors. Master's thesis, Virginia Polytechnic Institute, Blacksburg, VA, 1 1997.
- [3] Sadao Adachi. *The Handbook on Optical Constants of Metals: In Tables and Figures*. World Scientific Publishing Co. Pte. Ltd., 2012.
- [4] Damian Aherne, Deirdre M. Ledwith, Matthew Gara, and John M. Kelly. Optical properties and growth aspects of silver nanoprisms produced by a highly reproducible and rapid synthesis at room temperature. *Advanced Functional Materials*, 18:2005–2016, 2008.
- [5] Jeong-Ah Lee. *Plasmonic Enhancement of Nonlinear Optical Responses by Gold Nanorods*. PhD thesis, Virginia Polytechnic Institute, Blacksburg, VA, 12 2016.
- [6] Xinwei Lan, Qun Han, Jie Huang, Hanzheng Wang, Zhan Gao, Amerdeep Kaur, and Hai Xiao. Turn-around point long-period fiber grating fabricated by co2 laser for refractive index sensing. *Sensors and Actuators B: Chemical*, 117:1149–1155, 2013.
- [7] Kai Chen, Cemil Durak, James R. Heflin, and Hans D. Robinson. Plasmon-enhanced second-harmonic generation from ionic self-assembled multilayer films. *Nano Letters*, 7:254–258, 2007.

- [8] Gero Decher. Fuzzy nanoassemblies: Toward layered polymeric multicomposites. *Science*, 277:1232–1237, 1997.
- [9] Charles Figura, Patrick J. Neyman, Daniela Marciu, Charles Brands, Mandy Amanda Murray, Steve Hair, Rick M. Davis, Michael B. Miller, and James Randy Heflin. Thermal stability and immersion solution dependence of second order nonlinear optical ionically self-assembled films. In Donal D. C. Bradley and Bernard Kippelen, editors, *Proceedings of SPIE: Organic Photonic Materials and Devices II*, volume 3939, pages 214–222, May 2000.
- [10] Alexandru M. Avram, Pejman Ahmadiannamini, Anh Vu, Xianghong Qian, Arigit Sen Gupta, and S. Ranil Wickramasinghe. Polyelectrolyte multilayer modified nanofiltration membranes for the recovery of ionic liquid from dilute aqueous solutions. *Journal of Applied Polymer Science*, 134, 2017.
- [11] Pejman Ahmadiannamini, Xianfeng Li, Ward Goyens, Boudewijn Meesschaert, and Ivo F. J. Vankelecom. Multilayered PEC nanofiltration membranes based on SPEEK/PDDA for anion separation. *Journal of Membrane Science*, 360:250–258, 2010.
- [12] Jonathan S. Metzman, Guanyu Wang, John R. Morris, and James R. Heflin. Enhanced scratch resistance of self-assembled silica nanoparticle anti-reflection coatings. *Journal of Materials Chemistry C*, 6:823–835, 2018.
- [13] Dongjin Lee and Tianhong Cui. Layer-by-layer self-assembled single-walled carbon nanotubes based ion-sensitive conductometric glucose biosensors. *IEEE Sensors Journal*, 9:449–456, 2009.
- [14] Zhangpeng Li, Jingjing Wang, Xiaohong Liu, Sheng Liu, Junfei Ou, and Shenrong Yang. Electrostatic layer-by-layer self-assembly multilayer films based on graphene

- and manganese dioxide sheets as novel electrode materials for supercapacitors. *Journal of Materials Chemistry*, 21:3397–3403, 2011.
- [15] C. Q. Peng, Y. S. Thio, and R. A. Gerhardt. Conductive paper fabricated by layer-by-layer assembly of polyelectrolytes and ITO nanoparticles. *Nanotechnology*, 19:1–10, 2001.
- [16] Bill G. X. Zhang, Damian E. Myers, Gordon G. Wallace, Milan Brandt, and Peter F. M. Choong. Bioactive coatings for orthopaedic implants: Recent trends in development of implant coatings. *International Journal of Molecular Sciences*, 15:11878–11921, 2014.
- [17] Jouha Min, Ki Young Choi, Erik C. Dreaden, Robert F. Padera, Richard D. Braatz, Myron Spector, and Paula T. Hammond. Designer dual therapy nanolayered implant coatings eradicate biofilms and accelerate bone tissue repair. *ACS Nano*, 10:4441–4450, 2016.
- [18] Safitree Nawae, Jirut Meesane, Nantakan Muensit, and Chalongrat Daengngam. Layer-by-layer self-assembled films of silk fibroin/collagen/poly(diallyldimethylammonium chloride) as nucleating surface for osseointegration to design coated dental implant materials. *Materials and Design*, 160:1158–1167, 2018.
- [19] Gerd Keiser. *Optical Fiber Communications*. McGraw-Hill, 2011.
- [20] Turan Erdogan. Fiber grating spectra. *Journal of Lightwave Technology*, 15:1277–1294, 1997.
- [21] D. D. Davis, T. K. Gaylord, E. N. Glystis, S.G. Kosinski, S. C. Mettler, and A. M. Vengsarkar. Long-period fibre grating fabrication with focused CO₂ laser pulses. *Electronics Letters*, 34:302–303, 1998.

- [22] S. Savin, M. J. F. Digonnet, G. S. Kino, and H. J. Shaw. Tunable mechanically induced long-period fiber gratings. *Optics Letters*, 25:710–712, 2000.
- [23] Xuewen Shu, Lin Zhang, and Ian Bennion. Sensitivity characteristics of long-period fiber gratings. *Journal of Lightwave Technology*, 20, 2002.
- [24] Ziwei Zuo. *Development of an optical fiber biosensor with nanoscale self-assembled affinity layer*. PhD thesis, Virginia Polytechnic Institute, Blacksburg, VA, 11 2013.
- [25] Aloka B. Bandara, Ziwei Zuo, Kelly McCutcheon, Siddarth Ramachandran, James R. Heflin, and Thomas J. Inzana. Identification of histophilus somni by a nanomaterial optical fiber biosensor assay. *Journal of Veterinary Diagnostic Investigation*, 30:861–829, 2018.
- [26] Pavel Damborský, Juraj Švitel, and Jaroslav Katrlík. Optical biosensors. *Essays in Biochemistry*, 60:91–100, 2016.
- [27] Nikhil Bhalla, Pawan Jolly, Nello Formisano, and Pedro Estrela. Introduction to biosensors. *Essays in Biochemistry*, 60:1–8, 2016.
- [28] Sergey M. Borisov and Otto S. Wolfbeis. Optical biosensors. *Chemical Reviews*, 108:423–461, 2008.
- [29] Xudong Fan, Ian M. White, Sikya I. Shopova, Hongying Zhu, Jonathan D. Suter, and Yuze Sun. Sensitive optical biosensors for unlabeled targets: a review. *Analytica Chimica Acta*, 620:8–26, 2008.
- [30] Robert W. Boyd. *Nonlinear Optics*. Academic Press, 2008.
- [31] Paul Campagnola. Second harmonic generation imaging microscopy: Applications to diseases diagnostics. *Analytical Chemistry*, 83:3224–3231, 2011.

- [32] Peter Günter, editor. *Nonlinear Optical Effects and Materials*. Springer-Verlag, Berlin Heidelberg, 1 edition, 2000.
- [33] Stefan Alexander Maier. *Plasmonics: Fundamentals and Applications*. Springer US, 2007.
- [34] Heinz Raether. *Surface Plasmons on Smooth and Rough Surfaces and Gratings*. Springer-Verlag Berlin Heidelberg New York, 1988.
- [35] Stephan Link and Mostafa A. El-Sayed. Spectral properties and relaxation dynamics of surface plasmon electronic oscillations in gold and silver nanodots and nanorods. *Journal of Physical Chemistry B*, 103:8410–8426, 1999.
- [36] Assad U. Khan, Shuqi Zhao, and Guoliang Liu. Key parameter controlling the sensitivity of plasmonic metal nanoparticles: aspect ratio. *Journal of Physical Chemistry C*, 120:19353–19364, 2016.
- [37] Encai Hao and George C. Schatz. Electromagnetic fields around silver nanoparticles and dimers. *Journal of Chemical Physics*, 120:357–366, 2004.
- [38] A. C. Fou, O. Onitsuka, M. Ferreira, and M. F. Rubner. Fabrication and properties of light-emitting diodes based on self-assembled multilayers of poly(phenylene vinylene). *Journal of Applied Physics*, 79:7501–7509, 1996.
- [39] Michel Eckle and Gero Decher. Tuning the performance of layer-by-layer assembled organic light emitting diodes by controlling the position of isolating clay barrier sheets. *Nano Letters*, 1:45–49, 2001.
- [40] S. Antohe, Sorina Iftimie, Laura Hrostea, V. A. Antohe, and Mihaela Girtan. A critical review of photovoltaic cells based on organic monomeric and polymeric thin film heterojunctions. *Thin Solid Films*, 642:219–231, 2017.

- [41] P. Peumans, A. Yakimov, and S. R. Forrest. Small molecular weight organic thin-film photodetectors and solar cells. *Journal of Applied Physics*, 93:3693–3723, 2003.
- [42] Colin Reese, Mark Roberts, Mangmang Ling, and Zhenan Bao. Organic thin film transistors. *Materials Today*, 7:20–27, 2004.
- [43] John A. Rogers, Takao Someya, and Yonggang Huang. Materials and mechanics for stretchable electronics. *Science*, 327:1603–1607, 2010.
- [44] Frank Schreiber. Structure and growth of self-assembling monolayers. *Progress in Surface Science*, 65:151–256, 2000.
- [45] Katsuhiko Ariga, Jonathan P. Hill, and Qingmin Ji. Layer-by-layer assembly as a versatile bottom-up nanofabrication technique for exploratory research and realistic application. *Physical Chemistry Chemical Physics*, 9:2319–2340, 2004.
- [46] R. H. Tredgold. The physics of Langmuir-Blodgett films. *Reports on Progress in Physics*, 50, 1987.
- [47] Gleb B. Sukhorukov, Edwin Donath, Heinz Lichtenfeld, Eberhard Knippel, Monika Knippel, Axel Budde, and Helmuth Möhwald. Layer-by-layer self-assembly of polyelectrolytes on colloidal particles. *Colloids and Surfaces A: Physicochemical and Engineering Aspects*, 137:253–266, 1998.
- [48] Susan E. Burke and Christopher J. Barrett. Acid-base equilibria of weak polyelectrolytes in multilayer thin films. *Langmuir*, 19:3297–3303, 2003.
- [49] S. S. Shiratori and M. F. Rubner. pH-dependent thickness behavior of sequentially adsorbed layers of weak polyelectrolytes. *Macromolecules*, 33:4213–4219, 2000.

- [50] Harekrishna Ghosh and Thomas Bürgi. Adsorption of gold and silver nanoparticles on polyelectrolyte layers and growth of polyelectrolyte multilayers: An in-situ ATR-IR study. *Journal of Physical Chemistry C*, 117:26652–26658, 2013.
- [51] Jin-An He, Ravi Mosurkal, Lynne A. Samuelson, Lian Li, and Jayant Kumar. Dye-sensitized solar cell fabricated by electrostatic layer-by-layer assembly of amphoteric TiO₂ nanoparticles. *Langmuir*, 19:2169–2174, 2003.
- [52] Alexander G. Agrios, Ilkay Cesar, Pascal Comte, M. K. Nazeeruddin, and Michale Grätzel. Nanostructured composite films for dye-sensitized solar cells by electrostatic layer-by-layer deposition. *Chemistry of Materials*, 18:5395–5397, 2006.
- [53] Nichols A. Kotov, Imre Dékány, and Janos H. Fendler. Layer-by-layer self-assembly of polyelectrolyte-semiconductor nanoparticle composite films. *Journal of Physical Chemistry*, 99:13065–13069, 1995.
- [54] Jocelyn F. Hicks, Young Seok-Shon, and Royce W. Murray. Layer-by-layer growth of polymer/nanoparticle films containing monolayer-protected gold clusters. *Langmuir*, 18:2288–2294, 2002.
- [55] Stefan Mühlig, Alistair Cunningham, José Ditinger, Mohamed Farhat, Shakeeb Bin Hasan, Toralf Scharf, Thomas Bürgi, Falk Lederer, and Carsten Rockstuhl. A self-assembled three-dimensional cloak in the visible. *Scientific Reports*, 3, 2013.
- [56] Paula T. Hammond. Building biomedical materials layer-by-layer. *Materials Today*, 15:196–206, 2012.
- [57] Zhiyong Tang, Ying Wang, Paul Podsiadlo, and Nicholas A. Kotov. Biomedical applications of layer-by-layer assembly: From biomimetics to tissue engineering. *Advanced Materials*, 18:3203–3224, 2006.

- [58] Stephen T. Dubas and Joseph B. Schlenoff. Polyelectrolyte multilayers containing a weak polyacid: construction and destruction. *Macromolecules*, 34:3736–3740, 2001.
- [59] Benjamin Thierry, Françoise M. Winnik, Yahye Merhi, and Maryam Tabrizian. Nanocoatings onto arteries by layer-by-layer deposition: Toward the in-vivo repair of damaged blood vessels. *Journal of the American Chemical Society*, 125:7494–7495, 2003.
- [60] Michael J. Landry, Frédéric-Guillaume Rollet, Timothy E. Kennedy, and Christopher J. Barret. Layers and multilayers of self-assembled polymers: tunable engineered extracellular matrix coatings for neural cell growth. *Langmuir*, 34:8709–8730, 2018.
- [61] Sohyeon Park, Uiyoungh Han, Daheui Choi, and Jinkee Hong. Layer-by-layer assembled polymeric thin films as prospective drug delivery carriers: design and applications. *Biomaterials research*, 22, 2018.
- [62] Constant Vodouhê, Erell Le Guen, Juan Mendez Garza, Gregory Francius, Christophe Déjugnat, Joël Ogier, Pierre Schaaf, Jean-Claude Voegel, and Philippe Lavallo. Control of drug accessibility on functional polyelectrolyte multilayer films. *Biomaterials*, 27:4149–4156, 2006.
- [63] Fu Zhang, Qi Wu, Li-Jun Liu, Zhi-Chun Chen, and Xian-Fu Lin. Thermal treatment of galactose-branched polyelectrolyte microcapsules to improve drug delivery with reserved targetability. *International Journal of Pharmaceutics*, 357:22–31, 2008.
- [64] Y. F. Fan, Y. N. Wang, Y. G. Fan, and J. B. Ma. Preparation of insulin nanoparticles and their encapsulation with biodegradable polyelectrolyte via the layer-by-layer adsorption. *International Journal of Pharmaceutics*, 324:158–167, 2006.

- [65] Piaysi Mukhopadhyay, Roshnara Mishra, Dipak Rana, and Patit P. Kundu. Strategies for effective oral insulin delivery with modified chitosan nanoparticles: A review. *Progress in polymer science*, 37:1457–1475, 2012.
- [66] Michael T. Cook, George Tzortzis, Vitaliy V. Khutoryanskiy, and Dimitris Charalampopoulos. Layer-by-layer coating of alginate matrices with chitosan-alginate for the improved survival and targeted delivery of probiotic bacteria after oral administration. *Journal of Materials Chemistry B*, 1, 2013.
- [67] Rolf Kniprath, James T. McLeskey, Jürgen P. Rabe, and Stefan Kirstein. Nanostructured solid-state hybrid photovoltaic cells fabricated by electrostatic layer-by-layer deposition. *Journal of Applied Physics*, 105, 2009.
- [68] Jeri’ann Hiller, Jonas D. Mendelsohn, and Michael F. Rubner. Reversibly erasable nanoporous anti-reflection coatings from polyelectrolyte multilayers. *Nature Materials*, 1:59–63, 2001.
- [69] Vaihab Jain, Hank Yochum, Hong Wang, Reza Montazami, Mónica A. Vidales Hurtado, Arturo Mendez Galván, Harry W. Gibson, and James R. Heflin. Solid-state electrochromic devices via ionic self-assembled multilayers (ISAM) of a polyviologen. *Macromolecular Chemistry and Physics*, 209:150–157, 2008.
- [70] Toru Ishigami, Kuniaki Amano, Akihiro Fujii, Yoshikageg Ohmukai, Eiji Kamio, Tatsuo Marumaya, and Hideto Matsumaya. Fouling reduction of reverse osmosis membrane by surface modification via layer-by-layer assembly. *Separation and Purification Technology*, 99:1–7, 2012.
- [71] Sven H. Behrens and David G. Greger. The charge of glass and silica surfaces. *Journal of Chemical Physics*, 115:6716–6721, 2001.

- [72] Hassan H. Rmaile and Joseph B. Schlenoff. "Internal pKa's" in polyelectrolyte multilayers: Coupling protons and salt. *Langmuir*, 18:8263–8265, 2002.
- [73] Kevin G. Yager and Christopher J. Barrett. Chapter 17 azobenzene polymers as photomechanical and multifunctional smart materials. In *Intelligent Materials*, pages 424–446. The Royal Society of Chemistry, 2008.
- [74] Kevin G. Yager and Christopher J. Barrett. *Intelligent Materials*. The Royal Society of Chemistry, 2007.
- [75] Akhilesh Garg, Richey M. Davis, Cemil Durak, James R. Heflin, and Harry W. Gibson. Polar orientation of a pendant anionic chromophore in thick layer-by-layer self-assembled polymeric films. *Journal of Applied Physics*, 104, 2008.
- [76] Zhiyong Wang, J. R. Heflin, Rogers H. Stolen, and Siddharth Ramachandran. Analysis of optical response of long period fiber gratings to nm-thick thin-film coatings. *Optics Express*, 13:2808–2813, 2005.
- [77] H. H. Hopkins and N. Singh Kapany. A flexible fibrescope, using static scanning. *Nature*, 173:39–41, 1954.
- [78] Peter S. Emersone, editor. *Progress in Optical Fibers*. Nova Science Publishers, Inc., New York City, NY, 2011.
- [79] Davis J. Richardson, J. Nilsson, and W. A. Clarkson. High power fiber lasers: current status and future perspectives. *Journal of the Optical Society of America B Optical Physics*, 27:B63–92, 2010.
- [80] T. M. Shay and F. J. Duarte. Tunable fiber lasers. In *Tunable Laser Applications*.
- [81] Yiping Wang. Review of long period fiber gratings written by CO2 laser. *Journal of Applied Physics*, 108, 2010.

- [82] Raman Kashyap. *Fiber Bragg Gratings*. Academic Press, 2009.
- [83] Luigi Giacomazzi, L. Martin-Samos, A. Boukenter, Y. Ouerdane, S. Giarard, and N. Richard. Ge(2), Ge(1), and Ge-E' centers in irradiated Ge-doped silica: a first principles EPR study. *Optics Materials Express*, 5:1054–1064, 2015.
- [84] Kenneth O. Hill and Gerald Meltz. Fiber Bragg grating technology fundamentals and overview. *Journal of Lightwave Technology*, 15:1263–1276, 1997.
- [85] João M. P. Coelho, Marta Nespereira, Catarina Silva, Dionísio Pereira, and José Rebordão. Current developments in optical fiber technology. chapter 14. InTech, 2013.
- [86] Orazio Svelto. *Principles of Lasers*. Springer, 5 edition, 2010.
- [87] A. J. C. Grellier, N. K. Zayer, and C. N. Pannell. Heat transfer modelling in CO₂ laser processing of optical fibers. *Optics Communications*, 152:324–328, 1998.
- [88] Thomas Lee, Nibu A. George, GP Sureshkumar, P. Radhakrishnan, C. P. G. Vallabhan, and V. P. N. Nampoore. Chemical sensing with microbent optical fiber. *Optics Letters*, 26:1541–1543, 2001.
- [89] Brent L. Bachim. *Characteristics, Applications, and Properties of Carbon-Dioxide-Laser-Induced Long-Period Fiber Gratings*. PhD thesis, Georgia Institute of Technology, Atlanta, GA, 08 2005.
- [90] Marta Nespereira, D. Castro Alves, Joao M. P. Coelho, Fernando Monteiro, Manuel Abreu, and J. M. Rebordao. Repeatability analysis on LPFGs written by a CO₂ laser. *Proceedings of SPIE*, 9286, 2014.
- [91] S. G. Kosinski and A. M. Vengsarkar. Splicer-based long-period fiber gratings. *Optical Fiber Communication Conference and Exhibit Technical Digest*, pages 278–279, 1998.

- [92] Yuki Kondo, Kentaro Nouchi, and Tsuneo Mitsuyu. Fabrication of long-period fiber gratings by focused irradiation of infrared femtosecond laser pulses. *Optics Letters*, 24:646–648, 1999.
- [93] A. Martinez, M. Dubov, I. Khrushchev, and I. Bennion. Direct writing of fibre Bragg gratings by femtosecond laser. *Electronics Letters*, 40, 2004.
- [94] Makoto Fujimaki and Yoshimichi Ohki. Fabrication of long-period optical fiber gratings by use of ion implantation. *Optics Letters*, 25:88–89, 2000.
- [95] M. L. von Bibra and A. Roberts. Fabrication of long-period fiber gratings by use of focused ion beam irradiation. *Optics Letters*, 26:765–767, 2001.
- [96] Chunn-Yenn Lin and Lon A. Wang. Loss-tunable long period fibre grating made from etched corrugation structure. *Electronics Letters*, 35:1872–1873, 1999.
- [97] Chunn-Yenn Lin, Lon A. Wang, and Gia-Wei Chern. Corrugated long-period fiber gratings as strain, torsion, and bending sensors. *Journal of Lightwave Technology*, 19:1159–1168, 2001.
- [98] Joon Yong Cho and Kyung Shik Lee. A birefringence compensation method for mechanically induced long-period fiber gratings. *Optics Communications*, 213:281–284, 2002.
- [99] Ashish M. Vengsarkar, Paul J. Lemaire, Justin B. Judkins, Vikram Bhatia, Turan Erdogan, and John E. Sipe. Long-period fiber gratings as band-rejection filters. *Journal of Lightwave Technology*, 14:58–65, 1996.
- [100] Zhiyong Wang, James R. Heflin, Rogers H. Stolen, and Siddarth Ramachandran. Highly sensitive optical response of optical fiber long period gratings to nanometer-thick ionic self-assembled multilayers. *Applied Physics Letters*, 86, 2005.

- [101] L. Marques, F. U. Hernandez, S. W. James, S. P. Morgan, M. Clark, R. P. Tatam, and S. Korposh. Highly sensitive optical fiber long period grating biosensor anchored with silica core gold shell nanoparticles. *Biosensors and Bioelectronics*, 75:222–231, 2016.
- [102] Jiri Hromadka, Begum Tokay, Stephen James, Ralph P. Tatam, and Sergiy Korposh. Optical fibre long period grating gas sensor modified with metal organic framework thin films. *Sensors and Actuators B: Chemical*, 221:891–899, 2015.
- [103] Mateusz Smietana, Wojtek J. Bock, Predrag Mikulic, Andy Ng, Raja Chinnappan, and Mohammed Zourob. Detection of bacteria using bacteriophages as recognition elements immobilized on long-period fiber gratings. *Optics Express*, 19:7971–7978, 2011.
- [104] F. Chiavaioli, Palas Biswas, C. Trono, S. Bandyopadhyay, A. Giannetti, S. Tombelli, N. Basumallik, K. Dasgupta, and F. Baldini. Towards sensitive label-free immunosensing by means of turn-around point long period fiber gratings. *Biosensors and Bioelectronics*, 60:305–310, 2014.
- [105] F. Chiavaioli, Palas Biswas, C. Trono, A. Giannetti, S. Tombelli, S. Bandyopadhyay, N. Basumallick, K. Dasgupta, and F. Baldini. IgG/anti-IgG immunoassay based on a turn-around point long period grating. *Proceedings of SPIE*, 8935, 2014.
- [106] Xianfeng Chen, Kaiming Zhou, Lin Zhang, and Ian Bennion. Dual-peak long-period fiber gratings with enhanced refractive index sensitivity by finely tailored dispersion that uses the light cladding etching technique. *Applied Optics*, 46, 2007.
- [107] Sanjay Kher, Smita Chaubey, Jai Kishore, and Shrikant Madhusudan Oak. Detection of fuel adulteration with high sensitivity using turnaround point long period fiber gratings in B/Ge doped fibers. *IEEE Sensors Journal*, 13:4482–4486, 2013.

- [108] Tao Wang, Sergiy Korposh, Stephen James, Ralph Tatam, and Seung-Woo Lee. Optical fiber long period grating sensor with a polyelectrolyte alternate thin film for gas sensing of amine odors. *Sensors and Actuators B: Chemical*, 185:117–124, 2013.
- [109] Palas Biswas, Nandini Basumallick, Sankhyabrata Bandyopadhyay, Kamal Dasgupta, Ajay Ghosh, and Somnath Bandyopadhyay. Sensitivity enhancement of turn-around-point long period gratings by tuning initial coupling condition. *IEEE Sensors Journal*, 15:1240–1245, 2015.
- [110] Xu-dong Wang and Otto S. Wolfbeis. Fiber-optic chemical sensors and biosensors (2013-2015). *Analytical Chemistry*, 88:203–227, 2016.
- [111] W. E. Moerner. New directions in single-molecule imaging and analysis. *Proceedings of the National Academy of Sciences of the United States of America*, 104:12596–12602, 2007.
- [112] Daniel P. Campbell. chapter Interferometric Biosensors, pages 169–208. Springer, 2008.
- [113] Petr Kralik and Matteo Ricchi. A basic guide to real time PCR in microbial diagnostics: Definitions, parameters, and everything. *Frontiers in Microbiology*.
- [114] Ana-Maria Šimundić. Measures of diagnostic accuracy: Basic definitions. *The Journal of the International Federation of Clinical Chemistry and Laboratory Medicine*, 19, 2009.
- [115] Arthur Koch. *The Bacteria: Their Origin, Structure, Function and Antibiosis*. Springer, Dordrecht, 2006.
- [116] Karen Reiner. *Catalase test protocol*. American Society for Microbiology, 2010.

- [117] Sascha Sauer and Magdalena Kliem. Mass spectrometry tools for the classification and identification of bacteria. *Nature Reviews Microbiology*, 8:74–82, 2010.
- [118] Rudolf I. Amann, Wolfgang Ludwig, and Karl-Heinz Schleifer. Phylogenetic identification and in situ detection of individual microbial cells without cultivation. *Microbiological Reviews*, 59:143–169, 1995.
- [119] Kenneth L. Muldrew. Molecular diagnostics of infectious disease. *Current Opinion in Pediatrics*, 21:102–111, 2009.
- [120] Martin Dufva. *DNA microarrays for biomedical research: methods and protocols*. Humana Press, 2009.
- [121] Robert B. Cody, Casey R. McAlpin, Christopher R. Cox, Kirk R. Jensen, and Kent J. Voorhees. Identification of bacteria by fatty acid profiling with direct analysis in real time mass spectrometry. *Rapid Communications in Mass Spectrometry*, 29, 2015.
- [122] Mark H. Ebell, Mindy A. Smith, Henry C. Barry, Kathy Ives, and Mark Carey. Does this patient have strep throat? *Journal of the American Medical Association*, 284, 2000.
- [123] Paul de Figueiredo, Thomas A. Richt, Allison Rice-Ficht, Carlos A. Rossetti, and L. Garry Adams. Pathogenesis and immunobiology of Brucellosis: Review of *Brucella*-host interactions. *The American Journal of Pathology*, 185, 2015.
- [124] Jack C. Rhyan, Pauline Nol, Christine Quance, Arnold Gertonson, John Belfrage, Lauren Harris, Kelly Straka, and Suelee Robbe-Austerman. Transmission of brucellosis from elk to cattle and bison, greater Yellowstone area, USA, 2002-2012. *Emerging Infectious Diseases*, 19:1992–1995, 2013.

- [125] Jacques Godfroid. Brucellosis in livestock and wildlife: zoonotic diseases without pandemic potential in need of innovative one health approaches. *Archives of Public Health*, 75, 2017.
- [126] Rita M. Traxler, Mark W. Lehman, Elizabeth A. Bosserman, Marta A. Guerra, and Theresa L. Smith. A literature review of laboratory-acquired brucellosis. *Journal of Clinical Microbiology*, 51:3055–3062, 2013.
- [127] Centers for Disease Control and Prevention. Brucellosis, 2019. <https://www.cdc.gov/brucellosis/index.html>, 2019-01-11.
- [128] D. Baud and G. Greub. Intracellular bacteria and adverse pregnancy outcomes. *Clinical Microbiology and Infection*, 17:1312–1322, 2011.
- [129] A. Caminiti, F. Pelone, S. Battisti, F. Gamberale, R. Colafrancesco, M. Sala, G. La Torre, U. Della Marta, and P. Scaramozzino. Tuberculosis, brucellosis, and leucosis in cattle: a cost description of eradication programmes in the region of Lazio, Italy. *Transboundary and Emerging Diseases*, 64:1493–1504, 2016.
- [130] David J. Griffiths. *Introduction to Electrodynamics*. Prentice Hall, 1999.
- [131] Dongqing Li, editor. *Inversion Symmetry*, pages 872–872. Springer US, Boston, MA, 2008.
- [132] J. A. Armstrong, N. Bloembergen, J. Ducuing, and P. S. Pershan. Interactions between light waves in a nonlinear dielectric. *Physical Review*, 127:1918–1939, 1962.
- [133] Martin M. Fejer, G. A. Magel, Dieter H. Jundt, and Robert L. Byer. Quasi-phase-matched second harmonic generation: tuning and tolerances. *IEEE Journal of Quantum Electronics*, 28:2631–2654, 1992.

- [134] T. Thao Tran, Hongwei Yu, James M. Roninelli, Kenneth R. Poeppelmeier, and P. Shiv Halasyamani. Deep ultraviolet nonlinear optical materials. *Chemistry of Materials*, 28:5238–5258, 2016.
- [135] P. A. Franken, G. Weinrich, C. W. Peters, and A. E. Hill. Generation of optical harmonics. *Physical Review Letters*, 7:118–121, 1961.
- [136] J. Gopalakrishnan, K. Ramesha, K. Kasthuri Rangan, and Sondal Pandey. In search of inorganic nonlinear optical materials for second harmonic generation. *Journal of Solid State Chemistry*, 148:75–80, 1999.
- [137] Celest Samyn, Thierry Verbiest, and André Persoons. Second-order non-linear optical polymers. *Macromolecular Rapid Communications*, 21:1–15, 2000.
- [138] Abdur Razzaque Sarker. Growth of large size lithium niobate single crystals of high quality by tilting-mirror-type floating zone method. *Materials Research*, 19:505–512, 2016.
- [139] L. E. Myers, R. C. Eckardt, M. M. Fejer, R. L. Byer, W. R. Bosenberg, and J. W. Pierce. Quasi-phase-matched optical parametric oscillators in bulk periodically poled linbo3. *Journal of the Optical Society of America B*, 12:2102–2116, 1995.
- [140] M. Aillerie, P. Bourson, M. Mostefa, F. Abdi, and M. D. Fontana. Photorefractive damage in congruent linbo3. part ii. magnesium doped lithium niobate crystals. *Journal of Physics: Conference Series*, 416, 2013.
- [141] John D. Bierlin and Herman Vanherzeele. Potassium titanyl phosphate: properties and new applications. *Journal of the Optical Society of America B.*, 6:622–633, 1989.
- [142] Nataliya E. Novikova, Nataliya I. Sorokina, Igo A. Verin, Olga A. Alekseeva, Ekate-

- rina I. Orlova, Valentina I. Voronkova, and Michael Tseitlin. Structural reasons for the nonlinear optical properties of KTP family single crystals. *Crystals*, 8.
- [143] J. J. de Yoreo, A. K. Burnham, and P. K. Whitman. Developing kh₂po₄ and kd₂po₄ crystals for the world's most powerful laser. *Journal of International Materials Review*, 47:113–152, 2002.
- [144] Duanliang Wang, Tingbin Li, Shenglai Wang, Jiyang Wang, Chuanying Shen, Jianxu Ding, Weidong Li, Pingping Huang, and Chengwei Lu. Characteristics of nonlinear absorption and refractions for kdp and dkdp crystals. *Optics Materials Express*, 7:533–541, 2017.
- [145] Petra Becker. Borate materials in nonlinear optics. *Advanced Materials*, 10:979–992, 1998.
- [146] D. N. Nikogosyan. Beta barium borate (bbo): A review of its properties and applications. *Applied Physics A.*, 52:359–368, 1991.
- [147] Antonio Facchetti. pi-conjugated polymers for organic electronics and photovoltaic cell applications. *Chemistry of Materials*, 23:733–758, 2011.
- [148] M. Blanca Ros. Organic materials for nonlinear optics. In Juan J. Novoa, Dario Braga, and Lia Addadi, editors, *Engineering of Crystalline Materials Properties*. Springer, 2007.
- [149] Colin Reese and Zhenan Bao. Organic single-crystal field-effect transistors. *Materials Today*, 10:20–27, 2007.
- [150] Atsushi Sugita, Yasuaki Sato, Kazuma Ito, Kenta Murakami, Yasuaki Tamaki, Nobuyuki Mase, Yoshimasa Kawata, and Shigeru Tasaka. Second-order nonlinear op-

- tical susceptibilities of nonelectrically poled dr1-pmma guest-host polymers. *Journal of Physical Chemistry B*, 117:14857–14864.
- [151] A. Facchetti, E. Annoni, L. Beverina, M. Morone, P. Zhu, T. J. Marks, and G. A. Pagani. Very large electro-optic responses in H-bonded heteroaromatic films grown by physical vapor deposition. *Nature Materials*, 3:910–917, 2004.
- [152] Kai Chen, Cemil Durak, Akhilesh Garg, Charles Brands, Richey M. Davis, James R. Heflin, and Hans D. Robinson. Interface effects in plasmon-enhanced second-harmonic generation from self-assembled multilayer films. *Journal of the Optical Society of America B*, 27:92–98, 2010.
- [153] Patrick Neyman. *Second-order nonlinear optical characteristics of nanoscale self-assembled multilayer organic films*. PhD thesis, Virginia Polytechnic Institute, Blacksburg, VA, 06 2004.
- [154] James R. Heflin, C. Figura, D. Marciu, Y. Liu, and R. O. Claus. Thickness dependence of second-harmonic generation in thin films fabricated from ionically self-assembled monolayers. *Applied Physics Letters*, 74:495–497, 1999.
- [155] Kevin E. Van Cott, Matthew Guzy, Patrick Neyman, Charles Brands, J. R. Heflin, Harry W. Gibson, and Richey M. Davis. Layer-by-layer deposition and ordering of low-molecular-weight dye molecules for second-order nonlinear optics. *Angewandte Chemie International Edition*, 41:3236–3238, 2002.
- [156] C. Brands, P. J. Neyman, M. T. Guzy, S. M. Shah, R. M. Davis, K. E. Van Cott, H. Wang, H. W. Gibson, and J. R. Heflin. In situ second harmonic generation measurements of the formation of ionically self-assembled monolayers. *Proceedings of SPIE*, 4461, Linear and Nonlinear Optics of Organic Materials:311–318, 2001.

- [157] Elsa Gamire. Nonlinear optics in daily life. *Optics Express*, 21:30532–30544, 2013.
- [158] National Institute of Standards and Technology (NIST). Green laser pointer hazard: High infrared power levels found in some green lasers. *ScienceDaily*.
- [159] Lars Schneider and Wolfgang Peukert. Review: Second harmonic generation spectroscopy for in situ and online characterization of particle surface properties. *Particles and Particle Systems Characterization*, 23:351–259, 2007.
- [160] W. Daum, H. J. Krause, U. Reichel, and H. Ibach. Identification of strained silicon layers at si-sio₂ interfaces and clean si surfaces by nonlinear optical spectroscopy. *Physical Review Letters*, 71:1234–1237, 1993.
- [161] X. Zhuang, P. B. Miranda, D. Kim, and Y. R. Shen. Mapping molecular orientation and conformation at interfaces by surface nonlinear optics. *Physical Review B*, 59:12632–12640, 1999.
- [162] Poul B. Petersen and Richard J. Saykally. On the nature of ions at the liquid water surface. *Annual Review of Physical Chemistry*, 57:333–364, 2006.
- [163] Isaac Freund and Moshe Deutsch. Second-harmonic microscopy of biological tissue. *Optics Letters*, 11:94–96, 1986.
- [164] Robert Hellwarth and Paul Christensen. Nonlinear optical microscopic examination of structure in polycrystalline ZnSe. *Optics Communications*, 12:318–322, 1974.
- [165] Paul Campagnola. Second harmonic generation imaging microscopy: applications to disease diagnostics. *Anal. Chem.*, 83:3224–3231, 2011.
- [166] Warren R. Zipfel, Rebecca M. Williams, Richard Christie, Alexander Yu Nikitin, Bradley T. Hyman, and Watt W. Webb. Live tissue intrinsic emission microscopy us-

- ing multiphoton-excited native fluorescence and second harmonic generation. *PNAS*, 100:7075–7080, 2003.
- [167] Ellen C. Jensen. Overview of live-cell imaging: requirements and methods used. *The Anatomical Record*, 296, 2013.
- [168] Larry R. Dalton, Peter Günter, Mojca Jazbinsek, O-Pil Kwon, and Philip A. Sullivan. *Organic Electro-Optics and Photonics: Molecules, Polymers, and Crystals*. Cambridge University Press, 2015.
- [169] Z. L. Sàmsón, K. F. MacDonald, F. De Angelis, K. Knight, C. C. Huang, E. Di Fabrizio, D. W. Hewak, and N. I. Zheludev. Metamaterial electro-optic switch of nanoscale thickness. *Applied Physics Letters*, 96, 2010.
- [170] Ke Liu, Chen Ran Ye, Sikandar Khan, and Volker J. Sorger. Review and perspective on ultrafast wavelength-size electro-optic modulators. *Laser and Photonics Reviews*, 9:172–194, 2015.
- [171] Michal Lipson. Compact electro-optic modulators on a silicon chip. *IEEE Journal of Selected Topics in Quantum Electronics*, 12, 2006.
- [172] Cheng Wang, Mian Zhang, Brian Stern, Michal Lispon, and Marko Lončar. Nanophotonic lithium niobate electro-optic modulators. *Optics Express*, 26, 2018.
- [173] Y. Enami, C. T. Derose, D. Mathine, C. Loychik, C. Greenlee, R. A. Norwood, T. D. Kim, J. Luo, Y. Tian, A. K. y. Jen, and N. Peyghambarian. Hybrid polymer/sol-gel waveguide modulators with exceptionally large electro-optic coefficients. *Nature Photonics*, 1:180–185, 2007.
- [174] Anatoly V. Zayats, Igor I. Smolyaninov, and Alexei A. Maradudin. Nano-optics of surface plasmon polaritons. *Physics Reports*, 408:131–314, 2005.

- [175] Junichi Takahara, Suguru Yamagishi, Hiroaki Taki, Akihiro Morimoto, and Tetsuro Kobayashi. Guiding of a one-dimensional optical beam with nanometer diameter. *Optics Letters*, 22:475–477, 1997.
- [176] Kh. V. Nerkararyan. Superfocusing of a surface polariton in a wedge-like structure. *Physics Letters A*, 237:103–105, 1997.
- [177] Dmitri K. Gramotnev and Sergey I. Bozhevolnyi. Plasmonics beyond the diffraction limit. *Nature Photonics*, 4:83–91, 2010.
- [178] George H. Chan, Jin Zhao, Erin M. Hicks, George C. Schatz, and Richard P. Van Duyne. Plasmonic properties of copper nanoparticles fabricated by nanosphere lithography. *Nano Letters*, 7:1947–1952, 2007.
- [179] Alberto Comin and Liberato Manna. New materials for tunable plasmonic colloidal nanocrystals. *Chemical Society Review*, 43:3957–3975, 2014.
- [180] Gustav Mie. Beiträge zur optik trüber medien, speziell kolloidaler metallösungen. *Annalen der Physik*, 330, 1908.
- [181] Bruce T. Draine and Piotr J. Flatau. Discrete-dipole approximation for scattering calculations. *Journal of the Optical Society of America A*, 11:1492–1499, 1994.
- [182] Christy L. Haynes and Richard P. Van Duyne. Nanosphere lithography: a versatile nanofabrication tool for studies of size-dependent nanoparticle optics. *The Journal of Physical Chemistry B*, 105:5599–5611, 2001.
- [183] Xiaolu Huang, Daniel Ratchford, Pehr E. Pehrsson, and Junghoon Yeom. Fabrication of metallic nanodisc hexagonal arrays using nanosphere lithography and two-step lift-off. *Nanotechnology*, 27, 2016.

- [184] Rongchao Jin, YunWei Cao, Chad A. Mirkin, K. L. Kelly, George C. Schatz, and J. G. Zheng. Photoinduced conversion of silver nanospheres to nanoprisms. *Science*, 294:1901–1903, 2001.
- [185] Rongchao Jin, Y. Charles Cao, Encai Hao, Gabriella S. Métraux, George C. Schultz, and Chad A. Mirkin. Controlling anisotropic nanoparticle growth through plasmon excitation. *Nature*, 425:487–490, 2003.
- [186] Can Xue, Gabriella S. Métraux, Jill E. Millstone, and Chad A. Mirkin. Mechanistic study of photomediated triangular silver nanoprism growth. *Journal of the American Chemical Society*, 130:8337–8344, 2008.
- [187] Isabel Pastoriza-Santos and Luis M. Liz-Marzan. Colloidal silver nanoplates: State of the art and future challenges. *Journal of Materials Chemistry*, 18:1724–1737, 2008.
- [188] W. J. Nie, Y. X. Zhang, H. H. Yu, R. Li, R. Y. He, J. Wang, R. Hubner, R. Bottger, S. Q. Zhou, H. Amekura, and F. Chen. Plasmonic nanoparticles embedded in single crystals synthesized by gold ion implantation for enhanced optical nonlinearity and efficient q-switched lasing. *Nanoscale*, 10:4228–4236, 2018.
- [189] Chi Pang, Rang Li, Ziqi Li, Ningning Dong, Chen Cheng, Weijie Nie, Roman Bottger, Shengqiang Zhou, Jun Wang, and Feng Chen. Lithium niobate crystal with embedded au nanoparticles: A new saturable absorber for efficient mode-locking of ultrafast laser pulses at 1 μm . *Advanced Optical Materials*, 6, 2018.
- [190] Chi Pang, Rang Li, Yuxia Zhang, Ziqi Li, Ningning Dong, Liang We, Haohai Yu, Jun Wang, Feng Ren, and Feng Chen. Tailoring optical nonlinearities of linbo3 crystals by plasmonic silver nanoparticles for broadband saturable absorbers. *Optics Express*, 26:31276–31289, 2018.

- [191] Miki Ishifuji, Masay Mitsuishi, and Tokuji Miyashita. Bottom-up design of hybrid polymer nanoassemblies elucidates plasmon-enhanced second harmonic generation from nonlinear optical dyes. *Journal of the American Chemical Society*, 131:4418–4424, 2009.
- [192] Dennis Lehr, Jörg Reinhold, Illia Thiele, Holger Hartun, Kay Dietrich, Christoph Menzel, Thomas Pertsch, Ernst-B. Kley, and Andreas Tünnermann. Enhancing second harmonic generation in gold nanoring resonators filled with lithium niobate. *Nanoletters*, 15:1025–1030, 2015.
- [193] Wenjun Fan, Shuang Zhang, K. J. Malloy, S. R. J. Brueck, N. C. Panoiu, and R. M. Osgood. Second harmonic generation from patterned gaas inside a subwavelength metallic hole array. *Optics Express*, 14:9570–9575, 2006.
- [194] Eduardo Yraola, Pablo Molina, José L. Plaza, Mariola O. Ramírez, and Luisa E. Bausà. Spontaneous emission and nonlinear response enhancement by silver nanoparticles in a Nd³⁺-doped periodically poled LiNbO₃ laser crystal. *Advanced Materials*, 25, 2013.
- [195] Flavia Timpu, Nicholas R. Hendricks, Mihail Petrov, Songbo Ni, Claude Renaut, Heiko Wolf, Lucio Isa, Yuri Sivshar, and Rachel Grange. Enhanced second-harmonic generation from sequential capillarity-assisted particle assembly of hybrid nanodimers. *Nano Letters*, 17:5381–5388.
- [196] Heykel Aouani, Mohsen Rahmani, Miguel Navarro-Cia, and Stefan A. Maier. Third-harmonic-upconversion enhancement from a single semiconductor nanoparticle coupled to a plasmonic antenna. *Nature Nanotechnology*, 9:290–294, 2014.
- [197] Ye Pu, Rachel Grange, Chia-Lung Hsieh, and Demetric Psaltis. Nonlinear optical properties of core-shell nanocavities for enhanced second-harmonic generation. *Physical Review Letters*, 104, 2010.

- [198] Yu Zhang, Alejandro Manjavacas, Nathaniel J. Hogan, Linan Zhou, Ciceron Ayala-Orozco, Liangliang Dong, Jared K. Day, Peter Nordlander, and Naomi J. Halas. Toward surface plasmon-enhanced optical parametric amplification (SPOPA) with engineered nanoparticles: A nanoscale tunable infrared source. *Nano Letters*, 16:3373–3378, 2016.
- [199] Patricia C. Weber, D. H. Ohlendorf, J. J. Wendoloski, and F. R. Salemme. Structural origins of high-affinity biotin binding to streptavidin. *Science*, 243:85–88, 1989.
- [200] Pierce Biotechnology at Thermo Scientific. *EZ-Link Sulfo-NHS-LC-LC-Biotin*, 2016.
- [201] Ziwei Zuo. Fabrication of intensity-based long-period-grating fiber sensor with CO₂ laser for refractive index sensing. Master’s thesis, Virginia Polytechnic Institute, Blacksburg, VA, 5 2015.
- [202] Yunqi Liu and Kin Seng Chiang. CO₂ laser writing of long-period fiber gratings in optical fibers under tension. *Optics Letters*, 33:1933–1935, 2008.
- [203] Xinwei Lan, Qun Han, Tao Wei, Jie Huang, and Hai Xiao. Turn-around-point long-period fiber gratings fabricated by CO₂ laser point-by-point irradiations. *IEEE Photonics Technology Letters*, 23:1664–1666, 2011.
- [204] Leonid M. Goldenberg, Victor Lisinetskii, and Sigurd Schrader. Fast and simple fabrication of organic bragg mirrors; application to plastic microchip lasers. *Laser Physics Letters*, 10, 2013.
- [205] Thierry Verbiest, Koen Clays, and Vincent Rodriguez. *Second-order nonlinear optical characterization techniques: an introduction*. CRC Press.
- [206] P. D. Maker, R. W. Terhune, M. Nisenoff, and C. M. Savage. Effections of dispersion and focusing on the production of optical harmonics. *Physical Review Letters*, 8, 1962.

- [207] J. Jerphagnon and S. K. Kurtz. Maker fringes: A detailed comparison of theory and experiment for isotropic and uniaxial crystals. *Journal of Applied Physics*, 41, 1970.
- [208] Dee Griffin, M. M. Chengappa, Jennifer Kuszak, and D. Scott McVey. Bacterial pathogens of the bovine respiratory disease complex. *Veterinary Clinics of North America: Food Animal Practice*, 26:381–394, 2010.
- [209] Mohammad I. Braiwish, Brent L. Bachim, and Thomas K. Gaylord. Prototype CO₂ laser-induced long-period fiber grating variable optical attenuators and optical tunable filters. *Applied Optics*, 49:1789–1793, 2004.
- [210] Smita Chaubey, Sanjay Kher, Jai Kishore, and S. M. Oak. CO₂ laser-inscribed low-cost, shortest-period long-period fibre grating in B-Ge co-doped fibre for high-sensitivity strain measurement. *Pramana - Journal of Physics*, 82:373–377, 2014.
- [211] Xinwei Lan, Qun Han, Jie Huang, Xia Fang, Tao Wei, Zhan Gao, and Hai Xiao. High order mode long-period fiber grating refractive index sensor based on intensity measurement. *Proceedings of SPIE*.
- [212] Nikhil R. Jana, Latha Gearheart, and Catherine J. Murphy. Wet chemical synthesis of high aspect ratio cylindrical gold nanorods. *Journal of Physical Chemistry B*, 105:4065–4067, 2001.
- [213] L. Vidgerman and E. R. Zubarev. High-yield synthesis of gold nanorods with longitudinal SPR peak greater than 1200 nm using hydroquinone as a reducing agent. *Chemistry of Materials*, 25:1450–1457, 2013.
- [214] Hoang Minh Ngo and Isabelle Ledoux-Rak. Second harmonic generation from silver nanoparticles in aqueous solution with different protective agents. *Proceedings of SPIE*, 9171, Nanobiosystems: Processing, Characterization, and Applications VII, 2014.